The Radio Continuum Halos of the Edge-on Galaxies NGC 891 and NGC 4565

Dissertation
zur
Erlangung des Doktorgrades (Dr. rer. nat.)

von

Philip Schmidt

aus
Herford

angefertigt am
Max-Planck-Institut für Radioastronomie

vorgelegt der
Mathematisch-Naturwissenschaftlichen Fakultät
der
Rheinischen Friedrich-Wilhelms-Universität Bonn

im Februar 2016

Angefertigt mit Genehmigung der Mathematisch-Naturwissenschaftlichen Fakultät der
Rheinischen Friedrich-Wilhelms-Universität Bonn

1. Referent: Prof. Dr. Michael Kramer

2. Referent: Prof. Dr. Pavel Kroupa

Tag der Promotion: 24.06.16

Erscheinungsjahr: 2016

Abstract

The halos[1] of spiral galaxies are complex entities consisting of multiple matter components, generally including neutral and ionized gas phases, cosmic rays (CRs), dust, as well as extraplanar stars. The detection of extraplanar synchrotron radiation from cosmic-ray electrons (CREs) furthermore shows that halos, like galactic disks, are magnetized. Halos play an integral part in the circulation of matter in galaxies, as their gaseous content is closely connected to processes occurring in galactic disks, such as star formation. At the same time, halos represent an interface between the disk-internal interstellar medium (ISM) and the intergalactic medium (IGM). However, a coherent picture of how halos are connected to disks and to their environments, as well as of their role in galaxy evolution, has yet to be observationally established. Even so-called normal spiral galaxies are diverse in their physical properties, and studying their extraplanar matter distribution is a key contribution to our understanding of this diversity.

Edge-on galaxies are ideal laboratories to investigate the connection of halos to disks and to the IGM, since only in an edge-on view the properties of halos can be directly studied as a function of distance perpendicular to the disk. Two prominent examples of edge-on galaxies, NGC 891 and NGC 4565, which differ greatly in their star formation rates (SFRs), are the subject of this thesis. The main focus of the studies presented here is on the propagation of cosmic rays within the halos of the two galaxies and on their extraplanar magnetic field structure. Cosmic rays and galactic magnetic fields are traced by synchrotron radiation of the CREs, which is emitted in the radio continuum frequency regime. This thesis is primarily based on observations of NGC 891 and NGC 4565 in the framework of Continuum HAlos of Nearby Galaxies – an EVLA Survey (CHANG-ES). This full-polarization survey makes use of the novel broad-band technology of the recently upgraded Karl G. Jansky Very Large Array (JVLA) to study a sample of 35 edge-on galaxies at radio frequencies of 1.5 GHz (L-band) and 6 GHz (C-band), at various spatial resolutions.

We investigate the spectral index distribution in NGC 891 and NGC 4565 at an angular resolution of 12″. By comparing our results for the two galaxies, we find that spectral indices are consistently steeper in NGC 4565, in the halo as well as in the disk. In this galaxy, the steepening of the local spectra between the two observing frequencies is consistent with single-shot CR injection models rather than continuous CR injection. We conclude from this that NGC 4565 must locally feature very low CR injection rates compared to those in NGC 891, which would be consistent with its low SFR and would serve as a plausible explanation for its low-level disk and halo emission.

By fitting two-component (disk and halo) exponential profiles to the vertical emission distribution, we determine vertical scale heights at several positions along the major axis in both

[1] Throughout this thesis, the term “halo” describes the extraplanar distribution of baryonic matter in galaxies, as opposed to dark matter halos.

galaxies. On average, we obtain roughly similar scale heights for the halo components of the two galaxies, as already known from previous studies at lower spatial resolutions. However, while in NGC 891 the scale heights are basically identical at 1.5 and 6 GHz, for NGC 4565 we obtain slightly different results at the two frequencies. These findings tentatively indicate that CR transport is dominated by convection in NGC 891 and at least to a significant degree happening by diffusion in NGC 4565.

The average equipartition magnetic field strength in the disk is $10\,\mu$G for NGC 891 and $5\,\mu$G for NGC 4565. For the case of NGC 891, we model the CR transport in the halo by solving the vertical diffusion-loss equation. Along with the vertical emission profiles at 1.5 and 6 GHz, we simultaneously model the vertical decrease of the total magnetic field strength. We find that our data are fitted well by a purely convective CR propagation model, with convection speeds of likely more than $300\,\mathrm{km\,s^{-1}}$, indicating that CRs are able to leave the gravitational potential of the galaxy and escape as a galactic wind. Moreover, we obtain a halo magnetic field scale height $\approx 40\%$ lower than the expected equipartition value, which shows that the assumption of energy equipartition between CRs and magnetic fields is not valid in the halo of NGC 891.

To study the magnetic field structure in NGC 891 and NGC 4565, we analyze our polarization data by applying the technique of rotation measure (RM) synthesis. The insights gained from the determined RM distributions are rather limited, as the L-band data are severely affected by depolarization through differential Faraday rotation. Nonetheless, we are able to show by these measurements that NCG 4565 clearly possesses a non-plane-parallel halo field, which is probably X-shaped (like in NGC 891), as predicted by galactic dynamo models that include disk-halo outflows.

Our high-resolution ($3''$) total intensity maps of NGC 4565 reveal a ring-shaped structure of the inner spiral arms that was previously only seen in the dust and molecular gas components. Given the high inclination of 86°, the fact that the front side of this ring-shaped pattern is resolved from its back side implies that these inner spiral arms must be comparatively thin, either in the vertical or coplanar direction.

Contents

1 Introduction

A commonly accepted view on the formation and evolution of galaxies is that the massive galaxies observed in the local universe are the product of a series of mergers between less massive progenitor galaxies. The physical properties of an individual galaxy therefore largely depends on its specific merger history, star-forming history, and external environment. Hence, it is hardly surprising that even among evolved massive spiral galaxies (such as our own Milky Way) that show only minor signs of interaction with neighbouring galaxies or are entirely isolated, we still observe a relatively broad range in overall morphology, size, mass, luminosity, star-formation rate (SFR), distribution of stars and the interstellar medium (ISM), and kinematical properties.

An observational result that is still poorly understood in the context of galaxy evolution is that spiral galaxies differ considerably in the distribution of (baryonic) matter outside of their star-forming disks. Primarily as a result of feedback from supernovae and, if present, active galactic nuclei (AGNs), most spiral galaxies possess halos consisting of multiple gas phases, as multi-wavelength observations of galaxies seen at high inclination angles have shown. Much like the ISM of the disk, this extraplanar gas typically includes cold neutral hydrogen (HI), warm and hot ionized gas (HII and other species), as well as molecular gas, such as CO. However, radiation from galactic halos was first detected at radio continuum frequencies, which are primarily associated with synchrotron radiation of cosmic-ray electrons (CREs). These particles have relativistic energies and are believed to have been accelerated in shock fronts of supernova remnants. The observation of synchrotron emission of CREs (which is linearly polarized) implies that they are subjected to the Lorentz force and hence that magnetic fields are present wherever this radiation is detected. The existence of a synchrotron halo was proposed early on by Shklovsky (1952) for the Milky Way, and likewise for M31 by Baldwin (1954). However, it was the identification of a halo in the edge-on galaxy NGC 4631 at 610 MHz and 1.4 GHz by Ekers & Sancisi (1977) and at 2.7 and 4.8 GHz by Wielebinski & von Kap-Herr (1977) that initiated the investigation of galactic radio halos. Since then, synchrotron halos have been found for the majority of edge-on galaxies observed, often extending up to several kpc from the disk in vertical direction (whereas their radial extent hardly exceeds that of the stellar disk). Recently, a study of a statistically relevant sample of 35 edge-on spiral galaxies has shown that spiral galaxies without significant extraplanar synchrotron emission are, if anything, a rare exception (Wiegert et al. 2015). Still, the intensity and vertical extent of radio halos vary considerably between individual galaxies.

The close connection between radio continuum emission in galactic halos and star-forming activity in the underlying disk was first indicated by the discovery of an extraplanar diffuse ionized gas (eDIG) component in several star-forming galaxies (Rand et al. 1990; Dettmar 1992; Dahlem et al. 1994, 1995; Rossa & Dettmar 2003a,b; Rossa et al. 2008). In the case of NGC 891 even a spatial correlation between the radio continuum and diffuse Hα emission (the

latter tracing the eDIG) was found (Dahlem et al. 1994). Further halo constituents showing a direct connection to star formation include supernova-heated thermal gas emitting in the X-ray regime (e.g. Tüllmann et al. 2006) as well as extraplanar dust (e.g. Howk & Savage 1997; Hughes et al. 2014; Neininger & Dumke 1999). Hence, a lot of theoretical effort that links disk-halo interaction to star formation has been undertaken. Corresponding models describe processes auch as the blowout of supernova-generated superbubbles in the ISM (Mac Low & Ferrara 1999), galactic chimneys (Norman & Ikeuchi 1989), and galactic fountains, in which the blown-out material eventually condenses and falls back to the disk (Shapiro & Field 1976).
In spite of the substantial evidence for a connection between extraplanar gas and star formation, there are observational indications that star-forming activity alone is not sufficient as an explanation for the existence of galactic halos. For instance, optical line ratios seem to suggest that the ionization of the eDIG requires mechanisms other than photoionization from disk-based sources like massive stars (Tüllmann et al. 2000; Rand et al. 2011). Shocks and magnetic reconnection qualify as alternative sources of heating (Zimmer et al. 1997). In particular, the vertical scale height of a radio continuum halo does not seem to depend on the SFR (Krause 2009, 2011; Dumke & Krause 1998). For a small sample of edge-on galaxies ranging in halo extent and intensity from one of the weakest known cases (NGC 4565) to some of the brightest ones (NGC 253, NGC 891), and likewise covering a broad range in SFR and total magnetic field strength, similar exponential scale heights of 1.8 ± 0.2 kpc for the halo component at 4.85 GHz were found. For the disk component at the same frequency, a mean scale height of 300 ± 50 pc was measured. From the small scatter in the halo scale heights of the galaxies in spite of their different magnetic field strengths and hence different CRE lifetimes (since CREs generally lose a significant portion of their energy via synchrotron radiation), it was inferred that the CRE bulk outflow speed scales with the average total field strength and with SFR (Krause 2009).
Because CREs at higher energies are more strongly affected by synchrotron losses, the extent of radio continuum halos is expected to decrease with increasing observing frequency. The magnetic field strength is usually highest in the central regions of galaxies, implying higher central synchrotron loss rates. A common consequence of this are dumbbell-shaped radio halos, a prime example of which is that of NGC 253. From the synchrotron scale heights of this galaxy at several frequencies and the corresponding CRE lifetimes inferred from synchrotron, inverse-Compton, and adiabatic losses, Heesen et al. (2009a) determined a CRE bulk speed of $\approx 300\,\mathrm{km\,s^{-1}}$.

Since both the CRs and the magnetic field are strongly coupled to the ionized gas via the so-called streaming instability (Kulsrud & Pearce 1969), in disk-halo outflows all three components are to a certain degree transported together by convection. In addition, CRs can diffuse along or across magnetic field lines (e.g. Buffie et al. 2013). The brightness and shape of radio continuum halos appear to be influenced considerably by the relative amounts of convective and diffusive vertical CR transport. While the theoretical foundation of CR propagation from the disk into the halo was laid early on by e.g. Strong (1978), Lerche & Schlickeiser (1981, 1982), and Pohl & Schlickeiser (1990), the quality of the radio data at that time did not yet allow for conclusive observational testing.
If the convection speed exceeds the escape velocity of the galaxy, the outflowing gas is able to leave its gravitational potential as a galactic wind (along with the CRs), rather than circulating in a galactic fountain flow. The idea that CRs could in fact be the driving force in galactic

outflows was initially brought up by Ipavich (1975). This and further efforts in modelling CR-driven outflows (Breitschwerdt et al. 1991, 1993; Dorfi & Breitschwerdt 2012; Zirakashvili et al. 1996) indicated that the formation of a CR-driven wind is possible under a variety of physical conditions in the disk. Owing to the coupling between the CRs and the ionized gas, such a wind is expected to remove considerable amounts of mass, energy, and angular momentum (Ptuskin et al. 1997) and can thus significantly influence galactic evolution, e.g. in terms of altered metallicity gradients and SFRs. Galactic winds are furthermore being debated as a possible mechanism of magnetization of the intergalactic medium (IGM) (Kronberg et al. 1999). Evidence of how far magnetic fields in galaxy halos extend into the IGM is, however, observationally limited by the CRE energy losses.

While radio polarization observations of face-on galaxies so far have allowed extensive studies of the magnetic field structure in galactic disks (e.g. Krause 1993; Beck 2015; Ehle et al. 1996; Berkhuijsen et al. 1997; Fletcher et al. 2011; Harnett et al. 2004; Beck 2007; Tabatabaei et al. 2008; Frick et al. 2016), halo fields are still only marginally explored, since they are comparatively weak and less detectable due to CRE energy losses, as mentioned above. In those cases where polarized emission has been detected at large enough heights above the disk plane of edge-on galaxies (e.g. Heesen et al. 2009b; Krause 2009; Krause et al. 2006; Mora & Krause 2013; Dahlem et al. 1997; Soida et al. 2011), they show X-shaped halo fields, in addition to plane-parallel disk fields. Based on the present knowledge about galactic outflows, as outlined above, it is likely that magnetic fields in halos are transported there by outflows from the underlying disks. While the X-shaped morphology of halo fields might be simply a consequence of disk flaring at large radii (as commonly observed in HI, e.g. Brinks & Burton 1984; Kalberla & Kerp 2009; Zschaechner et al. 2012; Vollmer et al. 2015), X-shaped fields are predicted by models that combine field amplification by an α-Ω dynamo with disk-halo outflows. The concept of the α-Ω dynamo (e.g. Parker 1979; Ruzmaikin et al. 1988; Beck et al. 1996; Lesch & Chiba 1997) involves differential rotation as well as the bending of plane-parallel field lines in the vertical direction, caused by e.g. supernova explosions. Reproducing the X-shape of halo fields viewed edge-on requires that outflows at velocities of the order of a few hundred $\mathrm{km\,s^{-1}}$ are included in the modelling (Brandenburg et al. 1993; Moss et al. 2010). Such dynamo models predict symmetric quadrupolar halo fields, which actually have been indirectly evidenced for a number of moderately inclined galaxies from asymmetries in their polarized emission (Braun et al. 2010). Similarly, the magnetohydrodynamic (MHD) simulations of CR-driven dynamos by Hanasz et al. (2009) result in X-shaped halo field structures. On the other hand, the simulations of Dalla Vecchia & Schaye (2008), which do not incorporate magnetic fields, show X-shaped gas outflows of young galaxies as a consequence of pressure gradients.

In order to take the investigation of galactic halos to unprecedented levels of both consistency and sensitivity, Irwin et al. (2012a) observed a comprehensive sample of 35 nearby edge-on galaxies, utilizing the state-of-the-art capabilities of the recently upgraded Karl G. Jansky Very Large Array (JVLA, see Sect. 1.3). This extensive survey is called Continuum HAlos of Nearby Galaxies – an EVLA Survey (CHANG-ES, see Sect. 1.4), with a first set of resulting data products for each galaxy of the sample being presented in Wiegert et al. (2015). Two high-priority targets of CHANG-ES, NGC 891 and NGC 4565, are the subject of this thesis and will be introduced in the two following sections.

1.1 NGC 891

The galaxy NGC 891 has been repeatedly labelled the twin of the Milky Way, e.g. due to its similar optical luminosity and morphological type (van der Kruit & Searle 1981; de Vaucouleurs et al. 1991) as well as its similar rotation velocity of 225 km s^{-1} (Rupen 1991; Swaters et al. 1997). Its SFR is not particularly well constrained, and may be as high as 3.3 M$_\odot$ yr^{-1} (Krause 2011), while e.g. Wiegert et al. (2015) state a value of 1.55 M$_\odot$ yr^{-1}. NGC 891 contains approximately twice the amount of CO gas in the Milky Way (Scoville et al. 1993), therefore it is very likely to have a higher SFR than our Galaxy. Even though initially classified as Hubble type SAb (see de Vaucouleurs et al. 1991), it shows dynamical evidence for a bar (Garcia-Burillo & Guelin 1995), which makes the classification of NGC 891 as an SBb galaxy more appropriate. The galaxy is viewed almost perfectly edge-on at an inclination of 89.8° (Kregel & van der Kruit 2005), and is located at a distance of 9.1 Mpc (Radburn-Smith et al. 2011), as a member of the NGC 1023 group (Ciardullo et al. 1991). Owing to its similarities to our Galaxy and its easily detectable extraplanar emission in various wavelength regimes, NGC 891 is a preferred target for investigations of halo properties and the disk-halo connection, and arguably the most extensively studied edge-on galaxy to date.

NGC 891 was the first galaxy for which the radio continuum emission could be separated into a thin disk and a thick disk (or halo) component. This was performed by Allen et al. (1978), who observed the galaxy at 610 MHz, 1.4 GHz, and 5 GHz with the Westerbork Synthesis Radio Telescope (WSRT). The obtained vertical distributions of the spectral index between 610 MHz and 5 GHz and between 1.4 and 5 GHz showed a too rapid steepening with distance from the mid-plane to be explained by basic CR transport models (Strong 1978). Observations with the Effelsberg 100-m telescope at 8.7 GHz by Beck et al. (1979) and at 10.7 GHz by Klein et al. (1984a) resulted in less steep profiles of the spectral index with respect to the 610 MHz data. This discrepancy suggested a lack of large-scale structure in the 5 GHz map of Allen et al. (1978) due to the missing short-spacing problem of interferometric data. Later, Hummel et al. (1991b) observed NGC 891 at 327 and 610 MHz with the WSRT and at 1.49 GHz with the Very Large Array (VLA). The observed vertical extent of the halo at each frequency and the resulting spectral index profiles showed first indications of consistency with the dynamical halo models of Lerche & Schlickeiser (1982) and hence of the presence of a disk-halo outflow. Also, Hummel et al. (1991b) found that ≈65% of the total emission of the galaxy at 1.49 GHz originates from the halo component. Dumke (1997) for the first time combined interferometric (VLA) and single-dish (Effelsberg) data for this galaxy (at 4.85 GHz) to overcome the missing flux problem while retaining the angular resolution given by the interferometric observation (in this case 25″). From this combined map, average exponential scale heights of 0.27 kpc for the disk and 1.82 kpc for the halo were obtained. Moreover, Dumke (1997) determined the fractional contribution of thermal free-free emission to the total emission of the galaxy at 1.49, 4.85, and 10.55 GHz (these results are also shown in Table 4.3 of this thesis). Being also the first edge-on galaxy investigated with the Low Frequency Array (LOFAR), NGC 891 was recently observed by Mulcahy (2014) at 146 MHz. Scale heights at various positions along the major axis of the galaxy were determined from these data, with average values of 0.44 kpc for the disk and 2.25 kpc for the halo.
Polarized emission in the halo of NGC 891 was detected by Hummel et al. (1991a) from the

1.49 GHz VLA observations. These data did not provide much information on the magnetic field structure though, since at this frequency Faraday rotation (see Sect. 2.5) and related depolarization effects are significant. At 4.85 GHz these effects are much less severe, and the VLA data of Sukumar & Allen (1991) at this frequency revealed a mostly plane-parallel magnetic field orientation in the disk of NGC 891, as well as field lines tilting away from the disk into the halo, hinting at an X-shaped extraplanar field geometry. The same behaviour is evident from the 10.55 GHz data of Dumke et al. (1995). Later, Effelsberg observations at 8.35 GHz by Krause (2009, 2011) confirmed the presence of a large-scale X-shaped field configuration in the halo. Furthermore, from the distribution of Faraday rotation measures between 8.35 and 4.85 GHz, Krause (2009, 2011) inferred that the disk field of NGC 891 is most likely an axisymmetric spiral field with an outwards-pointing radial component.

High-sensitivity WSRT observations of NGC 891 in the HI 21-cm line (Oosterloo et al. 2007) revealed the most extended HI halo known to date. Almost 30% of the total HI mass of NGC 891 is contained in the halo, whereas for other galaxies this fraction is typically less than 15%. The HI distribution has an exponential scale height of 1.25 kpc in the central region, and flares up to a scale height of ≈2.5 kpc at large radii. The rotation of the extraplanar gas lags with respect to the disk rotation, with a vertical gradient in azimuthal velocity of ≈-15 $\mathrm{km\,s^{-1}\,kpc^{-1}}$. While the major part of the gaseous halo is most probably generated by the galactic fountain mechanism, the rotational lag suggests that an interaction between the fountain gas and material of lower angular momentum is taking place, possibly by gas accretion from the surrounding IGM. While NGC 891 does not feature an optical or HI warp, the HI distribution is known to be slightly lopsided, which is possibly casued by a flyby interaction with the companion dwarf galaxy UGC 1807 (Mapelli et al. 2008). The HI halo furthermore shows a giant filament in the northwest quadrant, which extends up to 22 kpc from the plane. Oosterloo et al. (2007) found that a galactic fountain is unlikely to transport this amount of gas (at least $1.6 \cdot 10^7\,\mathrm{M_\odot}$) to such heights. The fact that the filament is pointing towards the gas-rich companion UGC 1807 (which is located at a projected distance of ≈80 kpc) as well as the detection of counterrotating HI clouds in the halo may be direct evidence of external gas accretion.
Evidence of past accretion events was revealed by the deep optical imaging of Mouhcine et al. (2010), who detected a giant stellar stream, which loops around NGC 891 up to distances of ≈50 kpc, and can be associated with the remnants of disrupted dwarf companions. In addition, a coherent stellar halo component with a vertical extent of ≈15 kpc was detected. Apart from the aforementioned merger remnants, a total of seven dwarf galaxies in the vicinity of NGC 891 could be identified up to now (Schulz 2014).

Early evidence for the disk-halo connection via star-forming activity in NGC 891 was found by Rand et al. (1990) and Dettmar (1990), who independently discovered a prominent eDIG layer through narrow-band Hα imaging. Rand et al. (1990) observed that this gas component shows many vertical filaments reaching up to 2 kpc into the halo. Further spectroscopic measurements could detect the eDIG even at heights above 5 kpc (Keppel et al. 1991; Dettmar & Schulz 1992; Rand 1997, 1998). In addition, Howk & Savage (1997) discovered remarkable (partly vertical) dust filaments extending out to heights of 2 kpc, which are known today as a characteristic feature of the galaxy in its optical appearance (see Fig. 1.1). This extraplanar dust has since also been detected by its radiation in the far-infrared (FIR) (Popescu et al. 2004; Hughes et al.

2014). Rossa et al. (2004) detected HII regions at heights of several hundred pc above the plane, indicating the possible occurrence of extraplanar star formation. These authors also found direct evidence of supernova activity in the form of superbubbles and -shells in the disk, as well as filamentary structures that appear to be connected to them. These filaments possibly mark the locations where the hot gas breaks out from the bubbles and shells and ascends into the halo.

Figure 1.1: Optical image of NGC 891, composed of data from the Subaru Telescope (Mauna Kea Observatory) and the Hubble Space Telescope (Image credit: Hubble Legacy Archive, 2012).

Although Garcia-Burillo et al. (1992) detected a certain amount of molecular gas (traced by CO emission) in NGC 891 up to a vertical height of 1.4 kpc, the molecular gas is more concentrated to the plane compared to the atomic and ionized gas phases (Scoville et al. 1993), with an average scale height of ≈180 pc (Yim et al. 2014). From observations in the near-infrared (NIR), Schechtman-Rook & Bershady (2013) found that in addition to the well-known thin and thick disk components, NGC 891 even has an ultra-thin disk with a (exponential or sech^2) scale height of 60-80 pc. Moreover, rather than a classical de Vaucouleurs bulge, the galaxy shows a central continuation of the ultra-thin disk, increasing in brightness but not in scale height.
NGC 891 furthermore shows a large amount of diffuse X-ray emitting hot ionized gas, and in fact has the brightest X-ray halo observed so far in a normal (i.e. non-starburst) edge-on galaxy (Bregman & Houck 1997; Strickland et al. 2004). While the spatial correlation of the X-ray emission with the eDIG (Tüllmann et al. 2006) suggests that both gas components originate from the disk, Hodges-Kluck & Bregman (2013) found that the X-ray gas is likely to be of very low metallicity, which would imply that it must have been accreted from the IGM.

NGC 891 shows considerably more Hα emission in its northern half than in the southern half. This asymmetry is evident for the ionized gas in the plane as well as for the eDIG. A significant spatial correlation of the extraplanar Hα emission with the radio continuum emission at 1.49 GHz (Dahlem et al. 1994), and with the X-ray emission (Bregman & Pildis 1994; Tüllmann et al. 2006) in terms

of the north-south asymmetry is known. However, no substantial asymmetry is visible in the overall dust distribution, and there is no evidence for a direct small-scale correlation beetween extraplanar Hα filaments and dust filaments (Howk & Savage 2000). As indicated by Kamphuis et al. (2007), it is plausible that the asymmetry in Hα is caused by dust attenuation if one considers a trailing spiral pattern with the dust located behind HII regions (see their Fig. 3) and the fact that the northern (southern) half is the approaching (receding) half (see van der Kruit & Searle 1981; Garcia-Burillo & Guelin 1995). Rossa et al. (2004) argued that dust extinction can be excluded as a cause for the asymmetry in the *extraplanar* DIG, as this asymmetry also appears in the radio continuum emission, which is not affected by dust attenuation, and thus concluded that the asymmetry is purely a result of enhanced star formation in the northern half of the galaxy with respect to the southern half. On the other hand, Kamphuis et al. (2007) inferred from Spitzer 24 μm data that there is only a small asymmetry in star formation, and found that the asymmetry in Hα is largely due to dust extinction, even up to $\approx$2 kpc height above the plane. This scenario is also in line with the latest high-resolution FIR studies with the Herschel Space Observatory (Hughes et al. 2014).

Table 1.1: Basic parameters of NGC 891 and NGC 4565

	NGC 891	Ref.	NGC 4565	Ref.
RA (J2000)	$02^{h}\ 22^{m}\ 33^{s}.41$	(1)	$12^{h}\ 36^{m}\ 20^{s}.78$	(1)
DEC (J2000)	$+42^{d}\ 20^{m}\ 56^{s}.9$	(1)	$+25^{d}\ 59^{m}\ 15^{s}.6$	(1)
D [Mpc]	9.1	(2)	11.9	(2)
Morph. type	SBb	(3)	SB(r)b	(4)
i [°]	89.8	(5)	86.3	(6)
d_{25} [a] [′]	12.2	(1)	16.2	(1)
SFR [$M_\odot\,yr^{-1}$]	3.3 / 1.55	(7)/(8)	1.3 / 0.74	(7)/(8)
v_{rot} [$km\,s^{-1}$]	225	(9)	245	(10)
Total atomic gas mass[b] [$10^9 M_\odot$]	5.6	(11)	9.9	(12)

[a] Observed blue diameter at the 25th mag arcsec^{-2} isophote.

[b] Includes multiplication by a factor of 1.36 to account for neutral He.

References: (1) Irwin et al. (2012a), (2) Radburn-Smith et al. (2011), (3) Garcia-Burillo & Guelin (1995), (4) Kormendy & Barentine (2010), (5) Kregel & van der Kruit (2005), (6) this work, (7) Krause (2011), (8) Wiegert et al. (2015), (9) Swaters et al. (1997), (10) Heald et al. (2011), (11) Oosterloo et al. (2007), (12) Zschaechner et al. (2012)

1.2 NGC 4565

Another relatively well-known and frequently observed example among highly inclined galaxies is NGC 4565, also known as the Needle Galaxy. In the catalogue of de Vaucouleurs et al. (1991) it is classified as an SAb galaxy, however a bar is known to be present (see below). At a distance of 11.9 Mpc (Radburn-Smith et al. 2011), it is significantly larger in its physical disk diameter than NGC 891. It has a distinctly lower SFR (1.3 $M_\odot\,yr^{-1}$ (Krause 2011) or even as

low as $0.74\,M_\odot\,yr^{-1}$ (Wiegert et al. 2015)) than NGC 891 and one of the highest known rotation velocities of $245\,km\,s^{-1}$ (Heald et al. 2011; Zschaechner et al. 2012). From CO and HI rotation curves, Yim et al. (2014) derived an inclination angle of 86.5°, which closely matches the value of 86.3° we determined from our own high-resolution radio continuum data (see Sect. 4.1.2) and which will be adopted througout this thesis. From the orientation of the dust lane visible in the optical image of NGC 4565 (Fig. 1.2), it can be inferred that the part of the galaxy seen northeast of the major axis is the front side and the southwest side is the rear side.

The first radio continuum detection of NGC 4565, obtained by Hummel et al. (1984) at 610 MHz and 1.4 GHz with the WSRT indicated the presence of a thick radio disk or halo, with follow-up observations at 1.4 GHz at a higher angular resolution (Broeils & Sancisi 1985) allowed for a tentative separation of a thin and a thick emission component. Based on these early observations, it was estimated that the thick component contains 62% of the total flux density of the galaxy at 1.4 GHz. Although this is similar to the value found by Hummel et al. (1991b) for NGC 891, NGC 4565 shows a considerably smaller minor to major axis ratio than NGC 891 at all radio frequencies at which it has been observed so far. From combined VLA and Effelsberg data of NGC 4565 at 4.85 GHz, Dumke (1997) determined average exponential scale heights of 0.28 kpc for the thin disk and 1.68 kpc for the halo, which are similar to the values he obtained for NGC 891, in spite of the very different vertical halo extents of the two galaxies. The thermal fractions Dumke (1997) determined for NGC 4565 at various frequencies are consistently higher than those found for NGC 891 (see Table 4.3).
The polarized radio emission of NGC 4565, as detected by Sukumar & Allen (1991) at 1.48 GHz, Dumke (1997) at 4.85 GHz, and Dumke et al. (1995) at 10.55 GHz, exhibits an asymmetric distribution, with the bulk of the polarized emission occurring southeast of the galaxy centre. These observations indicate a magnetic field orientation that is predominantly parallel to the disk plane but also shows marginal vertical components away from the centre (thus hinting at an X-shaped halo field), particularly in the 10.55 GHz map of Dumke et al. (1995).

From 21-cm observations and detailed kinematic modelling, Zschaechner et al. (2012) concluded that NGC 4565 does not possess a particularly massive or extended HI halo, suggesting that there is no substantial disk-halo interaction. In particular, the vertical HI distribution was fitted well by single-component exponentials. A flaring of the HI disk was inferred, with scale heights ranging from ≈200 pc near the centre to ≈600 pc at the outer edge of the disk. Also for this galaxy, a vertically increasing rotational lag was detected, with vertical velocity gradients up to $-40\,km\,s^{-1}\,kpc^{-1}$. Among galaxies in which such a lag has been measured, a trend of steeper velocity gradients for galaxies with lower SFRs is observed (see also Heald et al. 2006, 2007; Fraternali et al. 2004; Schmidt et al. 2014).

Hα imaging by Rand et al. (1992) showed that the HII content of NGC 4565 is basically limited to compact star-forming regions in the disk plane and hence does not include any notable eDIG component. This appears to be consistent with its low SFR and its low extraplanar HI content. Also, only a small number of localized extraplanar dust filaments have been detected (Howk & Savage 1999). Moreover, the galaxy has an extremely low CO scale height of (on average) ≈35 pc Yim et al. (2014). On the other hand, contrary to the case of NGC 891, NGC 4565 does not feature an additional ultra-thin disk component (Schechtman-Rook & Bershady 2014).
Rather untypically of galaxies with a low SFR, NGC 4565 features a substantial amount of

extraplanar diffuse X-ray emission, which, as suggested by Vogler et al. (1996), might be a fossil remnant of former starburst activity.

Figure 1.2: Optical image of NGC 4565 (Image credit: U. Klein, 2015).

NGC 4565 is known to have two HI-rich dwarf companions: IC 3571 near the northern quadrant of the galaxy and NGC 4562 in the southwest, at projected distances of ≈15 and ≈50 kpc, respectively. Zschaechner et al. (2012) and van der Hulst & Sancisi (2005) detected a faint HI bridge connecting NGC 4565 and IC 3571, clearly indicating a minor interaction.
The HI distribution features an outer warp perpendicular to the line of sight, which is especially pronounced at the northwestern edge. The warp of the HI disk spatially conicides with a warp of the stellar disk (Näslund & Jörsäter 1997; Radburn-Smith et al. 2014). While the warp may have been excited through gravitational torques induced by either or both of the companions, the lack of old stars in the warped outer disk, as observed by Radburn-Smith et al. (2014), possibly suggests that the warp was formed from gas that was recently accreted from the companions or from the IGM. In any case, the asymmetry of the warp is likely to be influenced by the current interaction with IC 3571.

The optical bulge of NGC 4565 appears slightly box-shaped, which according to Kormendy & Barentine (2010) is evidence for the presence of a central bar. Using IR observations, these authors found that the galaxy harbours a pseudobulge, i.e. a very compact bright stellar concentration at the galactic centre that does not show the radial brightness profile of a classical bulge. In this terminology, what resembles a classical bulge in the edge-on view is in fact a bar that is oriented partially along the line of sight and much more luminous than the actual (pseudo)bulge. Kinematical proof for the existence of a bar was found by Neininger et al. (1996) and Zschaechner et al. (2012) in the form of radial motions of CO and HI gas, respectively.

Mid-infrared observations of NGC 4565 (Laine et al. 2010; Kormendy & Barentine 2010) furthermore reveal a prominent ring of dust emission at a radius of ≈5 kpc, coinciding with a ring of molecular gas (Sofue & Nakai 1994; Neininger et al. 1996; Yim et al. 2014). A similar ring-like structure is also traced in HI (Zschaechner et al. 2012). Kormendy & Barentine (2010)

suggest a re-classification of NGC 4565 as an SB(r)b galaxy, in which case the observed feature is an actual closed ring, as is often associated with bars in early-type spirals (Buta 1990). On the other hand, the appearance of a ring in a nearly edge-on view may as well be caused by the projection of spiral arms, which, as noted by Buta (1990), is more likely to happen for late-type galaxies.

In terms of nuclear activity, NGC 4565 is classified as a Seyfert galaxy. However, it shows an exceptionally low luminosity for a Seyfert galaxy (Ho et al. 1997; Chiaberge et al. 2006; Laine et al. 2010), which according to Chiaberge et al. (2006) indicates an accretion process of low radiative efficiency, which may have just recently started after the "switch-off" of a standard high-efficiency accretion disk. Also, as suggested by Schechtman-Rook & Bershady (2014), nuclear activity in NGC 4565 is possibly related to its low current SFR and might explain the absence of an ultra-thin disk.

1.3 The JVLA

The Karl G. Jansky Very Large Array (JVLA) is an interferometer consisting of 27 25-m radio telescopes arranged in a Y-shape, with arms pointing roughly in north, southeast, and southwest direction. It is a facility of the National Radio Astronomy Observatory (NRAO), and located at an elevation of 2100 m on the Plains of San Agustin in New Mexico, USA. There are four basic array configurations, which are distinguished by the spacing between antennas, and labelled A-, B-, C-, and D-configuration (or -array), where D is the most compact configuration and A is the most extended one. Additionally, the array can be operated in three hybrid configurations (AnB, BnC, CnD), in wich the antennas in the north arm have larger spacings than in the southeast and southwest ones. The interferometer generally stays in the same configuration over a 3-4 month period before it is changed, cycling through configurations in the order D→C→B→A→D. The minimum and maximum baseline length in each configuration are given in Table 1.2.

Table 1.2: JVLA configurations

Configuration	A	B	C	D
B_{min} [km]	0.68	0.21	0.035[a]	0.035
B_{max} [km]	36.4	11.1	3.4	1.03

[a] For the C-configuration, an antenna from the middle of the north arm is moved to the centre of the array, which results in the same minimum antenna spacing as for the D-configuration. While this slightly improves the imaging of extended sources, the overall sensitivity to extended emission is still significantly higher in D-configuration.

Formerly simply called VLA, the array has recently been upgraded with new electronic components, including a powerful and flexible new correlator as well as broad-band receivers, which increased the sensitivity of the array by up to an order of magnitude and collectively enable complete frequency coverage between 1 and 50 GHz – whereas previously only 22% of this frequency range was covered. Additionally, two receiver systems for observing at frequencies

below 1 GHz have recently been installed. The frequency bands corresponding to the different receivers are listed in Table 1.3. The conversion process lasted from 2001 through 2012, and was called the Expanded Very Large Array (EVLA) project; however the instrument was officaly named JVLA in 2012, shortly before completion. Table 1.4 provides a comparison between pre- and post-upgrade performance parameters.

Table 1.3: JVLA frequency bands

Band	Central wavelength	Frequency range [GHz]
4	4 m	0.058 - 0.084
P	90 cm	0.23 - 0.47
L	20 cm	1 - 2
S	13 cm	2 - 4
C	6 cm	4 - 8
X	3 cm	8 - 12
Ku	2 cm	12 - 18
K	1.3 cm	18 - 26.5
Ka	1 cm	26.5 - 40
Q	0.7 cm	40 - 50

Table 1.4: Overall (J)VLA performance before, during, and after the upgrade

Parameter	VLA	JVLA	Factor	EVLA (Feb. 2012)[a]
Continuum sensitivity (1σ, 12 hr)	10 μJy	1 μJy	10	2 μJy
Maximum bandwidth in each polarization	0.1 GHz	8 GHz	80	2 GHz
# of frequency channels at max. bandwidth	16	16,384	1024	16384
Coarsest frequency resolution	50 MHz	2 MHz	25	2 MHz
Finest frequency resolution	381 Hz	0.12 Hz	3180	1.9 Hz
Number of full-polarization spectral windows	2	64	32	64
Frequency coverage (1-50 GHz)	22%	100%	5	100%

[a]The listed values as of February 2012 correspond to the generally available capabilities for the Resident Shared Risk Observing (RSRO) programme, which the CHANG-ES observations were part of. The telescope name is given as EVLA here, as the name JVLA was not official yet at this time.

The receivers have circular feeds, i.e. the incoming signal is split into its right-hand circular (R) and left-hand circular (L) components. From their different cross-correlation products for each baseline, the four Stokes parameters are determined:

$$I = \frac{RR + LL}{2}, \qquad Q = \frac{RL + LR}{2}, \qquad U = \frac{RL - LR}{2i}, \qquad V = \frac{RR - LL}{2} \tag{1.1}$$

Stokes I represents the total intensity of the measured signal, while Stokes Q and U describe its

linearly polarized component and the orientation thereof in the plane of the sky, and Stokes V describes the amount of circular polarization[1]

Two different types of samplers are available: four 8-bit samplers and eight 3-bit samplers, with only one type being used within a given frequency band. The 8-bit samplers are arranged in two pairs – one for each polarization (R,L) – each pair providing a bandwidth of 1.024 GHz, resulting in a total bandwidth of 2.048 GHz. The 3-bit system consists of four sampler pairs of 2.048 GHz bandwidth each, adding up to 8.192 GHz per polarization. As the sensitivity of the 3-bit samplers is ∼15% worse than for the 8-bit samplers at the same bandwith, L-band observations are usually done using the 8-bit system, since only a 1 GHz bandwidth is required. The C-band observations presented in this thesis employed the 8-bit samplers as well, as during that time the 3-bit samplers were not yet fully implemented.

The new correlator of the JVLA, called Wideband Interferometric Digital Architecture (WIDAR), was designed and built at the Dominion Radio Astronomical Observatory (DRAO) in Canada. Although it was primarily designed for precise spectral line measurements, its flexible multi-channel structure also yields fundamental advantages for continuum observations. These include precise identification and excision of radio frequency interference (RFI), facilitation of multi-frequency synthesis (see Sect. 3.4) and RM synthesis (see Sect. 7.2), and prevention of bandwidth smearing.

The range of correlator configurations can be summarized as follows: For each of the used sampler pairs, a receiver can independently be tuned to a different frequency within the corresponding frequency band. This will be the centre frequency of a so-called baseband (also called intermediate frequency, IF), i.e. for observations done with the 8-bit samplers, two basebands, each up to 1.024 GHz wide, are sampled, while in case of the 3-bit samplers, there are four basebands of up to 2.048 GHz bandwidth. The different basebands, which do not have to be adjacent, are in turn divided into several spectral windows – up to 32 for each 8-bit baseband, and up to 16 for each 3-bit one. Spectral windows can have widths of 128, 64, 32, ..., 0.03125 MHz, and the number of channels as well as the number of polarization products can be selected independently for each spectral window. The total number of frequency channels multiplied by the number of polarization products is limited to 16384 (e.g. 64 spectral windows × 64 channels × 4 polarization products).

1.4 Continuum HAlos of Nearby Galaxies – an EVLA Survey (CHANG-ES)

The JVLA observations of NGC 891 and NGC 4565 presented in this work are part of CHANG-ES, which is a radio continuum survey conducted between March 2011 and August 2012 to probe the structure and physics of galactic radio halos and the disk-halo connection in a sample of 35 nearby edge-on galaxies. The observations were carried out using the L-band (1.5 GHz) and C-band (6 GHz) receivers, the bandwidths available during that time being 512 MHz and 2.048 GHz,

[1] An introduction to the polarization properties of synchrotron radiation and will be given in Sect. 2.5.

respectively. These large bandwidths allow for the first time to measure the spectral index *within* a given frequency band, and make for significant improvement in sensitivity compared to previous studies, with noise levels reaching a few μJy/beam in comparatively short integration times. In order to probe a variety of spatial scales, the survey makes use of the B-, C-, and D-array configurations. Moreover, CHANG-ES is the first survey of edge-on galaxies for which all polarization products (RR, LL, RL, LR, and thereby Stokes I, Q, U, and V) have been obtained. Further information on the observational setup of CHANG-ES is given in Sect. 3.1.

Being one of the first larger projects using the newly installed wide-band receivers and correlator of the JVLA, CHANG-ES was granted a total observing time of 405 hours in Resident Shared Risk Observing (RSRO) mode during the extensive commissioning period of the JVLA. The RSRO programme offered early access to the growing capabilities of the telescope as the upgrade was nearing completion. For every 20 hours of observing time awarded to a given project, the programme required one month of residence of a project consortium member at NRAO in Socorro, New Mexico, to assist with commissioning of the JVLA, WIDAR, or associated software systems. Of the 21 months of required residence time for the CHANG-ES project, nine months were fulfilled by T. Wiegert, and three months each by J. Irwin (PI of the project), D.J. Saikia, and P. Schmidt. Apart from the above-mentioned improvements achieved by the JVLA upgrade, the use of the large bandwidths of this essentially new instrument also constitutes major challenges in terms of data handling. Therefore, a major objective of this RSRO stay was to develop a data reduction strategy in close collaboration among members of the CHANG-ES consortium and with NRAO/JVLA staff members. CHANG-ES data are generally reduced in CASA (Common Astronomy Software Applications[2]), which is a Python-based software package developed by NRAO for the data processing of modern radio interferometers, primarily JVLA and ALMA. Throughout the time I spent at NRAO, apart from testing newly implemented functions in CASA, weekly meetings with CASA developers were attended, to help optimizing the software with regard to the new wide-band data processing requirements. A CHANG-ES data reduction guidelines document (created by J. Irwin) was continuously updated, and those consortium members who were currently reducing data engaged in weekly Skype sessions, which also continued beyond the RSRO phase. Altogether, the RSRO activities in the framework of the CHANG-ES project thus formed an essential contribution to the JVLA commissioning phase.

1.5 Structure of this thesis

In this thesis, the results of the CHANG-ES observations of the high-priority galaxies NGC 891 and NGC 4565 are presented and analyzed, with the main focus lying on the disk-halo interaction. Prior to describing our data and their scientific analysis, we first give a brief introduction to the physical properties of the measured radiation, primarily synchrotron radiation of CR electrons (Chapter 2). In Chapter 3, we provide information on the observational setup of CHANG-ES and give a description of the full data reduction process, leading from the raw interferometric visibility data to the basic image data products. In particular, this includes the application of essential concepts of imaging for wide-band wide-field interferometric observations. In

[2] `http://casa.nrao.edu`

Chapter 4, we present the final images in total intensity at 1.5 and 6 GHz in the various JVLA configurations and discuss morphological properties of the two galaxies deduced from these maps. We also provide an estimate of the amount of thermal free-free emission in both galaxies and present thermal-subtracted synchrotron intensity maps. Chapter 5 focusses on the spatial distribution of total and non-thermal spectral indices in the two galaxies. This part of the thesis will be of particular benefit for future observers, as here we discuss various sources of error in wide-band spectral index measurements (which also affect other data products) and describe the necessary corrections. In the last part of this chapter, we analyze the in-band spectral index maps for information on CR spectral aging. In Chapter 6, we determine for both galaxies the vertical radio scale heights at 1.5 and 6 GHz at various major-axis positions, and generate maps of the total magnetic field strength. Inferences about the CR propagation from the disk into the halo are drawn from these measurements, and in the case of NGC 891 we explicitly model the vertical emission distribution by solving the diffusion-loss equation. The polarized part of the radio emission in the two galaxies and their magnetic field structure are investigated in Chapter 7. This includes the determination of rotation measures using RM synthesis, as well as studying the variation of the fractional degree of polarization with vertical height above the plane. Finally, in Chapter 8 we discuss and summarize our main findings and provide an outlook on future research and improvements.

2 Synchrotron emission and related physical processes

The radio continuum of spiral galaxies at frequencies up to the order of 1 GHz is usually dominated by synchrotron radiation from cosmic-ray electrons (CREs). Synchrotron emission is therefore the main tracer of the radio continuum morphology of galaxies, and in particular of magnetic fields in galactic disks and halos. Before we describe our observations of NGC 891 and NGC 4565 and the subsequent data processing and analysis, we provide an overview of the basic physical properties inherent to the observed radio emission. To this end, we mainly follow the descriptions given by Longair (2011), Klein & Fletcher (2015), Pacholczyk (1970), and Murgia (1996), where detailed derivations of most of the equations presented below can be found.

2.1 Basic characteristics of synchrotron radiation

Relativistic electrons propagating at the velocity $\vec{v}$ in a magnetic field $\vec{B}$ are subject to the Lorentz force

$$\vec{F} = e(\vec{v} \times \vec{B}) \tag{2.1}$$

This forces the charged particles onto helical paths around the magnetic field lines, and the corresponding acceleration makes them emit synchrotron radiation, which is linearly polarized. The helical trajectories are characterized by the pitch angle θ between the $\vec{v}$ and $\vec{B}$ vectors and the Larmor radius r_L. The angular velocity in the plane perpendicular to the magnetic field lines is given by the Larmor frequency ω_L:

$$\omega_\mathrm{L} = \frac{eB}{\gamma m_0 c}, \qquad r_\mathrm{L} = \frac{v}{\omega_\mathrm{L}} \sin\theta = \frac{\gamma m_0 v c}{eB} \sin\theta \tag{2.2}$$

with the Lorentz factor $\gamma = 1/\sqrt{1-(v/c)^2}$. While in its rest frame an electron radiates in the form of a dipole pattern, in the reference frame of the observer, due to relativistic beaming, it emits the bulk of its radiation in the forward direction, within a narrow beam of half-power width $\theta_\mathrm{HP} \approx \gamma^{-1}$.

A single relativistic electron of energy $E = \gamma m_0 c^2$ emits a synchrotron spectrum with its peak at a characteristic frequency ν_c:

$$\nu_\mathrm{c} = \frac{3}{2}\gamma^3 \frac{\omega_\mathrm{L}}{2\pi} \sin\theta = \frac{3e}{4\pi m_0^3 c^5} B \sin\theta E^2 \tag{2.3}$$

The total (i.e. at all frequencies) emitted synchrotron power of a single electron corresponds to the associated energy loss rate:

$$-\left(\frac{\mathrm{d}E}{\mathrm{d}t}\right)_{\mathrm{syn}} = \frac{2e^4}{3m_0^4c^7}B^2\sin^2\theta E^2 \tag{2.4}$$

For an ensemble of electrons with a number-density distribution $N(E,\theta)$, the synchrotron spectrum is given by the synchrotron emissivity

$$J(\nu) = \frac{\sqrt{3}e^3}{m_0c^2}\int_0^{\pi}\int_0^{\infty} B\sin\theta F\left(\frac{\nu}{\nu_c}\right)N(E,\theta)\,\mathrm{d}E\,\mathrm{d}\theta\,, \tag{2.5}$$

where

$$F(x) = x\int_0^{\infty} K_{\frac{5}{3}}(z)\,\mathrm{d}z \tag{2.6}$$

and $K_{\frac{5}{3}}$ is the modified Bessel function of order $\frac{5}{3}$.

If unaffected by energy-dependent particle aging (see Sect. 2.3), the emission spectrum of CREs can be approximated by a (inverse) power law distribution with spectral index[1] α:

$$J(\nu) \propto (B\sin\theta)^{1-\alpha}\nu^{\alpha} \tag{2.7}$$

2.2 CRE energy loss processes

While propagating away from their injection sites, CREs may lose their energy through a variety of processes, involving interaction with other particles, with magnetic or radiation fields, or adiabatic expansion. In this section we describe these loss mechanisms by the time derivative of the particle energy, whereas the associated chracteristic time scales will be given in Sect. 6.3, where we calculate them explicitly for specific observational parameters.

Synchrotron losses

As will be described in Sect. 2.4, CREs can be expected to have an isotropic (i.e. random) distribution of pitch angles. Thus, the pitch-angle dependence of the single-electron synchrotron loss rate is replaced by the average value of $\langle\sin^2\theta\rangle = 2/3$, and Eq. 2.4 turns into

$$-\left(\frac{\mathrm{d}E}{\mathrm{d}t}\right)_{\mathrm{syn}} = \frac{4}{3}\sigma_{\mathrm{T}}c\gamma^2U_{\mathrm{mag}} = 6.6\cdot10^{-16}\gamma^2\left(\frac{B}{\mu\mathrm{G}}\right)^2\ \mathrm{eV\,s^{-1}} \tag{2.8}$$

Here, $\sigma_{\mathrm{T}} = e^4/(6\pi\varepsilon_0^2c^4m_0^2)$ is the Thomson cross section and $U_{\mathrm{mag}} = B^2/(8\pi)$ is the magnetic field energy density.

[1] For the sake of clarity, we note that throughout this thesis we define α to be positive if the spectrum increases with frequency, and vice-versa.

Inverse-Compton losses

Inverse Compton (IC) scattering is the interaction of relativistic electrons with photons of comparatively low energy ($h\nu \ll \gamma m_0 c^2$), in normal galaxies usually with photons of the interstellar radiation field (IRF) and of the cosmic microwave background (CMB). In this process, energy is transferred from the electrons to the photons, with a loss rate of

$$-\left(\frac{\mathrm{d}E}{\mathrm{d}t}\right)_{\mathrm{IC}} = \frac{4}{3}\sigma_{\mathrm{T}} c \gamma^2 U_{\mathrm{rad}}\,, \tag{2.9}$$

where $U_{\mathrm{rad}} = U_{\mathrm{IRF}} + U_{\mathrm{CMB}}$ is the energy density of the total radiation field. The CMB-equivalent magnetic field strength at redshift z is $B_{\mathrm{CMB}} = 3.25(1+z)^2\,\mu\mathrm{G}$, and $U_{\mathrm{CMB}} = B_{\mathrm{CMB}}^2/(8\pi)$, while U_{IRF} can be determined from observations at infrared wavelengths.

Ionization losses

CREs further experience energy losses by colliding with atoms in the ISM and thereby ionizing them. Since the most abundant atom in the universe is hydrogen, the ionization loss rate can be expressed as

$$-\left(\frac{\mathrm{d}E}{\mathrm{d}t}\right)_{\mathrm{ion}} = 7.64 \cdot 10^{-15} \left(\frac{n_{\mathrm{HI}}}{\mathrm{m}^{-3}}\right) (3\ln\gamma + 19.8)\,\mathrm{eV\,s^{-1}}\,, \tag{2.10}$$

where n_{HI} is the particle number density for atomic hydrogen.

Bremsstrahlung losses

Bremsstrahlung losses occur if CREs are deflected (and thereby decelerated) by charged particles, such as protons in an ionized hydrogen (HII) plasma or the protons and electrons bound in hydrogen atoms. In the fully ionized case, the corresponding loss rate is

$$-\left(\frac{\mathrm{d}E}{\mathrm{d}t}\right)_{\mathrm{brems}} = 7.0 \cdot 10^{-23} \left(\frac{n_{\mathrm{HII}}}{\mathrm{m}^{-3}}\right)\left(\frac{E}{\mathrm{eV}}\right) (3\ln\gamma + 0.36)\,\mathrm{eV\,s^{-1}} \tag{2.11}$$

In the case of purely atomic hydrogen (neglecting interactions with the electrons), bremsstrahlung losses behave as

$$-\left(\frac{\mathrm{d}E}{\mathrm{d}t}\right)_{\mathrm{brems}} = 3.66 \cdot 10^{-22} \left(\frac{n_{\mathrm{HI}}}{\mathrm{m}^{-3}}\right)\left(\frac{E}{\mathrm{eV}}\right) \mathrm{eV\,s^{-1}} \tag{2.12}$$

Adiabatic losses

CREs that are confined within an expanding volume experience adiabatic losses, as the internal energy of the expanding relativistic gas is reduced. These losses depend on the gradient of the expansion velocity v:

$$-\left(\frac{\mathrm{d}E}{\mathrm{d}t}\right)_{\mathrm{ad}} = \frac{1}{3}(\vec{\nabla}\cdot\vec{v})E \tag{2.13}$$

2.3 CRE spectral aging

The combined synchrotron and IC loss rate of a single electron can be obtained by including the total equivalent magnetic field associated with IC scattering in Eq. 2.4:

$$-\left(\frac{\mathrm{d}E}{\mathrm{d}t}\right)_{\mathrm{syn+IC}} = C_E(B^2 \sin^2\theta + B_{\mathrm{IC}}^2)E^2 \tag{2.14}$$

where $C_E = 2e^4/(3m_0^4c^7)$. If we now consider a single event of CRE injection at the time t_0 with initial energy E_0, we can integrate Eq. 2.14 to determine the time dependency of the energy of a single CRE:

$$E(t) = \frac{E_0}{1 + E_0/E_{\mathrm{br}}(t)} \tag{2.15}$$

with

$$E_{\mathrm{br}}^{-1}(t) = \int_{t_0}^{t} C_E(B^2 \sin^2\theta + B_{\mathrm{IC}}^2)\,\mathrm{d}t' \tag{2.16}$$

E_{br} is known as the break energy. Dividing both sides of Eq. 2.15 by E_{br} shows that $E(t) < E_{\mathrm{br}}$ for all $t \geq t_0$. The corresponding break frequency is given by

$$\nu_{\mathrm{br}} = \frac{3e}{4\pi m_0^3 c^5} B \sin\theta E_{\mathrm{br}}^2 \tag{2.17}$$

According to predictions by models of diffusive shock acceleration of CRs in shock fronts of supernova remnants (e.g. Blandford & Eichler 1987), the emission spectrum of a large ensemble of CREs is usually described by a single power law with spectral index α between -0.8 and -0.5 at $t = t_0$. Since E_{br} decreases over time, the spectral energy distribution observed at $t > t_0$ will feature a corresponding break, which marks a steepening of the spectral index above a certain energy (and frequency, respectively, for the emission spectrum)[2]. This effect is known as spectral aging. The position of the break in the CRE spectrum can be calculated under certain simplifying assumptions (in particular regarding the distribution of pitch angles), such as represented by the Kardashev-Pacholczyk (KP), Jaffe-Perola (JP), and continuous injection (CI) models. We will introduce these standard spectral aging models in Sect. 5.3.

2.4 Pitch-angle scattering

Magnetic fields in galaxies are never perfectly uniform, but contain irregularities that influence the motion of charged particles around the field lines. In particular, CREs can experience rapid changes in the pitch angles θ of their helical trajectories. If the size scale of these magnetic field fluctuations is large compared to the Larmor radius r_{L} of a gyrating electron, the rate of change

[2] It should be noted that the combination of ionization, bremsstrahlung, and adiabatic losses can induce an additional break in the spectrum, which typically occurs at frequencies below 1 GHz (see e.g. Pohl et al. 1991), and is therefore rather irrelevant for our considerations throughout this thesis.

in its pitch angle is accordingly slow. Similarly, if the field is fluctuating on scales much smaller than the Larmor radius, the fluctuations are "ignored" by the particle, and it simply moves on the helical orbit determined by the mean field, as illustrated in Fig. 2.1 *a)*. However, for field variations on scales comparable to the Larmor radius (Fig. 2.1 *b)*), resonance between the particle and the field variations occurs, and the pitch angle changes significantly within a single orbital period. For random field fluctuations, this process, called pitch-angle scattering, leads to an isotropic distribution of pitch angles of the particles.

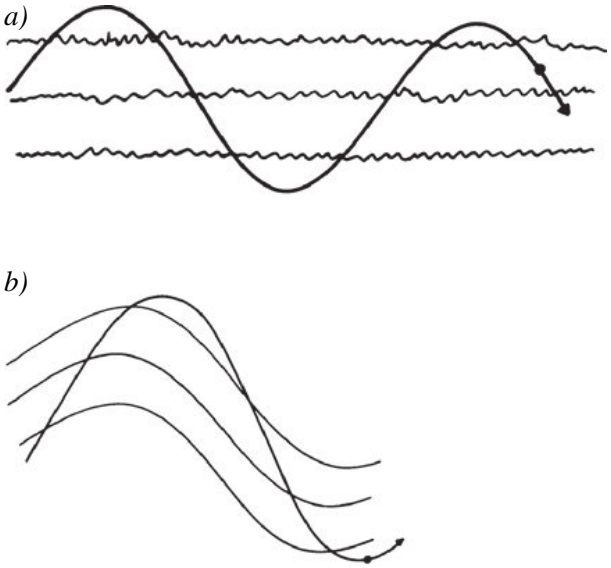

Figure 2.1: *a)* Small-scale magnetic field fluctuations do not influence the helical trajectory of the charged particle, which gyrates at a constant pitch angle around the mean field. *b)* For fluctuations on scales of the same order as the Larmor radius of the particle, significant pitch-angle scattering occurs. Image taken from Longair (2011).

Even if there were initially no magnetic field fluctuations, they are produced by the streaming motion of the highly relativistic electrons. The streaming of the particles generates Alfvén waves, which are transverse waves in a (fully or partially ionized) magnetized plasma, propagating in the direction of the field lines. Since these waves resonate with the motion of the particles that generate them, the waves grow in amplitude, as described by Wentzel (1974) and Cesarsky (1980). Due to the scattering off the field irregularities, the bulk streaming motion is limited by the Alfvén speed

$$v_\mathrm{A} = \frac{B}{\sqrt{4\pi\rho_\mathrm{ion}}} = 2.2 \left(\frac{B}{\mu\mathrm{G}}\right)\left(\frac{n_\mathrm{e}}{\mathrm{cm}^{-3}}\right)^{-\frac{1}{2}} \mathrm{km\,s}^{-1}\,, \tag{2.18}$$

where ρ_ion is the density of the inoized gas and n_e is the electron number density. The scattering process changes the pitch angle of a CRE by $\approx 90°$ after a mean free path length of

$$\lambda_\mathrm{sc} = r_\mathrm{L}\left(\frac{B_0}{B_1}\right)^2\,, \tag{2.19}$$

where B_0 is the mean magnetic field strength and B_1 is the strength of the fluctuation of the field. Hence, within a streaming distance of λ_sc a random, and therefore isotropic distribution of CRE pitch angles is achieved.

2.5 Polarization and Faraday rotation

2.5.1 Basic observables

The polarization state of electromagnetic radiation is commonly described by the Stokes parameters I, Q, U, and V. The latter three describe a coordinate system (the so-called Poincaré sphere),

in which Q and U form a plane representing the linearly polarized component of the radiation, and the V axis represents the circularly polarized component. Stokes I is the distance of a point in this coordinate system from its origin and corresponds to the total intensity of the emission. The polarized intensity, on the other hand, is defined as

$$PI_{\mathrm{pol}} = \sqrt{Q^2 + U^2 + V^2} \tag{2.20}$$

For synchrotron radiation, we assume $V = 0$, as it is linearly polarized. In general, synchrotron emission is only partially polarized, hence a commonly used quantity is the fractional degree of linear polarization

$$p = \sqrt{\frac{Q^2 + U^2}{I^2}} \tag{2.21}$$

By integration over the polarized energy spectrum (without accounting for spectral aging effects), one obtains a maximum theoretical degree of polarization of

$$p_{\mathrm{max}} = \frac{1 - \alpha}{\frac{5}{3} - \alpha} \tag{2.22}$$

In the ISM of galactic disks, a typical spectral index value is $\alpha = -0.7$, which yields $p_{\mathrm{max}} = 72\%$, while in galactic halos this theoretical limit is slightly higher, e.g. $p_{\mathrm{max}} = 75\%$ for $\alpha = -1.0$. The orientation of the electric field vector of a linearly polarized wave in the plane of the sky is given by the polarization position angle

$$\chi = \frac{1}{2}\arctan\left(\frac{U}{Q}\right) \tag{2.23}$$

which can be rotated by 90° to obtain the orientation of the magnetic field vector and hence (in the ideal case of no Faraday rotation, see below) of the magnetic field at the source of the emission.

2.5.2 Faraday rotation

A linearly polarized wave is the superposition of a left-handed and a right-handed circularly polarized wave (LHC and RHC) of equal amplitude. As the wave passes through a magneto-ionic plasma, the LHC and RHC components will interact in different ways with the free electrons in the plasma, as the RHC wave has the same helicity as the electrons, while the LHC component is of opposite helicity. This results in a relative phase shift between the two components, which causes a rotation of the linearly polarized electric field vector. This effect is known as Faraday rotation and is characterized by the dependence of the rotation angle $\Delta\chi$ on the square of the wavelength:

$$\Delta\chi = RM \cdot \lambda^2 \tag{2.24}$$

The rotation measure (RM) depends on the line-of-sight magnetic field component $B_{\parallel}$ and the number density of thermal electrons n_{e}. As the net rotation depends on the pathlength through

the magnetized plasma, the RM is the integral of the product of these two quantities along the line of sight:

$$RM = 0.81 \int_0^{r_0} \left(\frac{n_\mathrm{e}}{\mathrm{cm}^{-3}}\right)\left(\frac{B_\parallel}{\mu\mathrm{G}}\right)\left(\frac{\mathrm{d}r}{\mathrm{pc}}\right) \ \mathrm{rad\,m^2} \tag{2.25}$$

By convention, positive RMs mean that the magnetic field points away from the observer, while for negative values it points towards the observer.

2.5.3 Depolarization effects

In practice, the degree of linear polarization as given by Eq. 2.22 is never observed, due to a range of effects that can depolarize a signal on its way from the source to the observer. Some of these are instrumental effects, while others are the result of Faraday rotation, either within the synchrotron-emitting source itself or in a non-emitting magnetized plasma in the foreground. The mathematical formulae by which we describe the depolarizing mechanisms in this section are adopted from Burn (1966), Sokoloff et al. (1998), and Klein & Fletcher (2015).

Beam depolarization

If different magnetic field orientations occur within the telescope beam, the observed radiation will be partially or entirely depolarized. In particular, waves with a difference in polarization angle of 90° interfere destructively, as this corresponds to an angle difference of 180° in the QU plane. Note that this effect is not induced by Faraday rotation and is therefore wavelength-independent.

Bandwidth depolarization

Another instrumental depolarization effect can be caused by Faraday rotation of polarized emission over large bandwidths. Depending on the RM of the received radiation, the differences in rotation angle within the frequency band may be large enough to cause significant destructive interference when averaging the data in all frequency channels, as is the case for multi-frequency synthesis (MFS) imaging (see Sect. 3.4.1). By a total rotation of $\Delta\chi$ over the band, the degree of polarization is reduced to

$$p(\lambda^2) = p_\mathrm{i} \left|\frac{\sin \Delta\chi}{\Delta\chi}\right| , \tag{2.26}$$

where $\Delta\chi = RM(\lambda^2_\mathrm{max} - \lambda^2_\mathrm{min})$ and p_i is the intrinsic degree of polarization. Bandwidth depolarization can be overcome by separate imaging of narrow frequency intervals, the disadvantage of which would be a higher noise level in the individual images compared to the full-bandwidth image. However, if RM synthesis (Brentjens & de Bruyn 2005) is performed, this is not an issue, while at the same time bandwidth depolarization is avoided. For an introduction to this technique, see Sect. 7.2.

Differential Faraday rotation

If synchrotron radiation is emitted from a Faraday-rotating medium containing a regular magnetic field, the polarization vectors of waves emitted at different positions along the line of sight are rotated by different amounts due to their different pathlengths within the source. This is known

as differential Faraday rotation and leads to depolarization due to the averaging of different polarization angles within the same line of sight. In case of a uniform magnetic field and constant thermal electron number density, the resulting degree of polarization is

$$p(\lambda^2) = p_\mathrm{i} \left| \frac{\sin\left(2RM\lambda^2\right)}{2RM\lambda^2} \right| \tag{2.27}$$

Internal and external Faraday dispersion

Faraday dispersion is the variation of Faraday-rotation angles along the line of sight and within the telescope beam, induced by small-scale fluctuations of turbulent magnetic fields. In the case of internal Faraday dispersion, these variations occur within the synchrotron-emitting medium itself, and lead to a fractional polarization of

$$p(\lambda^2) = p_\mathrm{i} \frac{1 - \exp(-S)}{S} \tag{2.28}$$

If the effect occurs in a non-emitting foreground layer, it is called external Faraday dispersion, and the observed degree of polarization is

$$p(\lambda^2) = p_\mathrm{i} \exp(-S) \tag{2.29}$$

In both cases, S is proportional to the fourth power of the wavelength:

$$S = 2\sigma_{RM}^2 \lambda^4 \tag{2.30}$$

If the telescope beam size is similar to or less than the spatial scale of the RM variations, the RM dispersion σ_{RM}^2 of a turbulent magnetized plasma can be approximated to (Arshakian & Beck 2011):

$$\sigma_{RM}^2 = 0.81 \left(\left(\frac{\langle n_\mathrm{e} \rangle}{\mathrm{cm}^{-3}} \right) \left(\frac{\langle B_\mathrm{turb} \rangle}{\mu\mathrm{G}} \right) \right)^2 \left(\frac{d}{\mathrm{pc}} \right) \left(\frac{L}{\mathrm{pc}} \right) f^{-1} \ \mathrm{rad}^2\,\mathrm{m}^4 \,, \tag{2.31}$$

where $\langle n_\mathrm{e} \rangle$ and $\langle B_\mathrm{turb} \rangle$ are the average thermal electron density and magnetic field strength in a single turbulent cell of size d in the volume. L is the pathlength along the line of sight through the turbulent medium and $f = \langle n_\mathrm{e} \rangle / n_\mathrm{e}$ is the filling factor of thermal electrons in the cells.

2.6 Free-free radiation

In addition to the synchrotron radiation of the relativistic CR electrons, also emission of thermal electrons contributes to the radio continuum spectrum of galaxies, and in most cases constitutes a non-negligible fraction of emission in the GHz regime. This radiation is called free-free radiation, as it is generated by the Coulomb interaction between free electrons and ions, such as in HII regions. As the electrons move on hyperbolic orbits around the ions, they experience a permanent acceleration, which makes them radiate. They move at thermal velocities, following a Maxwell

distribution, according to the temperature of the electron gas. For free-free emission, the Planck law can usually be described by the Wien approximation at GHz frequencies, where it shows a spectral index of typically -0.1. Since synchrotron radiation has much steeper spectral indices of $\lesssim -0.5$, the fractional contribution of free-free emission to the total spectrum is notably larger at higher frequencies. Above 1 GHz, a reasonable interpretation of radio continuum observations of galaxies usually requires the separation of this thermal emission from the non-thermal (i.e. synchrotron) component (see Sect. 4.2). Moreover, free-free radiation is unpolarized due to the randomly oriented trajectories of the thermal electrons.

3 JVLA Observations and data reduction

In this chapter, details of the JVLA observations of our two target galaxies as part of the CHANG-ES survey are provided, followed by a description of the basic data reduction steps, most of which were carried out using CASA. While mostly standard flagging and calibration strategies were followed, wide-band JVLA data in particular require and allow for more advanced imaging techniques, which in turn imply special considerations regarding the imaging of wide fields of view and the application of primary-beam corrections. Moreover, a section on the important issue of short-spacing corrections is included.

3.1 CHANG-ES: galaxy sample and observational setup

The CHANG-ES sample was selected from the Nearby Galaxies Catalog (NBGC, Tully 1988), according to the following criteria: *i)* inclination $i > 75°$; *ii)* declination $\delta > -23°$, to be accessible from the JVLA with an adequate *uv*-coverage; *iii)* blue isophotal diameter d_{25} between $4'$ and $15'$, to avoid galaxies with poor spatial resolution as well as galaxies that would require more than two pointings; *iv)* 1.4 GHz flux density $S_{1.4} > 23$ mJy, to exclude galaxies for which the detection of a halo is unlikely. Three exceptions from these limitations (among them NGC 4565, with $d_{25} > 15'$) were included, as they were known to show extraplanar emission and have an abundance of ancilllary data available. For a full list of the galaxy sample, see Table 1 of Irwin et al. (2012a). The sample displays a wide range in morphological type, SFR, nuclear activity, and environment. A major goal of CHANG-ES is to quantify how magnetic fields and CRs in halos correlate with these properties.

Table 3.1 summarizes the basic parameters of the observations. Collectively adding up to 405 hours, the 35 target galaxies and calibrator sources were observed at 1.5 GHz (L-band) and 6 GHz (C-band), with bandwidths of 512 MHz (split into 2048 spectral channels, over 32 spectral windows) and 2.048 GHz (with 1024 channels, split into 16 spectral windows), respectively. While the C-band IFs are at 5.5 and 6.5 GHz, and hence the two basebands cover the range between 5 and 7 GHz continuously, the correlator setup for L-band had IFs of 1.375 and 1.775 GHz, which allowed measurements from 1.25 to 1.9 GHz, with the range between 1.5 and 1.65 GHz being omitted due to severe RFI contamination. The B-, C-, and D-array configurations were used at 1.5 GHz, and the C- and D-array configurations at 6 GHz. As indicated above, all four polarization products (RR, LL, RL, LR) were measured.

The on-source observing times for the different array configurations and frequency bands have been chosen such that: *i)* the noise decreases by a factor of ∼2 from one configuration to the next (at the same frequency), which takes into account that predominantly smaller structures are observed with more extended arrays; *ii)* the noise decreases by a factor of ∼2.5 from 1.5 GHz to 6 GHz (at the same resolution), so that the signal-to-noise ratios (S/N) are similar for an assumed spectral index of ~ -0.7 between the two frequencies.

The FWHM of the primary beam $\theta_{\rm PB}$ is 30′ at 1.5 GHz but only 7.5′ at 6 GHz. Therefore, the C-band observations of all galaxies with $d_{25} > 1.3 \cdot \theta_{\rm PB} = 9.75'$ (which include both NGC 891 and NGC 4565) were performed with two pointings, which were placed on the major axis on either side of the galaxy center, separated by $\sim \theta_{\rm PB}/2$. The pointing coordinates for both galaxies at 6 GHz are given in Table 3.2.

Galaxies located in the same region on the sky were generally observed together in one scheduling block (SB) per array configuration and frequency. For galaxies seen only at low elevations (such as NGC 891), the observing time was split into two SBs in each case (except C-band C-array), to improve the *uv*-coverage. A SB contains one 10 minute scan each of a flux calibrator (3C 48 in case of NGC 891 and 3C 286 for NGC 4565; also used for bandpass and polarization position angle calibration) and a polarization leakage calibrator, while the major part is made up of on-source scans flanked by phase calibrator scans.

Table 3.1: General observation parameters of CHANG-ES

Frequency band[a]	Configuration	Time[b] (per pointing)	Theor. noise rms[c] [μJy/beam]	Confusion[d] [μJy/beam]	$\theta_{\rm LAS}$ [e] [arcmin]
L (1.5 GHz)	B	120 min	7.7	0.4	2
	C	30 min	16	4.4	16.2
	D	20 min	20	48	16.2
C (6 GHz)	C	180 min	2.4	0.1	4
	D	40 min	4.8	1.3	4

[a] The central frequency of the respective band is given. The total bandwidth is 512 MHz for L-band and 2.048 GHz for C-band. See text for details.

[b] On-source time per individual pointing, not including overheads. At 6 GHz, the larger galaxies required two pointings, as the field of view given by the primary beam is too small at this frequency.

[c] Theoretical thermal noise (i.e. ignoring confusion) for each polarization product, taken from (Irwin et al. 2012a). See also the VLA Observational Status Summary (OSS) at `https://science.nrao.edu/facilities/vla/docs/manuals/oss/performance/sensitivity`

[d] Confusion limits, determined using Eq. 10 of Condon (2002), assuming in each case the average beam FWHM of the two galaxies (see Tables 3.3-3.6. These should only apply to total intensity (Stokes *I*), but not to polarization images (Stokes *Q*, *U* or *V*).

[e] Largest angular size scale detectable by the array in the given configuration, determined by the shortest antenna spacing.

Table 3.2: Pointing positions of C-band observations

Galaxy	RA (pt. 1)	Dec (pt. 1)	RA (pt. 2)	Dec (pt. 2)
NGC 891	02h 22m 37.21s	42d 22m 41.2s	02h 22m 29.61s	42d 19m 12.6s
NGC 4565	12h 36m 26.58s	25d 57m 54.7s	12h 36m 14.98s	26d 00m 36.6s

3.2 Hanning smoothing and RFI flagging

Apart from a number of a priori calibrations (see below), the first operation performed on the raw data was Hanning smoothing in frequency, to eliminate spectral Gibbs ringing and therefore make it easier to detect RFI throughout the band. This resulted in a frequency resolution of twice the channel width. A substantial amount of time was then spent on RFI excision, which was almost entirely done in `manual` mode, i.e. by selecting segments of data to be flagged in a series of `flagdata` commands. For the same array configuration, the contamination by RFI was significantly stronger in L-band than in C-band. While it was often reasonable to flag the data of a given bad antenna or baseline for the entire duration of the observation or to flag a certain frequency or time range for all antennas, a number of less obvious cases required a more precise localization of RFI in time/frequency/baseline parameter space, to save a certain amount of good data from being discarded. The strongest RFI signals generally occupy a well-defined frequency range and persist throughout the observation, which makes them easy to flag; however, a large number of RFI signals at lower amplitudes are successively revealed each time new calibration solutions are applied to the data (see below for a description of the calibration procedure). For each data set, two to four iterations of flagging and (re)calibration were required until the bad data were removed to a satisfactory extent.

As automated flagging routines did not provide sufficient control over the flagging process to fully rely on them for these data, manual flagging seemed to be the safest way to get rid of as many bad data as possible while retaining a reasonable (image-plane) S/N. To save a certain amount of time nonetheless, some of the data sets of NGC 891 were flagged in part using the automatic `rflag` mode. `Rflag` is based on a statistical filter, which selects visibilities according to the deviation of their amplitudes from the median value calculated across user-specified time and frequency intervals. For more information on automated flagging modes in CASA, see `http://www.aoc.nrao.edu/ rurvashi/FlaggerDocs/FlaggerDocs.html`.

3.3 Calibration

The wavefronts received by a radio interferometer are subjected to a variety of effects during their transmission through the earth's atmosphere, their reflection from the dish surfaces, and their processing through the receiver and correlator system. The purpose of calibration is to correct for these data corruptions and thereby transform the measured visibilities as precisely as possible into the visibilties that would have been measured in vacuum by an ideal interferometer.

A way to describe the relation between the observed and the ideal ("true") visibilities is the Hamaker-Bregman-Sault Measurement Equation. For the calibration performed in this work, it can be written as follows (for the baseline between antennas i and j):

$$\vec{V}_{ij}(\nu, t) = X(\nu)D_{ij}(\nu)C(\nu)P_{ij}(t)F(\nu)G_{ij}(\nu, t)B_{ij}(\nu, t)K_{ij}(\nu)E_{ij}A_{ij}\vec{V}_{ij}^{\text{ideal}}(\nu, t) \tag{3.1}$$

The measured visibilities $\vec{V}_{ij}$ and the ideal visibilities $\vec{V}_{ij}^{\text{ideal}}$ are vectors with one entry for each of the four cross-correlations (RR, LL, RL, LR), while the remaining factors are generally 4×4 matrices representing the various effects that need to be calibrated for (i.e. inverted) to recover the ideal visibilities from the measured ones. In Eq. 3.1 these so-called Jones matrices appear in the order (from right to left) in which they were applied to the data in this work. Each of them corresponds to one of the calibration steps explained in the following.

3.3.1 A priori calibration

While the main part of the time- and frequency-dependent data calibration requires that the strongest RFI signals have been flagged beforehand, a few calibration steps can (or should) be performed before flagging, since they depend on a priori known antenna-based quantities rather than on the actual observational data, or require non-Hanning-smoothed visibilities:

A_{ij} – **Antenna position corrections**: In case any antennas were moved during or shortly before the observation, the position information for these antennas stored in the data set might be slightly offset from their actual positions during the observation. CASA can automatically retrieve the correction values for each antenna in x-, y- and z-direction from the VLA baseline webpage (http://www.vla.nrao.edu/astro/archive/baselines/).

E_{ij} – **Gain-elevation curve**: Telescope dishes are not absolutely rigid, so for large antennas the forward gain and effective collecting area vary with elevation as the dish surface is deformed by gravity. The polynomial coefficients of the gain as a function of elevation are available directly from the CASA data repository and are looked up automatically by the program.

$P_{ij}(t)$ – **Parallactic angle**: Since the parallactic angle describes the orientation of the polarization coordinates on the plane of the sky, an antenna-based parallactic angle correction is an important step for the polarization calibration.

$K_{ij}(\nu)$ – **Antenna delays**: Antenna-based delays induce phase ramps in frequency for each spectral window. To remove this effect (at this point only for the parallel-hand correlations, RR and LL), a section of the flux calibrator scan is used to calibrate for relative delays of each antenna relative to a reference antenna. This step has to take place before Hanning smoothing, as this would otherwise decorrelate the visibility amplitudes.

3.3.2 Total intensity calibration

The task `setjy` is used to establish the flux density (Stokes I) scale of the flux calibrator (3C 48 or 3C 286) as a function of frequency, channel by channel. This is done by means of a model image of the flux calibrator and the Perley-Butler 2010 calibration scale.

$B_{ij}(\nu)$ – **Bandpass**: Each spectral window has its own bandpass response, which in turn is different for each antenna. It is best to solve for these frequency-dependent complex gains (amplitude and phase) before calibrating the time-dependent gains for all observed sources. In order to account for gain fluctuations during the observation of the bandpass calibrator itself (which is the same as the flux calibrator here), the data are averaged in time for each channel before the computation of B_{ij}. However, to ensure that phase variations do not decorrelate the data during this time-averaging, one first needs to determine an initial time-dependent gain phase solution for the bandpass calibrator, which is then applied on the fly while solving for the B_{ij} terms. This initial gain calibration is not used any further, as a proper gain calibration based on the bandpass solutions follows.

$G_{ij}(\nu, t)$ – **Time-dependent complex gains**: Time-dependent complex gain variations are in most cases the dominant calibration effect. This calibration yields a solution for each antenna, polarization (L and R), and spectral window, and is determined for each of the flux, phase, and polarization leakage calibrator scans, after pre-applying the previously obtained bandpass solutions and averaging the data in frequency for each spectral window.

$F(\nu)$ – **Flux density scale**: During the computation of the G_{ij} terms for the phase and leakage calibrators, the model assumed in each case is a point source of 1 Jy. To obtain the true absolute flux density scale for these secondary calibrators, it is assumed that their mean gain amplitudes are the same as for the flux calibrator. Using time-averaged gain amplitudes, the ratio between each secondary calibrator and the flux calibrator is formed for each antenna and polarization. The average of this ratio over all antennas and polarizations yields for each channel a correction factor $F(\nu)$ that is applied to the secondary calibrators' gains.

In the final step, the so determined bandpass and time-dependent gain solutions as well as the flux density scale are applied to all sources, with the gain solutions interpolated in time between the phase calibrator scans when applied to the target source. After this is done, the data are ready for total intensity imaging (unless it turns out that further RFI flagging is necessary, see above).

3.3.3 Polarization calibration

Calibration of the linearly polarized intensity and polarization position angle requires running `setjy` to set the Stokes Q and U values for the flux calibrator as a function of frequency. As calibrator models for the wide JVLA bands are not yet available for Q and U, they have to be calculated from the absolute polarization angle χ and fractional polarization p (given in %), which both have a known frequency-dependent behaviour (R. Perley 2011 / J. Irwin 2012, private

communication; see also Irwin et al. 2012b). For 3C 48, the dependence of the position angle has the form

$$\chi_L^{3C48}(\nu) = -0.002213 \cdot \nu^2 + 0.873 \cdot \nu - 655.7 \tag{3.2}$$

$$\chi_C^{3C48}(\nu) = 0.002819 \cdot \nu + 93.11 \tag{3.3}$$

in L-band and C-band, respectively, while the fractional polarization follows

$$p_L^{3C48}(\nu) = 2.49 \cdot 10^{-7} \cdot \nu^2 - 6.884 \cdot 10^{-5} \cdot \nu + 0.0894 \tag{3.4}$$

$$p_C^{3C48}(\nu) = 0.0005397 \cdot \nu + 1.488\,. \tag{3.5}$$

3C 286 is assumed to have a constant polarization angle of $\chi^{3C286} = 33°$ and a fractional polarization of

$$p_L^{3C286}(\nu) = -1.443 \cdot 10^{-6} \cdot \nu^2 + 0.006026 \cdot \nu + 3.858 \tag{3.6}$$

$$p_C^{3C286}(\nu) = 0.0001583 \cdot \nu + 10.57\,. \tag{3.7}$$

Stokes Q and U are then computed via

$$Q_\nu = (p(\nu)/100) \cdot I_\nu \cdot \cos(2\chi(\nu)) \tag{3.8}$$

$$U_\nu = (p(\nu)/100) \cdot I_\nu \cdot \sin(2\chi(\nu))\,, \tag{3.9}$$

where $I(\nu)$ is obtained from the respective calibrator model, like in Sect. 3.3.2. At the time of writing, CASA is not yet capable of channel-based polarization calibration. Therefore, only a single I, Q, and U value per spectral window is determined.

$C(\nu)$ – **Cross-hand delays**: The gain and bandpass calibration typically leave a single residual delay between the R and L polarizations, which is from the reference antenna that was used to solve for the parallel-hand delays. Applying the previously determined gain and bandpass solutions on the fly, the cross-hand (RL, LR) delay is calculated for each spectral window, using the flux calibrator scan, since both 3C 48 and 3C 286 are strongly polarized.

$D_{ij}(\nu)$ – **Instrumental polarization**: The polarization response of each antenna is corrupted by polarization leakage between the R and L feeds. A preferrably unpolarized calibrator is used to solve for these leakage terms (after pre-applying the bandpass, gain, and cross-hand delay calibrations). Such an unpolarized source was included in all CHANG-ES observing blocks except the one containing NGC 4565 in C-band D-array. In this situation, it was possible to use the phase calibrator for the leakage calibration, as it was observed with a sufficient parallactic angle coverage to simultaneously solve for its polarization (averaged in frequency).

$X(\nu)$ – **Polarization position angle**: After solving for the instrumental polarization, the polarized intensity calibration is completed, but the R-L phase difference still needs to be calibrated, to obtain the correct polarization position angle as a function of frequency. This is done based on the known position angles of the flux calibrator, after on-the-fly application of bandpass, gain, cross-hand delay, and leakage solutions.

Finally, all corrections are applied to the calibrators and the target source: bandpass, time-dependent complex gains, flux density scale, cross-hand delays, polarization leakage, and polarization position angle.

3.4 Imaging

Images of NGC 891 and NGC 4565 in all Stokes parameters were formed separately for each frequency band and array configuration. For the deconvolution ("cleaning") of the Fourier-inverted *uv* data, the Cotton-Schwab algorithm (Schwab 1984) was used in combination with the multi-scale multi-frequency synthesis algorithm (MS-MFS clean, Rau & Cornwell 2011), which is described further below. The images were cleaned until a peak residual corresponding to $\sim 2-4$ times the noise rms in the final image was reached. In some cases it was necessary to use masks (polygonal masks for the target galaxy and mostly circular ones for background sources) to avoid cleaning on side lobes induced by the dirty beam or to keep the algorithm from diverging. Masks were created by first running the `clean` task in `interactive` mode, which allows the user to draw masks in the CASA `viewer` before cleaning and to modify them after each intermediate step defined by a user-given number of clean iterations. Using masks was not necessary for cleaning Stokes Q and U. Unless otherwise specified, robust-0 weighting (Briggs 1995), which results in a good compromise between angular resolution and sensitivity, was applied to the visibilities before imaging. The pixel size of every image was chosen such that the FWHM of the synthesized beam was sampled with at least 3 pixels in RA and DEC.

In addition to imaging each array configuration separately, images were also produced from a combination of the (B-,) C- and D-array data for each frequency band. Here, an outer *uv*-taper was applied in addition to the robust weighting, to bring out somewhat more extended emission, since the number of recorded visibilities is much higher for more extended arrays, which results in a relative down-weighting of the more compact-array data. In each case, the spatial frequency at which the tapering takes place was set to the value that resulted in the lowest noise rms in the image, while staying in the range between the maximum spatial frequencies of the two most extended arrays (i.e. B- and C-array in L-band, and C- and D-array in C-band), to avoid sacrificing too much angular resolution. Further important aspects of imaging that are relavant to the data presented here, as well as post-deconvolution operations are explained in the following. Tables 3.3-3.6 give a summary of the imaging parameters for each data set.

3.4.1 Multi-frequency synthesis (MFS)

A major advantage of wide-band observations is the enabling of multi-frequency synthesis, which was initially developed by Conway et al. (1990) and produces images by combining the data from all channels of the frequency band. This not only increases the S/N compared to single-channel (or -spectral-window) images, but also significantly improves the *uv*-coverage, since each frequency channel is gridded separately (whereby also bandwidth smearing is prevented). As Fig. 3.1 illustrates, using wide frequency bands extends the *uv* coverage in radial direction,

Table 3.3: NGC 891: L-band (1.5 GHz) observations and imaging

Configuration	B	C	D	B+C+D combined
Obs. date	24/06/2012	11/02/2012 01/04/2012	16/12/2011 17/03/2013	N/A
Flux calibrator	3C 48	3C 48	3C 48	N/A
Phase calibrator	J0230+4032	J0314+4314	J0314+4314	N/A
Zero-pol. calibrator	3C 84	J2355+4950	3C 84	N/A
b_{maj} [arcsec][a]	3.16	10.64	36.42	4.09
b_{min} [arcsec][a]	2.90	9.66	32.48	3.73
Beam position angle [deg]	54.22	88.06	-74.29	50.65
Pixel size [arcsec]	0.5	2.5	5	0.5
Threshold for cleaning [μJy/beam]	50	50	100 / 40[b]	50
Scales for MS-cleaning [arcsec]	0, 6, 15	0, 10, 20, 40	0, 20, 100, 200	0, 6, 15, 50, 100, 200
Mask used for cleaning (Stokes I)	yes	yes	yes	yes
Self-calibration	1x phase	no	no	N/A[c]
Outer uv-taper	-	-	-	30 kλ
Noise rms (I) [μJy/beam]	16	28	60	14.5
Noise rms (Q,U) [μJy/beam]	18	26	40	12.5

[a] major- and minor-axis FWHM of the synthesized beam

[b] In the D-array image, after cleaning on NGC 891 to a threshold of 100μJy/beam, we continued cleaning down to 40 μJy/beam on the strong background source 3C 66A only.

[c] N/A in this case (as well as in Tables 3.4-3.6) means that the specified self-calibrations were already applied to the single-array data sets before producing the combined-array images.

such that even for relatively short integration times, an almost gapless filling of the uv-plane between the minimum and maximum spatial frequency of the observation is achieved, which in turn decreases the side lobes of the synthesized beam. The resulting images will have an angular resolution given by the longest baseline at the highest frequency of the band, while the largest detectable angular scale will be as large as for the shortest baseline at the lowest frequency.

MFS imaging furthermore means that the spectrum of the sky can (and generally has to) be modelled as part of the image reconstruction (Sault & Wieringa 1994). The intensity[1] at any position in the sky is assumed to be described by a power law in frequency:

$$I_\nu = I_{\nu_0} \left(\frac{\nu}{\nu_0}\right)^{\alpha+\beta\log\left(\frac{\nu}{\nu_0}\right)} . \tag{3.10}$$

ν_0 is a reference frequency usually corresponding to the centre frequency of the band, and I_{ν_0}, α and β are the intensity, spectral index and spectral curvature at this frequency. The MFS

[1] Although intensities are denoted by the letter I here, all considerations given on the following pages, up to and including Sect. 3.4.6, are analogously valid for Stokes Q, U, and V.

Table 3.4: NGC 891: C-band (6 GHz) observations and imaging

Configuration	C	D	C+D combined
Obs. date	06-07/02/2012	09/12/2011 18/12/2011	N/A
Flux calibrator	3C 48	3C 48	N/A
Phase calibrator	J0251+4315	J0230+4032	N/A
Zero-pol. calibrator	3C 84	3C 84	N/A
b_{maj} [arcsec]	2.77	9.00	3.88
b_{min} [arcsec]	2.61	8.81	3.50
Beam position angle [deg]	85.93	-79.46	80.49
Pixel size [arcsec]	0.5	2.5	0.5
Threshold for cleaning [μJy/beam]	10	15	10
Scales for MS-cleaning [arcsec]	0, 6, 14	0, 10, 20, 40	0, 6, 15
Mask used for cleaning	yes	yes	yes
Self-calibration	1x amp+phase	1x amp+phase	N/A
Outer *uv*-taper	-	-	34 kλ
Noise rms (I) [μJy/beam]	3.1	6.5	2.7
Noise rms (Q,U) [μJy/beam]	3.2	6.8	2.6

Table 3.5: NGC 4565: L-band (1.5 GHz) observations and imaging

Configuration	B	C	D	B+C+D combined
Obs. date	02-03/06/2012	02/04/2012	30/12/2011	N/A
Flux calibrator	3C 286	3C 286	3C 286	N/A
Phase calibrator	J1221+2813	J1221+2813	J1221+2813	N/A
Zero-pol. calibrator	J1407+2827	J1407+2827	J1407+2827	N/A
b_{maj} [arcsec]	3.31	10.49	34.50	10.16
b_{min} [arcsec]	3.01	10.01	32.32	9.40
Beam position angle [deg]	45.50	64.64	-89.06	47.75
Pixel size [arcsec]	0.5	2.5	5	0.5
Threshold for cleaning [μJy/beam]	50	40	90	50
Scales for MS-cleaning [arcsec]	0, 6, 15	0, 10, 20	0, 35, 80	0, 6, 15, 35, 70, 105
Mask used for cleaning	no	no	no	yes
Self-calibration	no	1x amp+phase	1x phase	N/A
Outer *uv*-taper	-	-	-	50 kλ
Noise rms (I) [μJy/beam]	14	20.5	34	20
Noise rms (Q,U) [μJy/beam]	14	21	27	11

algorithm approximates the power law spectrum as a Taylor expansion about ν_0, which results in

Table 3.6: NGC 4565: C-band (6 GHz) observations and imaging

Configuration	C	D	C+D combined
Obs. date	16/04/2012	29/12/2011	N/A
Flux calibrator	3C 286	3C 286	N/A
Phase calibrator	J1221+2813	J1221+2813	N/A
Zero-pol. calibrator	J1407+2827	J1221+2813	N/A
b_{maj} [arcsec]	2.63	9.02	3.57
b_{min} [arcsec]	2.59	8.82	3.52
Beam position angle [deg]	-61.72	85.48	-83.98
Pixel size [arcsec]	0.5	2.5	0.5
Threshold for cleaning [μJy/beam]	10	20	10
Scales for MS-cleaning [arcsec]	0, 5, 13	0, 10, 40	0, 5, 13
Mask used for cleaning	no	yes	yes
Self-calibration	1x phase	no	N/A
Outer *uv*-taper	-	-	34 kλ
Noise rms (I) [μJy/beam]	3.2	7.4	2.5
Noise rms (Q,U) [μJy/beam]	3.2	7.4	2.5

a polynomial least-squares fit to the spectrum, using all unflagged frequency channels:

$$I_\nu = \sum_{t=0}^{n_t-1} I_t \left(\frac{\nu - \nu_0}{\nu_0} \right)^t , \tag{3.11}$$

where I_t represents the Taylor coefficient image of t-th order and n_t is the user-specified number of Taylor terms to include. Since I_t is proportional to the t-th frequency derivative of I_ν, the following relations hold:

$$I_0 = I_{\nu_0} , \qquad \alpha = \frac{I_1}{I_0} , \qquad \beta = \frac{I_2}{I_0} - \frac{\alpha(\alpha-1)}{2} . \tag{3.12}$$

The more Taylor terms are included in the fit, the more accurate will be the image reconstruction, and as is obvious from Eq. 3.12, fitting the spectral index and curvature requires $n_t \geq 2$ and $n_t \geq 3$, respectively. Although all Taylor coefficients I_t as well as α, β and their formal errors[2] $\Delta\alpha$ and $\Delta\beta$ are written out by CASA as separate images, I_t for $t \geq 1$ are of little scientific use by themselves, but necessary inputs for self-calibration (Sect. 3.4.4) and primary-beam correction (Sect. 3.4.5). $I_0 = I_{\nu_0}$ will simply be referred to as the total intensity (or total power) map throughout most of this thesis (while "intensity map" will be used for the remainder of this chapter when generalizing to all Stokes parameters). Also, to save computing time, and

[2]The error on the spectral index is approximately given by propagation of the absolute errors of the first two Taylor coefficient images: $\Delta\alpha = \alpha \sqrt{\left(\frac{\Delta I_0}{I_0}\right)^2 + \left(\frac{\Delta I_1}{I_1}\right)^2}$, with ΔI_0 and ΔI_1 being inferred from the respective residual maps R_0 and R_1. According to Rau & Cornwell (2011), also deconvolution errors (which, for instance, occur when point-source based cleaning is applied to extended emission, see Sect. 3.4.2) contribute to the errors in the Taylor term images, and can thereby increase $\Delta\alpha$ by an order of magnitude.

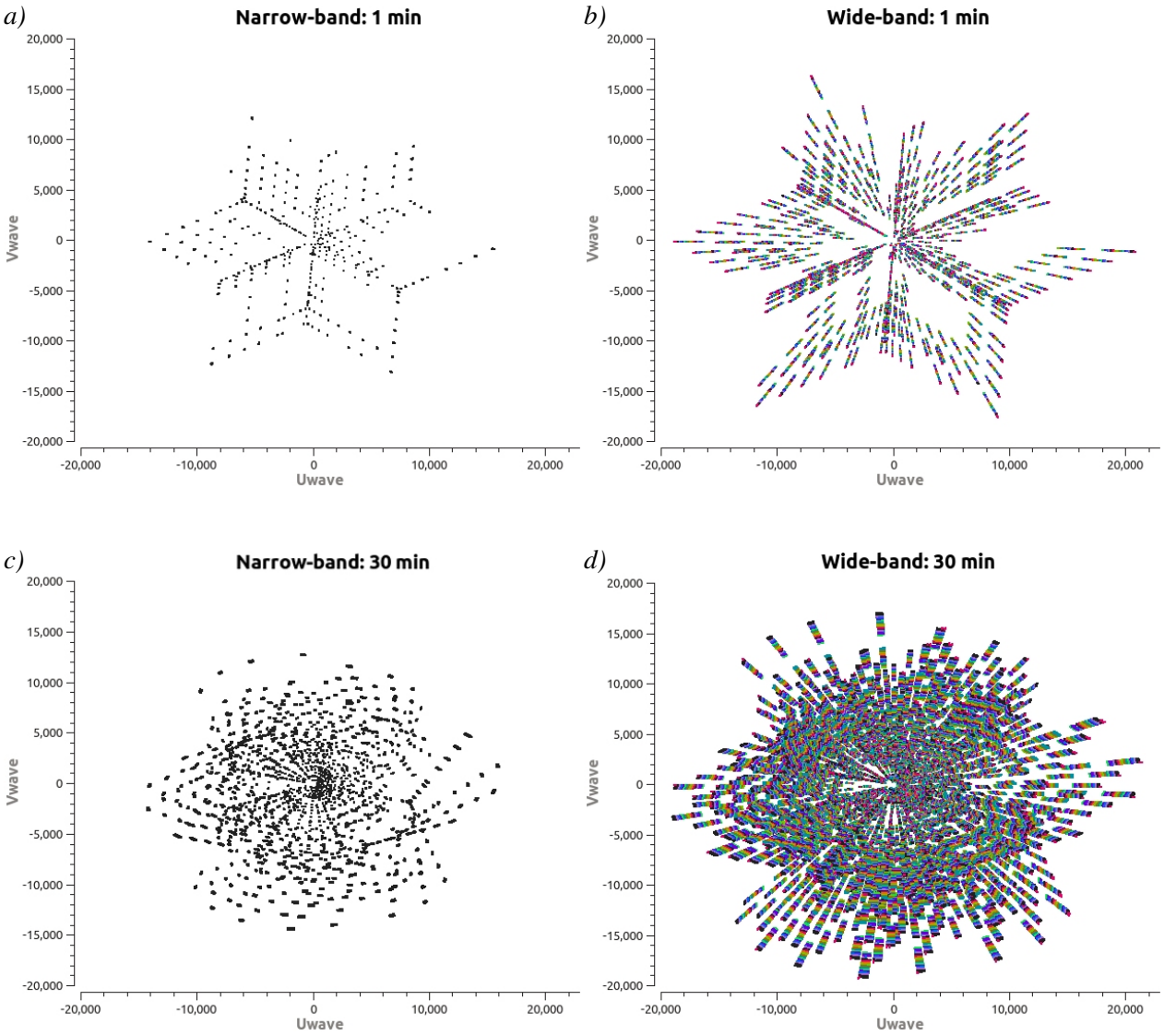

Figure 3.1: *uv*-plane distribution of visibilities measured for NGC 4565 in L-band C-array. Spatial frequencies are given in units of wavelength. In the four panels, different time and frequency ranges within the data set are displayed: *a)* 1-minute snapshot within a 16 MHz spectral window, *b)* 1-minute snapshot over the full 512 MHz bandwidth, *c)* Full 30-minute observation within a 16 MHz spectral window, *d)* Full 30-minute observation over the full 512 MHz bandwidth. The data points are colour-coded by spectral window number. The figure demonstrates how a dense filling of the *uv* plane can be achieved already in short integration times (here 30 minutes) using wide-band observations in combination with multi-frequency synthesis (MFS).

because no significant spectral curvature within the single frequency bands is expected for the galaxies presented here, the curvature term was neglected in this work and hence only the first two Taylor terms were considered in the spectral modelling, so that effectively a linear fit of the

form $\ln(I_\nu/I_{\nu_0}) = \alpha\ln(\nu/\nu_0)$ was performed. Moreover, even though in principle adding more Taylor terms should improve the imaging accuracy, in practice the efficiency of this is limited by the S/N of the data and by the quality of the calibration. Test runs of `clean` with $n_t \geq 3$ resulted in higher noise rms than for $n_t = 2$ when cleaning down to the same threshold.

3.4.2 Multi-scale (MS) cleaning

Unlike the classic clean algorithm, which generates sky models as a distribution of point sources (i.e. delta functions), multi-scale clean (Cornwell 2008) allows for clean components of arbitrary angular scales, which can improve the reconstruction of the spatial structure significantly if the scales are well-chosen. For a number n_s of discrete angular scales, a multi-scale model image can thus be described by

$$I^{\mathrm{MS}} = \sum_{s=0}^{n_s-1} K_s * I_s^\delta \,, \tag{3.13}$$

where I_s^δ is a set of delta functions representing the locations and amplitudes of flux components of the angular size of scale s in the image. This image is convolved with the scale function K_s, which is a tapered truncated parabola having a width proportional to the size of s. The convolution is performed in each clean iteration, which subsequently adds the resulting flux component to the model image I^{MS}. As usual, after the last iteration, the model is convolved with the clean beam and the residuals are added to form the clean image. The MS-MFS algorithm developed by Rau & Cornwell (2011) combines this method with the frequency-dependent modelling described above, so that the fitted spectrum has the form

$$I_\nu = \sum_{t=0}^{n_t-1}\sum_{s=0}^{n_s-1}[K_s * I_{s,t}^\delta]\left(\frac{\nu-\nu_0}{\nu_0}\right)^t \,, \tag{3.14}$$

where $I_{s,t}^\delta$ corresponds to I_s^δ from Eq. 3.13 for the t-th Taylor coefficient map.

In practice, it can require some trial and error to find the ideal angular scales to clean on, but according to the CASA cookbook, a rule of thumb is to use scales of 0 (which corresponds to traditional point-source deconvolution), 2, and 5 times the FWHM of the synthesized beam. For the images produced in this work, sticking to this rule yielded satisfactory results in most cases, however sometimes up to six different scales were applied. Particular care has to be taken that the applied scales are not too large, as this can lead to artifacts like diffuse patches of positive flux density in regions around noise peaks or side lobe structures that are erroneously treated like real emission.

3.4.3 Wide-field considerations

Utilizing the broad bandwidths of the JVLA via MFS also results in a considerably higher sensitivity to sources far from the pointing center than in pre-upgrade VLA observations. This is because the primary beam is different for each frequency channel (see Fig. 3.2), and hence, unlike

a monochromatic primary beam, the effective, i.e. frequency-averaged primary beam pattern never reaches an exact null and only gradually approaches zero with increasing distance from the pointing centre. In L-band for example, the average primary-beam gain in the side lobes at ∼1 degree from the centre can still be as high as a few %, as evident from Fig. 3.2 *d)* . Hence, side lobe patterns around strong radio sources like 3C 66A and B, which are located ∼ 40′ north of NGC 891 (see Fig. 3.3), can affect the image quality considerably, and therefore including such sources in the cleaning process is absolutely necessary. As the array is non-coplanar to emission from such off-centre sources, one needs to take account of the *w*-term, i.e. the aperture-domain coordinate in the line-of-sight direction. This is accomplished by the *w*-projection algorithm (Cornwell et al. 2008), which divides the sky solid angle into a number of tangent planes for which the *w*-terms are computed.

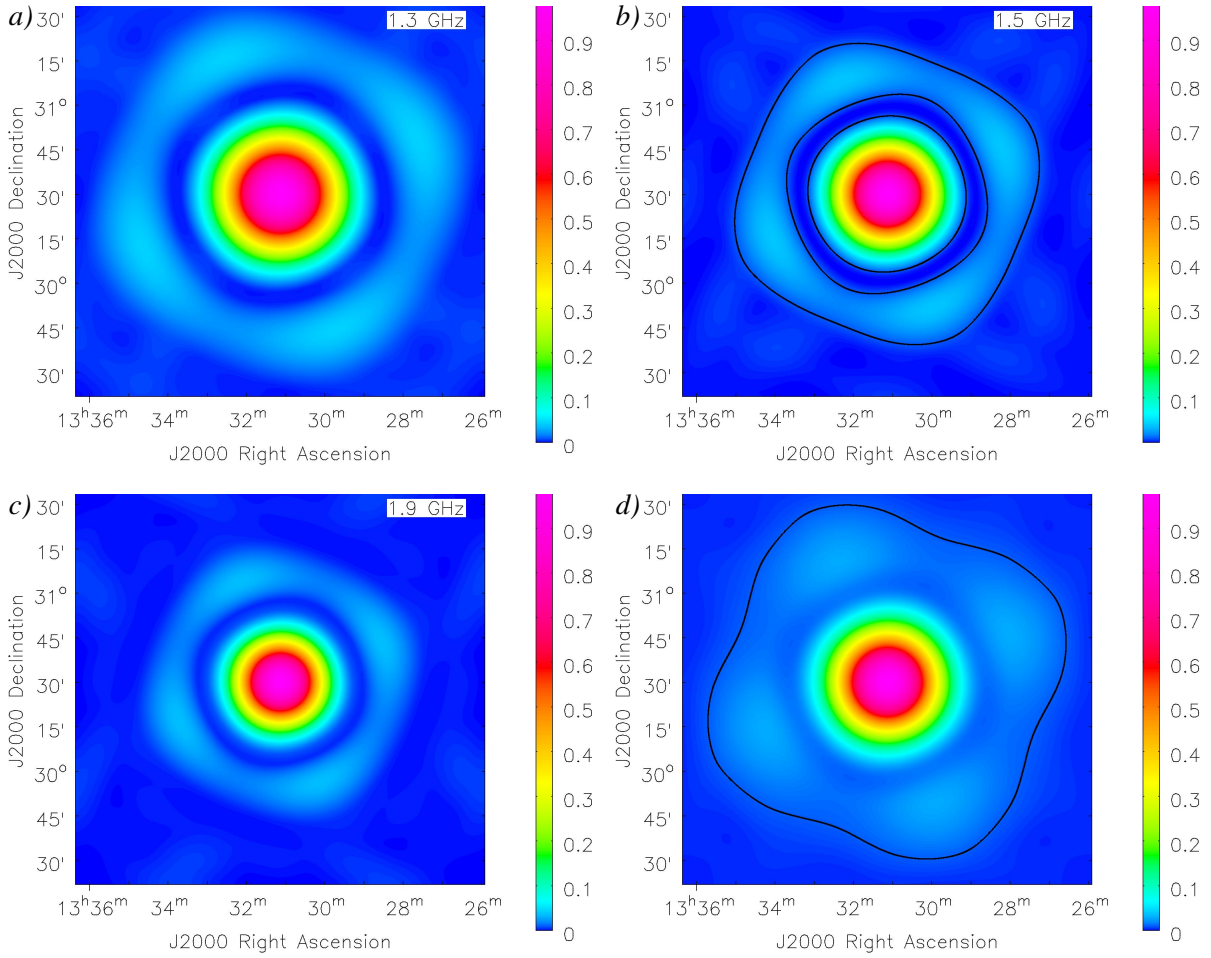

Figure 3.2: Model of the JVLA primary-beam pattern at different frequencies within L-band: *a)* 1.3 GHz, *b)* 1.5 GHz, *c)* 1.9 GHz, *d)* average of the primary beam models at 10 equidistant frequencies between 1.2 GHz and 1.9 GHz. Contours in panels *b)* and *d)* are placed at a primary-beam gain of 1%. The average primary-beam pattern is clearly more extended than the primary beam at the centre frequency of 1.5 GHz and does not reach a gain of zero in the annulus between the main peak and the first-order side lobes.

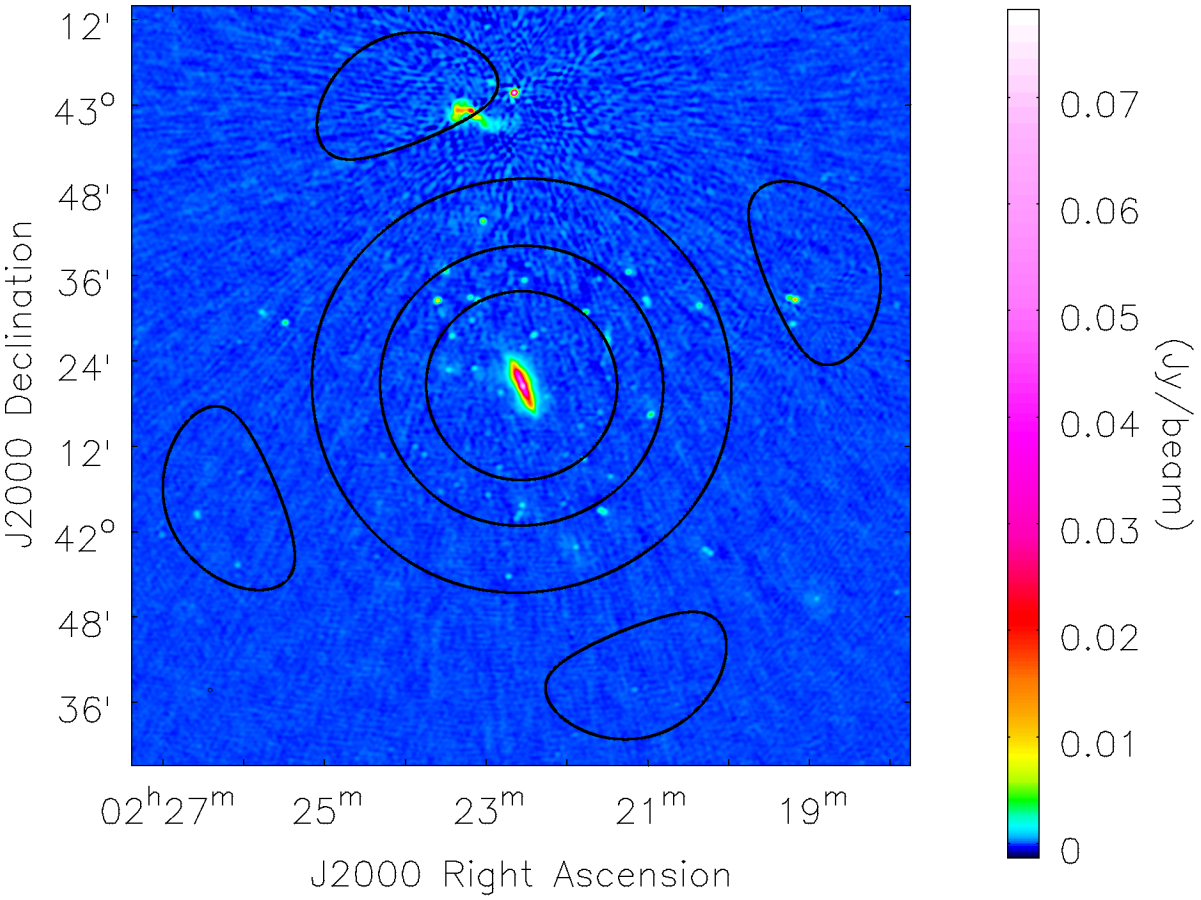

Figure 3.3: Cleaned L-band D-array map showing the observed field around NGC 891. Overlaid are contours of the average L-band primary beam (as shown in Fig. 3.2 *d)*) at gain levels of 2%, 20%, and 50%. The blazar 3C 66A and radio galaxy 3C 66B, located near the northern edge of the image, coincide with the side lobes of the primary beam (at a >2% level; note that the primary-beam pattern rotates on the sky during the observation), and hence contribute strongly in terms of side-lobe artifacts, which are still visible in the image after cleaning down to a low threshold.

The primary beam pattern also rotates on the sky over the time of the observation and is not rotationally symmetric, which necessitates yet another correction method called A-projection (Bhatnagar et al. 2008, 2013). However, this method is not yet implemented in CASA for combination with MFS imaging using two or more Taylor terms, and has therefore not been applied to CHANG-ES data so far. Furthermore, there seems to be a significant flexure-induced parallactic angle dependence of the primary beam shape itself, which does not cancel out for short observing times. Hence, it is not ensured that the NRAO-provided primary beam models that we applied are accurate, and consequently even primary-beam corrected data presented in this work need to be treated with some caution, especially in the context of spectral index measurements (Chapter 5).

3.4.4 Self-calibration

Model components obtained from cleaning an image can be used to refine the calibration and thereby further improve the image quality. This method is called self-calibration, as sources in the target field are used as their own calibrators. The model image is Fourier-transformed to the *uv*-plane, where the model visibilities are compared to the observed ones. After appyling the gain corrections obtained in this way to the observed visibilities, the cleaning is repeated on the newly calibrated data. By alternately cleaning and calibrating in this way, the model and the calibration can be improved iteratively, if it is done carefully. To prevent defective solutions to propagate throughout the process, it is generally recommended to start with a model containing a relatively small number of flux components, and cleaning deeper in each iteration. Likewise, as the model becomes more accurate, the time interval per gain solution should be decreased in each step, as long as there is sufficient S/N for this interval. Moreover, a choice has to be made whether to solve only for the gain phases (`p` mode) or for amplitudes and phases simultaneously (`ap` mode).

Whether self-calibration (only done in Stokes *I*) did successfully improve the final image, and also what type of calibration was performed (`p` or `ap`), is given for each data set in Tables 3.3-3.6. In fact, a single iteration was sufficient in all six cases, and further self-calibration had basically no more effect on the resulting image. Three data sets required `ap` calibration, while in two cases the `p` mode was the better choice, e.g. due to the strong central source of NGC 4565 in C-band, where the attempt to use `ap` solutions had caused a considerable decrease of its peak intensity.
As an attempt to eliminate the undesirable effects of 3C 66 from the L-band D-array image of NGC 891, so-called peeling, an iterative cleaning and self-calibration method (as described by Pizzo & de Bruyn (2009) and Adebahr (2013)), was performed. This, however, failed to improve the noise level in the image, and the resulting self-calibration solution was hence discarded.

3.4.5 Wide-band primary beam correction

As mentioned above, the primary beam of the antennas is frequency-dependent (it even has spectral curvature, as can be seen from Fig. 3.4), and therefore not only does the MFS intensity image I_{ν_0} have to be corrected for the primary beam at ν_0, but also the α map needs a correction for the artificial spectral index induced by the frequency-dependence of the primary beam pattern. In CASA, this is performed by the `widebandpbcor` task, which in the first step computes a set of primary beam maps at the user-specified frequencies. It is sufficient to form the beam at one frequency per spectral window, rather than using all channels, which would consume an unnecessarily large amount of computing time and disk space. Next, a Taylor polynomial is fitted to each pixel along the frequency axis of this data cube (here to first order, as has been done during MFS imaging), which results in coefficient images representing the primary beam spectrum, as well as a primary beam spectral index map. The primary beam correction of the intensity and spectral index maps of the sky is then executed via

$$I_{\nu_0}^{\mathrm{PBcor}} = \frac{I_{\nu_0}}{PB_{\nu_0}}\,, \qquad \alpha^{\mathrm{PBcor}} = \alpha - \alpha_{\mathrm{PB}}\,, \tag{3.15}$$

where PB_{ν_0} is the beam pattern at the same reference frequency about which the Taylor expansion was performed during MFS imaging, and α_{PB} is the primary beam spectral index at this frequency. Also, a primary beam threshold is applied when running `widebandpbcor`, which means that the Taylor-coefficient images are not formed in regions where the primary beam gain is below a certain value, and hence no primary beam correction below this threshold is performed. Throughout this work, the threshold has been set to a primary beam gain of 20%.

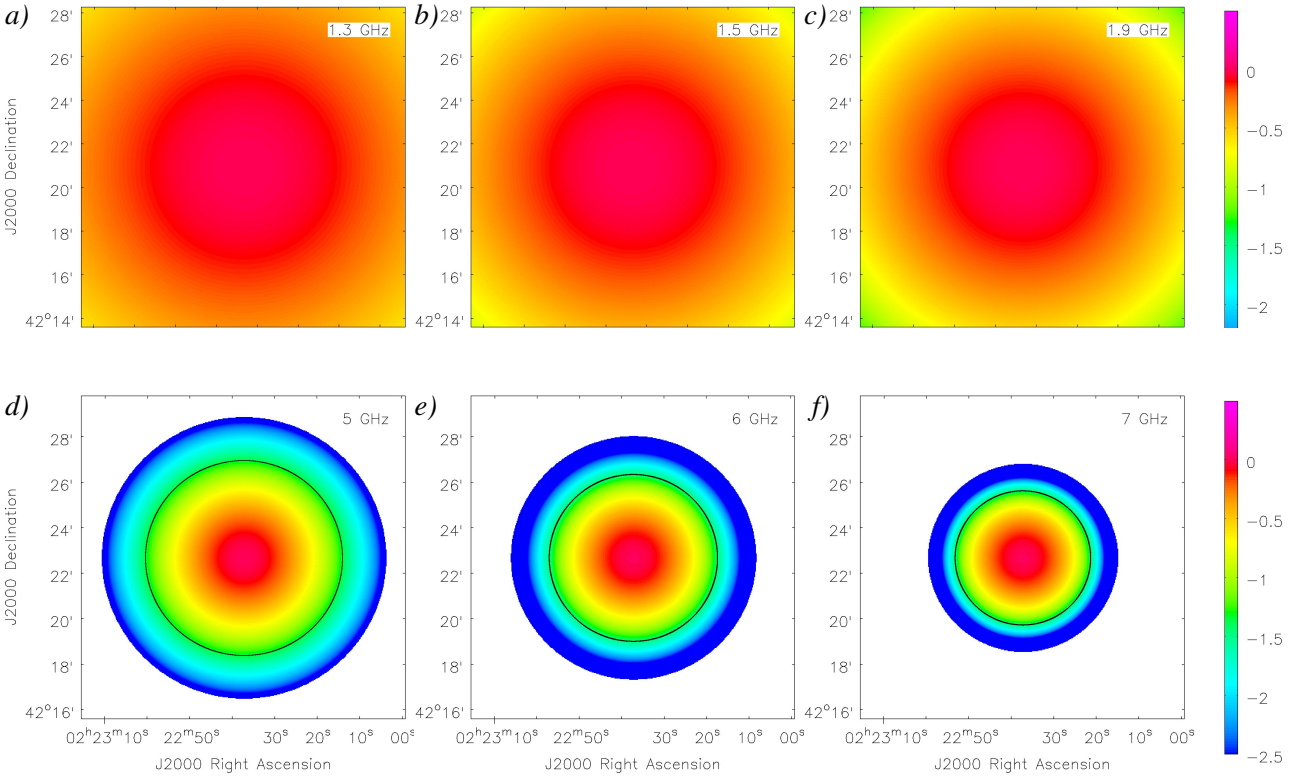

Figure 3.4: Spectral index of the (model) primary beam of the JVLA at the egde and centre frequencies of L-band (panels *a)* - *c)*) and C-band (panels *d)* - *f)*). All maps show an equally sized region on the sky, which is slightly larger than the major-axis angular size of NGC 891 or NGC 4565. The black contours in the C-band maps are placed at the half-power level of the respective primary-beam patterns, while for L-band the half-power level is located outside the displayed region. All maps are clipped at the 20% primary-beam level (again not visible in the L-band panels).

For our C-band D-array observations, the used primary beam model turned out to be very inaccurate for the reasons mentioned earlier, evidenced by significant differences between the two pointings in the total power and spectral index distribution. Therefore, we shifted the reference frequency ν_0 in `widebandpbcor` from 6.0 GHz to 6.25 GHz for both pointings, which yielded the best achievable agreement between them. In case of NGC 891, an additional separate run of `widebandpbcor` with $\nu_0 = 6.6$ GHz was necessary to optimize the spectral index agreement. Details of this procedure will be discussed in Sect. 5.1.1.

3.4.6 Mosaicking of two-pointing observations

Both NGC 891 and NGC 4565 were observed with two pointings in C-band, and while it would be preferable to merge the data in the *uv*-plane before imaging, this cannot be realized in CASA at the time of writing. Although there is a mosaic option in the `clean` task, it is not yet applicable for MFS with two or more Taylor terms. Therefore, a manual post-deconvolution combination of the pointings was necessary. This method, which is described in the following, was developed by NRAO staff members and myself during my RSRO stay at NRAO in Socorro.

After imaging both data sets separately, the `widebandpbcor` task was run for each pointing. In the next step, the reference-frequency primary beam as well as the non-primary-beam-corrected intensity maps were regridded to have the same map centre for both pointings. Two-pointing mosaics were then formed for the not yet primary beam corrected intensity map and the primary beam itself. While in regions where there is no overlap between the primary beams of the two pointings, the pixel values in the combined image remain the same as in the respective pointing, in the overlap region it is reasonable to weight the pixel values by their distance from the respective pointing centre, in order to minimize effects of low signal-to-noise and of possible errors in the used primary beam model. If, for instance, an intensity value at a certain position has been measured near the centre of pointing 1, it has a rather high signal-to-noise and requires only a slight correction for the primary beam of pointing 1, while at the same position a value has been measured further away from the centre of pointing 2, where the S/N is low and a larger correction for the primary beam of pointing 2 is needed. To take account of this weighting, the measured intensities I_{P1} and I_{P2} in the two pointings translate as follows to the mosaic image $\bar{I}_{\mathrm{mos}}$ in the overlap region:

$$\bar{I}_{\mathrm{mos}} = \frac{\left(\frac{B_{\mathrm{P1}}}{B_{\mathrm{P2}}}\right) I_{\mathrm{P1}} + \left(\frac{B_{\mathrm{P2}}}{B_{\mathrm{P1}}}\right) I_{\mathrm{P2}}}{\left(\frac{B_{\mathrm{P1}}}{B_{\mathrm{P2}}}\right) + \left(\frac{B_{\mathrm{P2}}}{B_{\mathrm{P1}}}\right)}\,, \tag{3.16}$$

where B_{P1} and B_{P2} are the two pointings of the primary beam. Likewise, the overlap region of the combined primary beam is formed via

$$\bar{B}_{\mathrm{mos}} = \frac{\left(\frac{B_{\mathrm{P1}}}{B_{\mathrm{P2}}}\right) B_{\mathrm{P1}} + \left(\frac{B_{\mathrm{P2}}}{B_{\mathrm{P1}}}\right) B_{\mathrm{P2}}}{\left(\frac{B_{\mathrm{P1}}}{B_{\mathrm{P2}}}\right) + \left(\frac{B_{\mathrm{P2}}}{B_{\mathrm{P1}}}\right)}\,, \tag{3.17}$$

and the primary beam correction of the combined intensity map can be carried out:

$$I_{\mathrm{mos}}^{\mathrm{PBcor}} = \begin{cases} \frac{I_{\mathrm{P1}}}{B_{\mathrm{P1}}} \text{ or } \frac{I_{\mathrm{P2}}}{B_{\mathrm{P2}}} & \text{no overlap} \\ \frac{\bar{I}_{\mathrm{mos}}}{\bar{B}_{\mathrm{mos}}} & \text{overlap} \end{cases} \tag{3.18}$$

Since the primary beam correction of the spectral index map is a subtraction rather than a division, the mosaicking of the spectral index is performed using the corrected single-pointing maps $\alpha_{\mathrm{P1}}^{\mathrm{PBcor}}$ and $\alpha_{\mathrm{P2}}^{\mathrm{PBcor}}$ that are output by `widebandpbcor`:

$$\alpha_{\mathrm{mos}}^{\mathrm{PBcor}} = \begin{cases} \alpha_{\mathrm{P1}}^{\mathrm{PBcor}} \text{ or } \alpha_{\mathrm{P2}}^{\mathrm{PBcor}} & \text{no overlap} \\ \bar{\alpha}_{\mathrm{mos}}^{\mathrm{PBcor}} & \text{overlap} \end{cases}\,, \tag{3.19}$$

where

$$\bar{\alpha}^{\mathrm{PBcor}}_{\mathrm{mos}} = \frac{\left(\frac{B_{\mathrm{P1}}}{B_{\mathrm{P2}}}\right)\alpha^{\mathrm{PBcor}}_{\mathrm{P1}} + \left(\frac{B_{\mathrm{P2}}}{B_{\mathrm{P1}}}\right)\alpha^{\mathrm{PBcor}}_{\mathrm{P2}}}{\left(\frac{B_{\mathrm{P1}}}{B_{\mathrm{P2}}}\right) + \left(\frac{B_{\mathrm{P2}}}{B_{\mathrm{P1}}}\right)} \tag{3.20}$$

is the primary-beam weighted spectral index in the overlap region. Before mosaicking the single-pointing α maps, an additional cutoff at 50% primary beam gain was applied to them, as α maps are usually strongly affected by incaccuracies of the used primary beam model, which increase with distance from the pointing centre (see Sect. 5.1.1 for more details on this). In the same way as the α maps, the two pointings of the spectral index error $\Delta\alpha$ were combined.

In Fig. 3.5, the difference between taking the strict average and the beam-weighted average of the two pointings in the overlap region of the primary beams is evident: in the weighted version of the combined beam, the two peak positions coincide with the pointing centres, and the transition between overlap and non-overlap regions is a lot smoother. Note that for the primary beam corrected intensity map there will be almost no difference between the strict average and the weighted average, due to the division of the combined intensity map by the combined primary beam. For the spectral index, however, the difference is significant, since the average is computed from the already primary beam corrected single-pointing images.

3.4.7 Polarization imaging

Although RM synthesis (Sect. 7.2) is currently the preferred method of imaging wide-band polarization data, Stokes Q, U, and V [3] were first imaged using MS-MFS clean with the same settings as for Stokes I. Although not explicitly indicated, all intensity quantities appearing in this section again refer to the centre frequency ν_0. Linearly polarized intensity (PI) images were formed via (Wardle & Kronberg 1974)

$$PI = \sqrt{Q^2 + U^2 - \sigma^2_{QU}}\,, \tag{3.21}$$

since the polarized intensity is always positive (following a Rice distribution, see e.g. Simmons & Stewart 1985) and $PI = \sqrt{Q^2 + U^2}$ therefore biased by the noise σ_{QU} in the Q and U maps. Also polarization position angle images were computed:

$$\chi = \frac{1}{2}\arctan\left(\frac{U}{Q}\right) \tag{3.22}$$

Two different χ maps were formed in each case, setting the threshold above which to calculate the polarization angle to $3\sigma_{QU}$ and $5\sigma_{QU}$, respectively. A threshold of 3 times the noise σ_I in total intensity was applied when computing fractional polarization maps:

$$p = \sqrt{\frac{Q^2 + U^2 - \sigma^2_{QU}}{I^2}} \tag{3.23}$$

[3] Since we are primarily interested in linearly polarized emission, Stokes V maps were produced only for a few data sets, to spot-check for any residual instrumental polarization.

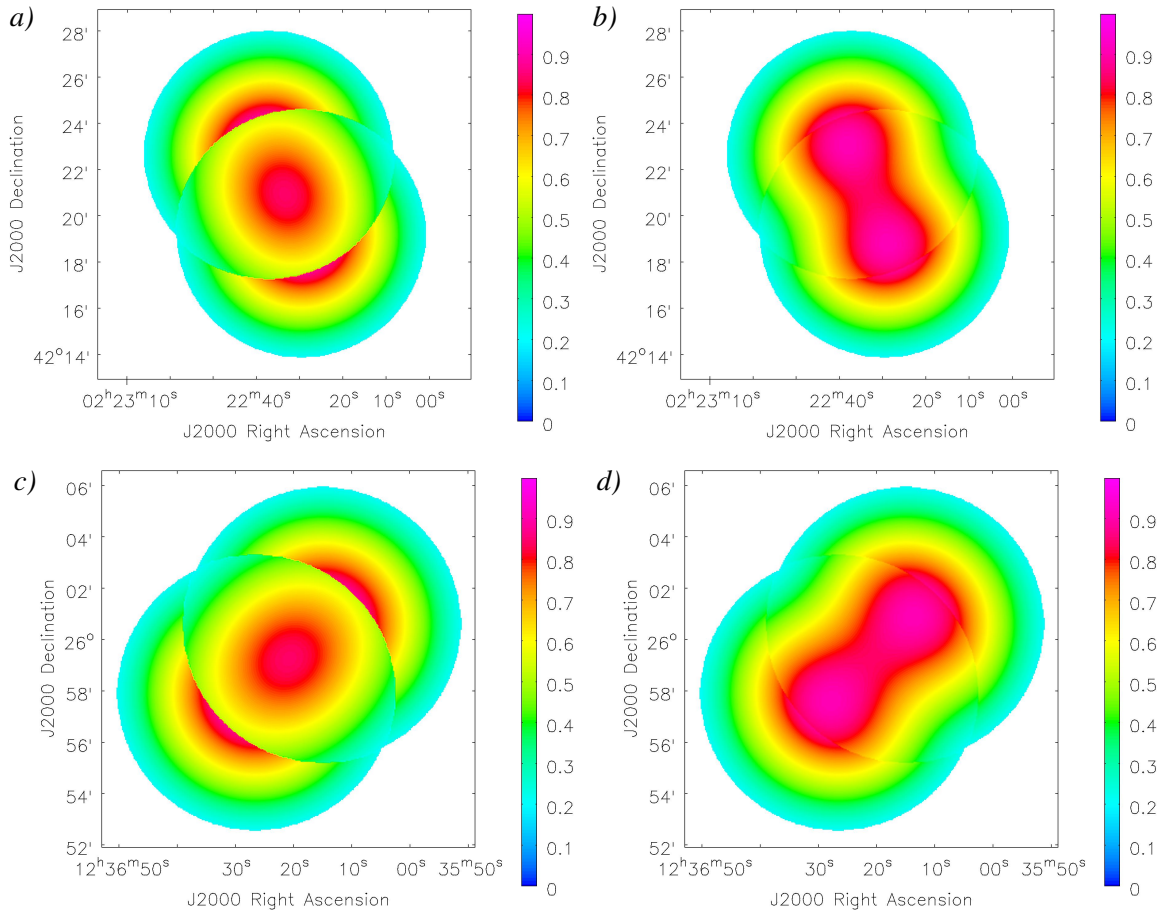

Figure 3.5: Mosaic of the 6 GHz primary-beam model at the two pointing positions for each galaxy, formed in two different ways of averaging the two pointings in the overlap region. *a)* NGC 891, strict average, *b)* NGC 891, weighted average, *c)* NGC 4565, strict average, *d)* NGC 4565, weighted average. All maps are clipped at the 20% primary-beam level.

All *PI*, p, and χ maps were formed from the non-primary-beam-corrected images of the relevant Stokes parameters (which in case of C-band were mosaicked beforehand, following the method described in Sect. 3.4.6), since for p and χ only the ratio of intensity values matters, and for the thresholding and debiasing a uniform noise background is preferable. Finally, the primary beam correction of the *PI* images was done using the same primary beam maps (again mosaicked in C-band) as were used for the total power images.

3.4.8 Short-spacing corrections

Since interferometric observations have a central gap in the *uv*-coverage, there is an upper limit to the detectable angular size scale depending on the shortest baseline(s) of the respective configuration and the observing frequency (see Table 1.2), and the synthesized beam features a central depression, such that the detected emission is superimposed on a bowl of negative flux

density. For edge-on galaxies, this effect is most apparent perpendicular to their major axis, which is particularly disadvatageous for studying the properties of galactic halos. Therefore, especially the correct determination of spectral indices and vertical scale heights require that short-spacing corrections are applied beforehand by merging the interferometric data with single-dish data. To fill in the short spacings for our 6 GHz data, we use observations done with the Effelsberg 100 m telescope at 4.85 GHz and 8.35 GHz (shown in panel panel *a)* and *b)* of Fig. 3.6 and 3.7, respectively). With the exception of the new 4.85 GHz observation of NGC 891, these data were obtained between 1997 and 2008, and were reduced by M. Dumke (1997), F. Tabatabaei, and M. Krause. From the Effelsberg total intensity maps, a map of the spectral index between these two frequencies was computed (following Eq. 4.3) for each galaxy, as shown in panel *c)* of Fig. 3.6-3.7. While in case of NGC 891 we used the spectral index map to do a pixel-by-pixel scaling of the 4.85 GHz map to the expected intensity at 6 GHz, the spectral index map of NGC 4565 turned out to be usable only for the north-western side of the galaxy, as the southward deformation of the south-eastern side in the 8.35 GHz map, which is possibly caused by residual scanning artifacts, likewise dominates the derived spectral index distribution. Since in additon, both sides of the galaxy are affected by edge artifacts (i.e. regions of unnatural flattening of the spectral index in z direction), and the southward bending already has a severe effect on the central region, a pixel-by-pixel approach, even with mirroring of the north-west to the south-east side, seems hardly reasonable in this case. Instead, to scale the inner part of the 4.85 GHz map to 6 GHz intensities, we use a spectral index of -0.81, which corresponds to the lower error limit of the integrated value determined by Dumke et al. (1995), while for the outer part we assume a spectral index of -1.0, which is roughly the average over the area in the north-western half where the halo spectral index seems plausible. We distinguish between the two domains using the 6 GHz intensity contour at 10.5 mJy/beam, which has a width corresponding to the beam FWHM of 147″ at zero galactocentric radius.

Unfortunately, for neither NGC 891 nor NGC 4565, single-dish observations at (or near) 1.5 GHz with sufficient sensitivity are presently available. On the other hand, we expect that the D-array data are not too severely affected by missing short spacings, as long as large enough clean components are considered for multi-scale imaging. However, at higher resolutions (even when cleaning B- and/or C-array in combination with D-array), we found it to be impossible to achieve the same total flux density as in the D-array maps, even if large deconvolution scales are used. As described below, at 1.5 GHz we used the D-array maps to at least partly correct for missing short-spacings in the combined B+C+D-array maps. Still, we keep in mind that the missing spacing problem is possibly still present to some degree in our 1.5 GHz observations, and will discuss its possible effects on our science results where appropriate.

We performed the short-spacing corrections using the `ImMerge` task in NOD3, which is a new software package currently being developed by P. Müller at the MPIfR. This programme convolves the interferometric image with the beam of the single-dish observation and subtracts this convolved map from the single-dish map. The resulting difference map, which is practically a map of the large-scale emission missing from the interferometric observation, is normalized to the interferometric resolution through multiplication by the volume ratio of the two observing beams $\theta^2_{\mathrm{interf.}}/\theta^2_{\mathrm{SD}}$. This map is then added to the interferometric map to yield the short-spacing corrected image.

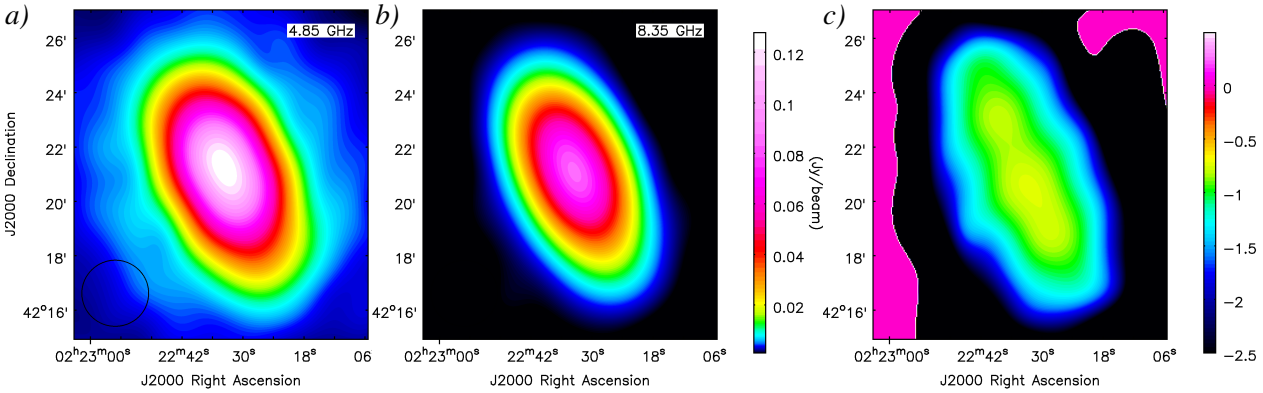

Figure 3.6: Total intensity distribution of NGC 891, observed with the Effelsberg 100 m telescope at 4.85 GHz (panel *a)*) and 8.35 GHz (panel *b)*). The 8.35 GHz map has been smoothed to the resolution of the telescope at 4.85 GHz, which is 147″. Panel *c)* shows the corresponding spectral index distribution between 4.85 and 8.35 GHz.

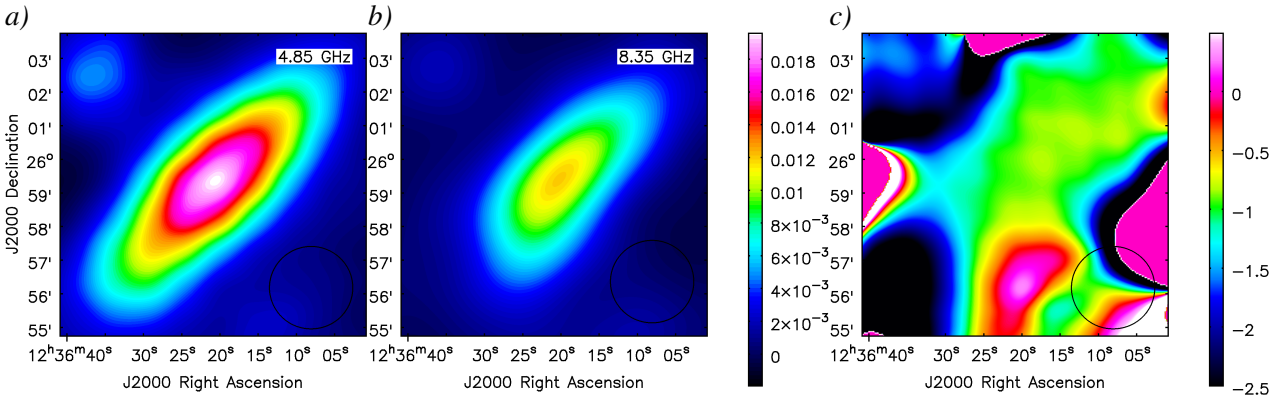

Figure 3.7: Total intensity distribution of NGC 4565, observed with the Effelsberg 100 m telescope at 4.85 GHz (panel *a)*) and 8.35 GHz (panel *b)*). The 8.35 GHz map has been smoothed to the resolution of the telescope at 4.85 GHz, which is 147″. Panel *c)* shows the corresponding spectral index distribution between 4.85 and 8.35 GHz.

Apart from this new, albeit simple approach, we also applied a more traditional method, called feathering, for comparison. Corresponding tasks are available in CASA as well as in AIPS (Astronomical Image Processing System)[4]. In case of the AIPS task `IMERG`, feathering is accomplished by first Fourier-transforming both the single-dish and the interferometer image to the *uv* domain, and normalizing the amplitudes of the single-dish data based on the interferometric amplitudes within a specific annulus in the *uv*-plane that corresponds to the range of angular scales to which both observations are considered to be similarly sensitive. Next, a weighted sum of the two data sets is formed, such that inside the annulus the single-dish and interferometric data have weights of 1 and 0, respectively, and vice versa outside the annulus, while for the annulus itself, a complementary weighting by a Gaussian-like function is applied, to enable a

[4] `http://www.aips.nrao.edu/index.shtml`

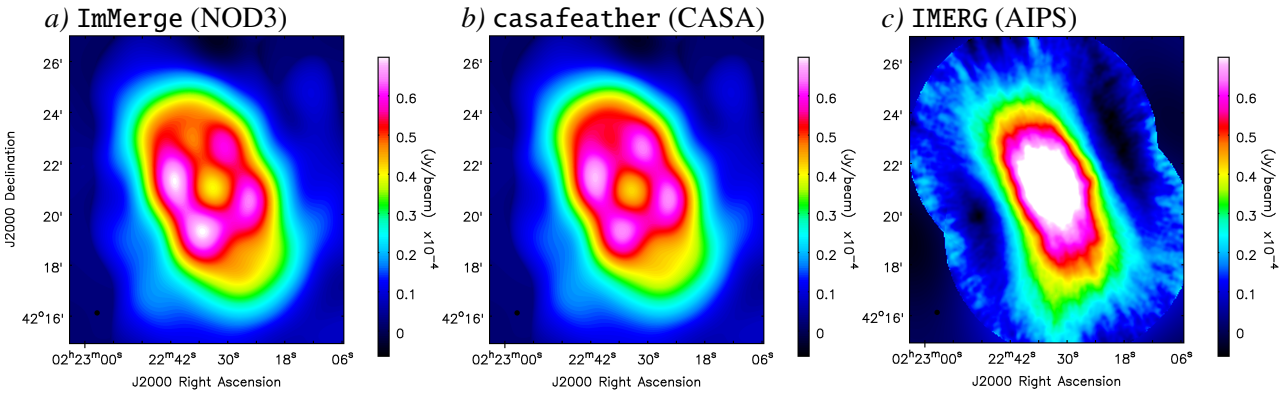

Figure 3.8: Difference maps between the 6 GHz JVLA D-array total intensity maps of NGC 891 after and before short-spacing correction, for three different merging routines.

smooth overlap within this region. Finally, the merged data set obtained in this way is inversely transformed back to the image domain. The correct scale factor for the normalization of the single-dish data is equal to $\theta^2_{\text{interf.}}/\theta^2_{\text{SD}}$, provided that both data sets are calibrated correctly. The scale factor can be given as input parameter, otherwise the user-specified *uv* overlap determines the factor in such a way as to optimize the agreement of single-dish and interferometric data within the overlap, and hence to achieve the smoothest possible transition between the two. A reverse approach is not possible, however, i.e. the program is unable to determine an optimal *uv* overlap for a given scale factor; therefore it is not recommended to set the factor manually. At 6 GHz, we found the closest possible agreement of the scale factor with $\theta^2_{\text{interf.}}/\theta^2_{\text{SD}}$ using a *uv* overlap range between 0.46 and 0.56 kλ in case of NGC 891, and between 0.37 and 0.44 kλ in case of NGC 4565.

Compared to `IMERG` in AIPS, the CASA task `feather` (or `casafeather`) does not allow to easily determine an ideal set of input parameters. Here, the *uv* overlap range cannot be given explicitly, but instead the down-weighting of the short-spacings in the interferometric image (and complementary weighting of the single-dish data) is accomplished by multiplying its Fourier transform with $1 - FTSDB(u, v)$, where $FTSDB(u, v)$ is the Fourier transform of the single-dish beam. This implies that the lower bound of the overlap range is always fixed at the centre of the *uv*-plane, while the upper bound is determined by specifying an effective dish diameter, which can be less or equal to the actual dish size, and hence there is an upper limit to the possible extent of the *uv* overlap region. Most importantly, the task does not provide any information on the ideal single-dish scale factor for a given effective dish diameter, but the scale factor always needs to be specified independently.

We compare the results of the three different methods using the combination of the 6 GHz D-array and Effelsberg map for NGC 891. For this purpose, we subtracted the pure JVLA map from each of the three short-spacing corrected maps. The resulting difference maps represent the distribution of the added large-scale emission and are displayed in Fig. 3.8. We see that in case of CASA and NOD3 the shape of the added emission is very similar and closely resembles the Effelsberg map, but with a depression along the galactic plane, where only a small amount of short-spacing correction is necessary. In contrast, the emission added by the AIPS routine

is more concentrated to the mid-plane by comparison, and contains structures on scales much smaller than the Effelsberg beam. We conclude from this that `IMERG` in AIPS is the least reliable of our three tested merging routines. Fig. 3.8 *c)* shows that the added emission is particularly lacking in those parts of the halo lying above and below the galaxy centre, which introduces an artificial dumbbell shape at low intensity levels in the merged image. Moreover, by trying out different sets of input parameters, we found that the AIPS task consistently produces images containing slightly more (usually between 3% and 5%) total flux density than the corresponding Effelsberg map.
Based on the above shortcomings of the AIPS task and on the lack of transparency of the CASA routine, we decide to use the `ImMerge` task in NOD3 for all necessary short-spacing corrections. Another argument in favour of this method is that no spatial frequency overlap is needed, which would pose a problem at 1.5 GHz, where we merge the JVLA D-array image with the combined-array image, in which the D-array data are already included.

At 6 GHz, we applied short-spacing corrections to the D-array and C+D-array total intensity image for each galaxy, as well as to the D-array Stokes Q and U images, using the Q and U channels of the same 4.85 GHz Effelsberg observations. For scaling these maps to 6 GHz, the non-thermal spectral index distribution needs to be known, since thermal radiation is unpolarized. To this end, we generated thermal radio maps at 4.85 and 8.35 GHz (following the method we will describe in Sect. 4.2) and smoothed these to the Effelsberg beam size. By subtracting the smoothed thermal maps from the Effelsberg Stokes I images, we formed non-thermal intensity maps and subsequently the non-thermal spectral index map between 4.85 and 8.35 GHz. After scaling of the 4.85 GHz Q and U maps to 6 GHz using the non-thermal spectral index map, we merged them with the JVLA Q and U maps. Finally, from the short-spacing corrected Q and U images, polarized intensity and polarization angle maps were computed for each galaxy, according to Eq. 3.21 and 3.22.

4 Morphology of the total and non-thermal radio emission

In the following part of this work, we present the final data products in total intensity (Stokes *I*) at 1.5 and 6 GHz, obtained after carrying out the basic data reduction and post-imaging steps described in the previous chapter. In addition to our short-spacing corrected data at both observing frequencies, we also show the non-corrected images obtained in each array configuration[1]. While addressing morphological poperties of NGC 891 and NGC 4565 based on our own observations, we also draw comparisons to previously published radio continuum data of the two galaxies as well as to ancillary observations at non-radio frequencies.

To be able to interpret radio continuum data correctly, a realistic estimate of the contribution of thermal bremsstrahlung to the observed emission has to be found. Since the non-thermal component can almost entirely be identified with synchrotron radiation of CREs, information on its distribution in the galaxies is important to facilitate reliable measurements of quantities such as synchrotron spectral indices, synchrotron scale heights, and magnetic field strengths. In the second part of this chapter, we first provide a short overiew of various techniques to separate the thermal from the non-thermal radio emission, and point out the particular difficulties in achieving an accurate solution for edge-on galaxies. Subsequently, we give a step-by-step description of the separation precedure we carried out for the two galaxies, where we ultimately had to rely on previously determined thermal fractions as a guideline. We computed maps of the predicted thermal and non-thermal radio emission at an angular resolution of 12″, which corresponds to ≈ 0.5 kpc in case of NGC 891 and ≈ 0.7 kpc in case of NGC 4565.

4.1 Total radio continuum emission

4.1.1 NGC 891

Figure 4.1 shows the observed total intensity distribution of NGC 891 at 1.5 and 6 GHz separately for all used array configurations, while short-spacing corrected maps are displayed in Fig. 4.2. In the 6 GHz images, the rms noise values agree quite well with the theoretically expected ones (including confusion limits, see Table 4.1), whereas at 1.5 GHz the noise is considerably higher,

[1] For the purpose of performing a major part of our analysis throughout this thesis at a uniform angular resolution for both galaxies, the C-band D-array, L-band C-array, and L-band combined-array images were smoothed to a circular beam of 12″ prior to the primary-beam and short-spacing corrections.

Table 4.1: Measured noise in the JVLA images and theoretical noise in each considered frequency band and array configuration. All values are given in μJy/beam.

Frequency band	Configuration	σ(NGC 891)	σ(NGC 4565)	Total theor. noise rms[a]
L (1.5 GHz)	B	16	14	7.7
	C	28	21	17
	D	60	34	52
	B+C+D	24	20.5	8.6
C (6 GHz)	C	3.1	3.2	2.4
	D	5.9	7.0	5.0
	C+D	2.7	2.5	2.2

[a] Total expected noise levels, computed from the thermal noise $\sigma_{\rm th}$ and the confusion noise $\sigma_{\rm c}$ (see Table 3.1) as $\sqrt{\sigma_{\rm th}^2 + \sigma_{\rm c}^2}$

Table 4.2: Integrated flux densities for all considered Stokes *I* images. All values are given in mJy.

	NGC 891	NGC 4565	Figure
L-band B-array	322±16	31.8±1.6	4.1 *c)* / 4.4 *c)*
L-band C-array	560±28	73.7±3.7	4.1 *b)* / 4.4 *b)*
L-band B+C+D-array	695±35	135±7	–
L-band B+C+D-array merged with D-array	737±37	139±7[b]	4.2 *a)* / 4.5 *a)*
L-band D-array	737±37	146±7[b]	4.1 *a)* / 4.4 *a)*
1.4 GHz WSRT	785±39	–	–
Thermal (1.5 GHz)	52.7±23.1	14.7±6.8	4.7 *a)* / 4.8 *a)*
Non-thermal (1.5 GHz)[a]	684±44	124±10	4.7 *c)* / 4.8 *c)*
C-band C-array	125±6	14.9±0.7	4.1 *e)* / 4.4 *e)*
C-band C+D-array	157±8	22.2±1.1	–
C-band D-array	207±10	36.6±1.8	4.1 *d)* / 4.4 *d)*
C-band D-array merged with 6 GHz Effelsberg	252±27	39.8±5.9	4.2 *b)* / 4.5 *b)*
C-band C+D-array merged with 6 GHz Effelsberg	252±27	39.5±5.9	4.2 *d)* / 4.5 *c)*+*d)*
6 GHz Effelsberg	255±14	48.2±3.9	3.6 / 3.7
Thermal (6 GHz)	46.1±20.2	13.2±6.3	4.7 *b)* / 4.8 *b)*
Non-thermal (6 GHz)[a]	206±34	26.9±8.6	4.7 *d)* / 4.8 *d)*

[a] For each galaxy, to obtain the non-thermal map at 1.5 GHz, the thermal map was subtracted from the combination of the L-band D-array and B+C+D-array maps. At 6 GHz, the thermal map was subtracted from the combination of the C-band D-array and Effelsberg maps.

[b] The reason for the difference between the flux density in the L-band D-array map and that in the combination of the L-band D-array and B+C+D-array maps of NGC 4565 is that in the latter case the lowest spatial frequencies were excluded from both images before merging (see Sect 5.1.2).

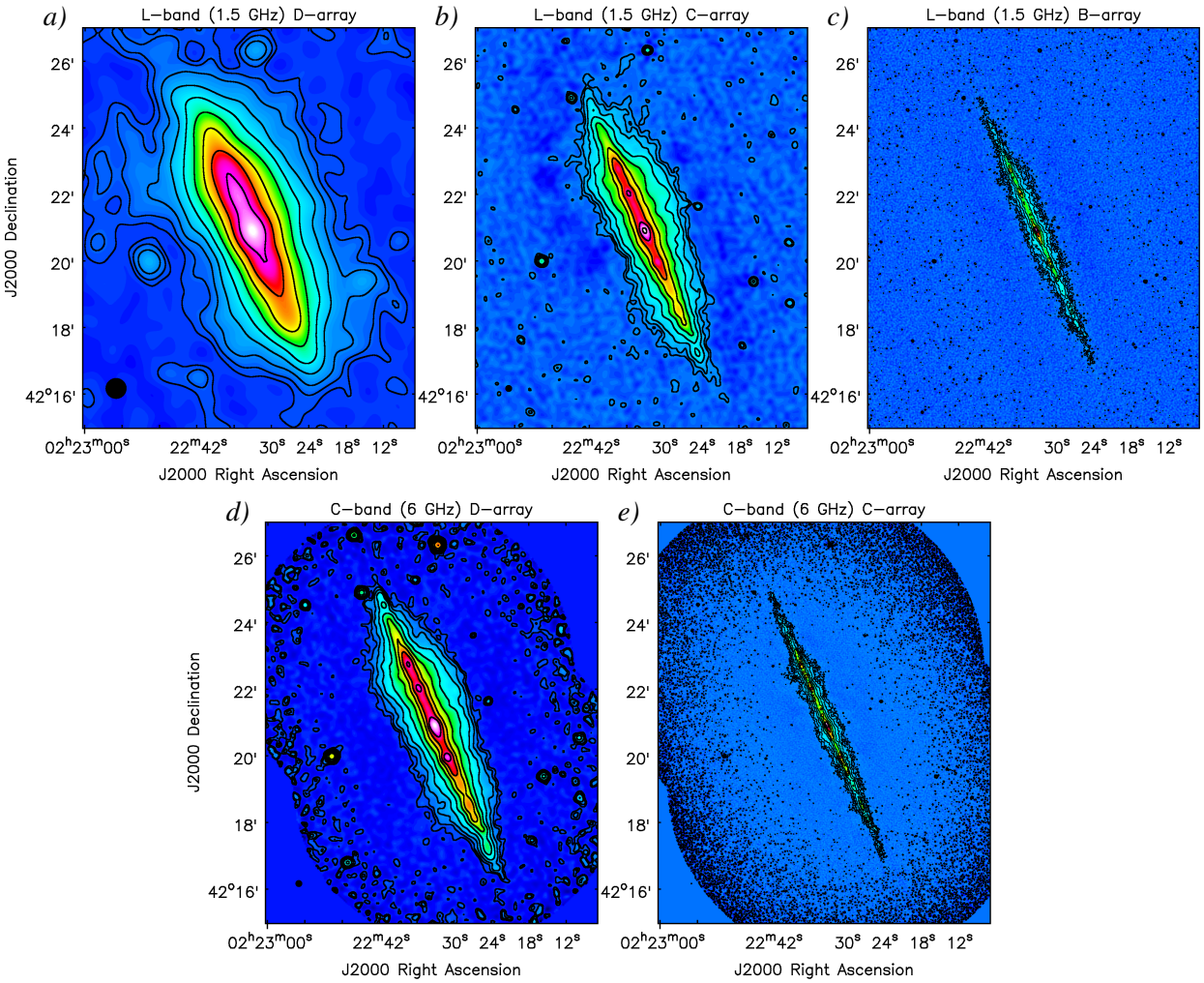

Figure 4.1: Total intensity distribution of NGC 891 at 1.5 and 6 GHz for each array configuration. *a)*: L-band D-array (beam FWHM: $36'' \times 32''$), *b)*: L-band C-array (beam FWHM: $12''$), *c)*: L-band B-array (beam FWHM: $3.2'' \times 2.9''$), *d)*: C-band D-array (beam FWHM: $12''$), *e)*: C-band C-array (beam FWHM: $2.8'' \times 2.6''$). All maps have been primary-beam corrected. Contour levels start at 3σ (see Table 4.1) and increase in powers of 2. The 3σ contours near the edges of the C-band maps are due to the radially increasing noise levels after primary-beam correction.

probably because a larger fraction of the data was flagged. For L-band D-array in particular, the noise rms of 60μJy beam^{-1} is also caused by residual sidelobe structures around 3C 66, by which almost the entire field of view is visibly contaminated. While most of the large-scale halo emission of NGC 891 is detected here, the shape of the outer intensity contours is notably affected by background sources, and also by residual cleaning artifacts of 3C 66 and NGC 891 itself. As indicated in Sect 3.4.4, our attempt at peeling to minimize the artifacts induced by 3C 66 was not successful.

With the possible exception of L-band D-array, the zero level has a negative bowl in all of the single-array images, which is a sign that a significant fraction of the large-scale emission was not detected due to missing short spacings. This is also reflected by the integrated flux density values given in Table 4.2. These were determined within elliptical regions enclosing the total emission of the galaxy, after subtracting all background sources within a sufficient radius from the galaxy centre. In L-band D-array, the integrated flux density of 737 mJy is in close agreement with the value of 740 ± 20 mJy Hummel et al. (1991b) obtained from 1.5 GHz VLA D-array observations, and higher than the VLA-based flux densities of Condon (1987) and Gioia & Fabbiano (1987), who measured 701 and 660 mJy, respectively. Even the catalogue of the Green Bank 1.4 GHz Northern Sky Survey (White & Becker 1992) lists a flux density value of only 658 mJy. As we did not find any single-dish-based flux density measurements of sufficient sensitivity in the literature, the true total flux density of the galaxy at this frequency range remains uncertain. On the other hand, from a more recent 1.4 GHz WSRT observation by Adebahr (2013) we obtain an integrated flux density of 785 ± 39 mJy, which suggests that at least a small fraction of the extended emission is still missing from our JVLA L-band D-array data. The problem of missing flux also occurs in the combined-array images, for the reasons mentioned in Sect. 3.4. Even if equally large deconvolution scales as for imaging D-array only are used (as we did for the combined-array L-band map), due to the bias towards the high-resolution data the integrated flux density is still lower than in the D-array maps.
There is a slight difference between the integrated flux density in the short-spacing corrected 6 GHz maps and that in the Effelsberg map used for this very correction. This discrepancy most likely arises from the fact that nearby background sources are not resolved from the halo emission in the Effelsberg image, and hence could not be subtracted.

As seen most clearly in the L-band C-array and C-band D-array maps (and as already mentioned by Dahlem et al. (1994), who published a similar map at 13″ resolution obtained with the VLA at 1.5 GHz), the disk and halo component of the radio continuum radiation of NGC 891 appear relatively well-separated from each other. The halo component appears to be somewhat less extended in radial direction than the disk component, which has a diameter comparable to that of the stellar disk. Except for the diffuse component visible in the L-band D-array map and in the short-spacing corrected images shown in Fig. 4.2, the vertical extent of the radio contours is clearly larger in the northern part of the galaxy at all angular resolutions. Dahlem et al. (1994) investigated this north-south asymmetry by comparing their 1.5 GHz data to the distribution of Hα, FIR, and CO emission. From the north-south asymmetry in all these components they inferred that the SFR is higher in the northern half of the galaxy. Moreover, they found a spatial correlation of the diffuse Hα emission with the radio continuum emission, which they interpreted as a convective outflow of hot gas and CRs into the halo, powered by star formation in the underlying disk. The correlation with the extraplanar Hα is confirmed very well not only by the new L-band C-array or C-band D-array data (see Fig. 4.3 *a)*), but is also evident in the high-resolution maps (Fig. 4.3 *b)*). However, especially with the clumpy structure of the disk being revealed in greater detail in the highest-resolution radio images, only a rough correlation with Hα on small scales can be observed. As Fig. 4.3 *b)* shows, the maxima in radio continuum are generally more closely aligned with the mid-plane than the maxima in Hα, which correspond to the HII regions nearest to the observer. A reason for this only partial correlation may be internal extinction, as also noted by Dahlem et al. (1994).

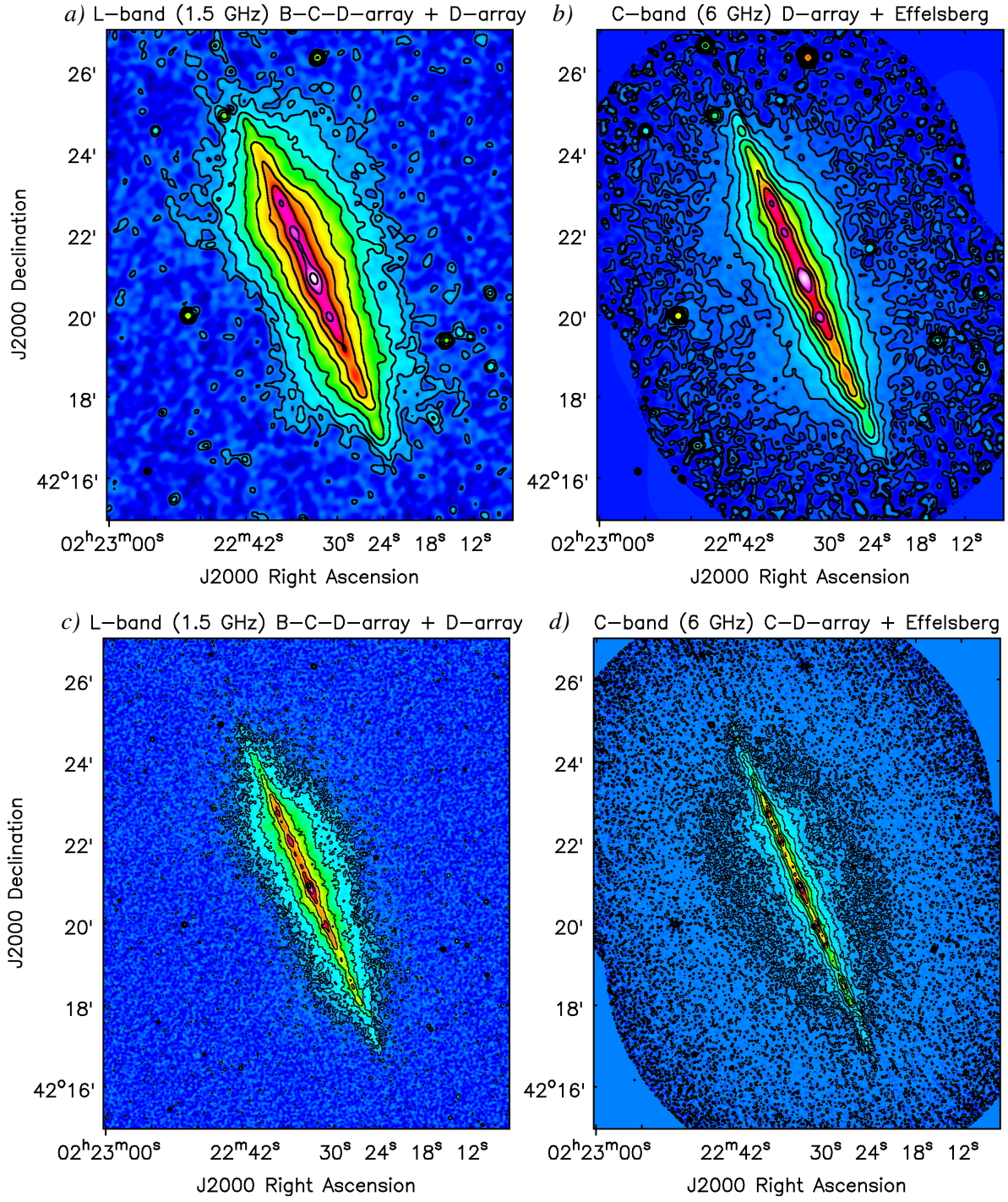

Figure 4.2: Short-spacing corrected total intensity images of NGC 891 at 1.5 and 6 GHz. The synthesized beam FWHM is 12″ in panels *a)* and *b)*, 4.1″ × 3.7″ in panel *c)*, and 3.9″ × 3.5″ in panel *d)*. All individual JVLA maps have been primary-beam corrected before short-spacing corrections were carried out. Contour levels start at 3σ (where σ is the noise rms in the respective B+C+D-array map at 1.5 GHz and in the respective JVLA map at 6 GHz, see Table 4.1) and increase in powers of 2. The 3σ contours near the edges of the C-band maps are due to the radially increasing noise levels after primary-beam correction.

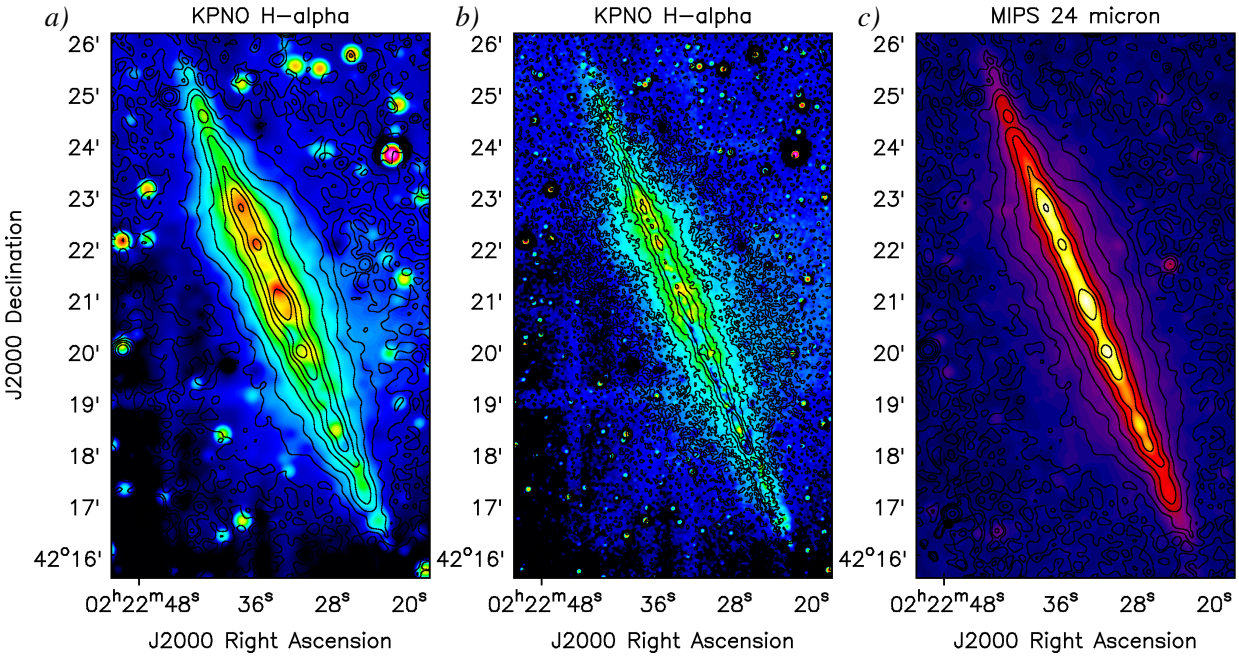

Figure 4.3: Hα and IR maps of NGC 891 in comparison to the short-spacing corrected data at 6 GHz. *a)*: KPNO Hα image, smoothed to a Gaussian beam of 12″ and overlaid with the same contours as in Fig. 4.2 b). *b)*: The same Hα image, but smoothed to a Gaussian beam of 3.5″ and overlaid with the same contours as in Fig. 4.2 d). *c)*: Spitzer MIPS 24 μm image, smoothed to a Gaussian beam of 12″ and overlaid with the same contours as in Fig. 4.2 b).

While the inner radio contours in all cases roughly follow the asymmetric distribution of the HII regions, contours become increasingly more peanut- or dumbbell-shaped towards larger z heights – however only moderately compared to extreme cases, such as NGC 253 (Heesen et al. 2009a), and with the northern part still being vertically more extended than the southern part. The dumbbell shape is somewhat less prominent on the western side, which in case of the L-band D-array image (Fig. 4.1 *a)*) is in part due to a background source located to the west above the galactic centre. Judging by the low-level contours of the short-spacing corrected maps at 12″ (Fig. 4.2 *a)* and *b)*), the halo seems to have a similar vertical extent at 1.5 and 6 GHz. However, it is not clear how much of the emission at the 3σ level in (Fig. 4.2 *b)*) is still believable, due to the primary-beam-induced increase of the noise level towards the edges of the rather narrow field-of-view. The merged VLA and Effelsberg map at 4.85 GHz formed by Dumke (1997, hereafter D97) does not show a comparable amount of diffuse emission, because the field of view chosen for the Effelsberg observation was too small to include the entire flux of the galaxy at this frequency. As a consequence of the lower S/N in the short-spacing corrected high-resolution maps (panels *c)* and *d)*), the lowest coherent contour levels therein happen to be less extended than in their 12″ counterparts. But also here, it is still unclear where exactly the added large-scale flux transitions into the increased noise near the primary-beam edges at 6 GHz. A quantitative description of the shape of the halo will be given in Sect. 6.1.

4.1.2 NGC 4565

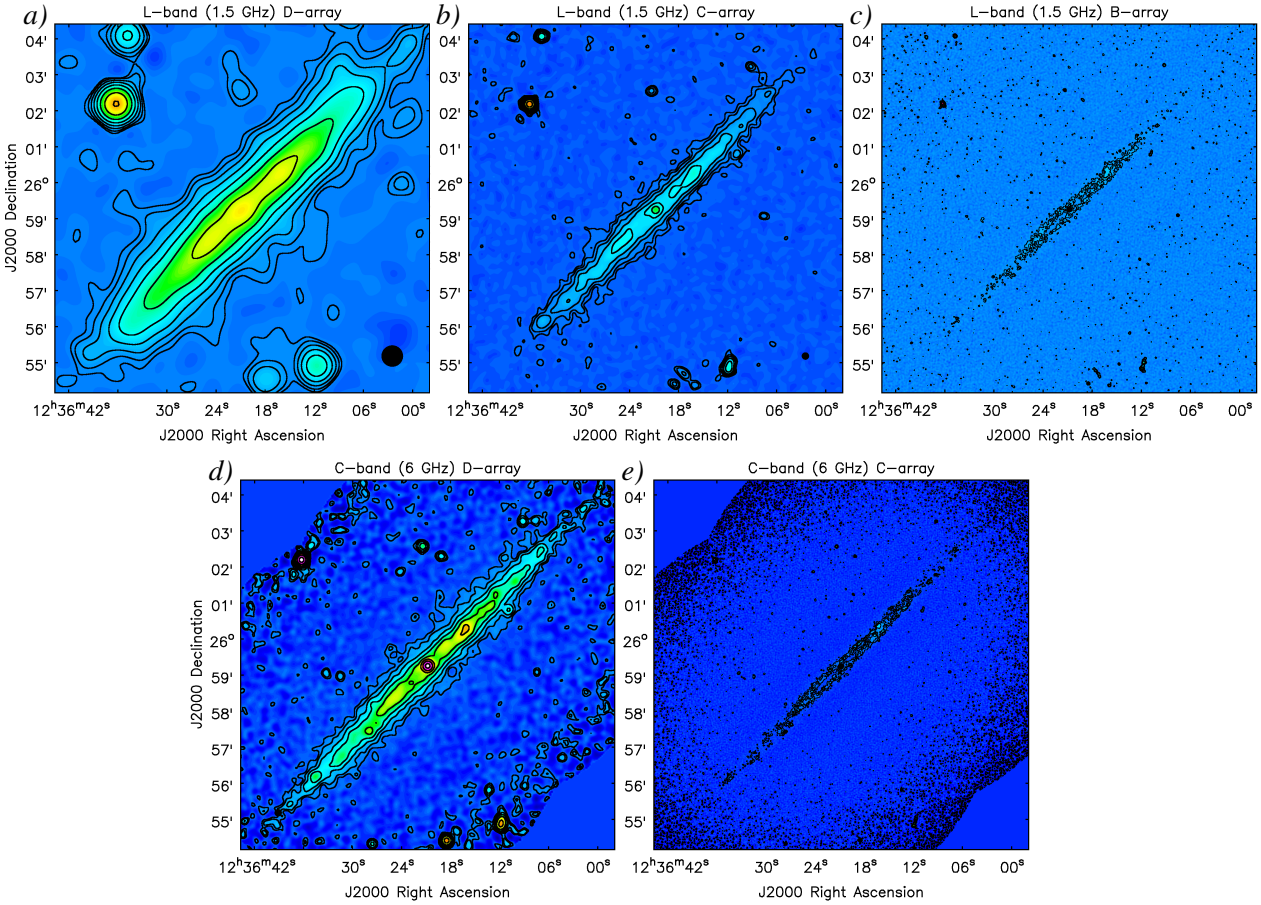

Figure 4.4: Total intensity distribution of NGC 4565 at 1.5 and 6 GHz for each array configuration. *a)*: L-band D-array (beam FWHM: 35″ × 32″), *b)*: L-band C-array (beam FWHM: 12″), *c)*: L-band B-array (beam FWHM: 3.3″ × 3.0″), *d)*: C-band D-array (beam FWHM: 12″), *e)*: C-band C-array (beam FWHM: 2.6″). All maps have been primary-beam corrected. Contour levels start at 3σ (see Table 4.1) and increase in powers of 2. The 3σ contours near the edges of the C-band maps are due to the radially increasing noise levels after primary-beam correction.

L- and C-band total power maps of NGC 4565 obtained in the individual array configurations are displayed in Fig. 4.4, and short-spacing corrected images are shown in Fig. 4.5. The noise levels are only slightly higher than the theoretical values, except for L-band B-array (and consequently also the combined-array L-band map), again presumably due to a higher relative amount of flagged data. With the possible exception of L-band D-array, the missing spacing problem is present in the single-array maps of NGC 4565 as well.

As a major difference to NGC 891, the overall radio continuum emission is significantly weaker for NGC 4565 at both frequencies in any array configuration, which is evident from the integrated

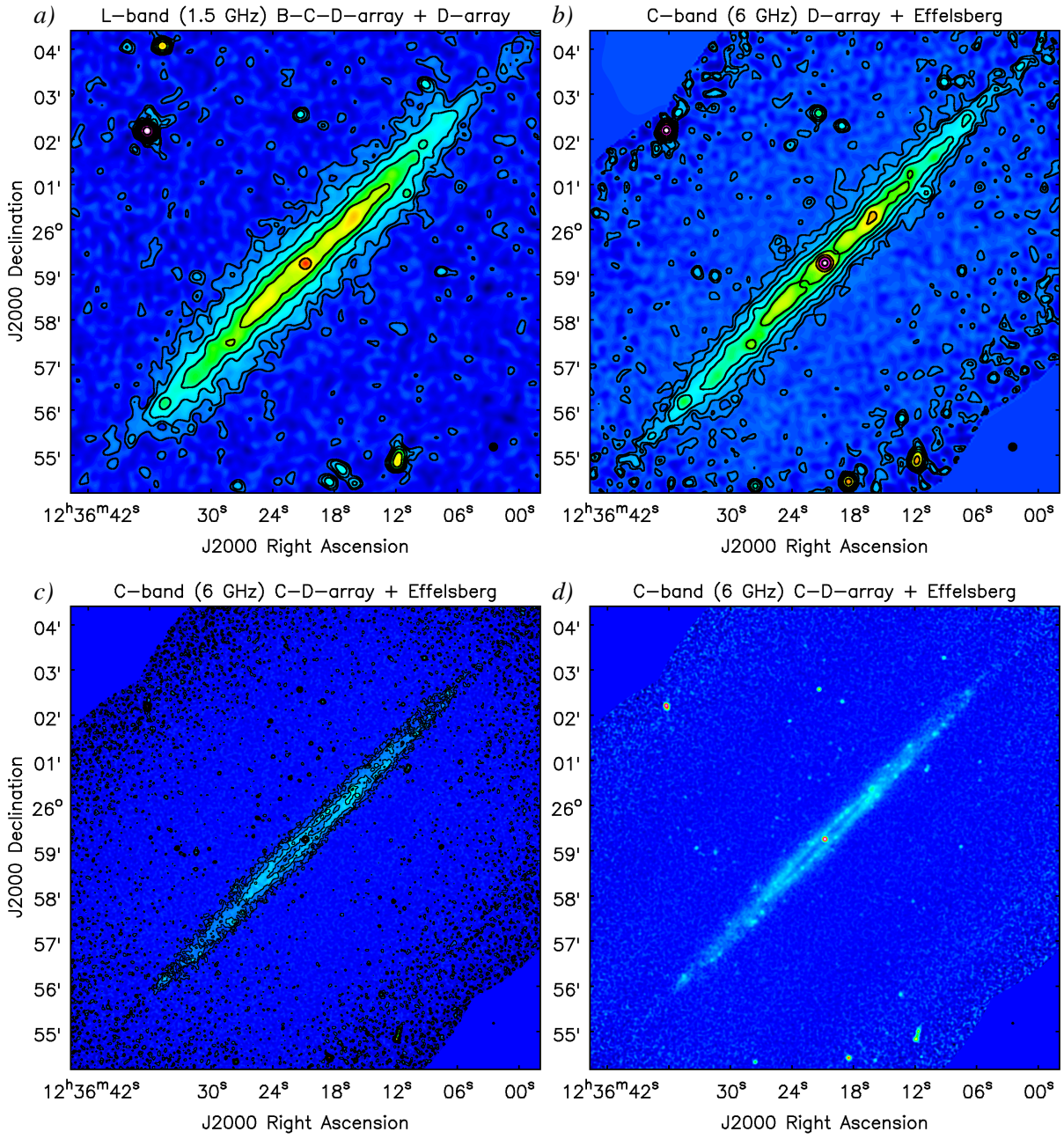

Figure 4.5: Short-spacing corrected total intensity images of NGC 4565 at 1.5 and 6 GHz. The synthesized beam FWHM is 12″ in panels *a)* and *b)*, and 3.6″ × 3.5″ in panels *c)* and *d)*. All individual JVLA maps have been primary-beam corrected before short-spacing corrections were carried out. Contour levels start at 3σ (where σ is the noise rms in the B+C+D-array map at 1.5 GHz and in the respective JVLA map at 6 GHz, see Table 4.1) and increase in powers of 2. The 3σ contours near the edges of the C-band maps are due to the radially increasing noise levels after primary-beam correction. Panel *d)* shows the same map as panel *c)*, but without contours, for better visibility of the resolved disk structure.

flux density values[2] (see Table 4.2) as well as from the general appearance of the total intensity maps. Basically, at the highest resolutions (L-band B-array, C-band C-array), no halo component is detected at all, and even in L-band D-array, the ratio of vertical to radial extent of the radio emission is clearly less than for NGC 891. Moreover, after short-spacing correction at 6 GHz (Fig. 4.5 *b)-d)*), practically all of the added large-scale emission still falls below the 3σ level. Like for NGC 891, the short-spacing corrected JVLA maps at 6 GHz contain somewhat less flux than the Effelsberg map, since it was not possible to remove all background sources (as well as the nucleus of the galaxy) from the Effelsberg map.
The combination of an earlier VLA observation with the Effelsberg map at 4.85 GHz (D97, Krause 2009), which had been obtained using the `AIPS` task `IMERG`, shows dumbbell-like vertical extensions of the otherwise narrow halo component, most prominently on the south-east side of the galaxy. No such feature is visible in any of the images presented here. On the one hand, errors in our own merging procedure at 6 GHz cannot be entirely ruled out. However, as described in Sect. 3.4.8, after testing the different merging routines on both NGC 891 and NGC 4565, we found that `IMERG` is more likely to produce filamentary, often dumbbell-shaped, extraplanar features than the corresponding routines in `CASA` and `NOD3`. Therefore, it can neither be ruled out that the extensions in the image of D97 are merely artifacts of the merging process. Anyhow, the shape of the 3σ and 6σ contours in our L-band D-array map (Fig. 4.4 *a)*) might be a hint that the halo takes on a dumbbell shape below our sensitivity limits. Also, as it is not guaranteed that we actually measure the total flux density of the galaxy at 1.5 GHz (though at least our result seems to be consistent with the 1.41 GHz flux density of 150 ± 10 mJy obtained with the WSRT by Hummel et al. 1984), the combination with single-dish data at this frequency might be able to comfirm such a behaviour.
The warp of NGC 4565 that has been observed in HI and in the optical is also present in radio continuum, as shown by the slight bending of both the disk and the extraplanar emission starting at a radius of $\approx 75''$, corresponding to ≈ 4 kpc. This is particularly visible in Fig. 4.4 *a)* and 4.5 *a)*. A strong warping like at the north-western end of the HI disk (Zschaechner et al. 2012) is not observed, however, since in radio continuum the galaxy is less extended in radial direction.

4.1.2.1 Spiral arm structure

Our observations in the most extended array configurations, C-array at 6 GHz in particular (Fig. 4.5 *c)*and *d)*), are the first to resolve the inner ring of NGC 4565 at radio frequencies. The ring is seen at a radius of roughly $100''$, which corresponds to 5.7 kpc. A counterpart to this radio ring is hardly visible in the optical image (Fig. 1.2), where the rear side (i.e. south-west of the centre) of the inner disk is largely outshined by the "bulge" (which is actually a bar and a pseudobulge). On the other hand, the almost identical appearance of the galaxy at IR wavelengths (e.g. Kormendy & Barentine 2010; Laine et al. 2010) suggests a tight small-scale radio-FIR correlation for the major part of the disk. The observed axis ratio of the ring in radio continuum implies an inclination of $i = 86.3° \pm 0.4°$ for this galaxy.
The fainter outer parts of the disk evident in the high-resolution radio maps can be associated

[2] In case of NGC 4565, in addition to background sources, also the central source of the galaxy was subtracted from each JVLA image before measuring integrated flux densities.

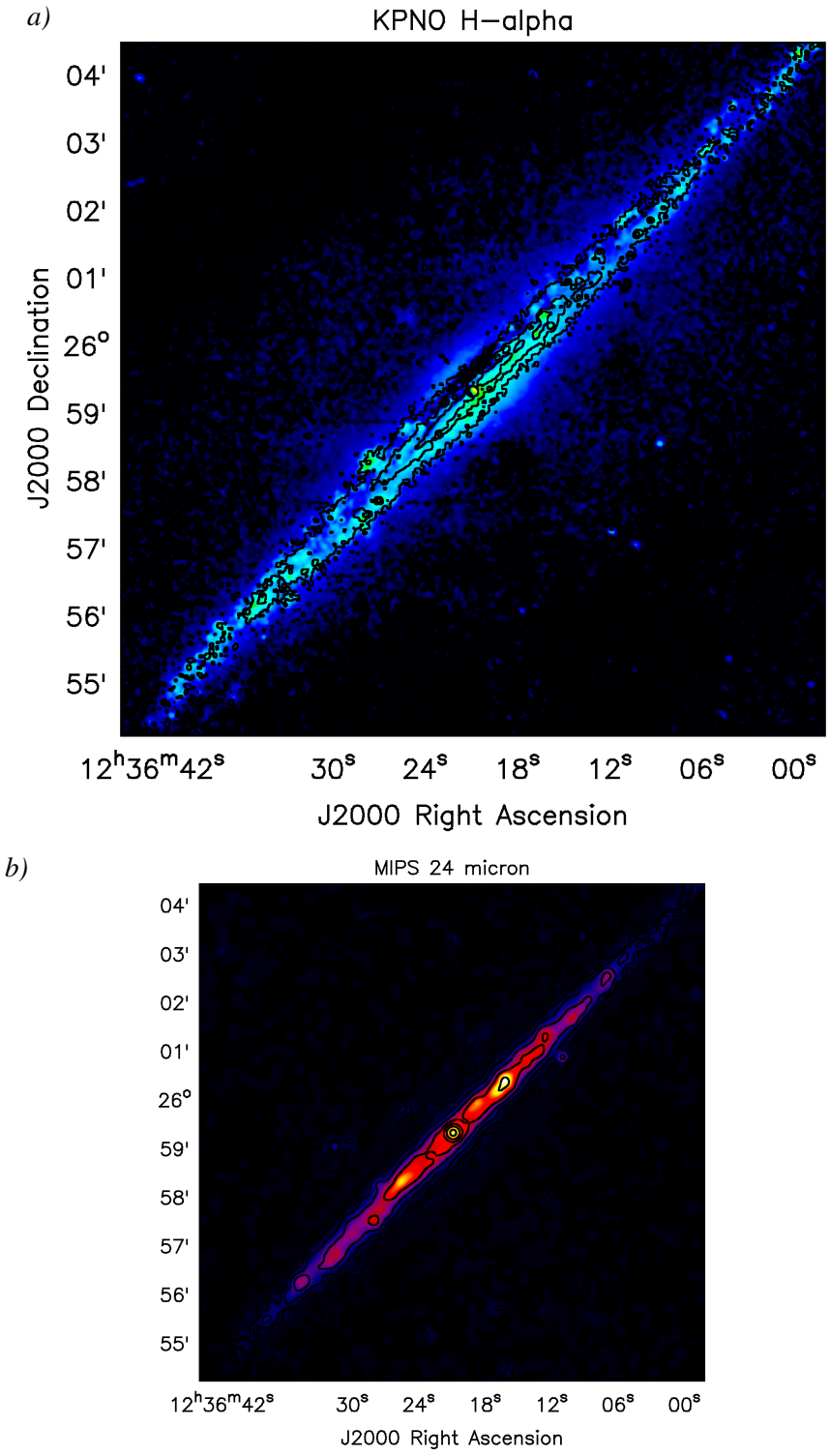

Figure 4.6: Hα and IR maps of NGC 4565 in comparison to the short-spacing corrected data at 6 GHz. *a)*: KPNO Hα image, smoothed to a Gaussian beam of 3.5″ and overlaid with the same contours as in Fig. 4.5 c). *b)*: Spitzer MIPS 24 μm image, smoothed to a Gaussian beam of 12″ and overlaid with the same contours as in Fig. 4.5 b).

with the outer spiral arms, and consequently these outer arms are expected to make a faint contribution to the inner ring-shaped emission (i.e. in the foreground on the front side and in the background on the back side). However, the inclination of the ring is still too high to clearly separate the outer from the inner arms where they overlap in projection.
Rather than the presence of a perfectly circular ring, it is more likely that the inner spiral arms are arranged in such a way as to form a near-circular ring-like structure (in which case the observed inner and outer emission may actually correspond to the inner and outer parts of the same spiral arms). Hence, for this galaxy we will use the terms "ring" and "inner spiral arms" synonymously throughout this work.

At the centre of the ring, we also observe emission that is much fainter and slightly more extended than the bright nuclear point source. This emission is most likely related to the central bar, which hence must be oriented almost entirely along the line of sight. Since bars are usually connected to spiral arms, this would imply that the bar is up to ≈11 kpc long, in which case it would constitute a substantial part of the disk. A bar of such a size, in turn, may possibly be associated with a strong inwards flow of material by way of the spiral arms. Such a bar flow could actually be part of the radiatively low-level AGN accretion process inferred by Chiaberge et al. (2006).

The fact that the inner spiral arms appear as a ring with a clearly distinguishable front and rear side allows a rough estimation of their width and thickness. For this purpose, the inner 10σ contour of the (short-spacing corrected) combined-array C-band image (Fig. 4.5 *c)*) is used, which seems to represent the ring-shaped structure to a satisfactory extent. With x being the total extent of the 10σ contour along the major axis, its observed minor axis extent amounts to $y = x \cos i + h \sin i$, where $(h \sin i)$ corresponds to the projected vertical thickness of the spiral arms. With $x \approx 240''$, $y \approx 20''$, $i = 86.3°$, and a distance of $D = 11.9$ Mpc, one obtains a vertical thickness of $h = 261$ pc. From the projected width y_1 of the front or rear side of the ring along its minor axis, one can determine the width of the inner spiral arms in the galactic plane: $w = (y_1 - h \sin i)/\cos i$. The typical width of the 10σ contour (excluding the nuclear radio source) near the minor axis of the ring is found to be $y_1 \approx 7''$, which results in $w \approx 2.2$ kpc. However, note that the determined width and thickness of the inner spiral arms are highly sensitive to the assumed inclination. For our lower error limit in inclination, i.e. $i = 85.9°$, we obtain $h = 164$ pc and $w \approx 3.4$ kpc, while using the upper limit of $i = 86.7°$ implies $h = 357$ pc and $w \approx 0.8$ kpc. Hence, in case the spiral arms have a vertical thickness comparable to the thin disk scale height of the Milky Way (≈ 300 pc), they have to be relatively narrow for the front and rear side of the disk to be separately visible in our images; otherwise they must be notably flatter than the disk of our Galaxy.

Figure 4.6 shows that, similar to the case of NGC 891, the radio continuum and Hα emission are only roughly correlated on small scales. Still, most of the maxima in the radio disk do have a clear counterpart in the Hα image, and can therefore be identified with HII regions.

4.2 Estimating the amount of thermal radio emission

In principle, the decomposition of the radio continuum emission into its thermal and non-thermal component can be performed based on radio observations at three or more frequencies (preferably between 1 and 10 GHz). In this case, the thermal fraction and the non-thermal spectral index can be solved for as described by Klein et al. (1984b) or Duric & Dixon (1991). Both of these methods require the assumption that the CREs effectively do not experience significant energy losses and hence that the synchrotron spectrum is a power law with a constant spectral index. The galaxy-integrated non-thermal (and even total) spectrum can often be fitted well by a single power law over a wide range of frequencies (e.g. Klein et al. 1984a; Duric et al. 1988; Niklas et al. 1997; Mulcahy et al. 2014; Basu et al. 2015). In the spatially resolved case, however, a steepening of the line-of-sight synchrotron spectrum at higher radio frequencies due to energy losses is expected in the halos of edge-on galaxies, and may also occur locally in their disks (see Chapt. 5).

Fitting of curved non-thermal spectra (e.g. Roy & Pramesh Rao 2004; Basu et al. 2015) requires at least four observing frequencies. While from the broad-band data of CHANG-ES such multi-frequency information could in principle be extracted, a sufficiently high S/N would be needed to either produce narrow-band total power maps or to yield reliable in-band spectral indices to form broad-band total power maps at different frequencies within a given band. As we will present in the next chapter, the extent to which this is fulfilled for our data is very limited. Also, previous observations of NGC 891 and NGC 4565 at additional frequencies in the relevant range (e.g. at 10.55 GHz by Dumke et al. 1995) were done at too low angular resolutions to be suitable for our studies.

Consequently, since thermal emission primarily traces regions of recent star formation, we are required to infer the thermal radio component from star formation tracers in other wavelength regimes. The application of such decomposition methods to egde-on galaxies is particularly challenging, owing to the long lines of sight through their disks (where the bulk of their thermal emission is expected to occur), and therefore has hardly been successfully accomplished so far. The most direct tracer of the ionized gas that produces thermal free-free radiation is emission in the Hα recombination line. Part of this emission is however attenuated by galaxy-internal dust absorption and then re-radiated at IR wavelegths. A range of different methods exist to correct for this attenuation, a few of which are briefly described in the following:

- (*i*) Tabatabaei et al. (2007) derived the optical depth of the dust in the moderately inclined galaxy M 33 from FIR data at 70 μm and 160 μm, and used this quantity to determine the intrinsic, i.e. extinction-corrected, Hα intensity distribution. This approach is not practicable for most edge-on galaxies, as usually the dust optical depth for a line of sight through an edge-on disk is so large that only Hα emission originating from regions near to the observer can be recovered, while emission from further back in the disk is entirely absorbed by dust.

- (*ii*) An empirical relation between the 24 μm luminosity and the intrinisic Hα luminosity was found by Relaño et al. (2007) based on a sample of individual HII regions in 41

galaxies. The shortcoming of inferring the Hα intensity directly from 24 μm observations using this relation is that it is non-linear and therefore not valid if applied to entire galaxies.

- (*iii*) Calzetti et al. (2007) and Kennicutt et al. (2009) established linear relations of the form

$$L_{\mathrm{H}\alpha,\mathrm{corr}} = L_{\mathrm{H}\alpha,\mathrm{obs}} + a \cdot \nu L_{\nu}(24\mu\mathrm{m})\,. \tag{4.1}$$

  Here, $L_{\mathrm{H}\alpha,\mathrm{obs}}$ and $L_{\mathrm{H}\alpha,\mathrm{corr}}$ are the bolometric lumiosities of the observed and extinction-corrected Hα emission, respectively, and ν and L_{ν} are the frequency and monochromatic luminosity at 24 μm. For the scaling coefficient of the 24 μm emission, Calzetti et al. (2007) found $a = 0.031 \pm 0.006$ from observations of HII regions in 33 nearby galaxies. The 24 μm luminosities of these regions are in the range $3 \cdot 10^{38}\mathrm{erg/s} \lesssim \nu L_{\nu}(24\mu\mathrm{m}) \lesssim 3 \cdot 10^{44}\mathrm{erg/s}$. Kennicutt et al. (2009) obtained $a = 0.02 \pm 0.005$ from integrated luminosities of 68 galaxies. Both galaxy samples were well-mixed in terms of morphological type and inclination. While in face-on galaxies the local amount of ionized gas appears to be tightly correlated with the dust-emitted IR radiation (at least on a scale of a few hundred pc), in the edge-on case the lines of sight through galactic disks are much longer and vary greatly in their sampled distribution of stars and of the various ISM phases. Therefore, we cannot expect this method to yield accurate corrections of the measured Hα intensities.

- (*iv*) Another alternative is to infer local SFRs from 24 μm measurements employing a linear relation found by Rieke et al. (2009), and convert these SFRs to thermal radio luminosities following Condon (1992). The latter conversion must be done using *recent* SFRs ($M \geq 5\mathrm{M}_{\odot}$), however IR radiation is not an optimal tracer of recent star formation, as also the radiation field of already evolved stars contributes to the dust heating. Thus, the thermal radio component may easily be overestimated by this method.

Among methods (*i*) through (*iv*), which were all tested for both galaxies, we found method (*iii*) to result in the most realistic thermal fractions. However, given the above complications for edge-on galaxies, we are not able to provide an independent estimate of the thermal contribution in NGC 891 and NGC 4565, and are therefore compelled to infer thermal fractions based on literature values (D97, see below). We do, however, make use of method (*iii*) as an initial estimator for the spatial distribution of the thermal emission and consequently (see Sect. 5.1.4) of the non-thermal spectral index distribution.

Hα images (see Fig. 4.3 *a)*, *b)* and 4.6 *a)*) taken at the Kitt Peak National Observatory (KPNO) as ancillary data to the HALOGAS survey were provided to us with kind permission of M. Patterson and G. Heald, together with information on their conversion from counts s^{-1} to $\mathrm{erg\,s^{-1}cm^{-2}pixel^{-1}}$. First, we removed foreground stars near and in front of the galaxies by interpolating the surrounding intensities across the removed areas. The maps were then converted from $\mathrm{erg\,s^{-1}cm^{-2}pixel^{-1}}$ to $\mathrm{Jy\,beam^{-1}}$, using the Hα filter FWHM of 8.062 nm, its central wavelength of 657.474 nm, and assuming a Gaussian point spread function (PSF) with a FWHM of 1″. Next, the maps were smoothed to a resolution of 12″, converted to $\mathrm{erg\,s^{-1}pixel^{-1}}$, clipped below the 3σ level, and finally brought onto the same pixel grid as our short-spacing corrected radio images at 12″.
For the extinction correction of the Hα maps, we make use of Spitzer Multiband Imaging Photometer (MIPS) images at 24 μm. We smoothed these maps, which have a 6.5″ PSF, to

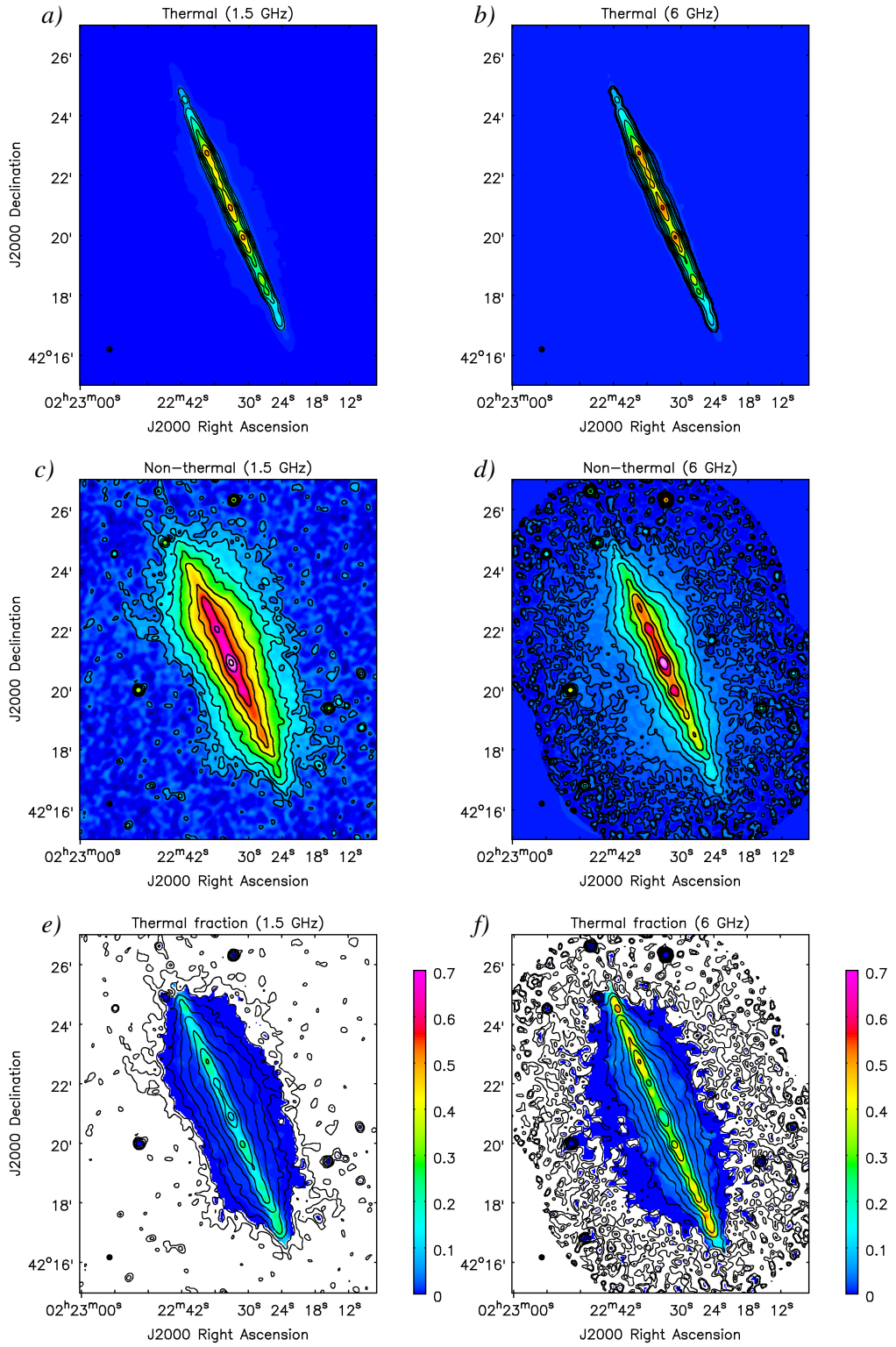

Figure 4.7: Results of the separation of thermal and non-thermal radio emission for NGC 891. *a)*: Thermal map at 1.5 GHz. *b)*: Thermal map at 6 GHz. *c)*: Non-thermal map at 1.5 GHz. *d)*: Non-thermal map at 6 GHz. *e)*: Thermal fraction map at 1.5 GHz, overlaid with contours of the total radio emission at this frequency (Fig. 4.2 *a)*). *f)*: Thermal fraction map at 6 GHz, overlaid with contours of the total radio emission at this frequency (Fig. 4.2 *b)*). The angular resolution in all panels is 12″. Contour levels start at the 3σ value of the corresponding total emission maps (see Table 4.1) and increase in powers of 2.

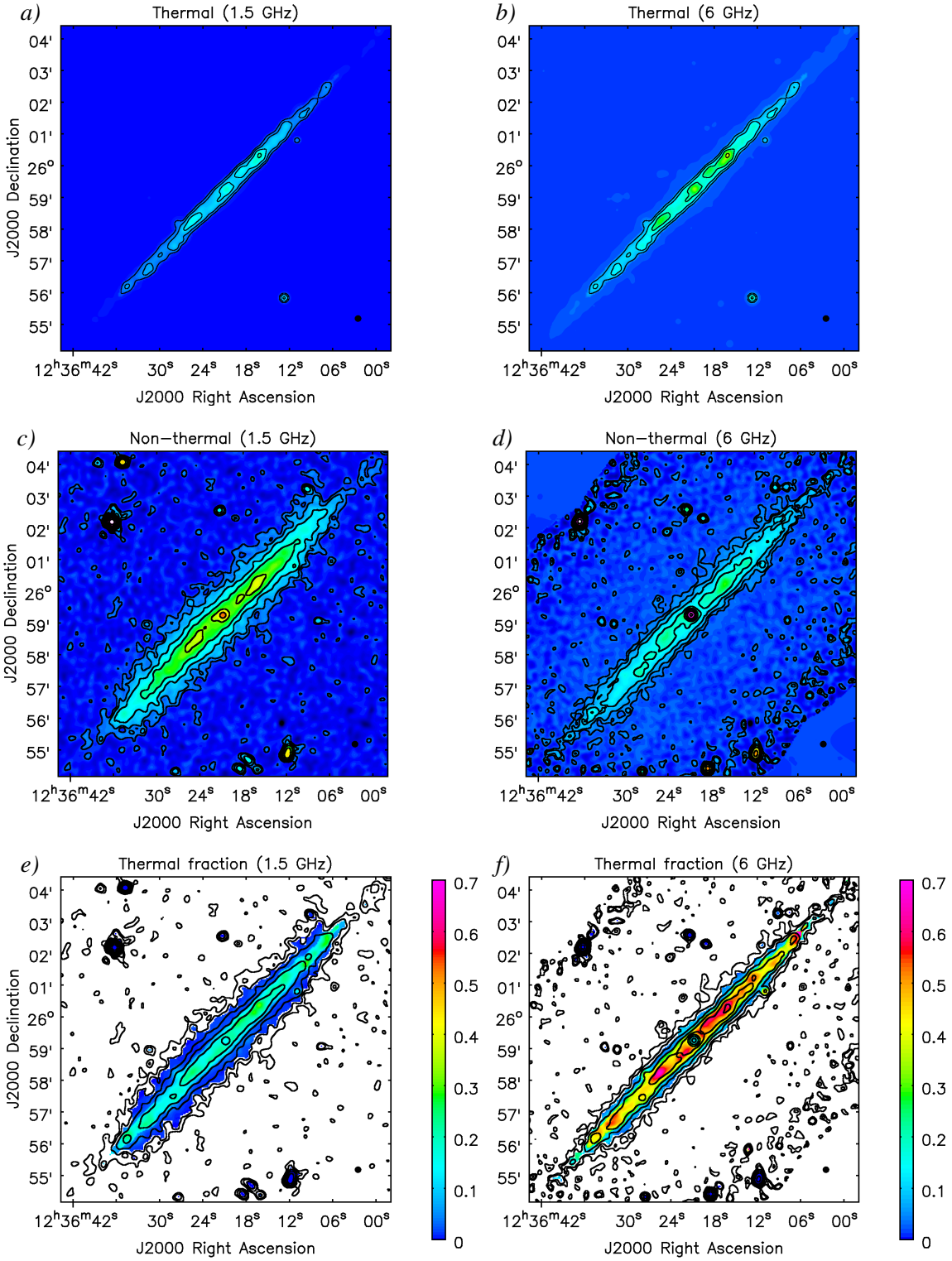

Figure 4.8: Results of the separation of thermal and non-thermal radio emission for NGC 4565. *a)*: Thermal map at 1.5 GHz. *b)*: Thermal map at 6 GHz. *c)*: Non-thermal map at 1.5 GHz. *d)*: Non-thermal map at 6 GHz. *e)*: Thermal fraction map at 1.5 GHz, overlaid with contours of the total radio emission at this frequency (Fig. 4.5 *a)*). *f)*: Thermal fraction map at 6 GHz, overlaid with contours of the total radio emission at this frequency (Fig. 4.5 *b)*). The angular resolution in all panels is 12″. Contour levels start at the 3σ value of the corresponding total emission maps (see Table 4.1) and increase in powers of 2.

a Gaussian beam of 12″ using the appropriate convolution kernel provided by Aniano et al. (2011). According to these authors, the application of this kernel lies between a "moderate" and a "very safe" convolution, meaning that not too much energy is moved from the wings of the original PSF into the Gaussian core, which would possibly amplify any potential image artifacts. After converting the original map units of MJy sr^{-1} to erg s^{-1}pixel^{-1}, the smoothed images were clipped at 3σ in case of NGC 4565 and at 10σ in case of NGC 891 (so as to reach not too far out into the halo, where no significant thermal contribution is expected). Lastly, remaining foreground stars near the galaxies were removed, and the maps were regridded to the shape of the radio images. The resulting maps are shown in Fig. 4.3 *c)* and Fig. 4.6 *b)*.

From the Hα and 24 μm images thus prepared, we computed extinction-corrected Hα maps by means of Eq. 4.1, using a scaling coefficient of $a = 0.031$ in regions where $\nu L_\nu(24\mu\mathrm{m}) \geq 3{\cdot}10^{38}$erg/s (which include the disks of both galaxies) and $a = 0.02$ for $\nu L_\nu(24\mu\mathrm{m}) < 3{\cdot}10^{38}$erg/s. We then followed Tabatabaei et al. (2007) to obtain the brightness temperature distribution T_b of the thermal radio emission. Finally, the brightness temperatures were converted to intensities at $\nu = 1.5$ GHz and $\nu = 6$ GHz using a relation given in Basu et al. (2012):

$$\left(\frac{I_{\nu,\mathrm{th}}}{\mathrm{Jy\,beam^{-1}}}\right) = 8.18 \cdot 10^{-7} \left(\frac{b_{\mathrm{maj}}}{\mathrm{arcsec}}\right)\left(\frac{b_{\mathrm{min}}}{\mathrm{arcsec}}\right)\left(\frac{\nu}{\mathrm{GHz}}\right)^2 \left(\frac{T_b}{\mathrm{K}}\right) \tag{4.2}$$

In addition, $I_{\nu,\mathrm{th}}$ maps at 5 and 7 GHz were formed (to be able to compute short-spacing corrected non-thermal spectral index maps, see Sect. 5.1.4). A more in-depth description of predicting the thermal radio contribution is given in the PhD thesis of C. Mora (in prep.).

Table 4.3: Thermal fractions at different radio frequencies, as found by Dumke (1997).

	NGC 891	NGC 4565
$f_{\mathrm{th,1.5GHz}}$	10%	16%
$f_{\mathrm{th,4.85GHz}}$	23%	35%
$f_{\mathrm{th,10.55GHz}}$	33%	46%

After forming non-thermal spectral index maps (as will be described in the following chapter) we found that using the above scaling coefficients for the 24 μm data does not lead to a successful prediction of the thermal radio emission in the two galaxies. The non-thermal spectral indices obtained within the disks of the galaxies were still considerably flatter at 6 GHz than at 1.5 GHz, indicating that the thermal contribution has been underpredicted. As an attempt to produce more reasonable results for the non-thermal spectral index distribution, we modified our 24 μm scaling factors such as to reproduce the thermal fractions found by D97, which are listed in Table 4.3. D97 obtained these values by fitting model spectra to measurements at three radio frequencies (with an angular resolution of 69″), approximating curved non-thermal spectra by splitting them up into a flat and a steep component with fixed spectral indices. For both galaxies, D97 determined these thermal fractions in the disk plane ($z = 0$), within a radial range between $50'' < |x| < 150''$ (with $x \equiv 0$ at the centre).

For comparison with the results of D97 at 1.5 and 4.85 GHz, we considered for each galaxy two rectangular regions, each ranging from 50″ to 150″ from the center on either side along the major axis and having a width of 69″ perpendicular to the major axis. Within these two boxes, we measured the integrated flux density in our predicted thermal maps at 1.5 and 5 GHz as well

as in the short-spacing corrected 1.5 and 5 GHz total intensity maps. Afterwards, we divided the resulting thermal flux density by the total flux density to obtain a value for the thermal fraction $f_{\rm th}$ at both frequencies. As shown in Table 4.4, using $a = 0.031$ in Eq. 4.1 (as found by Calzetti et al. 2007) for the disk region resulted in considerably lower thermal fractions than those determined by D97. Therefore, we increased the 24 μm scaling factor such that the following limits were fulfilled:

- Linear extrapolation of the D97 $f_{\rm th}$ values at 1.5 and 4.85 GHz to 5 GHz and linear interpolation between $f_{\rm th}$ at 4.85 and 10.55 GHz to 5 GHz yielded upper and lower limits, respectively, for $f_{\rm th}$ at 5 GHz. For NGC 891, these limits were found at 23.26% and 23.58%, while for NGC 4565 we obtained 35.29% and 35.84%.
- We required $f_{\rm th}$ at 1.5 GHz to be similar to the value found by D97 in case of NGC 891. For NGC 4565 we considered the D97 value as an upper limit, since it is based on the 20 cm image of Sukumar & Allen (1991), from which a considerable amount of the total flux of the galaxy at this wavelength is missing.

These conditions were fulfilled by the choice of $a = 0.058$ for NGC 891 and $a = 0.068$ for NGC 4565 (in both cases for $\nu L_\nu(24\mu\text{m}) \geq 3 \cdot 10^{38}$erg/s, as stated above), with resulting thermal fractions as given in Table 4.4. The $I_{\nu,\rm th}$ maps obtained in this way were subtracted from the short-spacing corrected total power maps (at 12″ resolution) to generate maps of the non-thermal emission $I_{\nu,\rm nth}$ at each frequency, and were divided by the same total power images to form corresponding $f_{{\rm th},\nu}$ maps. We present the $I_{\nu,\rm th}$, $I_{\nu,\rm nth}$, and $f_{{\rm th},\nu}$ maps of NGC 891 and NGC 4565 in Fig. 4.7 and 4.8, respectively.

Table 4.4: Thermal fractions at 1.5 and 5 GHz within the same regions as used by Dumke (1997), for different choices of the 24 μm scaling factor in Eq 4.1.

NGC 891	$f_{\rm th,1.5GHz}$	$f_{\rm th,5GHz}$
$a = 0.031$	5.9%	12.9%
$a = 0.058$	10.6%	23.5%
NGC 4565	$f_{\rm th,1.5GHz}$	$f_{\rm th,5GHz}$
$a = 0.031$	7.1%	17.7%
$a = 0.068$	13.9%	35.7%

Since the observed Hα emission contributes only very little to $L_{\rm H\alpha,corr}$, the $I_{\nu,\rm th}$ maps are basically scaled versions of the 24 μm images. While for both galaxies the resulting thermal fractions in the halo mostly stay below 1% at 1.5 GHz and below 10% at 6 GHz, they show strong radial variations in the disk. Here, the maxima in $I_{\nu,\rm th}$ for the most part appear to be well-correlated with the maxima in $I_{\nu,\rm nth}$; however, some major exceptions to this are present in both galaxies. In NGC 891, the maximum located $\approx 75''$ north-east of the centre in the total radio images has only a moderately bright counterpart in the thermal maps, which causes a drop in the $f_{\rm th}$ maps at this position. The same is especially true for the central region itself, where in fact a rather large thermal fraction is expected, but most probably a local underestimation of the thermal component is observed, owing to the above-mentioned line-of-sight effects. Conversely, the thermal maximum in the south-eastern half of NGC 4565 is offset by $\approx 20''$ from the nearest maximum in the radio emission, and hence $f_{\rm th}$ (at least at 6 GHz) is particularly high in this region. The largest thermal fraction per beam in NGC 891 is found to be 27% at 1.5 GHz and 49% at 6 GHz, while for NGC 4565 the maximum is 28% at 1.5 GHz and 65% at 6 GHz.

In Table 4.5 we present global values of the thermal fractions and of the total and non-thermal spectral index between the two observing frequencies. All of these are based on integrated flux density measurements as included in Table 4.2. The spectral index values between $\nu_1 = 1.5\,\mathrm{GHz}$ and $\nu_2 = 6\,\mathrm{GHz}$ were determined using

$$\alpha_{\nu_1-\nu_2} = \frac{\ln\left(\frac{I_{\nu_2}}{I_{\nu_1}}\right)}{\ln\left(\frac{\nu_2}{\nu_1}\right)}\,. \tag{4.3}$$

Both the total and non-thermal spectral index of NGC 891 are in close agreement with the values of -0.82 ± 0.03 and -0.9 ± 0.1, respectively, obtained by Klein et al. (1984a) from observations at multiple frequencies. Niklas et al. (1997) found unusually small thermal fractions for NGC 891, and consequently a relatively flat non-thermal spectral index of -0.78 ± 0.03. On the other hand, the thermal fractions and non-thermal spectral index (-1.18 ± 0.11) these authors determined for NGC 4565 appear to be consistent with our own results for this galaxy. Moreover, for NGC 4565 we obtain the same total spectral index of -0.93 as found by Hummel et al. (1984).

Table 4.5: Global thermal fractions and spectral indices, determined from total integrated flux density measurements. See text for details on the separation of the thermal and non-thermal emission.

	NGC 891	NGC 4565
$f_{\mathrm{th,1.5GHz}}$	7.2%±3.1%	10.6%±4.9%
$f_{\mathrm{th,6GHz}}$	18.4%±8.0%	32.9%±15.8%
$\alpha_{\mathrm{tot,1.5-6GHz}}$	-0.80±0.02	-0.93±0.02
$\alpha_{\mathrm{nth,1.5-6GHz}}$	-0.90±0.13	-1.14±0.25

5 Spectral index distribution

Measuring the spatially resolved radio spectral index distribution in edge-on galaxies is of crucial importance for the study of a wide range of disk-halo physics, in particular of CR transport. Apart from presenting the results of our spectral index measurements in NGC 891 and NGC 4565, a major portion of this chapter is dedicated to the analysis of the various sources of error occurring, some of which may seriously affect the credibility of the measurements. Special attention is given to the uncertainties that are specific to the determination of in-band spectral indices by applying the broad-band observing techniques of the JVLA in conjunction with (MS-)MFS imaging. We also describe methods to correct for some of these errors and investigate the residual post-correction uncertainties. Afterwards, the morphological properties of the thermal and non-thermal spectral index distributions we obtained after applying these corrections are discussed. In the final part of this chapter we introduce standard models for the temporal evolution of the synchrotron spectrum and investigate the extent to which these models are able to reproduce our spectral index data.

5.1 Post-imaging corrections to the spectral index measurements and assessment of uncertainties

In order to obtain reliable spectral index measurements from wide-band radio continuum data employing the MFS imaging technique, a number of corrections and amendments during and after deconvolution need to be considered in most cases. These may include choosing a primary-beam model at a frequency differing from the centre frequency of the band, exclusion of the lowest spatial frequencies from the *uv* data, and the addition of missing short spacings. In this section, we investigate the impact and importance of each of these corrections, and give estimates for the errors induced when not applying them (as well as for residual errors after performing corrections). As the scientific analysis of our spectral index data, which we present later in this chapter, will be done for the major part at an intermediate angular resolution, we demonstrate most of our correction methods using the example of our L-band C-array and C-band D-array data sets of both galaxies (also since C-band D-array is the only case that requires shifting the frequency of the model used for primary- beam correction). As mentioned at the beginning of Chapter 4, the first two Taylor-term images were smoothed to an angular resolution of 12″ before running `widebandpbcor` in each case, to obtain primary-beam corrected spectral index maps at a common resolution at both 1.5 GHz and 6 GHz. At 6 GHz the spectral index maps of the two pointings were mosaicked as described in Sect. 3.4.6.

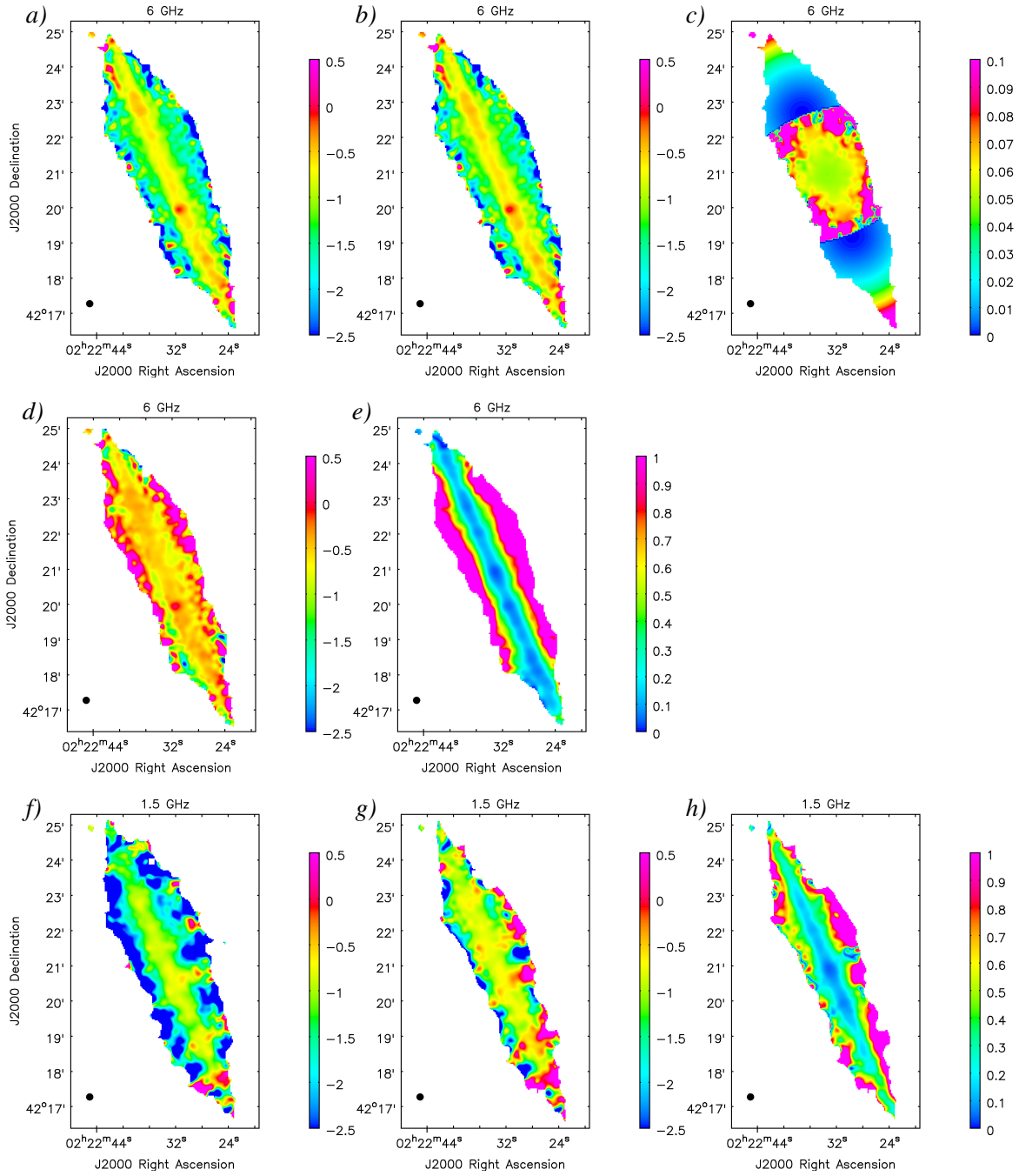

Figure 5.1: Distribution of the total spectral index in NGC 891 at 6 GHz (C-band D-array) and 1.5 GHz (L-band C-array). *a)*: 6 GHz map, PB-corrected using the 6.0 GHz PB model. *b)*: 6 GHz map, PB-corrected using the 6.6 GHz PB model. *c)*: Difference map between panels *b)* and *a)*. *d)*: 6 GHz map generated with an inner *uv*-cutoff at 0.8 kλ, PB-corrected using the 6.6 GHz PB model. *e)*: Difference map between panels *d)* and *b)*. *f)*: 1.5 GHz map, PB-corrected using the 1.5 GHz PB model. *g)*: 1.5 GHz map generated with an inner *uv*-cutoff at 0.8 kλ, PB-corrected using the 1.5 GHz PB model. *h)*: Difference map between panels *g)* and *f)*. All maps extend to the 5σ level in the corresponding total power images. The angular resolution in all panels is 12″.

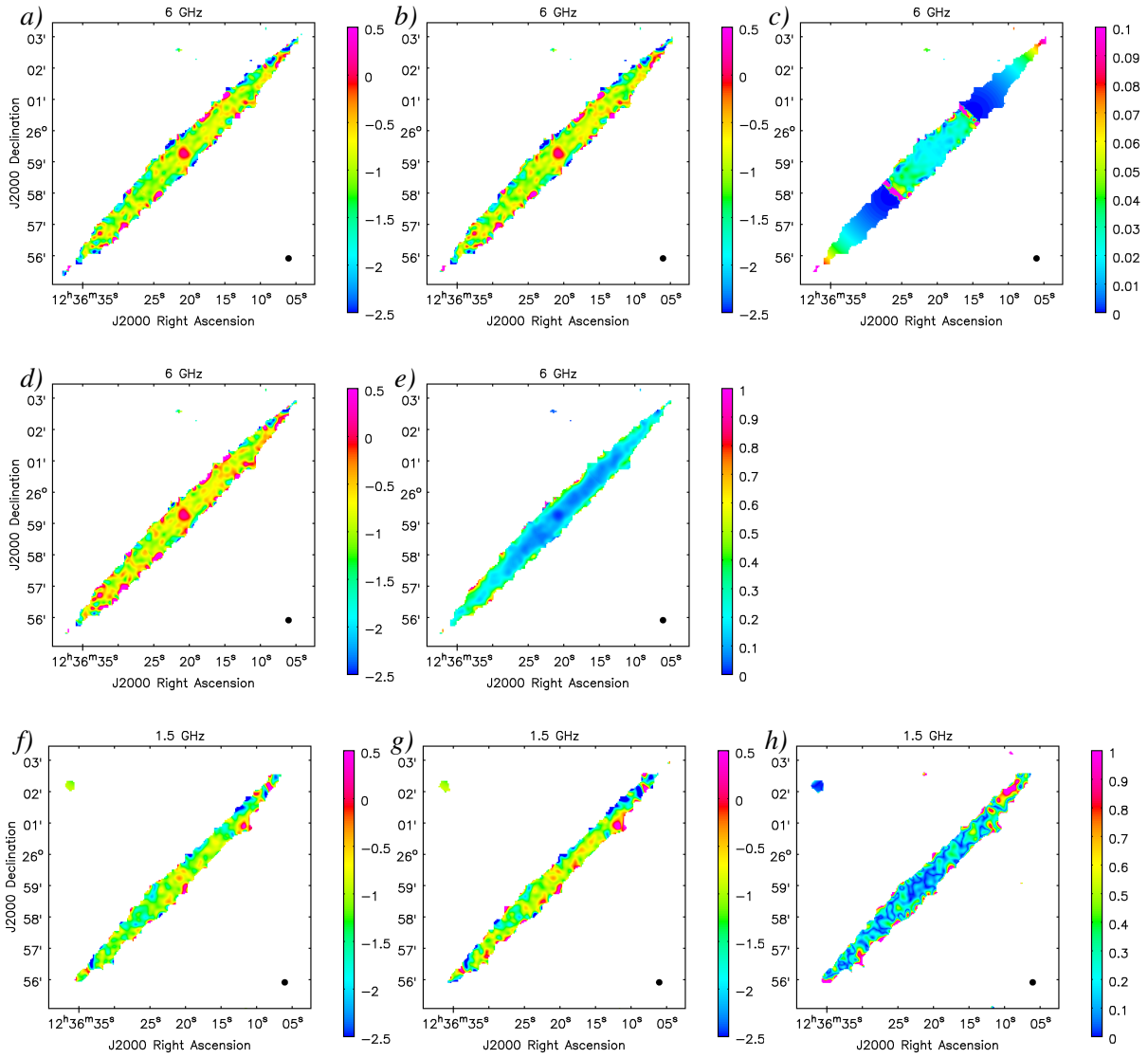

Figure 5.2: Distribution of the total spectral index in NGC 4565 at 6 GHz (C-band D-array) and 1.5 GHz (L-band C-array). *a)*: 6 GHz map, PB-corrected using the 6.0 GHz PB model. *b)*: 6 GHz map, PB-corrected using the 6.25 GHz PB model. *c)*: Difference map between panels *b)* and *a)*. *d)*: 6 GHz map generated with an inner *uv*-cutoff at 0.8 kλ, PB-corrected using the 6.25 GHz PB model. *e)*: Difference map between panels *d)* and *b)*. *f)*: 1.5 GHz map, PB-corrected using the 1.5 GHz PB model. *g)*: 1.5 GHz map generated with an inner *uv*-cutoff at 0.8 kλ, PB-corrected using the 1.5 GHz PB model. *h)*: Difference map between panels *g)* and *f)*. All maps extend to the 5σ level in the corresponding total power images. The angular resolution in all panels is 12″.

Panels *a)* and *f)* of Fig. 5.1 show maps of the total (i.e. still including the thermal component) spectral index distribution in NGC 891 obtained by MFS imaging of the C-band D-array and L-band C-array data, respectively, without any spatial frequency limitation. The maps have been primary-beam corrected using the primary-beam model at the central frequency of the band, and cut-off at the 5σ level in the respective (not yet primary-beam corrected) total power map. They

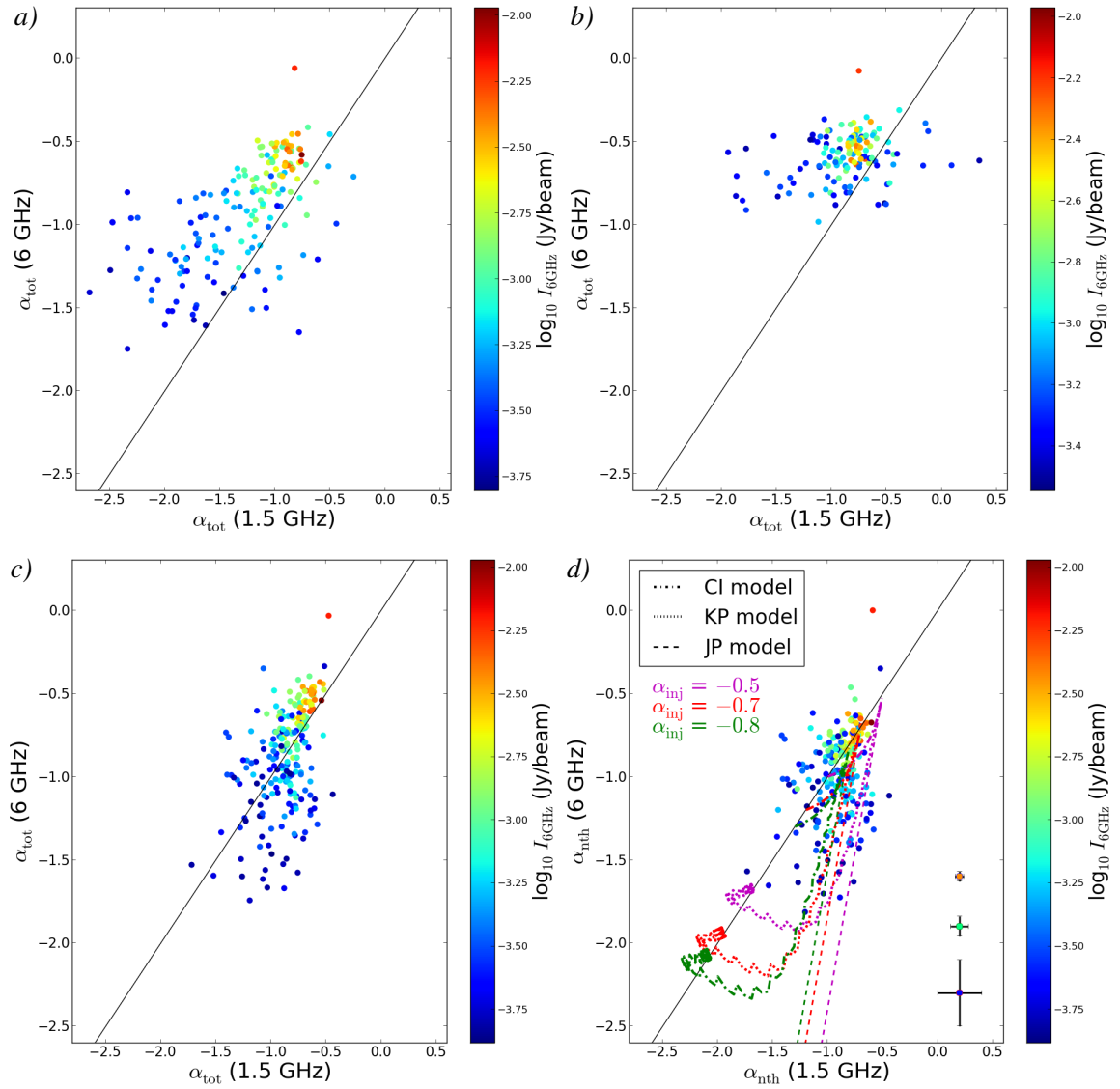

Figure 5.3: Scatter plots of the spectral index distribution at 6 GHz versus the spectral index distribution at 1.5 GHz, for the galaxy NGC 891. *a)*: Total spectral index, determined without *uv*-cutoff, no short-spacing correction (Fig. 5.1 *b)* vs Fig. 5.1 *f)*). *b)*: Total spectral index, determined using a 0.8 kλ *uv*-cutoff, no short-spacing correction (Fig. 5.1 *d)* vs Fig. 5.1 *g)*). *c)*: Short-spacing corrected total spectral index (Fig. 5.12 *c)* vs Fig. 5.12 *a)*). *d)*: Short-spacing corrected non-thermal spectral index (Fig. 5.12 *d)* vs Fig. 5.12 *b)*), in comparison with different spectral aging models. All α maps were cut off at 30σ in the respective total power maps before making the scatter plots. Each data point represents the 1.5 and 6 GHz spectral index averaged within one synthesized beam and is colour-coded based on the 6 GHz D-array total power map (Fig. 4.1 *d)*). The dash-dotted, dotted, and dashed lines in panel *d)* show the expected positions in the plot for the CI, KP, and JP models, respectively, for different break frequencies $\nu_{\rm br}$ and three different injection spectral indices $\alpha_{\rm inj}$. The wiggles in the KP graphs are merely artifacts of the numerical integration. The symbols with error bars represent the $\Delta\alpha_{\rm C15}$ errors (Fig. 5.7 *f)* and 5.17 *b)*), which depend on the S/N and are shown for three different total intensity values.

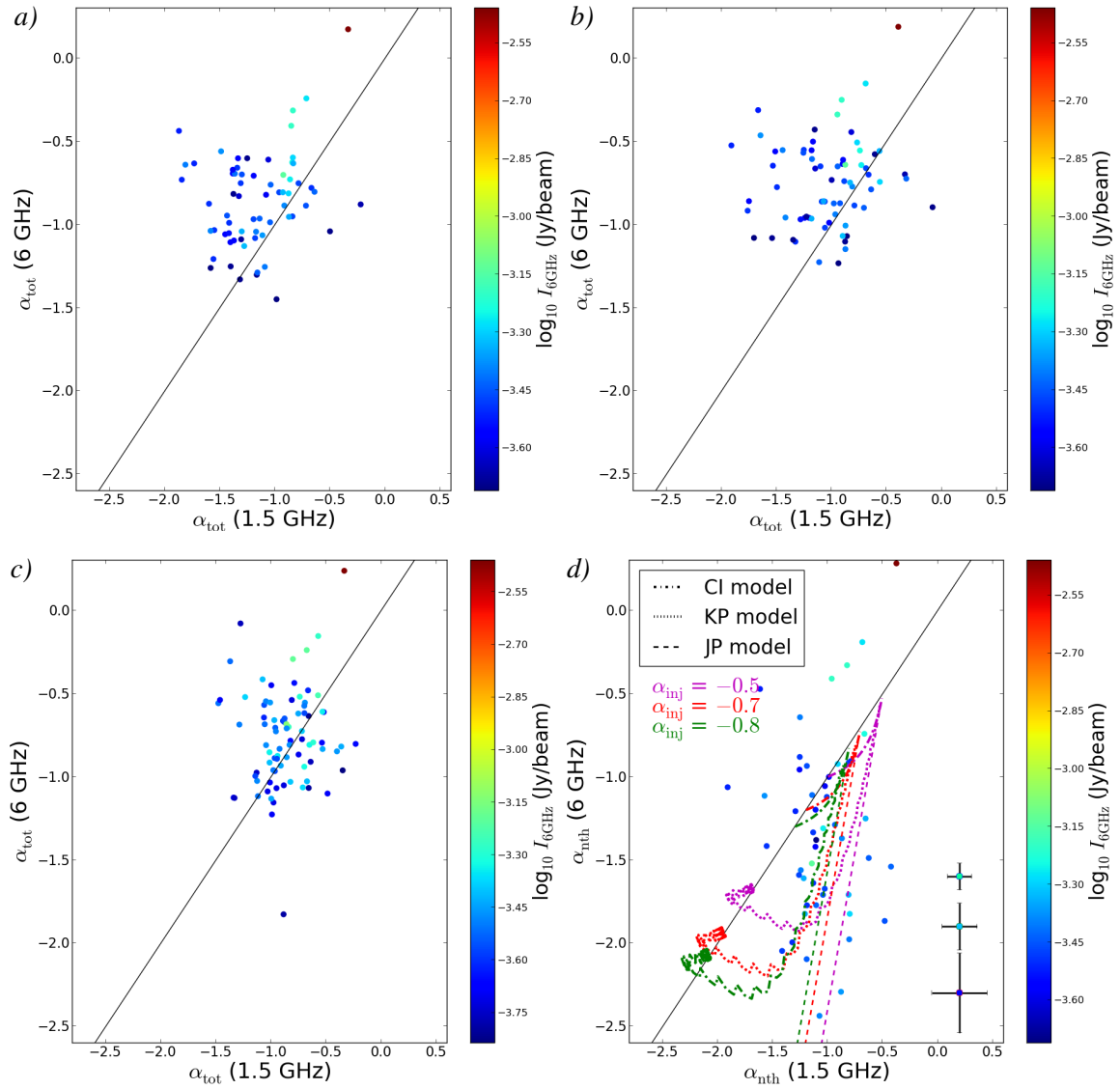

Figure 5.4: Scatter plots of the spectral index distribution at 6 GHz versus the spectral index distribution at 1.5 GHz, for the galaxy NGC 4565. *a)*: Total spectral index, determined without *uv*-cutoff, no short-spacing correction (Fig. 5.2 *b)* vs Fig. 5.2 *f)*). *b)*: Total spectral index, determined using a 0.8 kλ *uv*-cutoff, no short-spacing correction (Fig. 5.2 *d)* vs Fig. 5.2 *g)*). *c)*: Short-spacing corrected total spectral index (Fig. 5.14 *c)* vs Fig. 5.14 *a)*). *d)*: Short-spacing corrected non-thermal spectral index (Fig. 5.14 *d)* vs Fig. 5.14 *b)*), in comparison with different spectral aging models. All α maps were cut off at 20σ in the respective total power maps before making the scatter plots. Each data point represents the 1.5 and 6 GHz spectral index averaged within one synthesized beam and is colour-coded based on the 6 GHz D-array total power map (Fig. 4.4 *d)*). The dash-dotted, dotted, and dashed lines in panel *d)* show the expected positions in the plot for the CI, KP, and JP models, respectively, for different break frequencies $\nu_{\rm br}$ and three different injection spectral indices $\alpha_{\rm inj}$. The wiggles in the KP graphs are merely artifacts of the numerical integration. The symbols with error bars represent the $\Delta\alpha_{\rm C15}$ errors (Fig. 5.10 *f)* and 5.17 *d)*), which depend on the S/N and are shown for three different total intensity values.

exhibit the overall pattern that is typically observed in edge-on galaxies, consisting of rather flat spectral indices throughout the disk and steeper values in the halo, with a general steepening with increasing distance from the mid-plane. The angular resolution is sufficiently high to observe a relatively sharp transition between flat and steep spectral indices in the disk-halo interface region. Near the outer edges, the maps are dominated by either extremely steep, flat, or even positive spectral index values, which are artifacts of both missing short spacings and instabilities of fitting the spectrum where the signal-to-noise ratio is too low. The corresponding maps of NGC 4565 (Fig. 5.2, panels *a)* and *f)*) show large variations also in radial direction along the disk, i.e. the disk is not as clearly distinguished as in NGC 891, with steep spectral indices being observed also in the mid-plane. However, in the C-band map, at least some of the flatter regions appear to be elongated along the inner ring seen in the total power image. Because of the narrow shape of this galaxy, edge artifacts occur much closer to the mid-plane than in NGC 891, and therefore, in case of steep edge values, it is hardly possible to tell them apart from the natural steepening due to CRE aging.

Figure 5.3 (panel *a)*) shows a scatter plot of the L-band C-array (Fig. 5.1 *f)*) and C-band D-array (Fig. 5.1 *b)*[1]) spectral index distributions in NGC 891. The maps were first clipped below 30σ in total intensity, to reduce the effect of noise-induced edge artifacts. Each point in the plot represents a beam-averaged value and is colour-coded based on the position in the C-band D-array total intensity map, so that redder data points are associated with the disk, while bluer points represent the halo. Apart from the overall spectral steepening, we also observe an increasing scatter of the data points around the 1:1 line as we move in z-direction, i,e. to higher vertical distances from the plane. Also, due to the higher fraction of thermal emission at higher radio frequencies, the spectral index in the disk is somewhat flatter at 6 GHz than at 1.5 GHz. Also the plot[1] for NGC 4565 (panel *a)* of Fig. 5.4; for this galaxy we performed the clipping of the maps at the 20σ level) shows a trend towards flatter spectral indices in regions of higher intensity, albeit it is much less obvious than in NGC 891, and also here, the scatter tends to be larger for low-intensity regions.

5.1.1 Revised primary-beam correction

As already indicated in Sect. 3.4.3, the JVLA primary beam is not rotationally symmetric, and furthermore, due to gravitational flexure of the telescope dishes, there are variations in the shape of each individual telescope beam with pointing direction, which the static primary-beam models supplied with CASA do not take into account. Neither was it feasible to apply the A-projection algorithm to our data to correct for the rotation of the beam pattern on the sky. While for the pre-upgrade VLA each of these two effects would mostly cancel out on average over the observing duration, observations with the new broad-band receivers in general require shorter integration times. Therefore, both effects introduce systematic errors to the primary-beam correction, which increase with distance from the pointing centre. In particular, time-dependent variations of the primary-beam spectrum (cf. Sect. 3.4.5) are induced. As tests by Bhatnagar et al.

[1] All data points shown in Fig. 5.3 and 5.4 already include the revised primary-beam correction of the C-band data (see Sect. 5.1.1), which caused only a minor shift of the affected data points along the 6 GHz axis and therefore has no effect on our qualitative analysis of these plots.

(2013) have shown, spectral index errors due to rotational asymmetry of the primary beam are basically negligible within the primary-beam FWHM. With angular diameters of 12.2′ and 16.2′ respectively, NGC 891 and NGC 4565 are located well within the 30′ FWHM of the primary beam at 1.5 GHz, whereas at 6 GHz the FWHM is only 7.5′ (compare Fig. 3.4), and therefore spectral index errors become significant for both galaxies in the outer regions of each C-band pointing.

A way to investigate primary-beam induced errors is to compare the two different pointings at 6 GHz for a given galaxy. In case a correct model of the primary beam at 6 GHz is used, the Taylor-term and spectral index maps of both pointings should be identical for each position within their field-of-view overlap after primary-beam correction. However, for our C-band D-array observations this is not the case, as can be seen from Fig. 5.5-5.6 (NGC 891) and Fig. 5.8-5.9 (NGC 4565), which show maps of the absolute pixel-by-pixel difference between the two pointings in total power and spectral index[2], as well as major- axis profiles of the individual pointings. For both galaxies, after applying the model primary beam at the observing frequency of 6.0 GHz, the two pointings are neither in good agreement in total power nor for the spectral index (see panels *a)* and *b)* of Fig. 5.5-5.6 and 5.8-5.9). Especially for the spectral index, the differences increase considerably with distance from the centre of the overlap region. Here, each pointing shows a negative gradient in the direction of the other, which implies that a narrower primary-beam pattern is needed for correction. We were able to minimize the differences in total power for both galaxies by using the primary-beam model at 6.25 GHz (i.e. setting the `reffreq` parameter in `widebandpbcor` to this value), as seen most clearly for NGC 891 (Fig. 5.5 *c)* and *d)*). For NGC 4565, albeit shifting the primary-beam frequency to 6.25 GHz did not quantitatively improve on the overall difference between the two pointings (see Table 5.1), we found the most symmetric distribution of total-power differences with respect to the minor axis at this frequency. As shown in panels *c)* and *d)* of Fig. 5.6, in NGC 891 the spectral index in each pointing still has a strong gradient along the major axis. Here, we found the minimum distribution of differences at a primary-beam frequency of 6.6 GHz (see Fig. 5.6, panels *e)* and *f)*), whereas the agreement in total power becomes worse again using this value (Fig. 5.5 *e)* and *f)*). The same is true for NGC 4565 in total power, while on average only little change in the spectral index differences compared to the 6.25 GHz case is observed. There is a notable asymmetry between the two halves of the galaxy in the spectral index difference maps though, which is slightly reduced by the upwards shift (from 6.0 to 6.6 GHz) of the primary-beam frequency. The latter part is true for the absolute differences; however, as evident from the major-axis profiles, at 6.6 GHz the difference is reduced in the south-eastern half, whereas in the north-western half the differences are increased again with respect to those at 6.25 GHz. In Table 5.1 we list for each case the average pointing differences within the overlap area of the spectral index maps that were primary-beam corrected at 6.6 GHz.

For both galaxies, we formed a map of the spectral index error that arises from applying the inaccurate primary-beam model at 6.0 GHz (Fig. 5.7 *a)* and 5.10 *a)*) by computing the primary-

[2]The small-scale, sometimes closed, thread-like patterns of low values in the spectral index difference maps are artifacts, the positions of which depend on the choice of deconvolution scales. The same patterns appear in the MS-MFS-based spectral index error maps before we smooth them with a boxcar kernel (see Sect. 5.1.6).

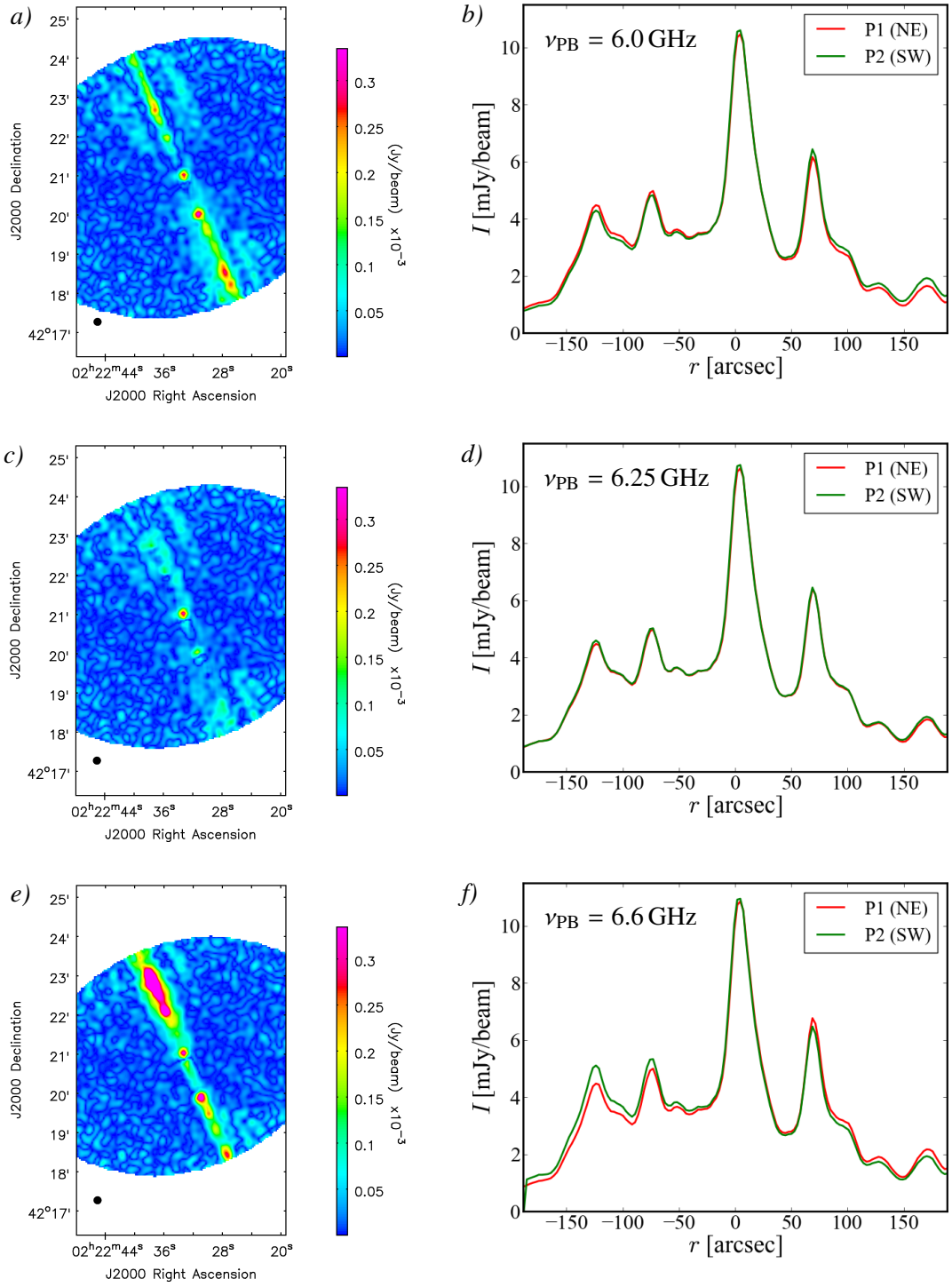

Figure 5.5: Total intensity difference between the two pointings of NGC 891 in C-band (6 GHz) D-array. Panels *a)*, *c)*, and *e)* show maps of the absolute pointing difference after PB correction using the PB model at 6.0, 6.25, and 6.6 GHz, respectively. The displayed field of view is the pointing overlap within the respective 20% PB level. Panels *b)*, *d)*, and *f)* show the corresponding major-axis intensity profiles of the individual pointings.

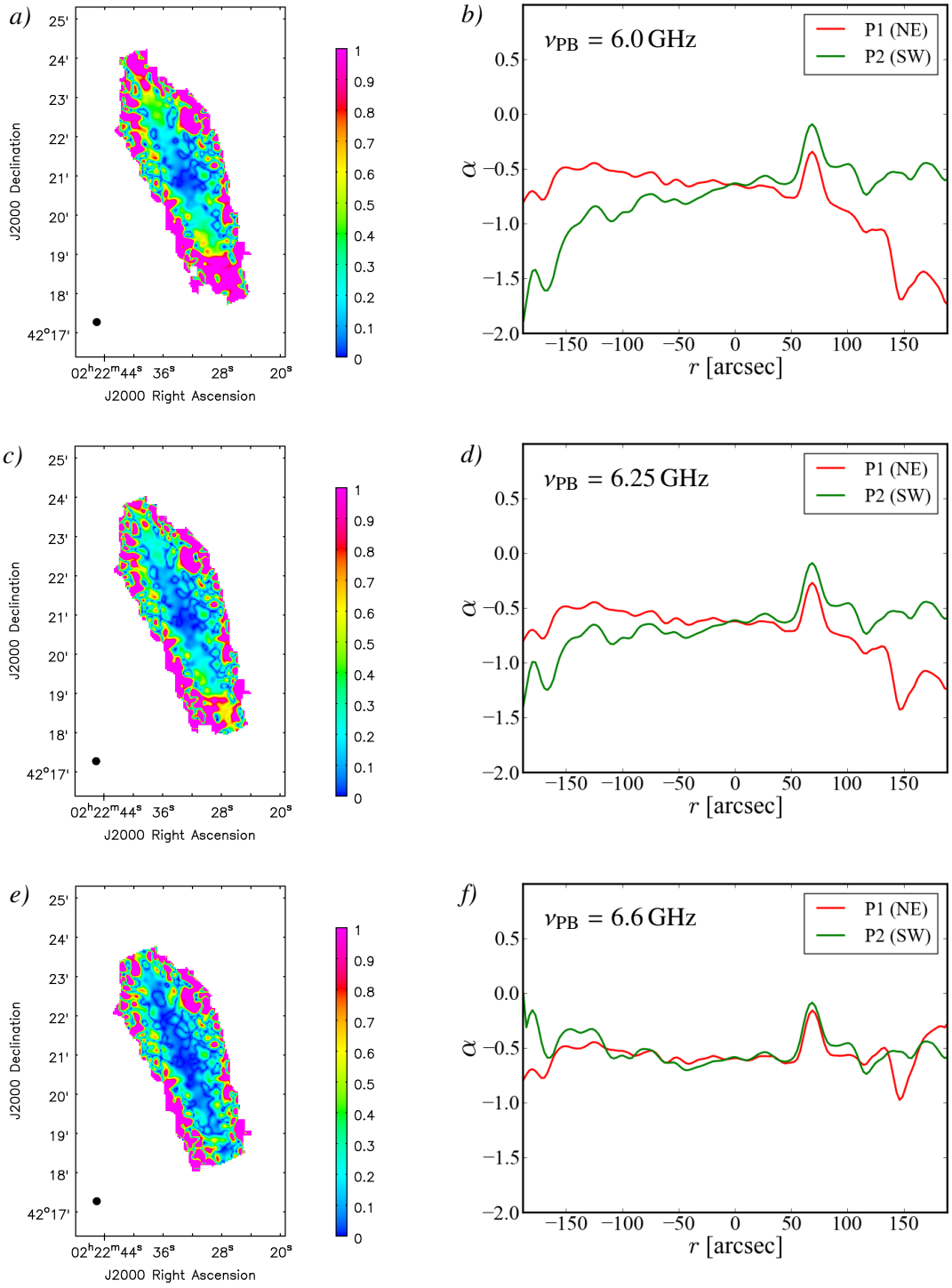

Figure 5.6: Spectral index difference between the two pointings of NGC 891 in C-band (6 GHz) D-array. Panels *a)*, *c)*, and *e)* show maps of the absolute pointing difference after PB correction using the PB model at 6.0, 6.25, and 6.6 GHz, respectively. The displayed maps are limited by the pointing overlap within the respective 20% PB level and the cutoff at 5σ in total intensity. Panels *b)*, *d)*, and *f)* show the corresponding major-axis spectral index profiles of the individual pointings.

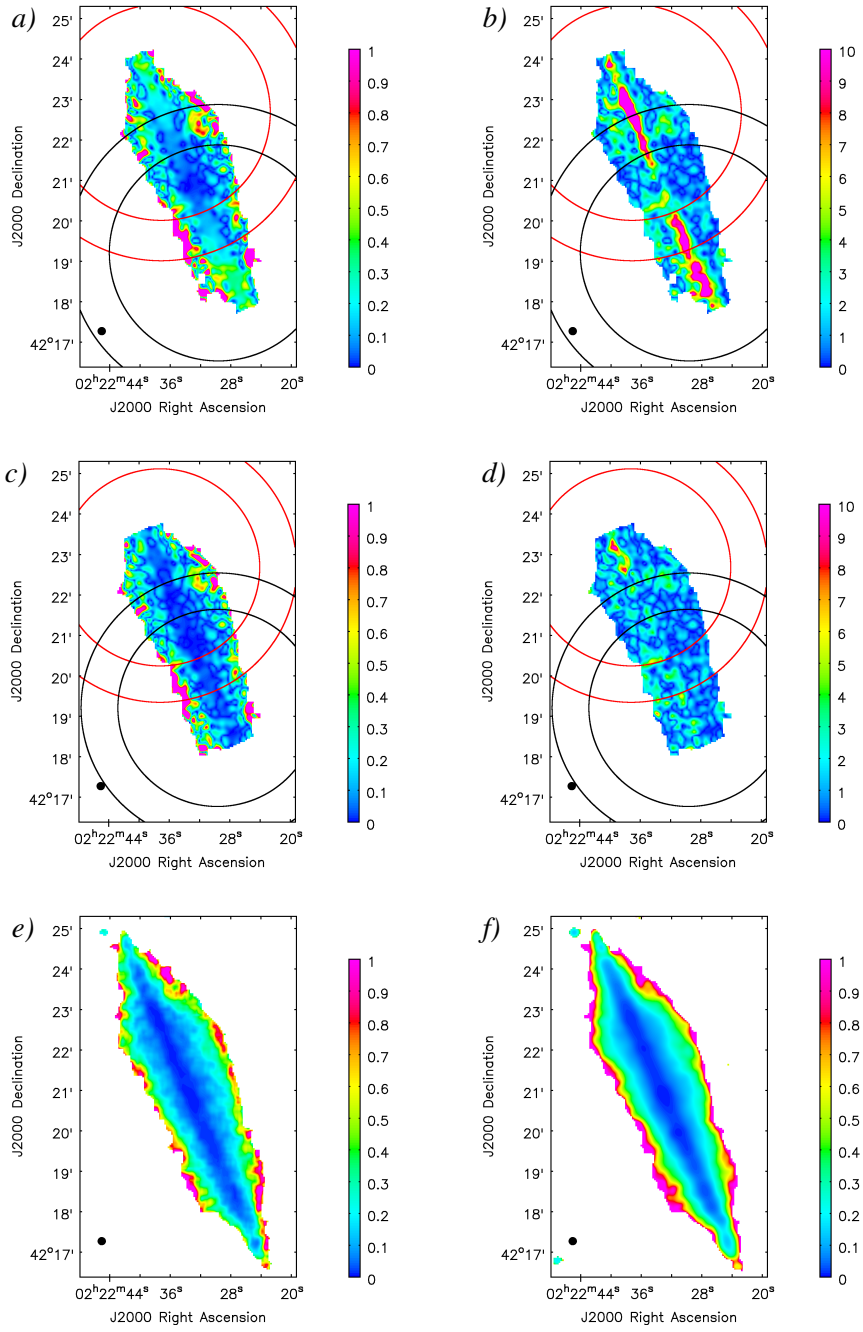

Figure 5.7: Comparison of 6 GHz spectral index error maps for NGC 891. *a)*: $\Delta\alpha_{\rm dev}$ map computed from the pointing differences (via Eq. 5.1) after PB correction using the 6.0 GHz PB model. *b)*: Ratio between $\Delta\alpha_{\rm dev}$ at $\nu_{\rm PB} = 6.0\,GHz$ (panel *a)*) and $\Delta\alpha_{\rm MFS}$ (panel *e)*). *c)*: $\Delta\alpha_{\rm dev}$ map computed from the pointing differences (via Eq. 5.1) after PB correction using the 6.6 GHz PB model. *d)*: Ratio between $\Delta\alpha_{\rm dev}$ at $\nu_{\rm PB} = 6.6\,GHz$ (panel *c)*) and $\Delta\alpha_{\rm MFS}$ (panel *e)*). *e)*: $\Delta\alpha_{\rm MFS}$, i.e. the error map computed by the MS-MFS clean algorithm. *f)*: $\Delta\alpha_{\rm C15}$ map obtained from the noise rms in the total power map using Eq. 5.5. The circular contours in panels *a)* - *d)* are placed at the 50% and 70% levels of the applied PB for each pointing.

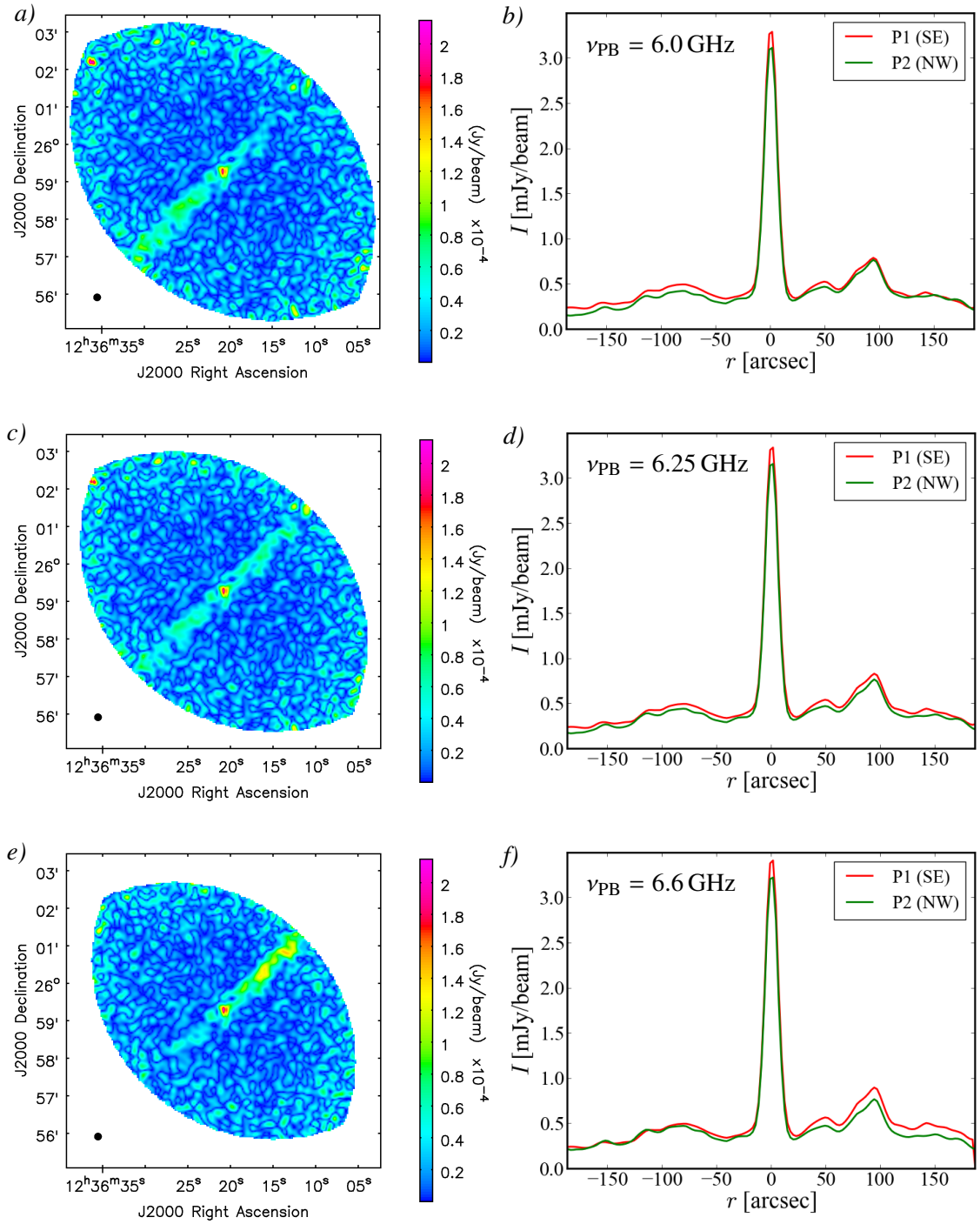

Figure 5.8: Total intensity difference between the two pointings of NGC 4565 in C-band (6 GHz) D-array. Panels *a)*, *c)*, and *e)* show maps of the absolute pointing difference after PB correction using the PB model at 6.0, 6.25, and 6.6 GHz, respectively. The displayed field of view is the pointing overlap within the respective 20% PB level. Panels *b)*, *d)*, and *f)* show the corresponding major-axis intensity profiles of the individual pointings.

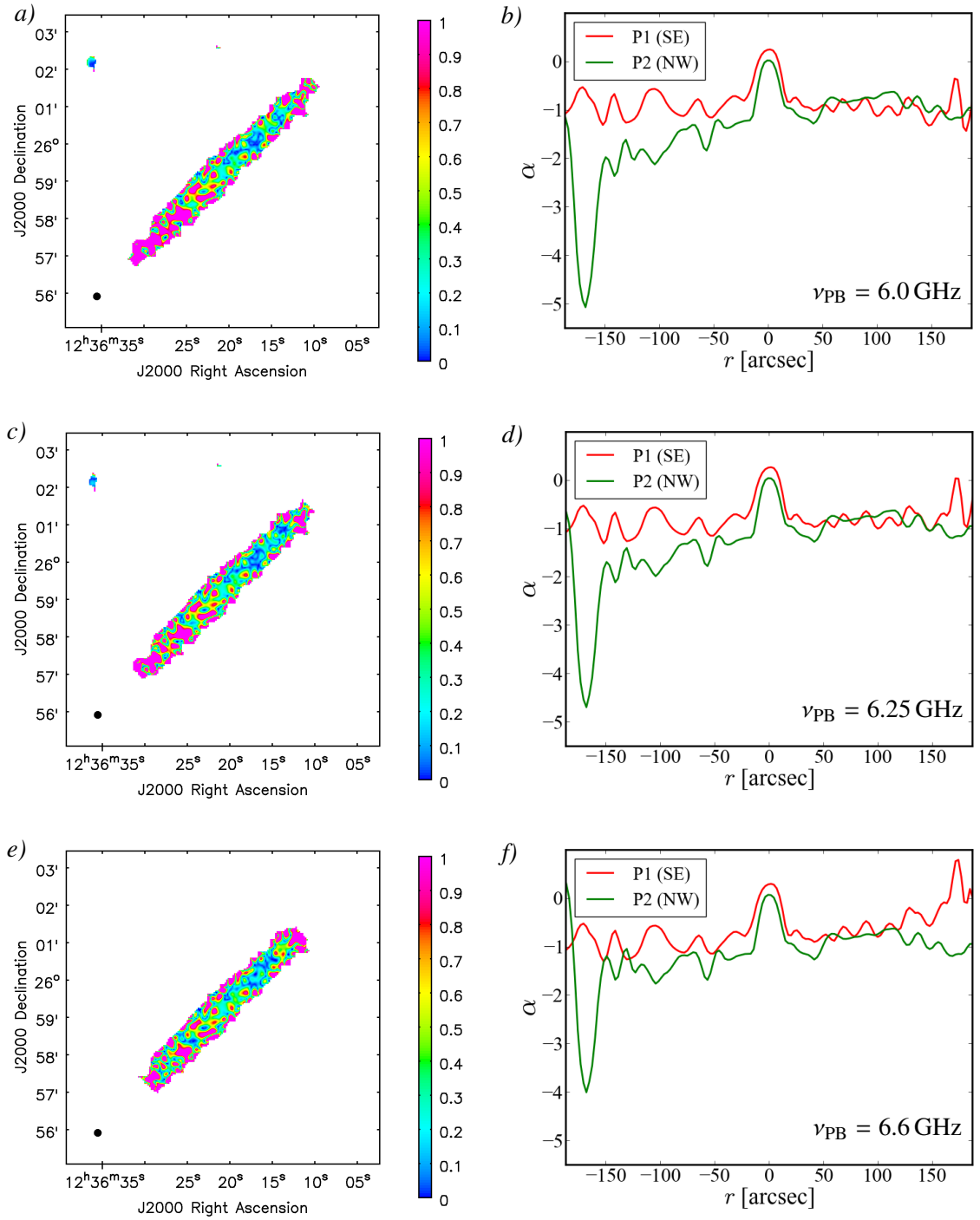

Figure 5.9: Spectral index difference between the two pointings of NGC 4565 in C-band (6 GHz) D-array. Panels *a)*, *c)*, and *e)* show maps of the absolute pointing difference after PB correction using the PB model at 6.0, 6.25, and 6.6 GHz, respectively. The displayed maps are limited by the pointing overlap within the respective 20% PB level and the cutoff at 5σ in total intensity. Panels *b)*, *d)*, and *f)* show the corresponding major-axis spectral index profiles of the individual pointings.

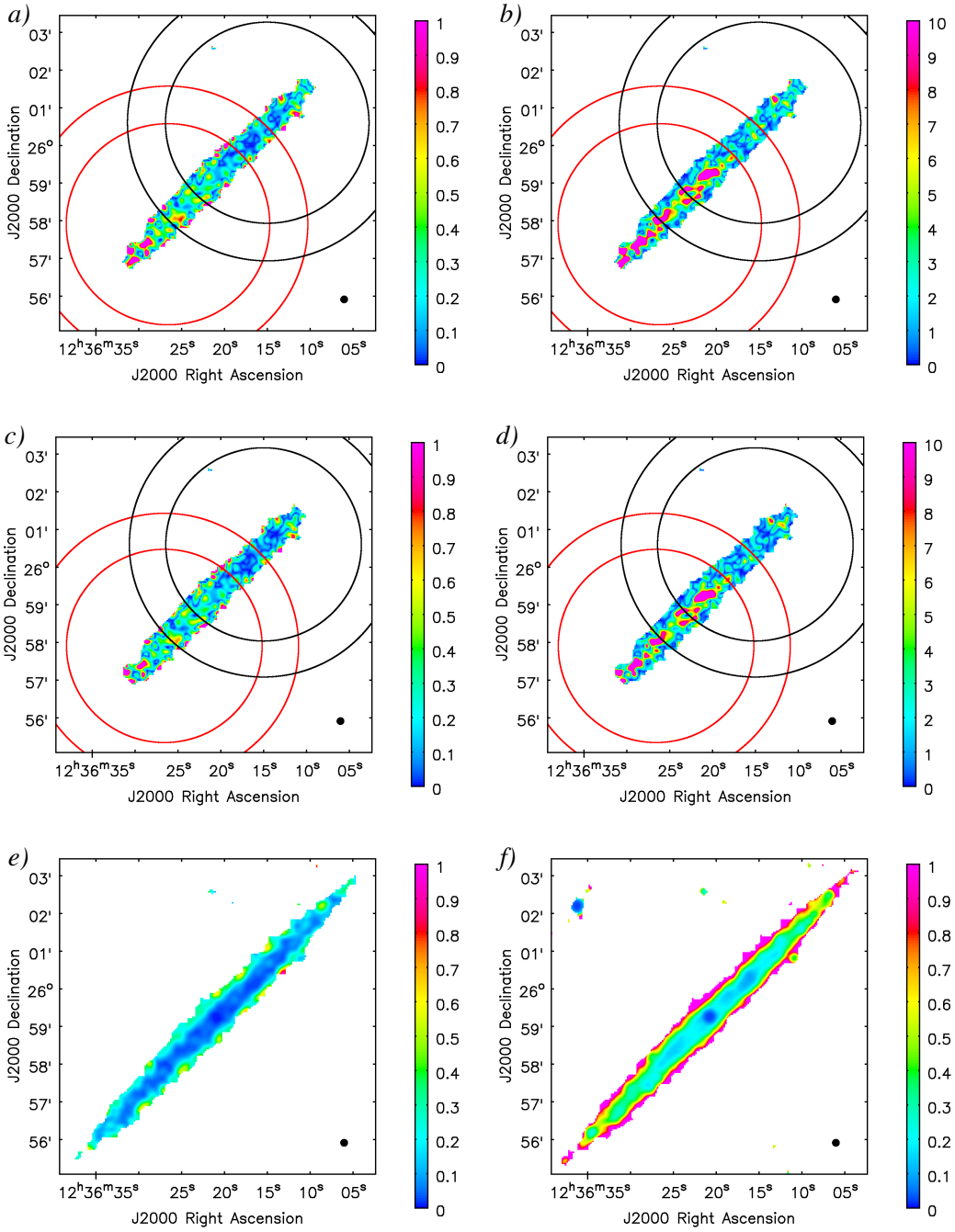

Figure 5.10: Comparison of 6 GHz spectral index error maps for NGC 4565. *a)*: $\Delta\alpha_{\rm dev}$ map computed from the pointing differences (via Eq. 5.1) after PB correction using the 6.0 GHz PB model. *b)*: Ratio between $\Delta\alpha_{\rm dev}$ at $\nu_{\rm PB} = 6.0\,GHz$ (panel *a)*) and $\Delta\alpha_{\rm MFS}$ (panel *e)*). *c)*: $\Delta\alpha_{\rm dev}$ map computed from the pointing differences (via Eq. 5.1) after PB correction using the 6.25 GHz PB model. *d)*: Ratio between $\Delta\alpha_{\rm dev}$ at $\nu_{\rm PB} = 6.25\,GHz$ (panel *c)*) and $\Delta\alpha_{\rm MFS}$ (panel *e)*). *e)*: $\Delta\alpha_{\rm MFS}$, i.e. the error map computed by the MS-MFS clean algorithm. *f)*: $\Delta\alpha_{\rm C15}$ map obtained from the noise rms in the total power map using Eq. 5.5. The circular contours in panels *a) - d)* are placed at the 50% and 70% levels of the applied PB for each pointing.

Table 5.1: Average[a] absolute differences between the two pointings at 6 GHz for different choices of the primary-beam reference frequency

Galaxy	NGC 891		NGC 4565	
ν_{PB} [GHz]	$\Delta I_{\mathrm{P1,P2}}$ [μJy beam^{-1}]	$\Delta\alpha_{\mathrm{P1,P2}}$	$\Delta I_{\mathrm{P1,P2}}$ [μJy beam^{-1}]	$\Delta\alpha_{\mathrm{P1,P2}}$
6.0	40	0.91	29	0.99
6.25	26	0.83	29	0.96
6.6	53	0.79	36	0.97

[a] All difference maps were averaged within the area that is limited by the smallest primary-beam overlap (which occurs at the highest frequency of 6.6 GHz) and the 5σ cutoff for the spectral index maps.

beam weighted deviation from the average of the two pointings in the overlap region:

$$\Delta\alpha_{\mathrm{dev}} = \sqrt{\frac{\left(\frac{B_{\mathrm{P1}}}{B_{\mathrm{P2}}}\right)(\alpha_{\mathrm{P1}}^{\mathrm{PBcor}} - \bar{\alpha}_{\mathrm{mos}}^{\mathrm{PBcor}})^2 + \left(\frac{B_{\mathrm{P2}}}{B_{\mathrm{P1}}}\right)(\alpha_{\mathrm{P2}}^{\mathrm{PBcor}} - \bar{\alpha}_{\mathrm{mos}}^{\mathrm{PBcor}})^2}{\left(\frac{B_{\mathrm{P1}}}{B_{\mathrm{P2}}}\right) + \left(\frac{B_{\mathrm{P2}}}{B_{\mathrm{P1}}}\right)}} \quad , \tag{5.1}$$

where B_{P1}, B_{P2}, $\alpha_{\mathrm{P1}}^{\mathrm{PBcor}}$, $\alpha_{\mathrm{P2}}^{\mathrm{PBcor}}$, and $\bar{\alpha}_{\mathrm{mos}}^{\mathrm{PBcor}}$ are defined as in Eq. 3.20. This new error map is for the most part comparable to the statistical error $\Delta\alpha_{\mathrm{MFS}}$ calculated by the MS-MFS algorithm (panel *e)*), as the map of the ratio of these two errors (panel *b)*) illustrates. A major exception to this are parts of the disks of both galaxies. For NGC 891, these parts are located predominantly outside the 70% primary-beam level (i.e. where the primary-beam gain is less than 0.7) of either pointing. The average error ratio in these narrow regions around the mid-plane is $\approx$ 5 (with individual pixel values up to $\approx$15), i.e. here the error that originates from the pointing differences is on average $\approx$400% higher than the error resulting from the MS-MFS spectral fitting. In NGC 4565, due to the asymmetry of the pointing differences, the entire south-eastern mid-plane region is strongly affected and has an average error ratio of $\approx$ 6.5. Such high error ratios are primarily a consequence of the small MS-MFS-based errors in regions of high signal-to-noise, yet the increase of the pointing differences with distance from the pointing centres is significant. In particular, beyond the half-power point (i.e. for a primary-beam gain less than 0.5) the mid-plane errors in the $\Delta\alpha_{\mathrm{dev}}$ map of NGC 891 increase up to $\approx$0.5, whereas in the $\Delta\alpha_{\mathrm{MFS}}$ map they remain below 0.1 throughout the disk. While the $\Delta\alpha_{\mathrm{dev}}$ values are in rough agreement with Bhatnagar et al. (2013) in the sense that they do not exceed 0.1 out to approximately the half-power point (not considering the above-mentioned edge effects), the error ratio map indicates that the simple primary-beam model used by the `widebandpbcor` task already shows significant inaccuracies at the 70% level. Panel *c)* of Fig. 5.7 and 5.10 display the $\Delta\alpha_{\mathrm{dev}}$ map formed after correction by the 6.6 GHz and 6.25 GHz model, respectively. At least in the case of NGC 891, this map is in good agreement with the $\Delta\alpha_{\mathrm{MFS}}$ map[3] even beyond the half-power primary-beam level, as can be seen from the corresponding ratio map (panel *d)*).

For use throughout the rest of this work, we correct our C-band D-array total power images of

[3] The $\Delta\alpha_{\mathrm{MFS}}$ maps computed after the 6.6 GHz or 6.25 GHz primary-beam correction are not shown, since they differ only marginally from those determined at 6.0 GHz.

both galaxies using the primary-beam model at 6.25 GHz, while for the spectral index map we adopt the 6.25 GHz correction in case of NGC 4565 and the 6.6 GHz correction for NGC 891. For the case of NGC 891, the reader should keep in mind that neither the 6.25 GHz nor the 6.6 GHz model corresponds to the true primary beam of the observation, but that they represent the best approximation with respect to the total intensity and spectral index measurements, respectively. Compared to the spectral index maps that were corrected by the 6.0 GHz primary beam (panel *a)* of Fig. 5.1 and 5.2), the newly corrected maps (panel *b)*) show somewhat flatter spectral indices within the overlap of the two pointings, which makes for a smoother transition at the edges of the overlap region[4]. This is particularly the case in NGC 891, where a larger frequency shift of the primary beam has been undertaken. For each galaxy, in panel *c)* the difference map between panels *b)* and *a)* is presented. The differences increase from the map center towards the edges of the overlap region, and are highest within the annular regions where the primary beam pointings overlap at 6.0 GHz but not at 6.25 GHz and 6.6 GHz, respectively. Within the primary-beam overlap, the differences are larger for NGC 891 than for NGC 4565, since different primary-beam frequencies were used. In those parts of the maps that are only observed by one of the pointings, the difference is close to zero near the overlap region, and increases towards the outer edges of the maps due to the radial increase of the pirmary-beam spectral curvature.

The results presented in this section demonstrate that inaccuracies of the primary-beam model can at least to some extent be taken care of with two-pointing observations, by shifting the primary-beam reference frequency, taking the primary-beam weighted average within the overlap region, and choosing appropriate primary-beam cutoff levels. On the other hand, the situation is critical if galaxies extend beyond the half-power level of the primary beam in regions where pointings do not overlap – especially for single-pointing observations, where it is not possible to assess primary-beam errors in the way presented here.

We performed similar tests for our C-band C-array data, but do not show their results, as we did not find any significant improvement of two-pointing discrepancies after changing the primary-beam reference frequency. We therefore assume that due to the longer on-source observing time in C-band C-array, any time-dependent primary-beam effects were averaged out to a sufficient degree, and adopt the primary-beam correction at the centre frequency of 6.0 GHz for these data.

5.1.2 Limiting the spatial frequency range

For a given observing frequency ν, the visibility function is sampled at spatial frequencies between $U_{\rm min} = \frac{\nu}{c} b_{\rm min}$ and $U_{\rm max} = \frac{\nu}{c} b_{\rm max}$, where $U = \sqrt{u^2 + v^2}$ is the *uv*-distance in wavelength units and b is the baseline length in the *uv*-plane. However, for a frequency band ranging from $\nu_{\rm min}$ to $\nu_{\rm max}$, only the spatial frequency range between $U_{\rm min}$ at $\nu_{\rm max}$ and $U_{\rm max}$ at $\nu_{\rm min}$ is overlapping for all frequencies in the band. Hence, if a resolved source with spectral structure is imaged at spatial frequencies below $U_{\rm min}$ at $\nu_{\rm max}$, emission at the largest spatial scales is

[4]For the mosaicking of the spectral index pointings we adopted a 50% primary- beam cutoff, which resulted in a smaller primary-beam overlap region than for the test images shown in Fig. 5.5 through 5.10, where a 20% cutoff was used.

measured only at the lowest frequencies of the band, so that at this low spatial frequency range there is progressively more flux missing as one moves to higher frequencies, which artificially steepens the spectrum measured at these scales. This bias towards steeper spectral indices can be avoided if data at spatial frequencies below U_{min} at ν_{max} are excluded from imaging by setting the `uvrange` parameter in `clean` accordingly. Even though applying an inner *uv*-taper, which is not yet implemented in `CASA` at the time of writing, would be more desirable than simply excluding the data in the respective *uv*-range, the fraction of data lost in this way is usually less than $\sim 3\%$ for the CHANG-ES data sets. On the other hand, according to Rau & Cornwell (2011), applying an upper limit to the imaged *uv*-range (corresponding to U_{max} at ν_{min}) is only necessary if the amplitude of a source changes by 100% or more across the frequency band, which is not the case for any of our data sets.
The C-band D-array and L-band C-array α maps resulting from the inner *uv*-cutoff are displayed in panels *d)* and *g)* of Fig. 5.1 and 5.2. Equal spatial frequency cutoffs were applied at both frequencies, to ensure that the same spatial scales are probed when comparing the two, i.e. the higher of the two U_{min} at ν_{max} values was adopted for both data sets of each galaxy. For both galaxies, this value is $U_{\mathrm{min}} = 0.8\,\mathrm{k}\lambda$ at ν_{max} of the C-band D-array data (the maximum spatial frequency is $\approx 21\mathrm{k}\lambda$ for L-band C-array and $\approx 24\mathrm{k}\lambda$ for C-band D-array). As expected, the overall spectral index distribution flattens considerably after applying the *uv*-cutoff. While previously the disk of NGC 891 showed L-band spectral indices steeper than -0.8 for the major part (panel *f)*), they are now mostly around -0.75, which seems more reasonable. In C-band, regions as flat as -0.5, which were previously confined to the mid-plane (panel *a)* and *b)*), are now found to be more extended in the *z*-direction. On the other hand, the *uv* limitation strengthens the effect of missing short spacings at the lower frequencies as opposed to the higher frequencies of the respective band, so that the MFS algorithm is more likely to fit extreme positive spectral indices in regions of low signal-to-noise. For NGC 891, this is particularly evident at the western edge of the L-band map and on both edges of the C-band map. Moreover, the *uv*-cutoff makes some of these edge artifacts blend into the disk almost seamlessly, such as in the region west of the galactic centre in the L-band map (Fig. 5.1 *g)*). Therefore it is unclear up to what vertical height the spectral index can still be considered realistic in such regions. From Fig. 5.3 *b)*, it is evident that even after a 30σ cutoff a large fraction of the halo now shows spectral indices comparable to those in the disk, or even flatter. For NGC 4565, the spectral flattening caused by the *uv*-cutoff does not affect the overall appearance of the spectral index maps and the scatter plot (Fig. 5.4 *b)*) as much as for NGC 891. This seems plausible considering that the disk of NGC 4565 shows structures on smaller scales that should be least affected by the *uv*-cutoff, while on the other hand emission detected at high *z*, where missing spacing effects would be visible in the fitted spectral indices, is comparatively weak and hence falls below our map cutoff levels. Especially the maps of the difference between the spectral index before and after applying the *uv*-cutoff (Fig. 5.1 *e)* and *h)*; Fig. 5.2 *e)* and *h)*) demonstrate that at least outside of the disk, this method generally does not yet provide correct spectral indices if missing short-spacings need to be added. We will return to this issue in Sect. 5.1.4.

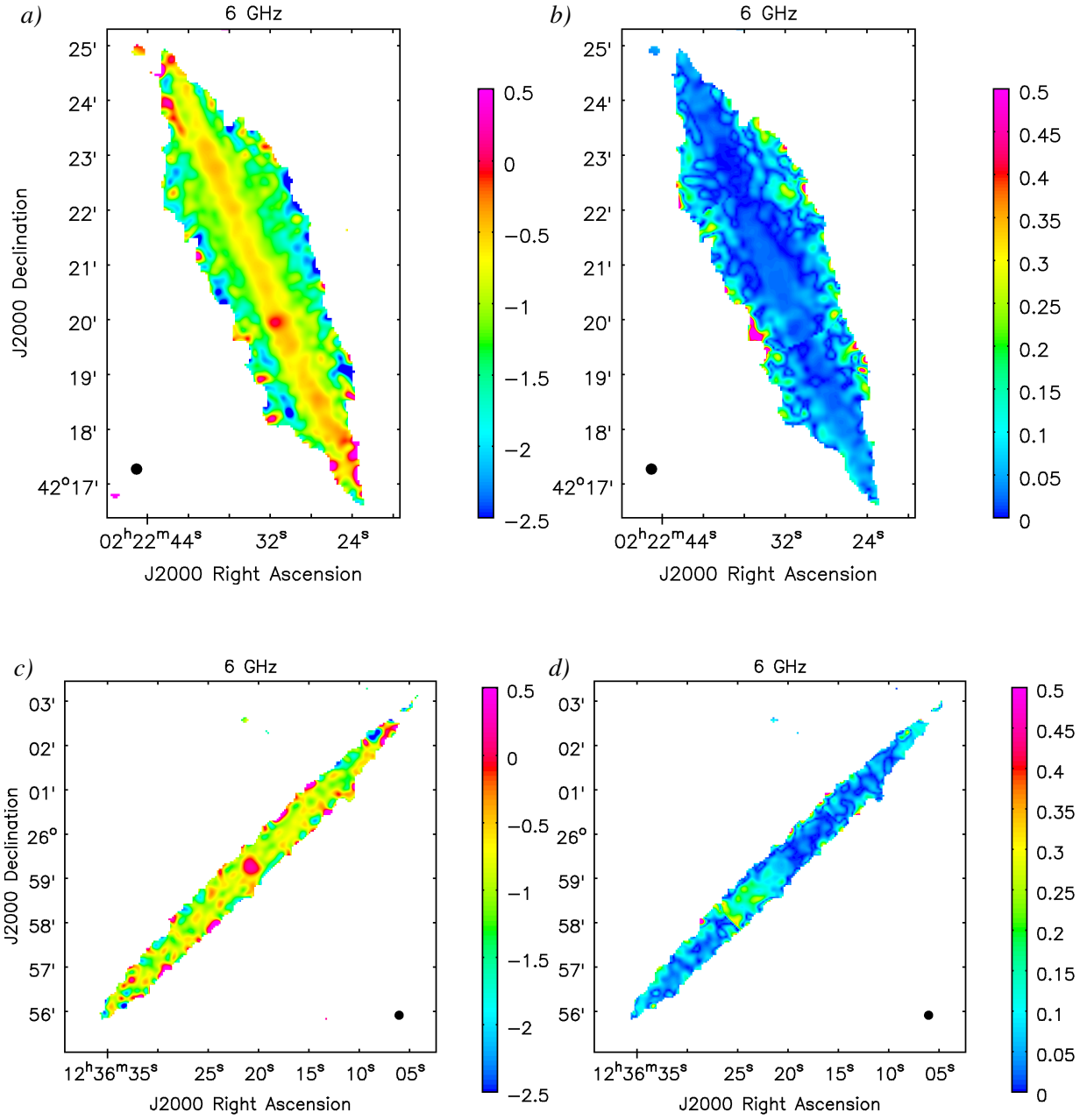

Figure 5.11: *a)*: Spectral index map of NGC 891 formed between the 5 and 7 GHz C-band D-array total power images. *b)*: Absolute difference between panel *a)* and the 6 GHz in-band spectral index map (Fig. 5.1 *b)*). *c)*: Spectral index map of NGC 4565 formed between the 5 and 7 GHz C-band D-array total power images. *d)*: Absolute difference between panel *c)* and the 6 GHz in-band spectral index map (Fig. 5.2 *b)*).

5.1.3 Comparison of MFS-generated and two-point spectral index maps at 6 GHz

Making use of the MFS technique to determine the spectral index also on larger angular scales than measured by the JVLA would require merging the JVLA data with wide-band single-dish data, which are not available to us for any of the two galaxies. As an alternative approach, we consider forming short-spacing corrected total power maps at the beginning (ν_1) and end (ν_2) of the frequency band, and computing the spectral index at the centre frequency in the "traditional" way, i.e. via Eq. 4.3. In the following, we call any maps computed in this fashion two-point spectral index maps.
First, to enable a direct comparison between this two-point method and the approach of fitting the spectrum using (MS-)MFS, we formed α maps at 5 GHz and 7 GHz from the C-band D-array data of both galaxies by performing the Taylor expansion about the respective frequency during deconvolution. Since we already employed the MS-MFS algorithm in this step, we implicitly also used it for calculating the two-point α maps, and hence only minor differences between the results of the two methods are expected. After smoothing all Taylor-term maps to 12″ (and before computing the two-point α maps), we carried out the primary-beam correction of the 5 GHz and 7 GHz maps using the model beam at 5.1 GHz and 7.5 GHz, respectively, which resulted in the best agreement of the two pointings in total intensity.
The resulting two-point α maps are shown in panels *a)* and *c)* of Fig. 5.11, while panels *b)* and *d)* display the difference to the MS-MFS-fitted α maps shown in panel *b)* of Fig. 5.1 and 5.2, respectively. Apart from the map edges, the differences in α are well below 0.1 in both galaxies. An exception (with differences up to ≈0.3) is the region west of the centre of NGC 4565, where we also found the largest deviations in α between the two pointings (compare Fig. 5.8 *a)*). Given the overall small differences between the two methods, we consider both to be equivalent, and therefore it seems justifiable to use the two-point method for computing the centre-frequency spectral index after missing short-spacings have been added.

5.1.4 Addition of missing short spacings

To obtain short-spacing corrected spectral index maps at 6 GHz, we scaled the 4.85 GHz Effelsberg maps to 5 and 7 GHz and merged them with the 5 and 7 GHz JVLA D-array maps, respectively, as already described in Sect. 3.4.8. For this, we used the JVLA maps with the applied 0.8 kλ *uv*-cutoff, since otherwise these images would still contain an unphysically steep-spectrum large-scale structure (see Sect. 5.1.2), which would furthermore introduce errors to the merging process. From the short-spacing corrected 5 and 7 GHz maps, the two-point α maps were then computed, which we adopt as the spectral index distribution at 6 GHz. The same was done for the non-thermal emission maps, obtained by computing the predicted thermal emission maps at 5 and 7 GHz (using the method described in Sect. 4.2) and subtracting these from the short-spacing corrected total emission images.

Since no single-dish observations are available for merging with our L-band data, we merge the total power maps produced by combined MFS-imaging of B-, C-, and D-array (again at

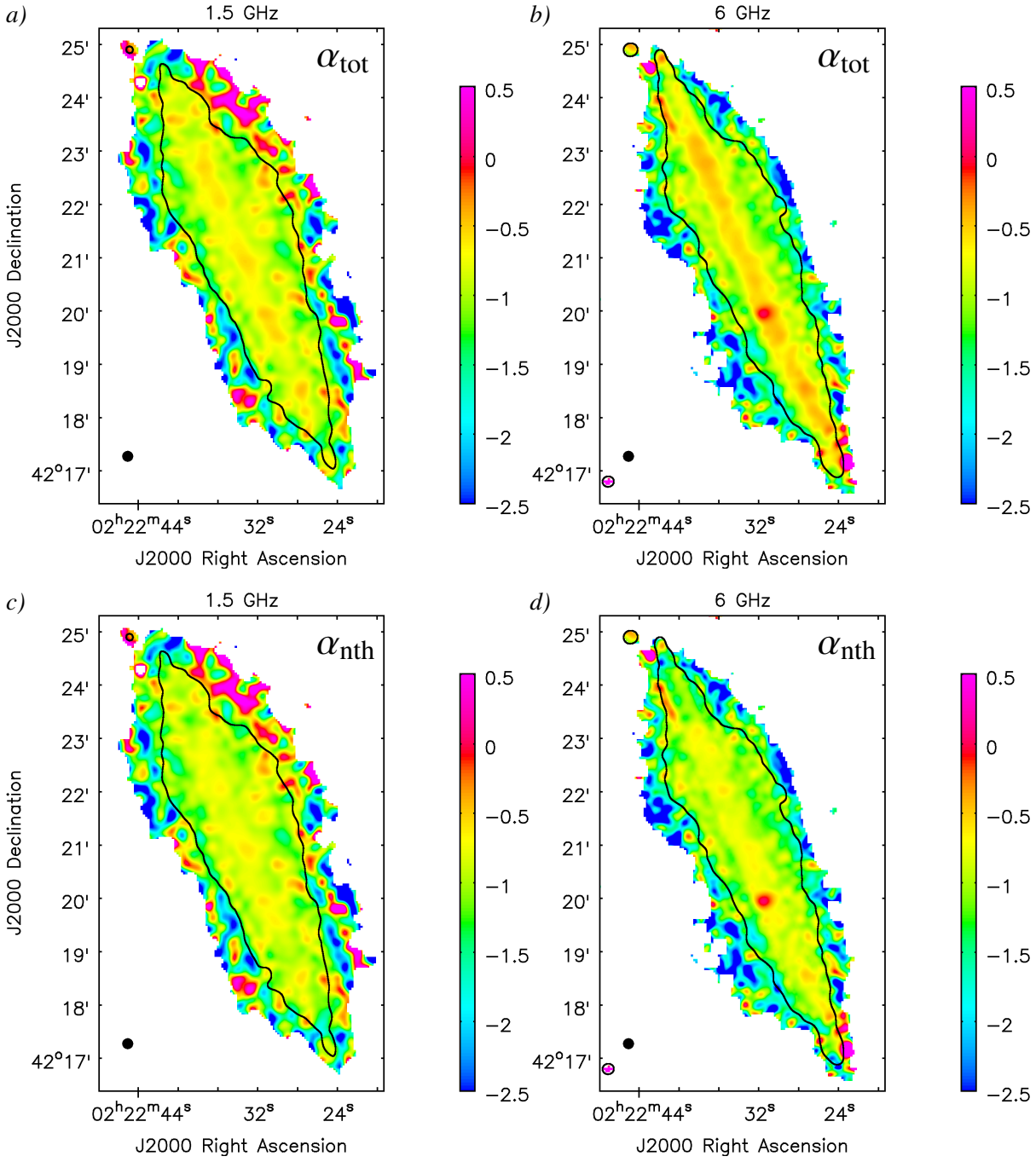

Figure 5.12: Short-spacing corrected total and non-thermal spectral index maps of NGC 891 at 1.5 and 6 GHz. *a)*: Total spectral index at 1.5 GHz. *b)*: Total spectral index at 6 GHz. *c)*: Non-thermal spectral index at 1.5 GHz. *d)*: Non-thermal spectral index at 6 GHz. The angular resolution in each panel is 12″. All maps extend to the 5σ level in the corresponding total power images. The black contours are placed at the 30σ level, where the maps were cut off before creating the scatter plots in Fig. 5.3 *c)* and *d)*. See text for more details.

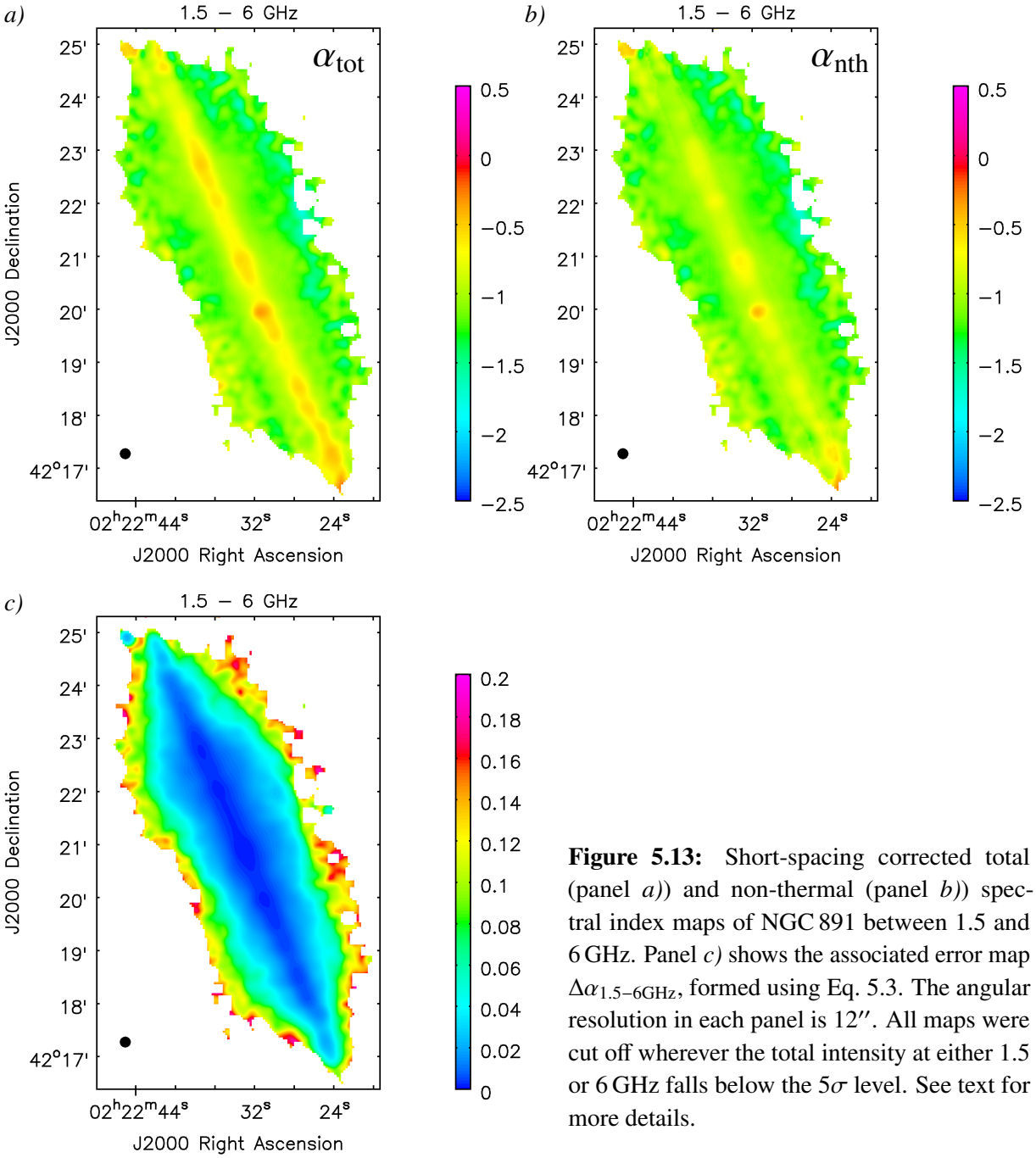

Figure 5.13: Short-spacing corrected total (panel *a)*) and non-thermal (panel *b)*) spectral index maps of NGC 891 between 1.5 and 6 GHz. Panel *c)* shows the associated error map $\Delta\alpha_{1.5-6\rm GHz}$, formed using Eq. 5.3. The angular resolution in each panel is 12″. All maps were cut off wherever the total intensity at either 1.5 or 6 GHz falls below the 5σ level. See text for more details.

12″ resolution) with the D-array-only maps (which contain the highest total flux densities), and likewise merge the second-Taylor-term maps I_1, to be able to compute the corresponding spectral index maps following Eq. 3.12. For the imaging of both the D-array and combined-array data we use a *uv*-cutoff at 0.25 kλ, which corresponds to $U_{\rm min}$ at $\nu_{\rm max}$ in D-array. For both galaxies, we found the resulting spectral index distribution to be only marginally steeper when applying no *uv*-cutoff. While this cutoff marginally strengthens the effect of missing short-spacings in terms of not detecting the outermost part of the halo (at least for NGC 4565, for which we obtain a fraction of ≈ 5% less in integrated flux density compared to the pure D-array map without *uv*-cutoff), it might actually counteract the missing spacings problem for the detected emission by the

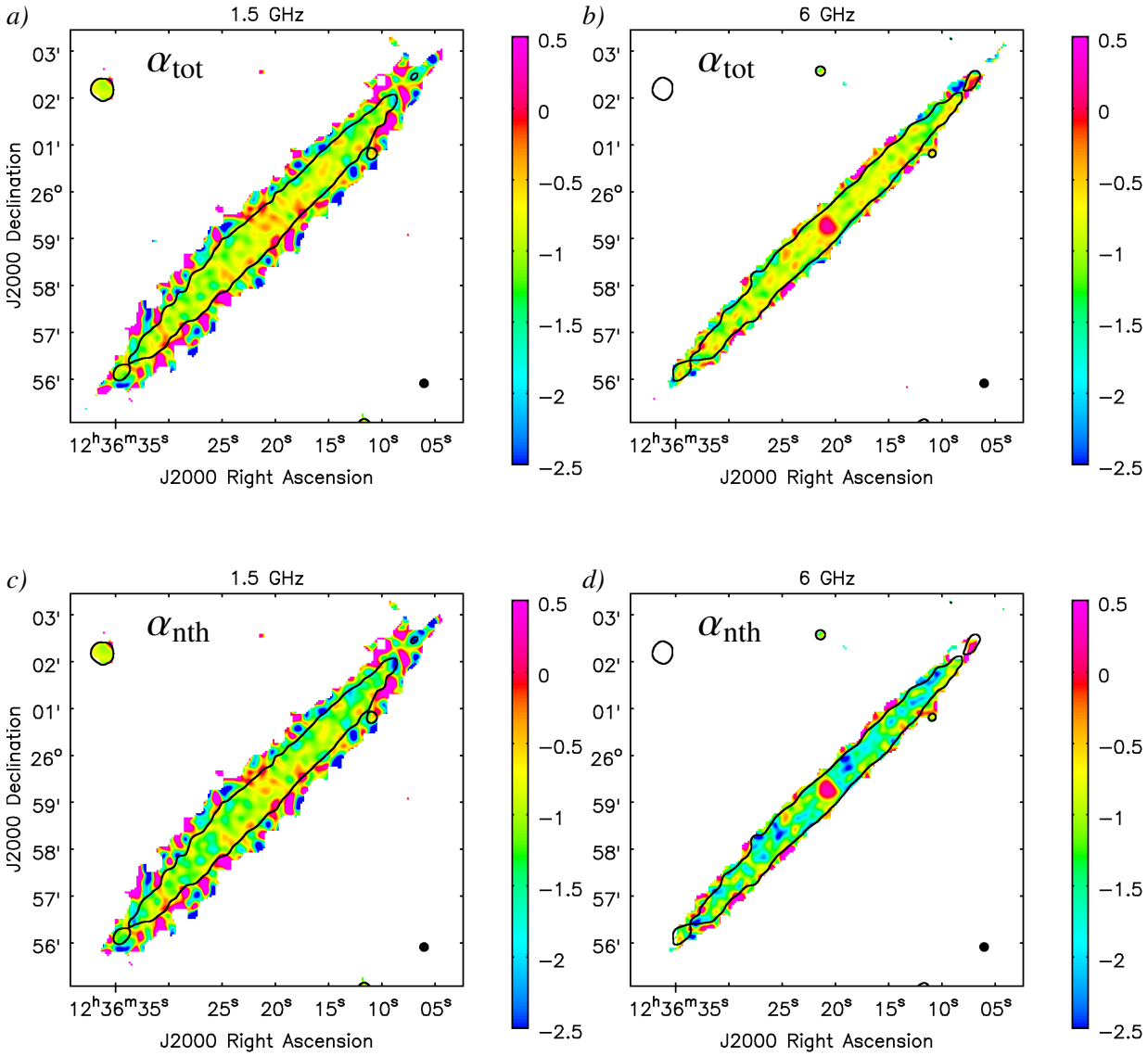

Figure 5.14: Short-spacing corrected total and non-thermal spectral index maps of NGC 4565 at 1.5 and 6 GHz. *a)*: Total spectral index at 1.5 GHz. *b)*: Total spectral index at 6 GHz. *c)*: Non-thermal spectral index at 1.5 GHz. *d)*: Non-thermal spectral index at 6 GHz. The angular resolution in each panel is 12″. All maps extend to the 5σ level in the corresponding total power images. The black contours are placed at the 20σ level, where the maps were cut off before creating the scatter plots in Fig. 5.4 *c)* and *d)*. See text for more details.

slight spectral flattening. Altogether, even if there is still some flux missing in our final L-band maps, we have at least performed a partial short-spacing correction compared to the C-array only map used in the above examples by including larger angular scales for deconvolution and adding the flux that is missing with respect to the pure D-array image. Since we use only JVLA data

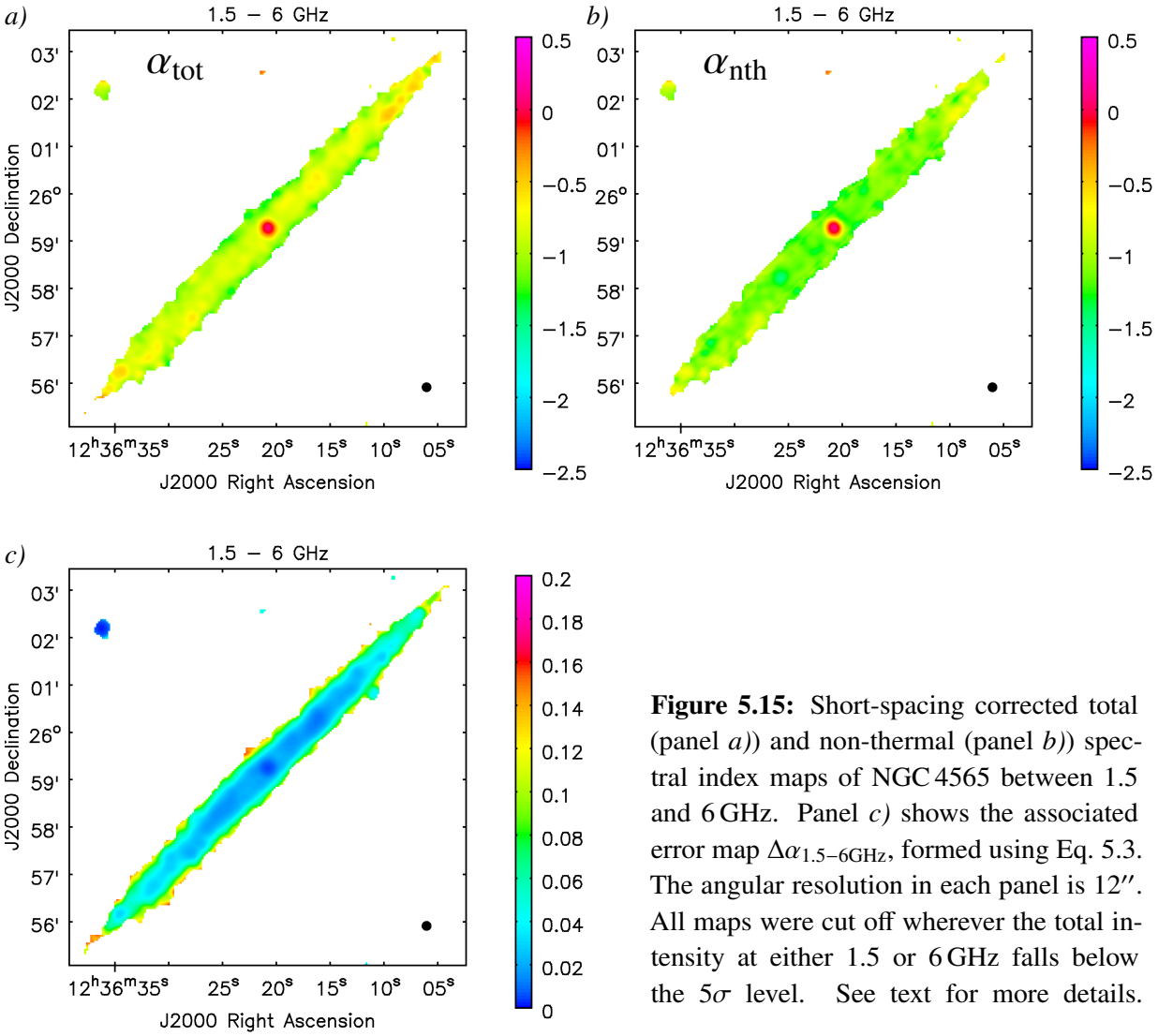

Figure 5.15: Short-spacing corrected total (panel *a)*) and non-thermal (panel *b)*) spectral index maps of NGC 4565 between 1.5 and 6 GHz. Panel *c)* shows the associated error map $\Delta\alpha_{1.5-6\rm GHz}$, formed using Eq. 5.3. The angular resolution in each panel is 12″. All maps were cut off wherever the total intensity at either 1.5 or 6 GHz falls below the 5σ level. See text for more details.

here, we can employ the short-spacing corrected first-order Taylor-term map to compute the non-thermal spectral index distribution from the thermal and non-thermal intensity maps:

$$\alpha_{\rm nth} = \frac{I_1 - \alpha_{\rm th} I_{0,\rm th}}{I_{0,\rm nth}}\,, \tag{5.2}$$

where $\alpha_{th} = -0.1$. Figures 5.12 and 5.14 display our final total and non-thermal α maps at 1.5 and 6 GHz, while Fig. 5.13 and 5.15 show two-point $\alpha_{1.5-6\rm GHz}$ maps formed between the short-spacing corrected 1.5 GHz and 6 GHz total power maps, and accordingly between their non-thermal counterparts. The errors of the two-point spectral index maps (panel *c)* of Fig. 5.13 and 5.15) were determined from the noise rms in the total intensity maps:

$$\Delta\alpha_{1.5-6\rm GHz} = \frac{\sqrt{\left(\frac{\sigma_{1.5\rm GHz}}{I_{1.5\rm GHz}}\right)^2 + \left(\frac{\sigma_{6\rm GHz}}{I_{6\rm GHz}}\right)^2}}{\ln\left(\frac{6\,\rm GHz}{1.5\,\rm GHz}\right)}\,, \tag{5.3}$$

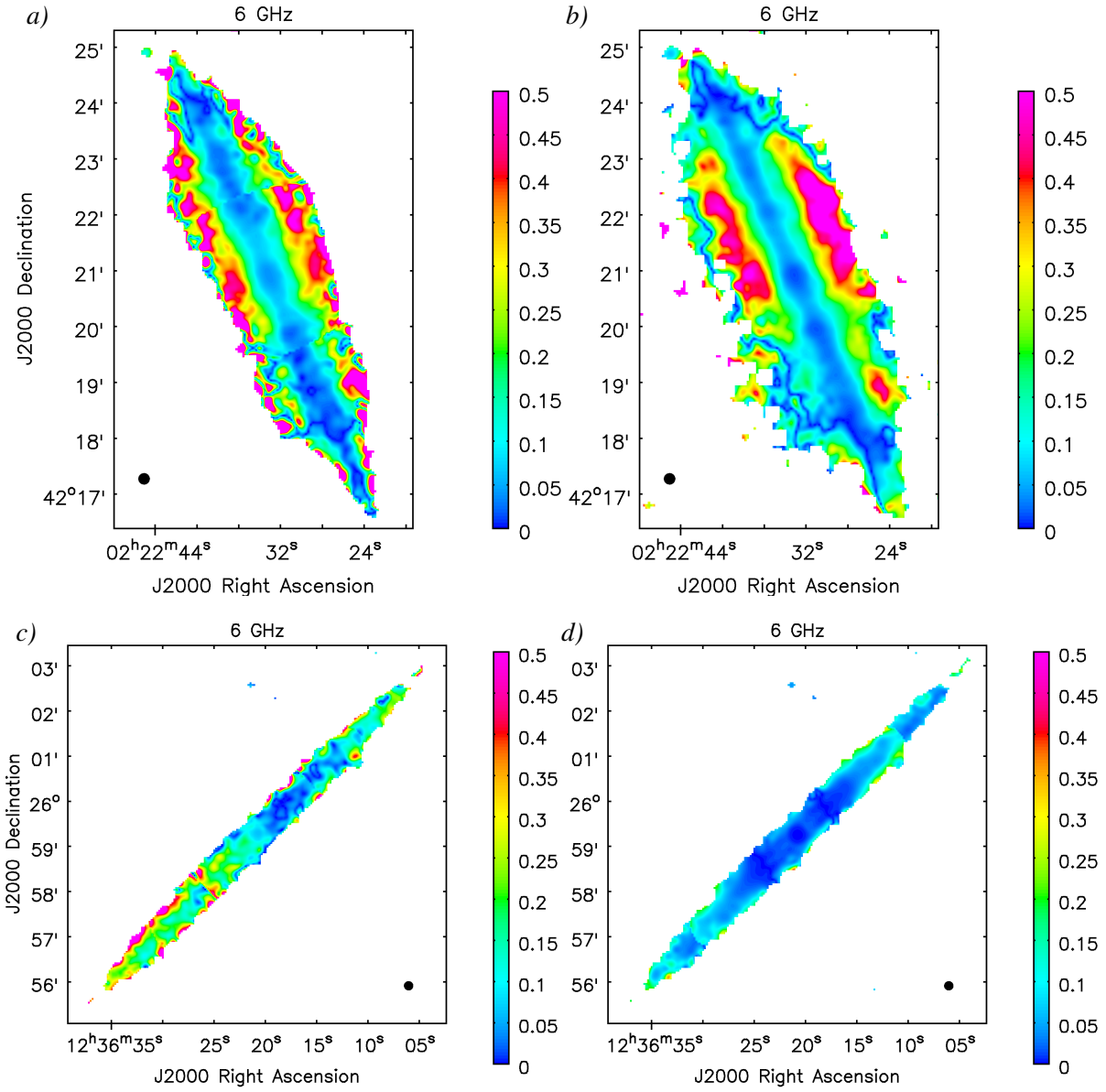

Figure 5.16: *a)*: Difference map between the 6 GHz total spectral index maps of NGC 891 after and before short-spacing correction and *uv*-cutoff (Fig. 5.12 *b)* − Fig. 5.1 *b)*). *b)*: Difference map between the short-spacing corrected 6 GHz total spectral index map of NGC 891 (Fig. 5.12 *b)*) and a short-spacing corrected map with no *uv*-cutoff applied to the JVLA data before merging them with the Effelsberg images. *c)*: Difference map between the 6 GHz total spectral index maps of NGC 4565 after and before short-spacing correction and *uv*-cutoff (Fig. 5.14 *b)* − Fig. 5.2 *b)*). *d)*: Difference map between the short-spacing corrected 6 GHz total spectral index map of NGC 4565 (Fig. 5.14 *b)*) and a short-spacing corrected map with no *uv*-cutoff applied to the JVLA data before merging them with the Effelsberg images.

where at 6 GHz we adopted the noise value of the pure JVLA maps, i.e. the $\Delta\alpha_{1.5-6\mathrm{GHz}}$ maps do not take account of the noise in the Effelsberg maps or any other errors introduced by the merging process.

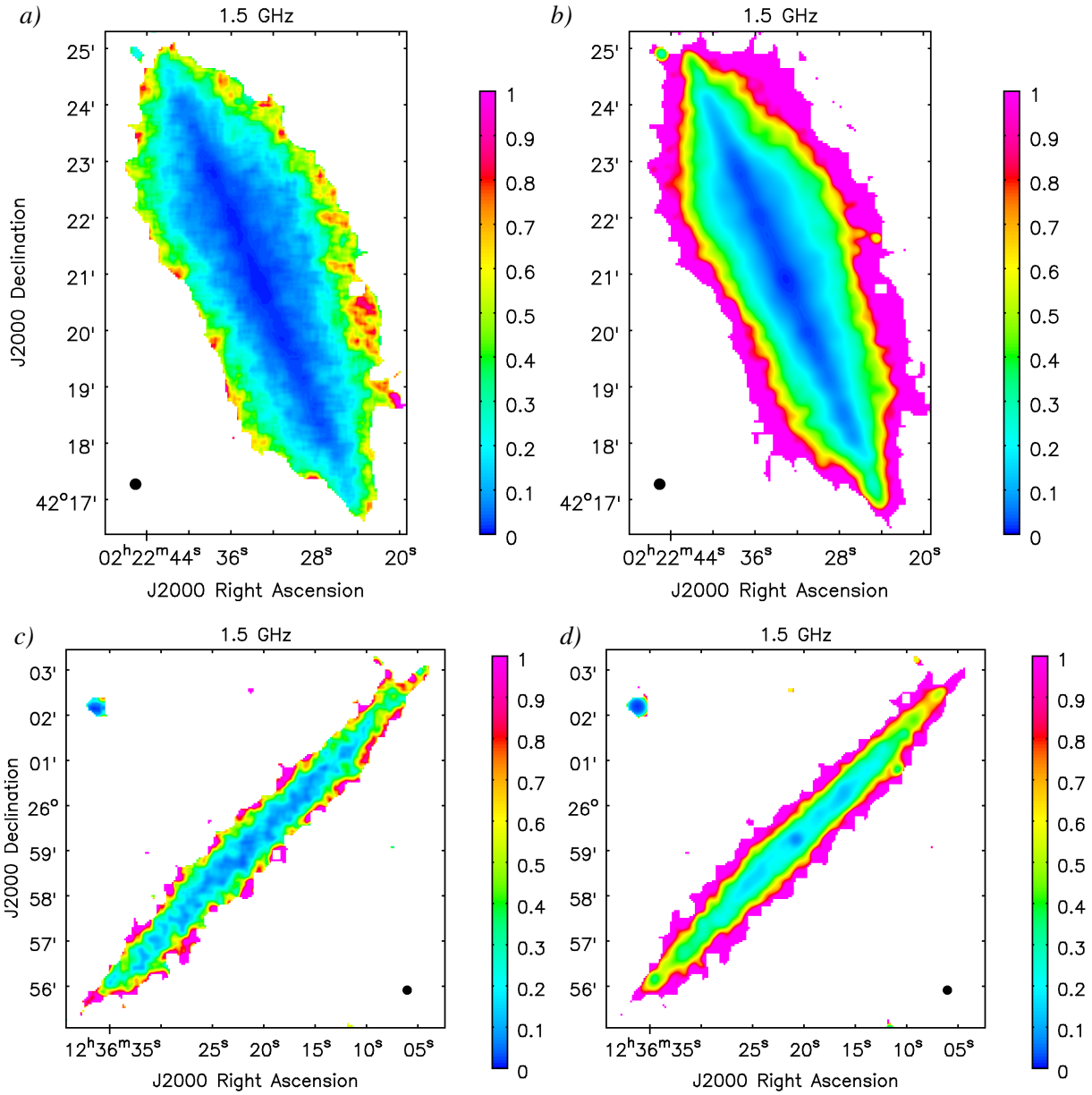

Figure 5.17: Spectral index error maps at 1.5 GHz. *a)*: $\Delta\alpha_{\mathrm{MFS}}$ map of NGC 891, i.e. the error map computed by the MS-MFS clean algorithm. *b)*: $\Delta\alpha_{\mathrm{C15}}$ map of NGC 891 obtained from the noise rms in the total power map using Eq. 5.5. *c)*: $\Delta\alpha_{\mathrm{MFS}}$ map of NGC 4565, i.e. the error map computed by the MS-MFS clean algorithm. *d)*: $\Delta\alpha_{\mathrm{C15}}$ map of NGC 4565 obtained from the noise rms in the total power map using Eq. 5.5.

Panels *a)* and *c)* of Fig. 5.16 show the difference of the 6 GHz spectral index before and after short-spacing correction and *uv*-cutoff. Similarly to Fig. 5.1 *e)* , in NGC 891 we find a rather sharp separation between disk and halo at $z \sim 2$ kpc, above which the differences increase rapidly, and hence the errors due to missing spacings become significant. Ignoring the outermost map

edges, we measure per-beam spectral index differences of up to ≈ 0.75. For NGC 4565, the intensity of the filled-in extended emission is for the most part still below our 5σ map cutoff, therefore we obtain only small α differences, except for the map edges and several regions in the south-eastern half of the disk. Here, the maximum beam-averaged difference is ≈ 0.4. The difference the *uv*-cutoff makes for the total spectral index at 6 GHz after short-spacing correction is shown for each galaxy in Fig. 5.16, panels *b)* and *d)* . For NGC 891, we see that this difference map bears a close resemblance to panel *a)*, which means that applying the *uv*-cutoff is of similar importance here as correcting for missing spacings. Still, Fig. 5.1 *d)* and *e)* prove that the *uv*-cutoff overcorrects for the bias of large-scale steepening if short spacings are not included. On the other hand, in NGC 4565 the *uv*-cutoff does not seem to play a major role after missing spacings have been added, but again a direct comparison to NGC 891 is difficult, as our short-spacing corrected data still do not allow to quantify spectral index uncertainties at larger heights in the halo of NGC 4565.

The short-spacing corrected total 1.5 and 6 GHz spectral index maps of NGC 891, as well as the corresponding scatter plot (Fig. 5.3 *c)*) indicate that the true spectral indices are generally flatter than those measured without applying any short-spacing corrections, however not as flat (especially at high z) as in the case where the *uv*-cutoff was applied but no missing spacings were added. Moreover, the overall scatter between the 1.5 and 6 GHz values has considerably decreased. For NGC 4565, as already observed in the above-mentioned difference maps, the newly obtained total spectral index distributions at both frequencies are still very similar to those with a *uv*-cutoff and no short-spacing correction.

5.1.5 Noise-induced spectral index errors

According to Condon (2015, hereafter C15), the error of the spectral index determined by a multi-channel least-squares fit over a frequency band ranging from $\nu_{\rm min}$ to $\nu_{\rm max}$ relates in the following way to the signal-to-noise ratio of the fit $(S/N)_{\rm f}$, for a source with $\alpha = -0.5$:

$$\Delta\alpha_{\rm C15} \cdot ({\rm S/N})_{\rm f} = \frac{\sqrt{12}}{\ln(\nu_{\rm max}/\nu_{\rm min})} \tag{5.4}$$

In Fig. 4 of C15, $\Delta\alpha_{\rm C15}\cdot({\rm S/N})_{\rm f}$ is plotted as a function of α for S-band observations ($\nu_{\rm min} = 2$ GHz, $\nu_{\rm max} = 4$ GHz), which has its minimum at $\Delta\alpha_{\rm C15} \cdot ({\rm S/N})_{\rm f} \approx 5.0$ for $\alpha = -0.5$. Figure 5 of C15 shows that the S/N of the image behaves similarly to $(S/N)_{\rm f}$, but with a small offset along each axis, such that in S-band $\Delta\alpha_{\rm C15} \cdot ({\rm S/N}) \approx 4.83$ for $-0.8 < \alpha < -0.5$ and $\Delta\alpha_{\rm C15} \cdot ({\rm S/N}) \approx 4.9$ for $\alpha = -1.3$. Consequently, we calculated alternative error maps

$$\Delta\alpha_{\rm C15} = \frac{\sqrt{12} \cdot 4.85/5}{({\rm S/N}) \cdot \ln(\nu_{\rm max}/\nu_{\rm min})} \tag{5.5}$$

for our short-spacing corrected L-band ($\nu_{\rm min} = 1.29$ GHz, $\nu_{\rm max} = 1.89$ GHz, after flagging) and C-band ($\nu_{\rm min} = 5$ GHz, $\nu_{\rm max} = 7$ GHz) spectral index maps. At 6 GHz, in the same way as for $\Delta\alpha_{1.5-6{\rm GHz}}$, the noise values of the purely interferometric maps were used, i.e. any single-dish related errors are not included. As evident from Fig. 5.17, for L-band $\Delta\alpha_{\rm C15}$ is consistently

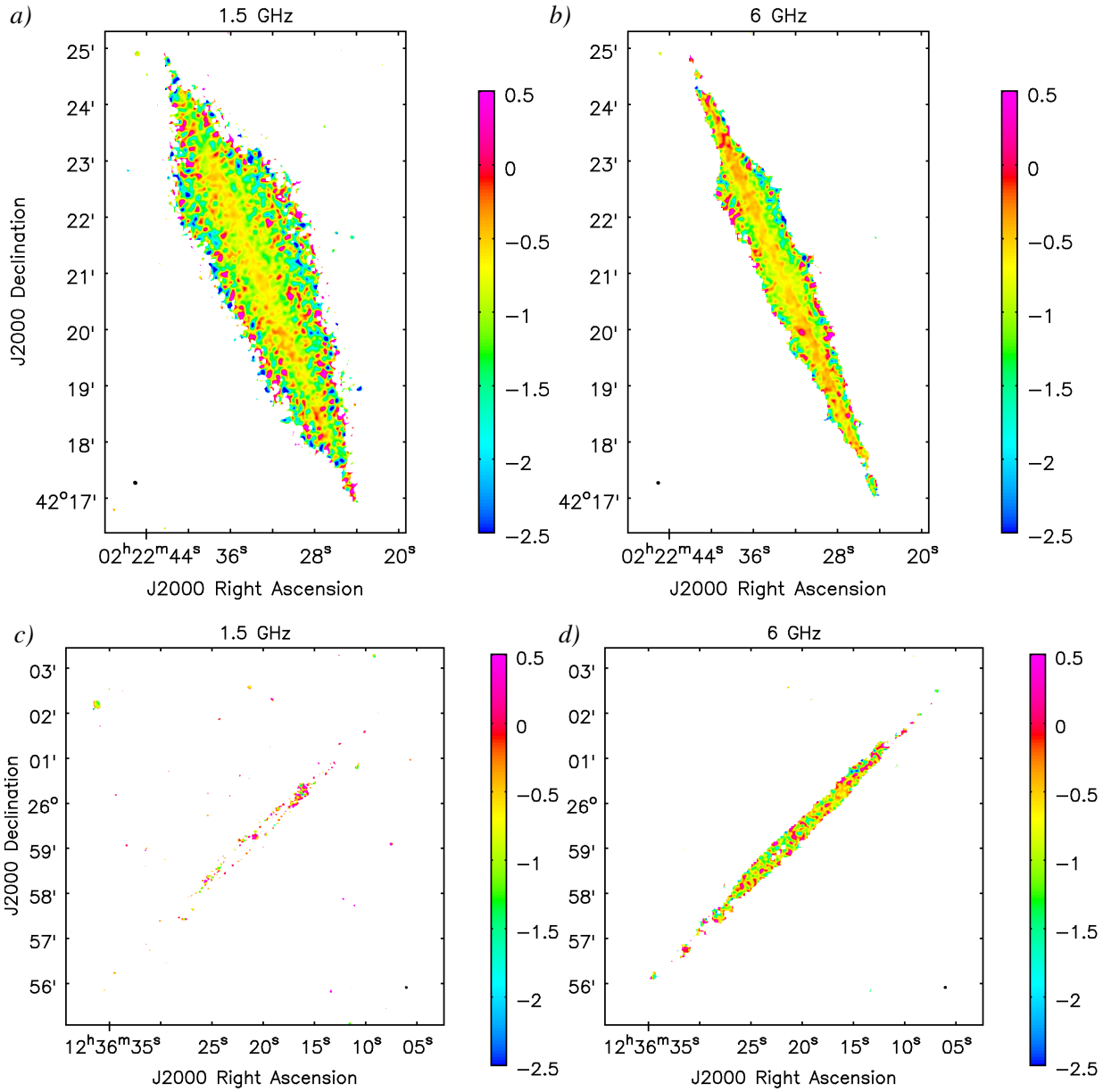

Figure 5.18: Total spectral index maps at high angular resolution. *a)*: 1.5 GHz map of NGC 891 at 4.4″ × 4.0″ resolution, obtained by simultaneous cleaning of the L-band B-, C-, and D-array data. *b)*: 6 GHz map of NGC 891 at 3.7″ × 3.6″ resolution, obtained by simultaneous cleaning of the C-band C- and D-array data. *c)*: 1.5 GHz map of NGC 4565 at 3.5″ × 3.2″ resolution, obtained by cleaning the L-band B-array data. *d)*: 6 GHz map of NGC 4565 at 3.8″ resolution, obtained by simultaneous cleaning of the C-band C- and D-array data. All maps were cut off at the 5σ level in the corresponding total power images. None of them have been corrected for missing short spacings.

higher than $\Delta\alpha_{\mathrm{MFS}}$, showing that noise errors are accounted for to a lesser degree in the latter maps. For NGC 891, we find the C-band $\Delta\alpha_{\mathrm{C15}}$ (Fig. 5.7 *f)*) to be in relatively close agreement

with the JVLA-only $\Delta\alpha_{\mathrm{MFS}}$ (Fig. 5.7 *e)*), possibly due to the higher S/N in the short-spacing corrected total power map. For NGC 4565 the fraction of added flux is significantly lower and hence $\Delta\alpha_{\mathrm{C15}}$ (Fig. 5.10 *f)*) is notably higher than $\Delta\alpha_{\mathrm{MFS}}$ (Fig. 5.10 *e)*) also at 6 GHz.

5.1.6 Smoothing out sub-beam spectral index variations

The usual procedure to form the clean image after deconvolution is to convolve the obtained clean-component model image with the restoring beam and then add the residual map. As a consequence of convolving the model image, pixel-to-pixel variations larger than those expected within the beam area can still occur in the clean image. While the overall appearance of the Taylor-term images themselves is usually not much affected by this, spectral index maps often do show significant sub-beam fluctuations, since they are formed by a pixel-by-pixel division of I_1/I_0. These spectral index fluctuations do not occur, however, if I_0 and I_1 are smoothed to a larger beam size prior to the division, which has been done, as stated above, for our low- and intermediate-resolution data. For the L-band B-array, L-band B+C+D-array (when not smoothing to 12″), and C-band C+D-array maps (all shown in Fig. 5.18), we desired to keep the high angular resolution given by the restoring beam; therefore it was necessary in these cases to smooth out any unphysical pixel-to-pixel variations in the spectral index maps. To achieve this, we artifically changed the beam FWHM in the header of these maps to the FWHM that would result in a Gaussian beam area equal to the respective pixel area, i.e. to $\theta_{header} = \theta_{pix}\sqrt{(4\ln 2)/\pi}$, and then smoothed the maps to the actual beam size of the image. Unlike the smoothing of intensity maps, which requires conservation of integrated flux densities, the purpose of this quasi-smoothing of spectral index maps is rather to average the pixel values over the beam area. Therefore, we convolve the images with a boxcar kernel instead of a Gaussian one, also since a Gaussian would introduce a bias towards lower (i.e. flatter) spectral indices. To obtain a kernel size that corresponds to the original Gaussian beam solid angle, the width of the boxcar kernel was set to the original Gaussian FWHM multiplied by $\sqrt{\pi/(4\ln 2)}$. Note that this procedure does not change the true angular resolution of the maps, but eliminates structures on scales smaller than the beam size.

We applied the same smoothing method to all MS-MFS error maps shown in this work, as the residual maps had not been smoothed beforehand (which would have produced wrong error maps) and hence the error maps are likewise affected by sub-beam fluctuations.

5.1.7 Sources of error: summary and conclusions

The above tests have shown that spectral index maps formed by the MS-MFS algorithm are prone to a variety of systematic uncertainties that can exceed the statistical errors of the spectral fit given by the `clean`- and `widebandpbcor`-generated $\Delta\alpha_{\mathrm{MFS}}$ maps. As can be easily seen by comparing our findings for NGC 891 with those for NGC 4565, these effects behave differently for different galaxies, and can therefore be generalized only to a limited extent. The different error sources and their significance for our observations can be summarized as follows:

- Depending on array configuration and observing frequency, the most important step to obtain meaningful results for the spectral index distribution in edge-on galaxies with large radio halos, such as NGC 891, consists in the addition of missing short spacings to interferometric data. As expected, the short-spacing problem induces the largest errors at high distances from the mid-plane (in our example of NGC 891 in C-band D-array up to ≈ 0.5 at the 50σ level), but even close to the mid-plane this effect is still larger than the statistical errors.

- Extreme spectral index values around map edges result not only from missing short spacings, but also from the inability of the MFS algorithm to perform stable spectral fits in regions of low signal-to-noise. These edge effects are often underestimated by the formal MFS-error maps, even though they likewise show increasing values towards their edges.

- Excluding data at short spatial frequencies that are not measured across the entire frequency band is necessary to avoid large-scale artificial steepening of in-band spectral indices. However, in case the effect of missing short spacings is significant, this procedure would overcorrect for the steepening if no short-spacing correction is performed.

- Provided that short-spacing corrections have been carried out successfully in case of strong halo emission, the largest source of uncertainty in the spectral index determination at frequencies around 6 GHz relates to the time- and direction-dependent shape of the primary beam pattern. When applying the NRAO-provided standard primary-beam models, this causes spectral index errors to increase substantially with distance from the pointing centre. For NGC 891, we found that beyond the 70% primary-beam level of either pointing at 6 GHz (i.e. at distances greater than $2'.25''$ from the respective pointing centre) the MS-MFS-based error maps typically underestimate the primary-beam induced errors *in the disk* by a factor ~5, while in the halo both errors are roughly comparable. At 1.5 GHz, however, we assume this effect to be negligible, since neither of our two galaxies extends beyond the 70% level at this frequency.

  By using the primary-beam model at 6.25 GHz (NGC 4565) and 6.6 GHz (NGC 891) for the correction of the 6.0 GHz maps, the differences between the two pointings in spectral index could be minimized, and thus a rough correction for model inaccuracies could be achieved. At least for NGC 891, the remaining errors based on the pointing differences are comparable to the MS-MFS statistical errors.

- The measured spectral index distribution can vary between different observations of the same pointing, e.g. due to differences in *uv* coverage. Tests carried out by Wiegert et al. (2015) for galaxies that CHANG-ES observed in two separate SBs (at the same sky pointing) revealed differences between the two observations of around 5% (in terms of rms values across the α maps), which is typically about 20% higher than the MS-MFS-based errors (up to 50% in high signal-to-noise regions). Apart from different *uv* distributions, also residual cleaning artifacts may cause spectral index differences larger than the individual MS-MFS error maps would indicate.

- Also the noise-based spectral index errors as given by Condon (2015) generally turn out to be higher than the MS-MFS-based errors. While for NGC 4565 at 6 GHz, the errors

due to missing short spacings are almost negligible compared to the noise-based $\Delta\alpha_{\rm C15}$ errors, $\Delta\alpha_{\rm dev}$ (i.e. the error arising from the difference between the two pointings) is higher than $\Delta\alpha_{\rm C15}$ throughout most of the south-eastern side of this galaxy, even after changing the frequency of the primary-beam model. Conversely, in the north-western half, $\Delta\alpha_{\rm dev} < \Delta\alpha_{\rm C15}$. While the reason for this asymmetry in $\Delta\alpha_{\rm dev}$ is still unclear, the global rms values of these two error maps are in relatively good agreement. Altogether, we regard the $\Delta\alpha_{\rm C15}$ maps for both galaxies as the best representation of the (primarily statistical) spectral index errors that remain after short-spacing- and improved primary-beam corrections have been applied.

- We found the two-point spectral index between the edge frequencies of a given band to be roughly equivalent to the MS-MFS spectral index map, at least in case this map as well as the two total power maps used to form the two-point map are determined by an MS-MFS fit over the same frequency range. In C-band, we have to opt for the two-point method to be able to compute short-spacing corrected spectral index maps.
- In case the Taylor-term images have not been smoothed to a larger beam size before forming spectral index maps, these often contain variations on scales smaller than the beam area. Such artifacts can be eliminated by artificially setting the beam size in the header of the spectral index maps equal to the pixel size, and subsequently convolving the maps with a boxcar kernel equivalent to the original restoring beam.

5.2 Final spectral index maps

In this section, we describe details as well as global characteristics of our short-spacing- and primary-beam-corrected (using the revised method) spectral index maps presented in Fig. 5.12-5.15 (and also provide a brief note on the high-resolution spectral index maps shown in Fig. 5.18).

5.2.1 NGC 891

NGC 891, as mentioned earlier in this chapter, shows a regular pattern of rather flat mid-plane spectral indices (Fig. 5.12-5.13) and, when viewed on large scales, monotonic steepening of the spectra with increasing vertical height. An outstanding feature in the $\alpha_{\rm 6GHz}$ and $\alpha_{\rm 1.5–6GHz}$ maps is the radio supernova SN 1986J at RA = $02^h22^m31^s.32$, Dec = $42°19'57''.26$ (Bietenholz et al. 2010), with a spectral index at its centre of ≈ 0.0 at 6 GHz and ≈ -0.5 at 1.5 GHz. The total spectral index in the mid-plane region of NGC 891 is considerably flatter at 6 GHz than at 1.5 GHz, due to a higher contribution of thermal emission at the higher frequency. Around the edges, all in-band[5] spectral index maps are contaminated by erroneously computed extreme α values, both positive (or unnaturally flat) and negative. We are able to exclude these edge

[5] In the following, we also refer to our final 6 GHz α maps as in-band maps, even though strictly speaking they are a kind of hybrid between in-band and two-point spectral index maps.

artifacts from our further analysis to a satisfactory extent by clipping our α maps at the 30σ level, as we already did in the previous steps before creating scatter plots. Though not as extreme as in the in-band maps, also the two-point spectral index turns out relatively flat near the map edges, especially in the south-eastern quadrant, where $\alpha_{1.5-6\mathrm{GHz}}$ reaches values around -0.7, which otherwise only appear in the mid-plane. In consideration of the corresponding errors given by Fig. 5.13 *c)* and Eq. 5.3, this flattening at high z would still be significant. Note, however, that this error map does not account for the uncertainties of the spectral fitting, which also affect the total intensity maps used for calculating $\alpha_{1.5-6\mathrm{GHz}}$. Neither does it include any potential errors arising from the combination with single- dish data at 6 GHz. Apart from this, the small fraction of still missing flux in the 1.5 GHz total intensity image might also contribute to these flat values. While apart from said edge peculiarities the total and non-thermal $\alpha_{1.5-6\mathrm{GHz}}$ maps have a fairly regular appearance and seem to correlate tightly with the respective intensity distributions, we observe somewhat higher local variations in the in-band maps. Still, the overall scatter between $\alpha_{1.5\mathrm{GHz}}$ and $\alpha_{6\mathrm{GHz}}$ has been substantially reduced after applying short-spacing corrections, as can be seen from Fig. 5.3 *c)* and *d)*. At 6 GHz, the spectral index distribution in the disk takes on a somewhat more fragmented appearance after the rather coherent thermal component is subtracted (Fig. 5.12 *d)*), while in the 1.5 GHz map a similarly fragmented disk shape is present already before the thermal subtraction (Fig. 5.12 *a)*). Around the mid-plane, the non-thermal spectral index values turn out to be in close agreement at both frequencies, which indicates that we found a realistic estimate of the thermal contribution in the disk. But especially outside of the disk, the in-band maps often show strong variations from one resolution element to the next (i.e. small compact regions and narrow filaments of flat spectral index next to steep-spectrum "holes"), which are however not well-correlated between the two frequencies or with the $\alpha_{1.5-6\mathrm{GHz}}$ map, and are hence unlikely to be real. In particular, whereas $\alpha_{1.5-6\mathrm{GHz}}$ stays flatter than -1.3 throughout most of the galaxy, much steeper values (even above our 30σ cutoff level) are reached in *both* the 1.5 and the 6 GHz in-band map, which seems highly unphysical. On the other hand, we also find $\alpha_{6\mathrm{GHz}}$ to be still somewhat flatter than $\alpha_{1.5-6\mathrm{GHz}}$ throughout the disk after thermal subtraction, which is likewise inconsistent with the expected shape of the non-thermal spectrum. While we cannot rule out that we simply underestimated the thermal contribution in this galaxy, we found that in order to achieve $\alpha_{6\mathrm{GHz}} \approx \alpha_{1.5-6\mathrm{GHz}}$ for the major part of the disk, unnaturally high thermal intensities are required, such that in some regions the thermal fraction of the total emission would be close to 100%. It is therefore more likely that the observed discrepancy is related to uncertainties in the spectral index between 4.85 and 8.35 GHz, which we used for scaling the Effelsberg data at 4.85 GHz to C-band frequencies (see Sect 3.4.8).

Filamentary extensions of flat or moderately steep spectral index sticking out of the disk are present in all cases, but their α values and positions in the in-band maps are rather unreliable for the above reasons. In the two-point maps (both total and non-thermal), however, where we measure $\alpha_{1.5-6\mathrm{GHz}} \approx -1$ for most of these features, they correlate well with the diffuse Hα emission, as can be seen from Fig. 5.19. Prime examples are the region in the north-east quadrant, where two such extensions line up very well with two HII filaments, and another filament located slightly north-west of the centre. Also, an apparent bifurcation of the disk at its northern edge is observed, which shows up most prominently in $\alpha_{6\mathrm{GHz}}$. Here, the disk seemingly splits up into two long filaments, with $\alpha_{6\mathrm{GHz}}$ in the eastern filament being flatter than elsewhere in the disk (with the exeption of SN 1986J). While this bifurcation may well be just another edge artifact,

and the spectral index in the eastern part is unlikely to be as flat as in the 6 GHz map, we find that this feature would be aligned with another Hα filament if the latter were more extended (the possibility that part of this filament falls below the detection limit of the Hα observation cannot be ruled out). Moreover, we observe a correlation of $\alpha_{1.5-6\mathrm{GHz}}$ with bright compact HII regions, however (just like in total power) for the most part with slight positional offsets.

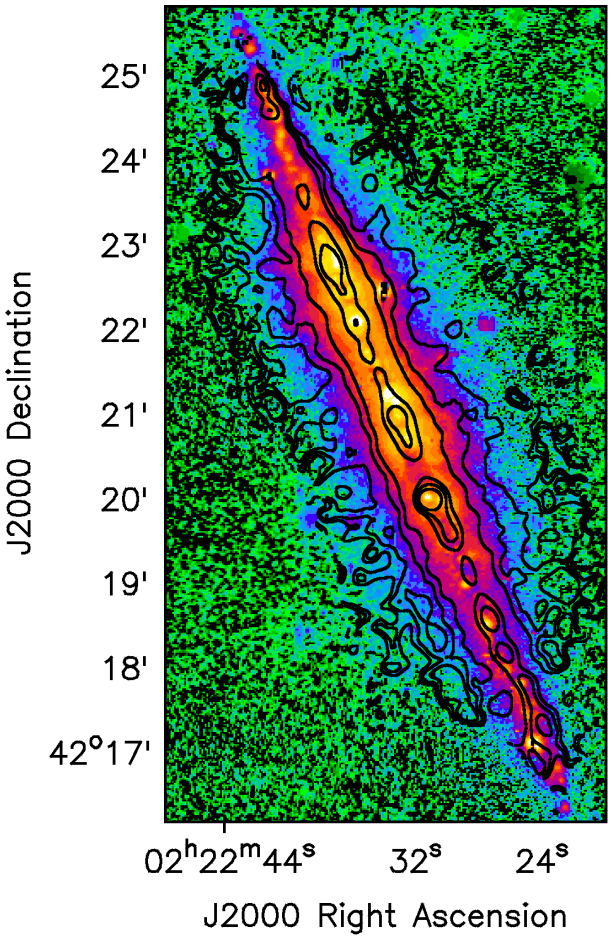

Figure 5.19: Hα image of NGC 891 (Rand et al. 1990) overlaid with contours of the short-spacing corrected non-thermal spectral index map between 1.5 and 6 GHz (Fig. 5.13 *a)*). Contours are placed at $\alpha_{1.5-6\mathrm{GHz}} = -1.2, -1.1, -1.0, -0.8, -0.7, -0.6$.

The high-resolution $\alpha_{1.5\mathrm{GHz}}$ and $\alpha_{6\mathrm{GHz}}$ maps (Fig. 5.18 *a)* and *b)*, respectively), like the corresponding total power maps, show the existence of a thin disk component that is not resolved in the 12″ images. Again, as one would expect, many small-scale features are present in these maps, however it is hardly possible to tell real structures apart from random variations, especially since the signal-to-noise ratio is even lower at these high resolutions. These spectral index maps will not be used for the remaining analysis in this work, since we do not have any FIR data at the same resolution available to derive a corresponding estimate for the distribution of thermal emission, and also since we did not apply any short-spacing corrections.

5.2.2 NGC 4565

Contrary to NGC 891, where a relatively clear distinction between disk and halo is visible in the spectral index distribution, only a very small portion of the halo is covered by our spectral index maps of NGC 4565 (Fig. 5.14-5.15), as in this galaxy low S/N values are already reached at small z heights. In the in-band spectral index maps, the disk does not appear as a single coherent structure like in NGC 891, and is instead characterized almost entirely by seemingly random local variations, which is not true for the maps of $\alpha_{1.5-6\mathrm{GHz}}$. We find the standard deviation measured within larger regions in the in-band maps to be close to the average value in the corresponding $\Delta\alpha_{\mathrm{C15}}$ maps. In addition, $\alpha_{1.5\mathrm{GHz}}$ and $\alpha_{6\mathrm{GHz}}$ are basically uncorrelated on small scales. From these findings, we conclude that the local spectral index fluctuations are primarily artifacts arising

from the low S/N and therefore large spectral fit uncertainties. While the radio luminosity of NGC 4565 is much lower than that of NGC 891 to begin with, also the fact that NGC 4565 is somewhat less inclined than edge-on reduces the S/N by a small amount, since the disk is resolved along its projected minor axis. As mentioned earlier, the ring-shaped structure seen in total intensity is also clearly identifiable in the total $\alpha_{6\mathrm{GHz}}$ map, in the form of elongated flat-spectrum regions. Apart from this and the flat spectal index in the nucleus, no correlation between the in-band maps and total power is observed. Also for this galaxy, the total $\alpha_{6\mathrm{GHz}}$ is flatter on average than $\alpha_{1.5\mathrm{GHz}}$, owing to the spectral behaviour of the thermal component.

Ignoring the noise-based fluctuations in the in-band spectral index maps, both total and non-thermal spectra in NGC 4565 are found to be steeper overall than in the disk of NGC 891. In particular, as also clearly reflected by the scatter plots in Fig. 5.4 *c)* and *d)*, in NGC 4565 $\alpha_{6\mathrm{GHz}}$ is considerably steeper than $\alpha_{1.5\mathrm{GHz}}$ after subtracting the thermal contribution, whereas in the disk of NGC 891 we measure similar non-thermal spectral indices at both frequencies. Even the non-thermal $\alpha_{1.5-6\mathrm{GHz}}$ map shows values as steep as in the lower halo (≈ -1.2) over a large portion of the disk. These remarkable differences between the non-thermal spectra of the two galaxies appear to be a direct consequence of their very different SFR surface densities, as we will discuss further below. Lastly, Fig. 5.20 shows that most of the flatter regions in the total $\alpha_{1.5-6\mathrm{GHz}}$ map coincide with compact HII regions, which is not the case for the in-band maps.

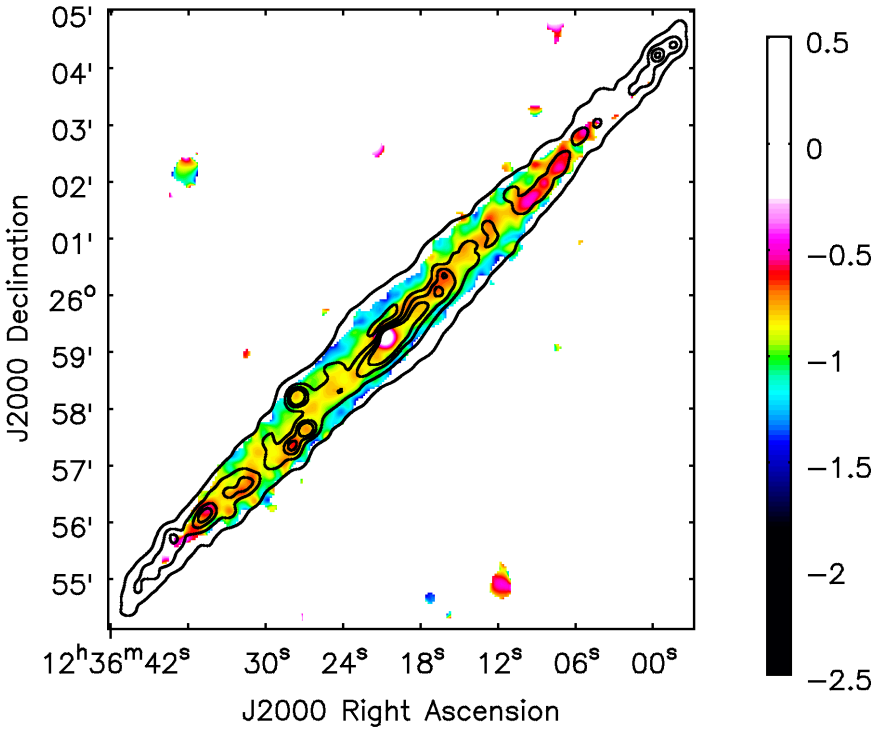

Figure 5.20: Short-spacing corrected total spectral index map of NGC 4565 between 1.5 and 6 GHz (same as in Fig. 5.15 *a)*), overlaid with contours of the KPNO Hα image. Contours are placed at the 20, 100, 200, and 300σ levels.

Even more so than for NGC 891, the high-resolution in-band spectral index maps of NGC 4565 (Fig. 5.18 *c)* and *d)*) are dominated by random fluctuations, and therefore do not provide any reliable information on the small-scale spectral distribution. The 1.5 GHz map[6] even has such a low S/N that only the inner ring is left after clipping the map at the 5σ level. At 6 GHz, by

[6] At 1.5 GHz, we show the pure B-array spectral index map instead of the combined B+C+D-array map, as for the latter we only achieved an angular resolution similar to that of C-array (see Table 3.5).

recomputing the combined C+D-array map after smoothing the associated total power maps to 12″ and adding missing short spacings, it would be possible to improve the S/N over that of the short-spacing-corrected D-array-only map. However, we do not expect this to result in any significant changes in the measured spectral index distribution. For the same reasons as in the case of NGC 891, we will not consider these high-resolution α maps any further in this thesis.

5.3 Spectral aging models

Having determined the spatially resolved non-thermal spectral index distribution at two well-separated frequencies, it is possible to put constraints on the shape of the spectrum for a given line of sight. The CRE spectral energy distribution, and thus the shape of the emisson spectrum (and its evolution with time), depends on the CRE injection process (i.e. the injection spectral index and injection time scale) and their energy loss rate, which in turn depends on the magnetic field strength and on the distribution of their pitch angles with respect to the magnetic field lines (see Eq. 2.14). The pitch angle distribution determines the form of the spectral break characterized by the break energy $E_{\rm br}$ and the corresponding frequency $\nu_{\rm br}$. Here, the standard theory distinguishes between two models for a single epoch of particle injection: the Kardashev-Pacholczyk (KP) model (Kardashev 1962; Pacholczyk 1970), where the individual electrons maintain their original pitch angles, and the Jaffe-Perola (JP) model (Jaffe & Perola 1973), in which the pitch angles vary continuosuly between $\theta = 0°$ and $\theta = 90°$ on time scales much shorter than the radiation time scale, whereby an isotropic distribution of pitch angles is generated. In both models, a constant, homogeneous, and spatially uniform magnetic field is assumed.

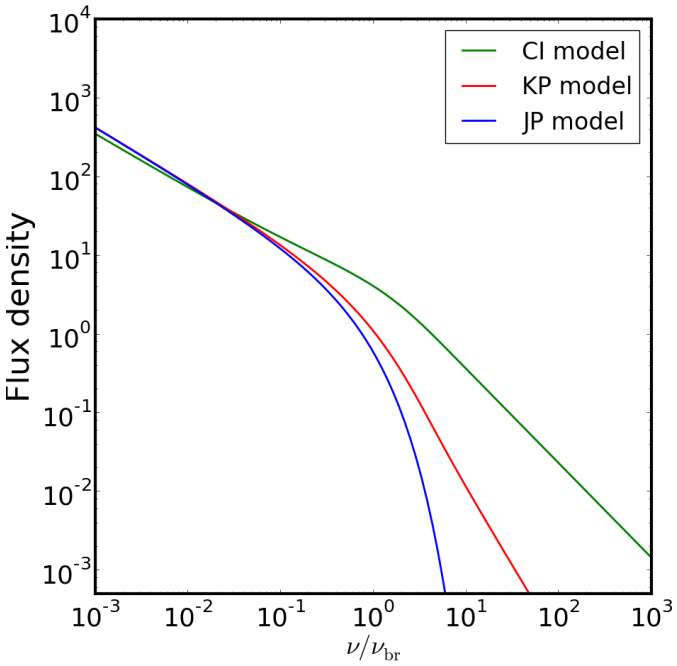

Figure 5.21: Synchrotron spectra as predicted by the CI, KP, and JP spectral aging models. The normalization in flux density is arbitrary, while the frequency axis is normalized by the break frequency $\nu_{\rm br}$.

The KP and JP model represent two special cases regarding the break energy of a single particle. Since for the KP model the pitch angle θ of each electron is time-independent, we can write Eq. 2.16 as

$$E_{\rm br,KP}^{-1}(t) = C_E(B^2 \sin^2\theta + B_{\rm IC}^2)(t - t_0)\ , \tag{5.6}$$

whereas in the JP model, due to the rapid continuous pitch angle randomization, the energy loss of each particle is the average loss over all possible pitch angles ($0° \leq \theta \leq 90°$), and thus

$$E_{\mathrm{br,JP}}^{-1}(t) = C_E(B^2\langle\sin^2\theta\rangle + B_{\mathrm{IC}}^2)(t - t_0) = C_E \cdot \frac{2}{3}(B^2 + B_{\mathrm{IC}}^2)(t - t_0)\ , \tag{5.7}$$

which means that there is effectively no pitch angle dependence, and hence the energy loss rate (Eq. 2.14) depends only on the particle energy itself, so that CREs at high energies always lose their energy more rapidly than those at low energies. This behaviour leads to an exponential cutoff in the spectrum at the break frequency, as shown further below.

Neglecting inverse-Compton losses ($B_{\mathrm{IC}} = 0$), we obtain

$$E_{\mathrm{br,KP}}(\theta = 90°) = \frac{2}{3}E_{\mathrm{br,JP}}\ , \quad E_{\mathrm{br,KP}}(\theta = 0°) = \infty\ , \tag{5.8}$$

i.e. for the KP model there is a fraction of high-energy CREs that lose their energy more slowly than in the JP model, due to their constantly low pitch angles. As a consequence, the spectrum cuts off less steeply than in the JP case. The analytical form of the synchrotron spectrum for the different models is specified in the following, where we additionally consider a model describing continuous injection (CI) of CREs (Pacholczyk 1970). The following equations 5.9-5.15 are presented in the form given by Murgia (1996), however with the form factor $F(x)$ approximated as $F(x) \propto (\nu/\nu_{\mathrm{c}})^{1/3} \cdot \exp(-\nu/\nu_{\mathrm{c}})$ (Pohl et al. 1991). A graphic illustration of the CRE spectrum for all three cases is given in Fig. 5.21.

5.3.1 The Kardashev-Pacholczyk (KP) model

Ignoring inverse-Compton losses, the shape[7] of the synchrotron spectrum for the KP model is given by

$$I_{\mathrm{KP}}(\nu) \propto \int_0^{\pi/2}\int_0^{1/\sin^2\theta}\left(\frac{\nu}{\nu_{\mathrm{br,KP}}\sin\theta\, x^2}\right)^{1/3}\exp\left(\frac{\nu}{\nu_{\mathrm{br,KP}}\sin\theta\, x^2}\right)x^{\mathrm{g}}\,(1 - x\sin^2\theta)^{-g-2}\sin^2\theta\,\mathrm{d}x\,\mathrm{d}\theta\ , \tag{5.9}$$

where $x = E/E_{\mathrm{br,KP}}$, and $E_{\mathrm{br,KP}}$ and $\nu_{\mathrm{br,KP}}$ have been chosen as the break energy and frequency for $\theta = 90°$, as the population of CREs with $\theta = 90°$ dominates the received synchrotron radiation.

For $\nu \ll \nu_{\mathrm{br,KP}}$ the KP spectrum is a power law with spectral index $\alpha_{\mathrm{inj}} = (g + 1)/2$, and for $\nu \gg \nu_{\mathrm{br,KP}}$ the spectrum declines as a power law with spectral index $4/3\alpha_{\mathrm{inj}} - 1$:

$$I_{\mathrm{KP}}(\nu) \propto \begin{cases} \left(\dfrac{\nu}{\nu_{\mathrm{br,KP}}}\right)^{\alpha_{\mathrm{inj}}} & \nu \ll \nu_{\mathrm{br,KP}} \\ \left(\dfrac{\nu}{\nu_{\mathrm{br,KP}}}\right)^{4/3\alpha_{\mathrm{inj}}-1} & \nu \gg \nu_{\mathrm{br,KP}} \end{cases} \tag{5.10}$$

[7] The precise expression for the synchrotron spectrum includes for each model a generally time-dependent normalization factor, which we do not specify though, as for the comparison of the models with our observations (Sect. 5.4) only the shape of the spectrum matters.

5.3.2 The Jaffe-Perola (JP) model

For the JP model, the synchrotron spectrum has the form

$$I_{\mathrm{JP}}(\nu) \propto \int_0^{\pi/2} \int_0^1 \left(\frac{\nu}{\nu_{\mathrm{br,JP}} \sin\theta\, x^2} \right)^{1/3} \exp\left(\frac{\nu}{\nu_{\mathrm{br,JP}} \sin\theta\, x^2} \right) x^{\mathrm{g}} \, (1-x)^{-g-2} \sin^2\theta \, \mathrm{d}x \, \mathrm{d}\theta \,, \tag{5.11}$$

with $x = E/E_{\mathrm{brJP}}$. In the $\nu \ll \nu_{\mathrm{br,JP}}$ limit, also the JP spectrum is a power law with spectral index α_{inj}, whereas for $\nu \geq \nu_{\mathrm{br,JP}}$ it cuts off exponentially:

$$I_{\mathrm{JP}}(\nu) \propto \begin{cases} \left(\dfrac{\nu}{\nu_{\mathrm{br,JP}}} \right)^{\alpha_{\mathrm{inj}}} & \nu \ll \nu_{\mathrm{br,KP}} \\ \left(\dfrac{\nu}{\nu_{\mathrm{br,JP}}} \right)^{\alpha_{\mathrm{inj}}} \cdot \mathrm{e}^{-\nu/\nu_{\mathrm{br,JP}}} & \nu \geq \nu_{\mathrm{br,KP}} \end{cases} \tag{5.12}$$

5.3.3 The continuous injection (CI) model

While the KP and JP models describe the evolution of the spectrum after a single injection event and hence only apply to an ensemble of particles that have the same spectral age, we now look at the case of ongoing supply of new particles at a constant injection rate. The CI model spectrum has the following shape:

$$I_{\mathrm{CI}}(\nu) \propto \int_0^{\pi/2} \int_0^{\infty} \left(\frac{\nu}{\nu_{\mathrm{br,CI}} \sin\theta\, x^2} \right)^{1/3} \exp\left(\frac{\nu}{\nu_{\mathrm{br,CI}} \sin\theta\, x^2} \right) x^{\mathrm{g}-1} \, J(x,g) \sin^2\theta \, \mathrm{d}x \, \mathrm{d}\theta \,, \tag{5.13}$$

where $x = E/E_{\mathrm{brCI}}$, E_{brCI} is given by Eq. 2.16, and

$$J(x,g) = \begin{cases} 1 - (1-x)^{-g-2} & x < 1 \\ 1 & x \geq 1 \end{cases} \tag{5.14}$$

Like for the other models, the asymptotic behaviour for $\nu \ll \nu_{\mathrm{br,CI}}$ is a power law with spectral index α_{inj}. For $\nu \gg \nu_{\mathrm{br,CI}}$, the spectrum is still a power law, but with a spectral index of $\alpha_{\mathrm{inj}} - 0.5$ (and thus less steep than for the single-shot injection models):

$$I_{\mathrm{CI}}(\nu) \propto \begin{cases} \left(\dfrac{\nu}{\nu_{\mathrm{br,CI}}} \right)^{\alpha_{\mathrm{inj}}} & \nu \ll \nu_{\mathrm{br,CI}} \\ \left(\dfrac{\nu}{\nu_{\mathrm{br,CI}}} \right)^{\alpha_{\mathrm{inj}}-0.5} & \nu \gg \nu_{\mathrm{br,CI}} \end{cases} \tag{5.15}$$

While for $\nu < \nu_{\mathrm{br,CI}}$ the normalization of the spectrum increases linearly in time, the spectrum is stationary for $\nu > \nu_{\mathrm{br,CI}}$, as the number of CREs transitioning from $E > E_{\mathrm{br,CI}}$ to $E < E_{\mathrm{br,CI}}$ is exactly compensated by the number of newly injected CREs at $E > E_{\mathrm{br,CI}}$. The pitch angle distribution of the injected CREs, as given by the KP or JP model, does affect the normalization as well as the position of the spectral break at a given point in time, however the shape of the CI spectrum is independent of whether KP or JP electrons are injected.

5.4 Comparing predictions of spectral aging models to the observed spectral index distribution

To help interpreting the scatter plots of our measured non-thermal spectral indices at 1.5 and 6 GHz, we constructed synthetic KP, JP, and CI spectra for different choices of break frequency $\nu_{\rm br}$ and injection spectral index $\alpha_{\rm inj}$. For diffusive shock acceleration (see e.g. Blandford & Eichler 1987), the injection spectral index depends on the Mach number M as $\alpha_{\rm inj} = -(M^2+3)/(2M^2-2)$. The Mach number in turn is proportional to the inverse of the sound speed and thus to the square root of the gas density ($M \propto \sqrt{\rho}$). This usually leads to an expected range of $\alpha_{\rm inj}$ values between -0.8 and -0.5.
In Fig. 5.3 *d)* and 5.4 *d)* we show the trajectories in $\alpha_{1.5\rm GHz}$-$\alpha_{6\rm GHz}$ space that the different models predict for an injection spectral index of -0.5, -0.7, and -0.8. Moving from flatter to steeper $\alpha_{1.5\rm GHz}$ and $\alpha_{6\rm GHz}$ values along these trajectories corresponds to a decrease in $\nu_{\rm br}$ and hence a forward movement in time, which in turn means an expected increase in z for edge-on galaxies.

As in the CI model a maximum difference between $\alpha_{1.5\rm GHz}$ and $\alpha_{6\rm GHz}$ is reached at $\nu_{\rm br} = 3.75$GHz, we find for both galaxies that the majority of data points below the 1:1 line (i.e. where a spectral steepening between 1.5 and 6 GHz is observed) cannot be explained by a continuous injection process, but are reproduced well by the KP and JP models. For NGC 891, the maximum steepening among the plotted data points corresponds to $\nu_{\rm br} \approx 5$ GHz for the JP model and $\nu_{\rm br} \approx 1.5$ GHz for the KP model. In NGC 4565, of the three standard models only the JP model matches the points of maximum steepening, which are found at $\nu_{\rm br} \approx 3$ GHz.
For edge-on galaxies, a significant occurrence of spectral index differences incompatible with continuous injection are a rather unexpected finding. While in more face-on galaxies, injection rates along a given line of sight are expected to be lower than the typical synchrotron loss rates, and therefore single-shot injection models are more likely to serve as a valid explanation for strong spectral steepening (Basu et al. 2015), in edge-on galaxies the line-of-sight injection rates that result from the supernova rates in the underlying disk should be considerably higher, which rather suggests a CI scenario.

In NGC 891, spectral indices steeper than ≈ -1.3 above the 30σ level seem hardly plausible (at least at 1.5 GHz), as we pointed out earlier on the basis of the two-point spectral index map. If we ignore all α values steeper than -1.3 in Fig. 5.3 *d)* , the remaining data points are roughly consistent with the CI model within their errors, with $\alpha_{\rm inj}$ lying in the typically expected range between -0.8 and -0.5. When ignoring only $\alpha_{1.5\rm GHz} < -1.3$, most of the remaining points at steeper $\alpha_{6\rm GHz}$ are still found in that same range of $\alpha_{\rm inj}$ if a KP or JP model is considered. Note that the error bars plotted in Fig. 5.3 *d)* and 5.4 *d)* are based on the $\Delta\alpha_{\rm C15}$ maps, which represent only statistical errors and thus do not account for any residual errors related to primary-beam correction, short-spacing correction, or uncertainties in estimating the thermal contribution.

Even though for NGC 4565 the noise-induced spectral index errors are quite large, a clear trend towards stronger steepening between the two frequencies than in NGC 891 is seen, especially considering that all data points shown in Fig. 5.4 *d)* are still located in the disk of the galaxy. As previously indicated, this trend is already evident by comparing the non-thermal two-point spectral index maps of the two galaxies, which are affected much less by uncertainties than the

corresponding in-band maps. As a consequence of the large spectral index differences, the data points in the scatter plot predominantly conform to the JP and KP models. Considering that NGC 4565 has an extremely low SFR surface density of $\Sigma_{\mathrm{SFR}} = 0.73 \cdot 10^{-3} \mathrm{M}_{\odot} \mathrm{yr}^{-1} \mathrm{kpc}^{-2}$, and unless we severely overestimated the thermal emission component, it is very likely that in this galaxy the CRE injection rates are lower than the synchrotron loss rates, which would explain why the spectra are best described by models for single-epoch injection. While the somewhat lower inclination of 86° is indeed expected to have an effect on the line-of-sight CRE injection rates, it is certainly not the primary cause of the observed spectral steepening, particularly since we are resolving the disk in no more than three beams perpendicular to its major axis. We infer from this that the injection rates are intrinsically low in NCC 4565. We will continue discussing the seemingly different behaviour of the two galaxies in terms of spectral aging effects in Chapter 8.

Lastly, it should be noted that the above analysis of our spectral index measurements is rather rudimentary, since we have data at only two observing frequencies available. More detailed modelling of the synchrotron spectra would require measurements at several additional frequencies. Since reliable in-band spectral index maps demand exceptionally high quality in terms of S/N and *uv*-coverage, also traditional two-point spectral index maps formed between sufficiently separated frequency pairs should be utilized for this purpose. Moreover, we emphasize that the standard spectral aging models considered here are not necessarily the most appropriate ones to describe the overall synchrotron radiation in normal galaxies. For instance, the KP model happens to be valid in SN shock fronts rather than in the general ISM. In particular, the JP and KP model represent the two extreme cases of an isotropic and maximally anisotropic pitch-angle distribution, whereas in reality also intermediate cases are expected to occur. A range of more sophisticated models exist, e.g. incorporating the diffusion of electrons between regions of different magnetic field strength (Tribble 1993; Eilek et al. 1997). If radio data of high enough quality are used, such models may facilitate a more accurate description of CRE energy losses in galactic disks and halos.

6 Cosmic-ray transport in the halo

The following chapter focusses on the quantification of the vertical emission distribution in NGC 891 and NGC 4565, along with the analysis of CR propagation away from the galactic plane. Since the observed vertical extent of galactic halos is always determined by the sensitivity of the observation, a more meaningful characterization of the size of synchrotron halos is found in the (exponential or Gaussian) scale heights of the vertical emission profiles. The angular resolution of our images allows us to measure scale heights at various positions along the major axis, and hence to improve on previous studies of this kind for both galaxies (Dumke 1997; Krause 2009). In particular, this is one of the first studies which uses maps corrected for the thermal emission component to determine scale heights.
Assuming energy equipartition between the CRs and the magnetic fields, we generate maps of the total magnetic field strength for both galaxies. Based on the the vertical profiles of the synchrotron intensity at 1.5 and 6 GHz as well as of the spectral index between the two frequencies, and using the obtained information on magnetic field strengths, we are able to model the CR transport in NGC 891 by solving the one-dimensional diffusion-loss equation. As NGC 4565 only features a relatively faint halo component, modelling the CR propagation is currently not feasible for this galaxy, meaning that observations of still higher sensitivity are required.

6.1 Synchrotron scale heights

6.1.1 Fitting of vertical intensity profiles

To determine scale heights of the radio continuum emission of NGC 891 and NGC 4565, we follow the approach described initially by Dumke et al. (1995). The observed vertical distribution of the emission is the intrinsic distribution convolved with the observing beam (and is furthermore affected by the inclination of the galaxy, s.b.). An exact deconvolution is not possible, therefore an exponential vertical distribution

$$w_{\mathrm{exp}}(z) = w_0 \exp\left(-z/h\right) \tag{6.1}$$

or a Gaussian distribution

$$w_{\mathrm{gauss}}(z) = w_0 \exp\left(-z^2/h^2\right) \tag{6.2}$$

with peak intensity w_0 and scale height h is assumed, which is convolved with the Gaussian telescope beam

$$g(z) = \frac{1}{\sqrt{2\pi\sigma^2}} \exp\left(-z^2/2\sigma^2\right), \tag{6.3}$$

where $2\sqrt{2\ln 2}\cdot\sigma$ is the beam FWHM. The convolved emission profile has the form

$$W_{\exp}(z) = \frac{w_0}{2} \exp\left(-z^2/2\sigma^2\right) \left[\exp\left(\frac{\sigma^2 - zh^2}{\sqrt{2}\sigma h}\right)^2 \operatorname{erfc}\left(\frac{\sigma^2 - zh^2}{\sqrt{2}\sigma h}\right) + \exp\left(\frac{\sigma^2 + zh^2}{\sqrt{2}\sigma h}\right)^2 \operatorname{erfc}\left(\frac{\sigma^2 + zh^2}{\sqrt{2}\sigma h}\right) \right] \tag{6.4}$$

in case of an exponential intrinsic distribution, where erfc is the complementary error function, defined as

$$\operatorname{erfc} x = \frac{2}{\sqrt{\pi}} \int_x^\infty \exp\left(-r^2\right) \mathrm{d}r\,. \tag{6.5}$$

For a Gaussian intrinsic distribution, the convolution yields

$$W_{\text{gauss}}(z) = \frac{w_0 h}{\sqrt{2\sigma^2 + h^2}} \exp\left(-z^2/(2\sigma^2 + h^2)\right). \tag{6.6}$$

The normalization w_0 and intrinsic scale height h of such distributions are determined by least-squares fits to the data. As yet, exponential profiles have been found to best describe the vertical intensity distribution in edge-on galaxies, in most cases consisting of the superposition of two exponential components, representing a thin disk and a thick disk or halo distribution[1]. Using exponential models is motivated by the assumption of pressure equilibrium between different layers of relativistic electrons that are gravitationally bound to the disk. As an exception to this, the vertical distribution of NGC 4594 (Krause et al. 2006) was found to be fitted better by a Gaussian model, presumably owing to its dominant central bulge component.
For inclinations of $i < 90°$, using the σ value of the observing beam in Eq. 6.4 or 6.6 will result only in an upper limit for h, as in this case the vertical distribution is intrinsically narrower than the one observed in projection. To take this inclination effect into account and thus obtain deprojected scale heights, an effective beam size larger than the telescope beam is determined (see below), to be used for the convolution given by Eq. 6.4 or 6.6.

We determined vertical intensity profiles using the short-spacing corrected 1.5 and 6 GHz images at 12″ resolution, from which we had already removed background sources close to the galaxies (as well as the supernova SN 1986j in NGC 891 and the central source of NGC 4565) before measuring integrated flux densities (see Sect. 4.1). The NOD3 task `BoxModels` was used to measure vertical profiles at different positions along the major axis of each galaxy and perform the fitting procedure described above. `BoxModels` computes the integrated flux density within rectangles of equal width Δr in major-axis direction and equal vertical height Δz, arranged in a gapless rectangular grid covering the bulk of the visible disk and halo emission. In each case, the centre of this grid was set to coincide with the galaxy centre. In both galaxies, we sampled the vertical distribution in steps of $\Delta z = 5''$, which is somewhat smaller than half the beam FWHM

[1] Different terminologies for the two components have been used in the literature over the decades. Some authors refer to them as a thin disk and a thick disk, while in other publications they are called disk and halo component. We decide to use the latter terms throughout this work.

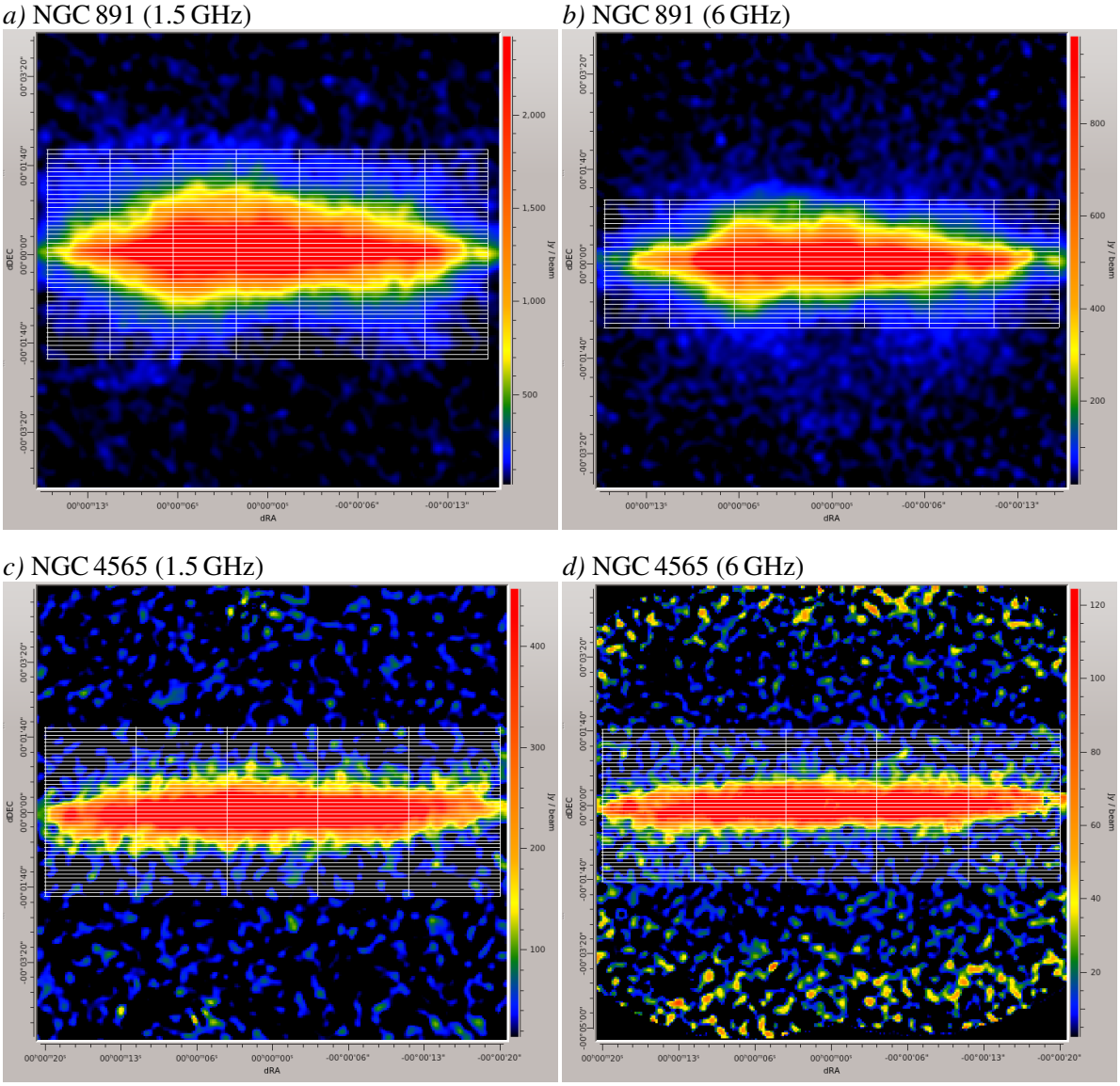

Figure 6.1: Placement of integration boxes for the determination of scale heights (NOD3 task `BoxModels`). For each vertical column (containing n boxes of width Δr and height Δz) a z-profile was fitted. *a)*: NGC 891 (1.5 GHz): $\Delta r = 3.1$ kpc, $\Delta z = 220$ pc, $n = 47$. *b)*: NGC 891 (6 GHz): $\Delta r = 3.1$ kpc, $\Delta z = 220$ pc, $n = 27$. *c)*: NGC 4565 (1.5 GHz): $\Delta r = 6.9$ kpc, $\Delta z = 290$ pc, $n = 45$. *d)*: NGC 4565 (6 GHz): $\Delta r = 6.9$ kpc, $\Delta z = 290$ pc, $n = 41$.

and corresponds to 0.22 kpc at the distance of NGC 891 and 0.29 kpc in case of NGC 4565. To investigate the behaviour of the scale heights along the major axis of NGC 891, we used seven columns of width $\Delta r = 3.1$ kpc, while for NGC 4565, due to its much lower S/N, we chose five columns with $\Delta r = 6.9$ kpc. The grid of sampling boxes constructed in this way is illustrated for each galaxy in Fig. 6.1. For NGC 891 at 6 GHz (panel *b)*) we had to use less boxes in z-direction than usual, as the emission of the galaxy appears to be superimposed on a plateau of extended emission at very low intensities (see Fig. 6.7). This artifact may have been caused by inaccuracies in interpolating the Effelsberg map from 4.85 to 6 GHz. If we had not excluded

these outer regions from the vertical fitting process, they would have artificially broadened our fitted model profiles.
While running `BoxModels`, the effective beam size is automatically computed. To this end, the programme first generates a Gaussian function the total width of which corresponds to the length of the major axis out to ≈2 times the (user-specified) rms noise in the map. The x-axis of this Gaussian is compressed by multiplication with $\cos i$. The compressed Gaussian, which represents the minor-axis intensity distribution, is then convolved with the observing beam. The FWHM of this convolved distribution is adopted as the effective beam size. However, this is only strictly the case at the centre of the major axis, and the effective beam becomes smaller towards the outer edges of the major axis, where it is again equal to the observing beam. `BoxModels` takes this behaviour into account by computing individual effective beam sizes at each specified major-axis position.
As already noted by various authors, describing the vertical emission distribution clearly requires two-component models for both galaxies. We found the vertical profiles of NGC 891 to be represented much better by two-component exponentials than by two-component Gaussians. Exponential models were also used by Dahlem et al. (1994) at 1.5 GHz and by D97 at 4.85 GHz. For NGC 4565, we found exponential and Gaussian models to provide similarly good fits to our data. Also for this galaxy, D97 chose exponential fits at 4.85 GHz, while Broeils & Sancisi (1985) used a Gaussian model at 1.4 GHz. Given the physical motivation mentioned above, and to enable the comparison of our scale heights to those obtained for other edge-on galaxies, we adopt the results of the exponential fits for the subsequent analysis and discussion.

6.1.2 Results

Since previous studies of this kind did not include any correction for the thermal contribution, we determined scale heights of both the total and the non-thermal emission at 1.5 and 6 GHz. Logarithmic plots of the measured intensity profiles[2] are displayed along with the best-fit models in Fig. 6.2-6.3. Here, the error of each data point was computed as the average value of the standard deviations within each horizontal row of pixels in the corresponding rectangular box. The purpose of this method is to avoid the effect of a vertical gradient within a given box on the error. The resulting scale heights $h_{\rm disk}$ and $h_{\rm halo}$ are presented in Table 6.1 for NGC 891 and in Tables 6.2 and 6.3 for NGC 4565, including the reduced χ^2 value for each fit. Corresponding plots of scale heights versus position on the major axis are shown in Fig. 6.4. Unlike the authors named above, who applied the modelling to only one side beyond the major axis at a time and then averaged their results for the upper and lower side of each galaxy, we attempted to fit both sides simultaneously. For NGC 4565 this type of fit was not always successful. In such cases we performed separate fits for the upper and lower side and adopted the averaged scale heights (replacing the formal fit errors by half the difference between the upper and lower value in each case). The values determined in this way are marked by asterisks in Table 6.2 and 6.3. The large χ^2 values for NGC 891 in the central columns are most probably resulting from the east-west asymmetry of its intensity distribution, i.e. from different shapes of the vertical profile on each

[2]For brevity, only the profiles of the non-thermal emission are presented.

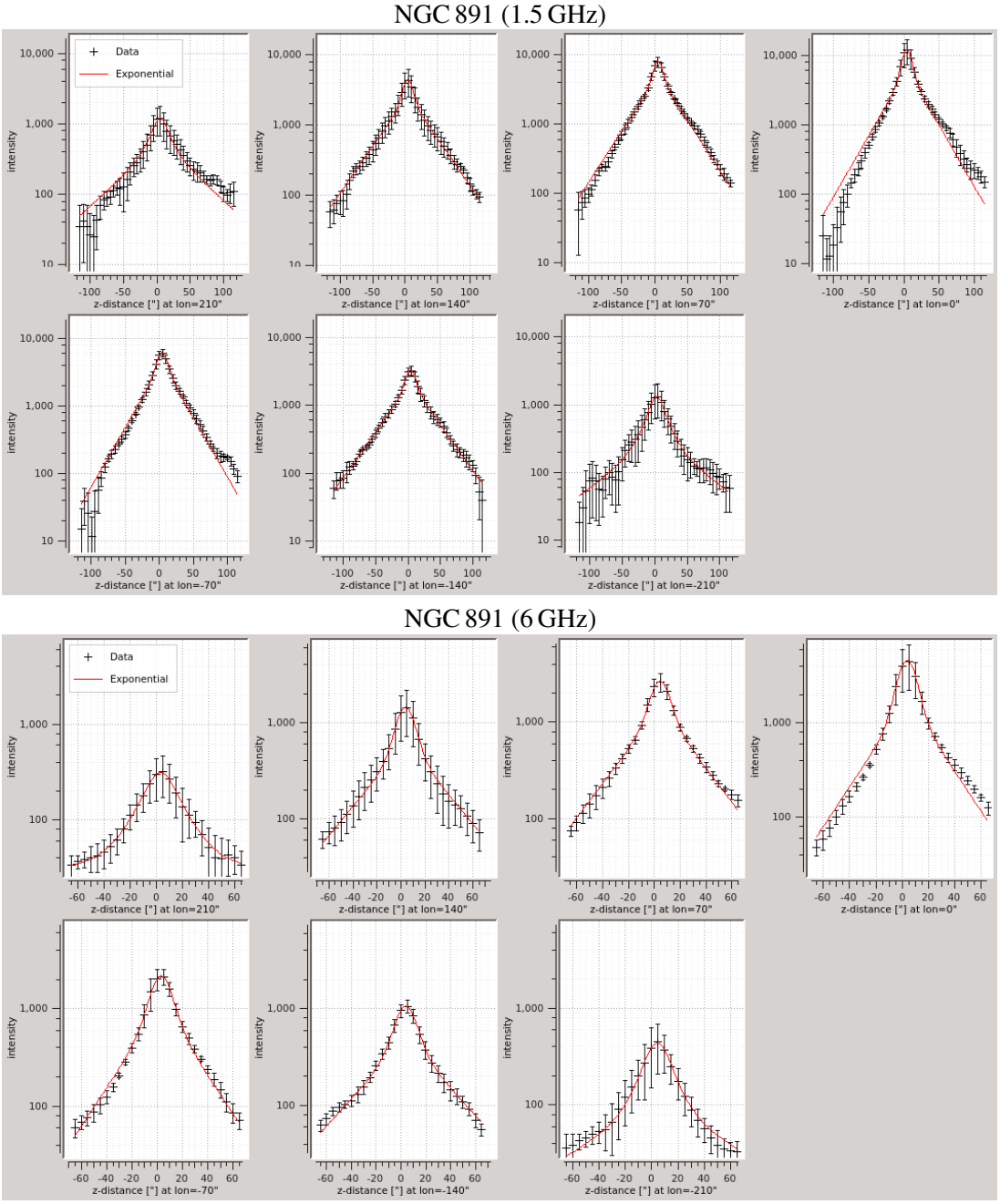

Figure 6.2: Vertical profiles of the non-thermal intensity in NGC 891 at 1.5 and 6 GHz, as a function of position z with respect to the galactic mid-plane, where positive z values are on the northwest side and negative ones on the southeast side of the mid-plane. The galactic longitude at the centre of each vertical column is indicated below each sub-panel ($1'' \equiv 44$ pc). The data points correspond to the average intensity (in μJy beam^{-1}) within each rectangular box defined in `BoxModels` (see Fig. 6.1). The solid lines denote two-component exponential least-squares fits to the data (see Table 6.1).

side of the major axis. We found that separate fits for each side achieved much lower reduced χ^2 values (not shown here) in the central columns for this galaxy.

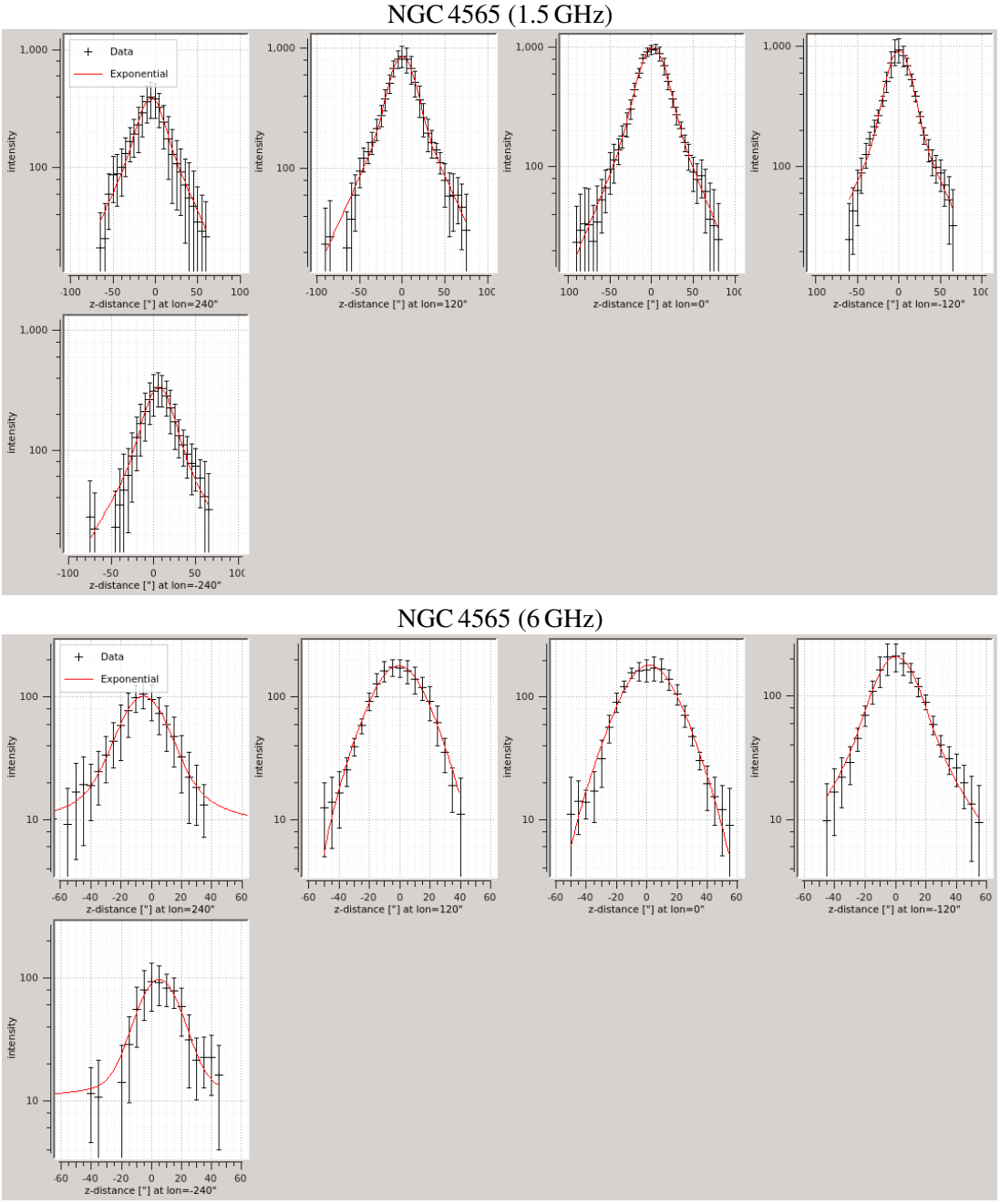

Figure 6.3: Vertical profiles of the non-thermal intensity in NGC 4565 at 1.5 and 6 GHz, as a function of position z with respect to the galactic mid-plane, where positive z values are on the northeast side and negative ones on the southwest side of the mid-plane. The galactic longitude at the centre of each vertical column is indicated below each sub-panel ($1'' \equiv 58$ pc). The data points correspond to the average intensity (in μJy beam^{-1}) within each rectangular box defined in `BoxModels` (see Fig. 6.1). The solid lines denote two-component exponential least-squares fits to the data (see Table 6.2). Note that in a few cases we did not use the fits to the entire vertical profile (as shown here), but instead fitted the parts at positive and negative z separately and in each case adopted the mean value of the two resulting scale heights.

Table 6.1: Exponential scale heights of NGC 891

	1.5 GHz, total			1.5 GHz, non-thermal		
r [kpc]	$h_{\rm disk}$ [kpc]	$h_{\rm halo}$ [kpc]	$\chi^2_{\rm red}$	$h_{\rm disk}$ [kpc]	$h_{\rm halo}$ [kpc]	$\chi^2_{\rm red}$
-9.26	0.41 ± 0.03	2.28 ± 0.27	0.16	0.61 ± 0.04	3.58 ± 0.96	0.12
-6.18	0.25 ± 0.01	1.49 ± 0.05	0.46	0.28 ± 0.02	1.48 ± 0.04	0.40
-3.09	0.26 ± 0.03	1.18 ± 0.09	3.97	0.30 ± 0.05	1.16 ± 0.08	3.56
0	0.21 ± 0.02	1.18 ± 0.10	6.80	0.22 ± 0.03	1.17 ± 0.09	6.39
3.09	0.22 ± 0.02	1.34 ± 0.07	2.79	0.23 ± 0.03	1.34 ± 0.06	2.21
6.18	0.22 ± 0.01	1.50 ± 0.05	0.34	0.25 ± 0.02	1.49 ± 0.04	0.32
9.26	0.39 ± 0.07	2.13 ± 0.33	1.10	0.56 ± 0.12	2.50 ± 0.69	1.02
average	0.28 ± 0.08	1.59 ± 0.41		0.35 ± 0.15	1.82 ± 0.83	

	6 GHz, total			6 GHz, non-thermal		
r [kpc]	$h_{\rm disk}$ [kpc]	$h_{\rm halo}$ [kpc]	$\chi^2_{\rm red}$	$h_{\rm disk}$ [kpc]	$h_{\rm halo}$ [kpc]	$\chi^2_{\rm red}$
-9.26	0.28 ± 0.02	2.17 ± 0.58	0.16	0.45 ± 0.05	3.70 ± 2.92	0.17
-6.18	0.25 ± 0.01	1.60 ± 0.20	0.46	0.32 ± 0.03	1.61 ± 0.20	0.48
-3.09	0.25 ± 0.03	1.24 ± 0.33	1.65	0.33 ± 0.06	1.24 ± 0.40	1.56
0	0.21 ± 0.02	1.19 ± 0.27	5.27	0.23 ± 0.02	1.14 ± 0.22	4.97
3.09	0.22 ± 0.02	1.28 ± 0.18	0.92	0.25 ± 0.03	1.24 ± 0.13	0.60
6.18	0.22 ± 0.02	1.53 ± 0.27	0.05	0.27 ± 0.03	1.47 ± 0.22	0.03
9.26	0.34 ± 0.03	2.45 ± 0.87	0.07	0.56 ± 0.03	5.61 ± 0.83	0.32
average	0.25 ± 0.04	1.64 ± 0.45		0.34 ± 0.11	2.29 ± 1.59	

As evident from Fig. 6.4 *a)* and *b)*, the dumbbell shape of the halo of NGC 891 is reflected in the radial behaviour of its scale heights. The enormous increase of scale heights at the outermost radii ($\approx \pm 9$ kpc) is certainly also affectd by the overall decrease in intensity, which is why these scale heights are only poorly constrained. The same effect is observed for the scale height of the disk, which does not seem to be dumbbell-shaped or show any kind of flaring at the edges. Also, at these outer radii the non-thermal scale heights are larger than those of the total emission, as here the radio intensity decreases more rapidly with radius than that of the thermal emission (which we inferred from Hα and IR maps, see Sect. 4.2).
In spite of the north-south-asymmetry in absolute intensity, $h_{\rm disk}$ and $h_{\rm halo}$ of NGC 891 (except for the edge values of the non-thermal component) show a remarkable radial symmetry – the 1.5 GHz scale heights at radii of 3 and 6 kpc in the northern halo are only marginally higher than those on the southern side. This seems to be further evidence for a tight disk-halo correlation. Moreover, we find the scale heights of NGC 891 to be almost equal at both frequencies, which is suggestive of predominantly convective CR transport.

The scale height distribution of NGC 4565 (Fig. 6.4 *c)* and *d)*), unlike that of NGC 891, differs substantially for the two observing frequencies. While at 6 GHz, a dumbbell-like behaviour of the halo scale heights is observed (like for NGC 891 with large uncertainties at the edges), scale heights remain basically constant throughout the galaxy at 1.5 GHz. The high edge values

Table 6.2: Exponential scale heights of NGC 4565

	1.5 GHz, total			1.5 GHz, non-thermal		
r [kpc]	h_{disk} [kpc]	h_{halo} [kpc]	χ^2_{red}	h_{disk} [kpc]	h_{halo} [kpc]	χ^2_{red}
-13.85	0.02 ± 0.01	1.36 ± 0.21	0.16	0.02 ± 0.01	1.19 ± 0.11	0.12
-6.92	0.02 ± 0.01	1.70 ± 0.22	0.52	0.02 ± 0.09	1.34 ± 0.11	0.19
0	0.03 ± 0.13*	1.41 ± 0.13*	0.18	0.18 ± 0.11*	1.30 ± 0.15*	0.16
6.92	0.02 ± 0.01	1.70 ± 0.21	0.29	0.02 ± 0.09	1.41 ± 0.08	0.21
13.85	0.02 ± 0.01	1.50 ± 0.16	0.13	0.02 ± 0.11	1.35 ± 0.12	0.09
average	0.02 ± 0.004	1.53 ± 0.14		0.05 ± 0.004	1.32 ± 0.07	

	6 GHz, total			6 GHz, non-thermal		
r [kpc]	h_{disk} [kpc]	h_{halo} [kpc]	χ^2_{red}	h_{disk} [kpc]	h_{halo} [kpc]	χ^2_{red}
-13.85	0.02 ± 0.08	2.47 ± 1.07	0.23	0.40 ± 0.12	3.30 ± 0.96	0.22
-6.92	0.02 ± 0.04*	1.53 ± 0.29*	0.51	0.02 ± 0.32	0.95 ± 0.18	0.25
0	0.32 ± 0.10*	1.64 ± 0.41*	0.23	0.52 ± 0.06*	0.95 ± 0.30*	0.26
6.92	0.04 ± 0.20	0.92 ± 0.16	0.24	0.57 ± 0.16	1.10 ± 0.28	0.22
13.85	0.02 ± 0.010	2.13 ± 0.40	0.21	0.53 ± 0.09	4.70 ± 1.30	0.13
average	0.08 ± 0.12	1.74 ± 0.53		0.41 ± 0.20	2.20 ± 1.54	

* The marked values are average values between the separately determined scale heights on the upper and lower side of the major axis.

at 6 GHz are again most likely influenced by the decreasing sensitivity, as explained above. Also here, the non-thermal scale heights at the edges are larger than the total ones, as the thermal disk appears to be radially more extended than the radio continuum emission. While in NGC 891 the total and non-thermal scale heights are basically identical, the values for NGC 4565 show substantial differences in this respect, which at least at 6 GHz can be explained by its higher thermal fractions. This galaxy furthermore differs from NGC 891 by its for the most part extremely low h_{disk} values, which have not been observed previously. A similar difference between the two galaxies in their CO scale heights was found by Yim et al. (2014). In the south-eastern half of the galaxy, we obtain unusually large non-thermal disk scale heights at 6 GHz. It is possible that these have been fitted erroneously, as here the disk emission in the non-thermal map (Fig. 4.8 *d)*) is not aligned well with the mid-plane from a radius of ≈ 5 kpc onwards. In addition, the relatively large disk scale heights at the centre are probably induced by the partially resolved spiral arm pattern, but might as well be an artifact of the removal of the nuclear source. The signature of the spiral arms (or rather of the gap between them) is visible in the central vertical emission profiles (lon = 0 in Fig. 6.3) as a flattening of the peak region, which makes it difficult to fit these profiles accurately. Note that in these subplots the simultaneous fit of both sides of the major axis is displayed, even though in these cases we adopted as scale height the average result of the upper- and lower-side fits. Furthermore, we observe the position of the peak to shift from the mid-plane to negative galactic latitudes on the south-east side of the galaxy and to positive ones on the north-west side. This is likewise caused by the spiral

Table 6.3: Gaussian scale heights of NGC 4565

	1.5 GHz, total			1.5 GHz, non-thermal		
r [kpc]	$h_{\rm disk}$ [kpc]	$h_{\rm halo}$ [kpc]	$\chi^2_{\rm red}$	$h_{\rm disk}$ [kpc]	$h_{\rm halo}$ [kpc]	$\chi^2_{\rm red}$
-13.85	0.03 ± 0.01	2.84 ± 0.40	0.16	0.67 ± 0.13	3.30 ± 0.59	0.12
-6.92	0.01 ± 0.02	3.34 ± 0.80	0.59	0.02 ± 0.02	2.59 ± 0.29	0.26
0	0.29 ± 0.10	2.87 ± 0.22	0.13	0.58 ± 0.06	2.95 ± 0.16	0.10
6.92	0.02 ± 0.01	3.05 ± 0.21	0.18	0.02 ± 0.16	2.65 ± 0.12	0.13
13.85	0.01 ± 0.01	2.76 ± 0.42	0.13	0.02 ± 0.01	2.50 ± 0.09	0.08
average	0.07 ± 0.11	2.97 ± 0.21		0.26 ± 0.30	2.80 ± 0.29	

	6 GHz, total			6 GHz, non-thermal		
r [kpc]	$h_{\rm disk}$ [kpc]	$h_{\rm halo}$ [kpc]	$\chi^2_{\rm red}$	$h_{\rm disk}$ [kpc]	$h_{\rm halo}$ [kpc]	$\chi^2_{\rm red}$
-13.85	0.02 ± 0.15	7.39 ± 2.82	0.17	0.57 ± 0.14	9.61 ± 1.54	0.16
-6.92	0.20 ± 0.12*	2.73 ± 0.19*	0.09	0.28 ± 0.23*	2.13 ± 0.36*	0.03
0	0.59 ± 0.07	3.35 ± 1.06	0.24	1.06 ± 0.15	1.13 ± 0.21	0.23
6.92	0.13 ± 0.10	1.71 ± 0.38	0.12	1.03 ± 0.10	5.50 ± 1.13	0.16
13.85	0.02 ± 0.27	4.56 ± 0.64	0.16	0.70 ± 0.07	6.16 ± 1.24	0.06
average	0.19 ± 0.21	3.95 ± 1.95		0.73 ± 0.29	4.92 ± 3.03	

* The marked values are average values between the separately determined scale heights on the upper and lower side of the major axis.

arm structure, as already indicated by Broeils & Sancisi (1985), and at larger radii is mainly a consequence of the warp and hence of the change in position angle.

Table 6.4: Exponential scale heights measured by Dumke (1997) at 4.85 GHz & assumed inclinations and distances therein.

	NGC 891	NGC 4565
$h_{\rm disk}$ [kpc]	0.27	0.28
$h_{\rm halo}$ [kpc]	1.82	1.68
D [kpc]	9.6	10.0
i	88°	87.5°

On average, the scale heights we obtained for the total emission of both galaxies at 6 GHz are roughly comparable to those found by D97 at 4.85,GHz (who assumed, however, somewhat different inclinations and distances; see Table 6.4). The most obvious exception to this is our much lower $h_{\rm disk}$ for NGC 4565. This discrepancy certainly arises from the fact that D97 assumed a higher inclination of 87.5° for this galaxy. For NGC 891, our averaged $h_{\rm halo}$ is slightly lower than that found by D97, as this author had excluded the central region from his measurements.

Especially when neglecting the two edge data points in each case, the previously reported finding of roughly similar halo scale heights for the two galaxies is verified by our data. Nevertheless, at 6 GHz we observe a slight trend towards lower non-thermal halo scale heights for NGC 4565. Since for NGC 891 it is more likely than for NGC 4565 that there is flux missing in the 1.5 GHz maps, it is possible that the synchrotron scale heights of NGC 4565 are in fact systematically

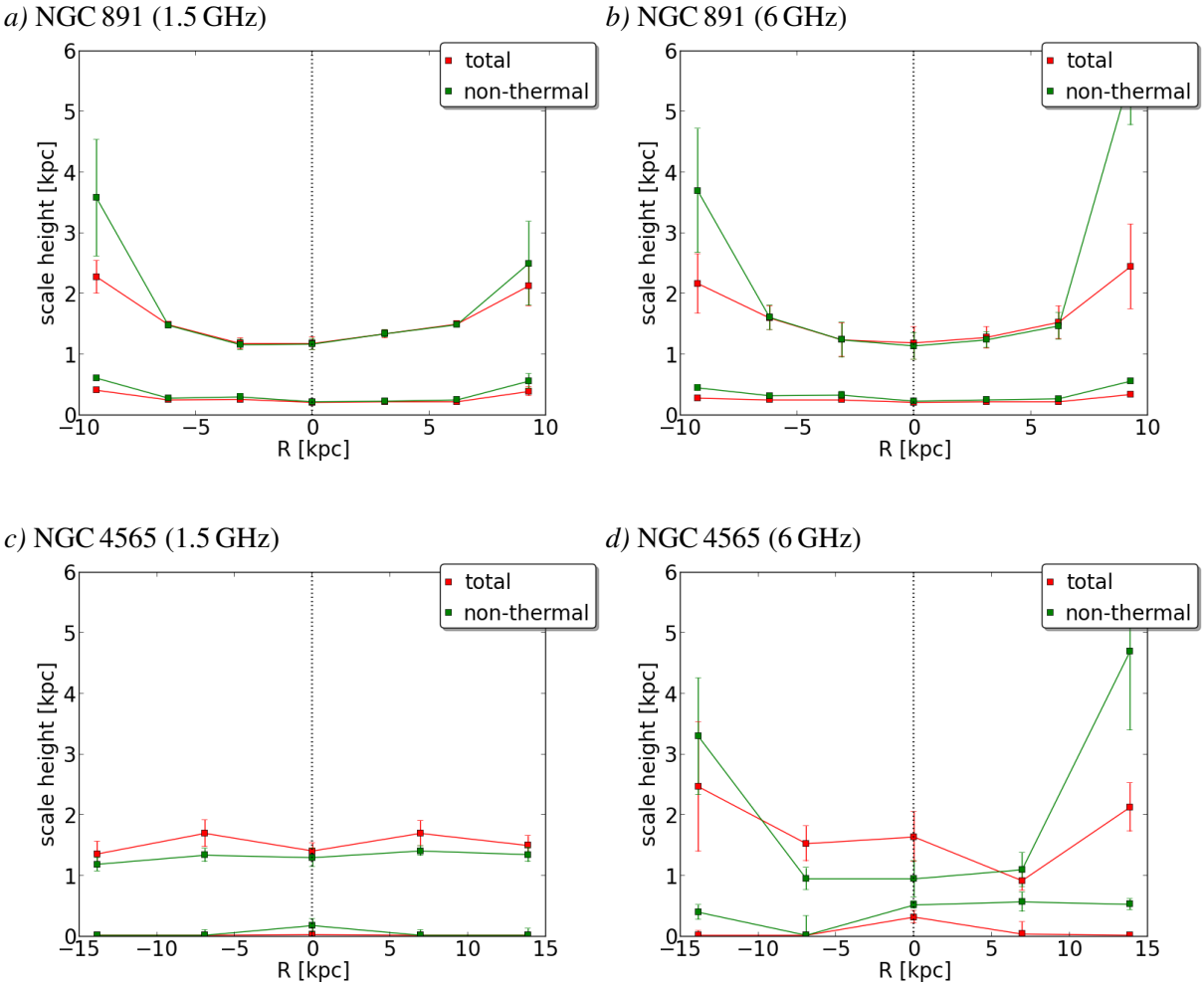

Figure 6.4: Vertical exponential scale heights of the total (red symbols) and non-thermal (green symbols) emission of NGC 891 and NGC 4565 at 1.5 and 6 GHz, as a function of position along the major axis. For both galaxies, negative values of R are on the east side and positive ones on the west side. In each panel, the lower data points denote h_{disk} and the higher ones denote h_{halo}.

lower than those of NGC 891. Apart from single-dish data of NGC 891 at 1.5 GHz, especially more sensitive data of NGC 4565 (preferably at additional frequencies) would be required to investigate this trend properly.

6.2 Total magnetic field strength distribution

Assuming energy equipartition between CRs and magnetic fields, using the revised equipartition relation of Beck & Krause (2005), we generated maps of the total magnetic field strength B_{eq} from the non-thermal 1.5 GHz intensity maps and the non-thermal spectral index maps formed

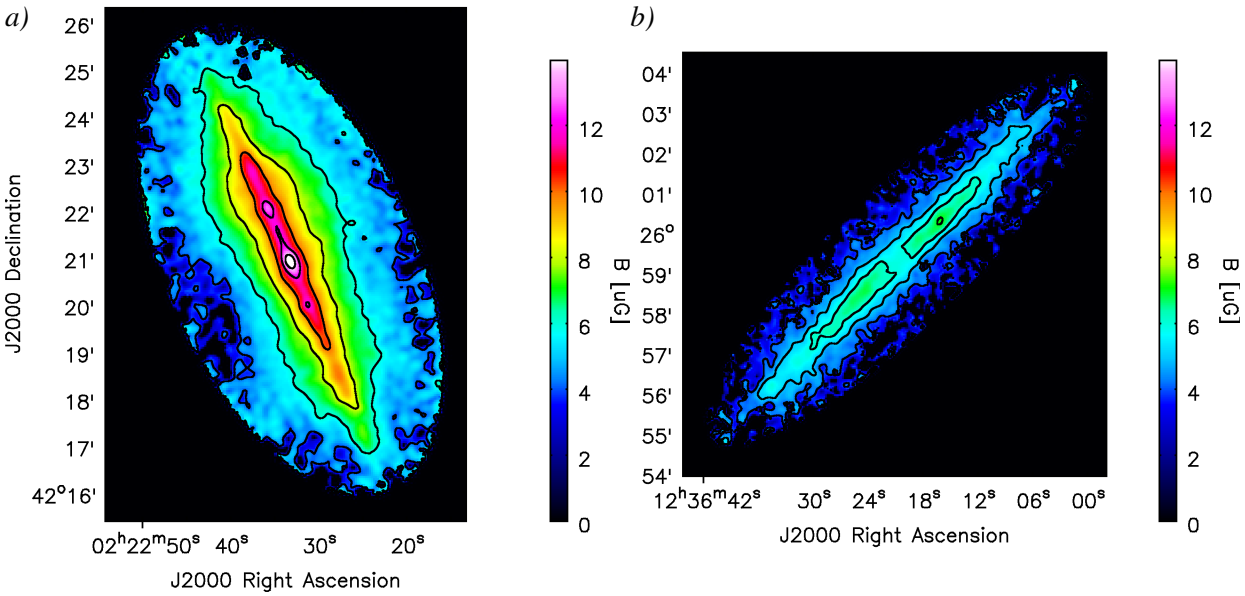

Figure 6.5: Maps of the total magnetic field strength in NGC 891 (panel *a)*) and NGC 4565 (panel *b)*), computed assuming energy equipartition and an oblate spheroid geometry (see text). The field strength was not calculated in regions where the spectral index between 1.5 and 6 GHz is steeper than −1.2. The angular resolution in both panels is 12″.

between 1.5 and 6 GHz (all short-spacing corrected). The field strength was not calculated in regions where the spectral index is steeper than −1.2. We assumed a constant number-density ratio of CR protons to CR electrons of $K_0 = 100$, which is reasonable for the disk but yields only a lower limit for $B_{\rm eq}$ in the halo, as the protons are much less affected by synchrotron losses than the electrons, and hence K_0 is expected to increase in vertical (z-) direction. For a non-thermal spectral index of -1, the uncertainty in $B_{\rm eq}$ scales as $(K/K_0)^{\frac{1}{4}}$ (see Beck & Krause 2005), so that e.g. for a local ratio of $K = 300$ the field strength would be underestimated by $\approx 32\%$. To determine $B_{\rm eq}$, also the pathlength through the galaxies along the line of sight has to be known, which we estimated for each map coordinate by assuming an oblate spheroidal geometry for each galaxy. The pathlength through an oblate spheroid with semi-major axis length R and semi-minor axis length H depends is $l = 2R\sqrt{1-(x^2/R^2)-(z^2/H^2)}$, where x and z are the distances from the centre on the major and minor axis, respectively. This is strictly valid only for an inclination of 90°, but still serves as a reasonable approximation for nearly edge-on galaxies like NGC 4565 ($i = 86.3°$). R and H were determined for each galaxy from the 3σ levels in the L-band D-array map, with H being chosen as the average between the maximum vertical extent and the minimum extent above the central region. We obtained $R = 14.1$ kpc and $H = 7.1$ kpc for NGC 891, and $R = 22.1$ kpc and $H = 5.8$ kpc for NGC 4565.

The resulting maps of the (line-of-sight averaged) total magnetic field strength are presented in Fig. 6.5. Except for a few edge artifacts in the map of NGC 891 caused by low S/N and the region where we had subtracted the nucleus of NGC 4565, $B_{\rm eq}$ decreases monotonically with vertical distance from the mid-plane. The maximum magnetic field strength (averaged within the 12″ beam) is 15 μG in NGC 891 and 7 μG in NGC 4565. Averaged over the regions in which we determined vertical scale heights (see Fig. 6.1 *a)* and *c)*), we obtain field strengths of

8 μG and 5 μG for NGC 891 and NGC 4565, respectively. NGC 891 thus features rather typical field strengths for normal galaxies (cf. e.g. Heesen et al. 2014), while those in NGC 4565 are comparatively weak.
We used a Monte-Carlo method to estimate the uncertainties in the determined magnetic field strenth, based on the pathlength through the galaxy and the noise rms in the used total intensity maps. In the disk of NGC 891, we find that the error of $B_{\rm eq}$ is typically 3.5%, while at a vertical height of ≈5 kpc we obtain an uncertainty of 21%. For NGC 4565, typical errors are 3.6% in the mid-plane and 28% at a height of ≈3 kpc.

6.3 CRE lifetimes

After their injection into the ISM, CREs are subjected to several energy loss mechanisms, which operate on different time scales and thus determine the lifetime of the particles, usually defined as the time after which the particles have lost half of their initial energy. At the radio frequencies considered here, the dominant processes are usually synchrotron and inverse-Compton losses, the combination of which results in a CRE lifetime of (e.g. Heesen et al. 2015)

$$t_{1/2} = 1.0815 \cdot 10^9 \left(\frac{\nu}{\mathrm{GHz}}\right)^{-0.5} \left(\frac{B}{\mu\mathrm{G}}\right)^{-1.5} \left(1 + \frac{U_{\rm rad}}{U_{\rm mag}}\right)^{-1} \mathrm{yr}\,, \tag{6.7}$$

where $U_{\rm mag} = B^2/(8\pi)$ is the magnetic field energy density and $U_{\rm rad} = U_{\rm IRF} + U_{\rm CMB}$ is the energy density of the radiation that is relevant for inverse-Compton scattering. The energy density of the interstellar radiation field (IRF), in turn, can be expressed as the sum of the stellar and dust radiation fields, $U_{\rm IRF} = U_{\rm star} + U_{\rm dust}$. $U_{\rm dust} = L_{FIR}/(2\pi R^2 c)$ can be obtained from the total far-infrared luminosity L_{FIR} and the radial extent R of the galaxy, which we determined in the previous section. We used the L_{FIR} values from Sanders et al. (2003) after scaling them for each galaxy by the squared ratio between our assumed distance and the distance these authors used. Moreover, we assumed $U_{\rm star} = 1.73 U_{\rm dust}$, as found for the solar neighbourhood (Draine 2011), and thus $U_{\rm IRF} = 2.73 U_{\rm dust}$. With $U_{\rm CMB} = 4.2 \cdot 10^{-13}\,\mathrm{erg\,cm^{-3}}$ (at redshift 0), we obtain global radiation energy densities of $U_{\rm rad} = 1.04 \cdot 10^{-12}\,\mathrm{erg\,cm^{-3}}$ for NGC 891 and $U_{\rm rad} = 4.98 \cdot 10^{-13}\,\mathrm{erg\,cm^{-3}}$ for NGC 4565. Using the above-specified average equipartition field strengths yields $U_{\rm mag} = 2.55 \cdot 10^{-12}\,\mathrm{erg\,cm^{-3}}$ and $U_{\rm mag} = 1.08 \cdot 10^{-12}\,\mathrm{erg\,cm^{-3}}$, respectively. Hence, for NGC 891 $U_{\rm rad}/U_{\rm mag} = 0.41$, and for NGC 4565 $U_{\rm rad}/U_{\rm mag} = 0.46$, which means that on average synchrotron losses are clearly dominating over IC losses in both galaxies.

We computed $t_{1/2}$ in each of the vertical columns that were used for the determination of scale heights, inserting into Eq. 6.7 the global $U_{\rm rad}$ values quoted above, the mid-plane magnetic field strengths B_0, and $U_{\rm mag} = B_0^2/(8\pi)$. To obtain B_0, we applied the `BoxModels` routine to the $B_{\rm eq}$ maps and measured the average value within the central box of each column. Note that using $B = B_0$ in Eq. 6.7 results in lower limits for $t_{1/2}$, as in z-direction the magnetic field strength decreases, and hence also the local energy loss rate. In Table 6.5 we list the measured values of B_0 and $t_{1/2}$ for the different major-axis positions.
Similar to the case of NGC 253 (Heesen et al. 2009a), we find for both galaxies that while the

Table 6.5: Mid-plane magnetic field strengths, CRE lifetimes, and CR bulk speeds

NGC 891		1.5 GHz		6 GHz	
r [kpc]	B_0 [μG]	$t_{1/2}$ [Myr]	v [km s^{-1}]	$t_{1/2}$ [Myr]	v [km s^{-1}]
-9.26	8.1	27.4 ± 7.3	174	13.7 ± 3.6	782
-6.18	10.5	19.9 ± 5.3	142	9.9 ± 2.6	282
-3.09	11.9	16.8 ± 4.5	152	8.4 ± 2.2	281
0	13.0	15.1 ± 4.0	148	7.5 ± 2.0	289
3.09	11.3	18.0 ± 4.8	123	9.0 ± 2.4	263
6.18	9.9	21.4 ± 5.7	132	10.7 ± 2.8	287
9.26	8.1	27.2 ± 7.2	251	13.6 ± 3.6	518

NGC 4565		1.5 GHz		6 GHz	
r [kpc]	B_0 [μG]	$t_{1/2}$ [Myr]	v [km s^{-1}]	$t_{1/2}$ [Myr]	v [km s^{-1}]
-13.85	5.5	47.8 ± 12.7	56	23.9 ± 6.4	391
-6.92	6.4	39.8 ± 10.6	71	19.9 ± 5.3	110
0	6.3	40.6 ± 10.8	64	20.3 ± 5.4	93
6.92	6.5	36.3 ± 10.5	68	19.7 ± 5.2	96
13.85	5.2	51.0 ± 13.6	46	25.5 ± 6.8	257

scale height of the halo increases with radius, the magnetic field strength in the disk decreases, and hence the CRE lifetimes show a similar radial behaviour to the scale heights. However, since our measured lifetimes are lower limits due to the decrease of the magnetic field strength with z, the observed relation between halo scale height and CRE lifetime is generally not linear. As evident from Fig. 6.6, we observe a clearly linear correlation between these two quantities only in NGC 891 for the shorter lifetimes ($\lessapprox 10$ Myr) determined from the 6 GHz data. The linearity apparently breaks down for longer lifetimes, since for this galaxy we measured similar scale heights at both frequencies. However, as our scale heights at 1.5 GHz represent lower limits due to possible missing short spacings, the behaviour for $t_{1/2} > 10$ Myr is not well-constrained by our measurements. For NGC 4565, we find that the lifetime does not vary significantly with radius at 6 GHz, except at the largest radii, where the actual uncertainties are probably larger than indicated by our error bars. The data points at 1.5 GHz suggest a saturation of the halo scale height for large CRE lifetimes.

For a hypothetically linear scale height-lifetime relation, we calculated the vertical bulk speed $v = h_{\mathrm{CRE}}/t_{1/2}$ of the CRs at each position (see Table 6.5). Here h_{CRE} is the CRE scale height, which, if assuming equipartition, relates to the scale height of the synchrotron emission (in our case h_{halo}) as

$$h_{\mathrm{CRE}} = \frac{3 - \alpha_{\mathrm{nth}}}{2} h_{\mathrm{halo}} \,, \tag{6.8}$$

where we used the global $\alpha_{\mathrm{nth,1.5–6GHz}}$ values given in Table 4.5. We emphasize that the CRE bulk speeds obtained in this way cannot be expected to be accurate, not only as the vertical decrease of the magnetic field strength is not taken into account (in that sense, our bulk speed values are

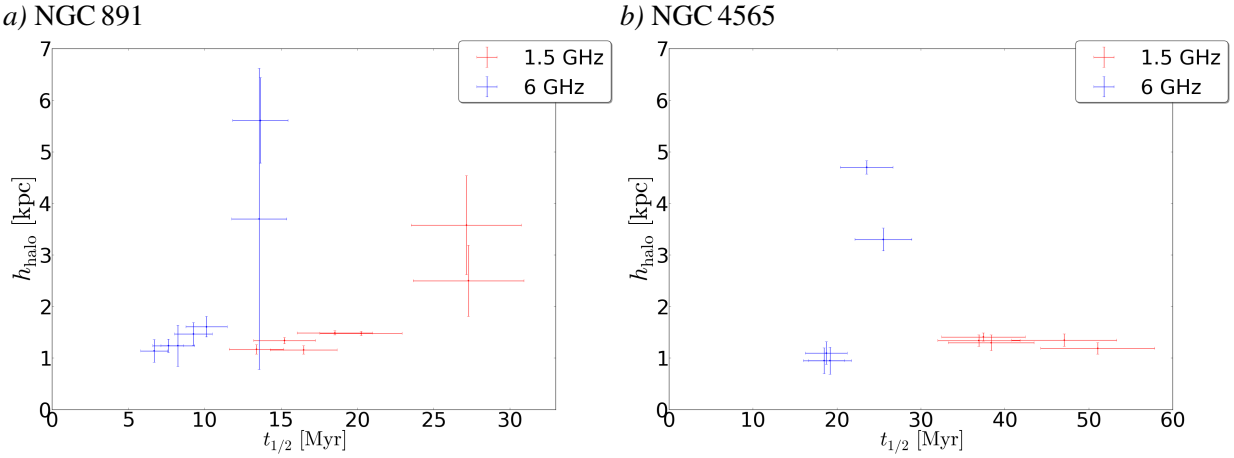

Figure 6.6: Scale heights of the halo component of NGC 891 and NGC 4565 as a function of the CRE lifetime $t_{1/2}$ resulting from synchrotron and IC losses. These lifetimes were calculated based on the mid-plane equipartition magnetic field strength, without taking the vertical decrease of the magnetic field strength into account.

upper limits), but also because the equipartition condition we used to determine h_{CRE} may break down at high z. Anyhow, it is worth mentioning that from the 6 GHz data of NGC 891 (except at the largest radii) we find bulk speeds consistently around 280km s^{-1}, which is comparable to the average speed Heesen et al. (2009a) obtained for the northeastern half of NGC 253. In the Sect. 6.4 we present a method to determine CR speeds which takes the vertical gradient of the magnetic field strength into account and does not rely on the assumption of energy equipartition in the halo.

In addition to synchrotron and IC losses, ionization losses occur on a time scale of (Murphy 2009)

$$t_{\mathrm{ion}} = 4.1 \cdot 10^9 \left(\frac{\langle n \rangle}{\mathrm{cm}^{-3}}\right)^{-1} \left(\frac{E}{\mathrm{GeV}}\right) \left[3 \ln\left(\frac{E}{\mathrm{GeV}}\right) + 42.5\right]^{-1} \mathrm{yr} \tag{6.9}$$

as well as bremsstrahlung losses, the time scale of which is given by

$$t_{\mathrm{brems}} = 3.96 \cdot 10^7 \left(\frac{\langle n \rangle}{\mathrm{cm}^{-3}}\right)^{-1} \mathrm{yr}\,, \tag{6.10}$$

where $\langle n \rangle$ is the average particle number density of neutral gas in the ISM, and the CRE energy can be written as $E(\mathrm{GeV}) = (\nu/16.1\mathrm{MHz})^{1/2}(B/\mu\mathrm{G})^{-1/2}$. We estimate $\langle n \rangle$ in both galaxies from the total atomic gas masses given in Table 1.1, assuming that this amount of gas is distributed in an oblate spheroid of radius R as given in Sect. 6.2 and semi-minor axis length corresponding to the HI disk scale height of 1.25 kpc for NGC 891 (Oosterloo et al. 2007) and 0.3 kpc for NGC 4565 (Zschaechner et al. 2012). Assuming for simplicity that all atoms are hydrogen nuclei ($m_{\mathrm{p}} = 1.673 \cdot 10^{-27}$ kg), we find $\langle n \rangle = 0.22\,\mathrm{cm}^{-3}$ for NCG 891 and $\langle n \rangle = 0.65\,\mathrm{cm}^{-3}$ for NGC 4565. Further, we use the above-specified maximum field strengths of 15 μG and 7 μG, respectively. In case of NGC 891, we thus obtain $t_{\mathrm{ion,1.5GHz}} = 1.0 \cdot 10^9$ yr, $t_{\mathrm{ion,6GHz}} = 2.0 \cdot 10^9$ yr, and $t_{\mathrm{brems}} = 1.8 \cdot 10^8$ yr, and for NGC 4565 $t_{\mathrm{ion,1.5GHz}} = 4.9 \cdot 10^8$ yr, $t_{\mathrm{ion,6GHz}} = 9.5 \cdot 10^8$ yr, and $t_{\mathrm{brems}} = 6.1 \cdot 10^7$ yr. Thus, in both galaxies, ionization loss rates are at least one order of magnitude

lower than those of synchrotron and IC losses, and can hence be neglected. The same is true for bremsstrahlung losses in NGC 891, while in NGC 4565 bremsstrahlung losses may have a minor flattening effect on the spectrum at 1.5 GHz.

6.4 Modelling the vertical cosmic-ray transport in NGC 891

To determine more accurate CRE lifetimes than those obtained in the previous section would require integration over the vertical magnetic field strength distribution. As we describe further below, the field strengths computed using the equipartition formula of Beck & Krause (2005) can be approximated by exponential z-profiles. However, it is unclear up to what z-height these equipartition values can still be considered as a valid approximation. Therefore, we followed the approach presented by Heesen at al. (2015, submitted) to numerically solve the diffusion-loss equation and thereby generate synthetic z-profiles of the CRE number density, synchrotron intensity, and synchrotron spectral index, which can be compared to our data. This was accomplished using the `SPINNAKER` (SPectral INdex Numerical Analysis of K(c)osmic-ray Electron Radio-emission) code[3] written by V. Heesen. We restricted this part of our analysis to NGC 891, as the vertical spectral index profile is crucial for distinguishing between different models, and we were not able to extract meaningful spectral index profiles for NGC 4565 due to its inclination and the low S/N of these data.

The temporal behaviour of the CRE number density $N(E)$ in a given volume is described by the diffusion-loss equation (e.g. Longair 2011):

$$\frac{\mathrm{d}N(E)}{\mathrm{d}t} = D(E)\nabla^2 N(E) + \frac{\partial}{\partial E}[b(E)N(E)] + Q(E,t)\,, \tag{6.11}$$

where

$$b(E) = -\left(\frac{\mathrm{d}E}{\mathrm{d}t}\right) = \frac{4}{3}\sigma_\mathrm{T}^2 c\left(\frac{E}{m_\mathrm{e}c^2}\right)^2 (U_\mathrm{mag} + U_\mathrm{rad}) \tag{6.12}$$

(with the Thomson cross section $\sigma_\mathrm{T} = 6.6 \cdot 10^{-25}\,\mathrm{cm}^2$) is the combined synchrotron and IC loss rate of a single CRE and D is the diffusion coefficient, assumed to be spatially constant. We are interested in a steady-state solution ($\frac{\partial N}{\partial t} = 0$), as we assume a constant CR injection rate and thus the source term $Q(E,t)$ is not explicitly time-dependent. Further, we assume that all CREs are generated in the mid-plane, therefore we require $Q(E,t) = 0$ for $z > 0$.

In one dimesion (z), and incorporating CR transport by convection at a constant speed v_conv, the steady-state diffusion-loss equation becomes (e.g. Lerche & Schlickeiser 1980)

$$D(E)\frac{\partial^2 N(E,z)}{\partial z^2} - v_\mathrm{conv}\frac{\partial N(E,z)}{\partial z} + \frac{\partial}{\partial E}[b(E)N(E)] = 0 \tag{6.13}$$

While CR transport in galaxies is generally a combination of convection and diffusion, here we only consider cases where one process is significantly dominating over the other. With the above

[3] https://www.github.com/vheesen/Spinnaker

assumptions, in the case of purely convective CR transport, Eq. 6.13 reduces to

$$\frac{\partial N(E,z)}{\partial z} = \frac{1}{v_{\rm conv}} \left(\frac{\partial}{\partial E} [b(E) N(E,z)] \right) \tag{6.14}$$

For purely diffusive transport one obtains

$$\frac{\partial^2 N(E,z)}{\partial z^2} = \frac{1}{D(E)} \left(\frac{\partial}{\partial E} [b(E) N(E,z)] \right) \tag{6.15}$$

where the diffusion coefficient D depends on the energy as

$$D(E) = D_0 \left(\frac{E}{\rm GeV} \right)^{\mu} \tag{6.16}$$

with $0.3 \lesssim \mu \lesssim 0.6$ (Strong et al. 2007). For the numerical integration of Eq. 6.14 or 6.15, we use the boundary condition at $z = 0$ of $N(E,0) = N_0 E^g$, where $g = 2\alpha_{\rm nth,0} - 1$ is the injection value of the CRE energy spectral index.

Along with modelling $N(E,z)$ by solving Eq. 6.14 or 6.15, SPINNAKER computes the corresponding z-distributions of the non-thermal intensity $I_{\rm nth}$ and the non-thermal spectral index $\alpha_{\rm nth}$ (a more detailed documentation will be available in the appendix of Heesen at al. 2015 (submitted)). For comparison with the model distributions, we measured a single global intensity profile (at each frequency) and and a single spectral index profile of NGC 891 by performing the box integration on the (short-spacing corrected) non-thermal 1.5 and 6 GHz intensity maps as well as on the $\alpha_{\rm nth,1.5-6GHz}$ map (Fig. 5.13 *b)*). For the intensity profiles (shown in Fig. 6.7 *a)*), we chose a single column perpendicular to the major axis of width $\Delta r = 21.6$ kpc and, as before, a vertical box separation of $\Delta z = 0.22$ kpc. In case of the spectral index profile (Fig. 6.7 *b)*) we used only the northern half of the galaxy (i.e. $\Delta r = 10.8$ kpc), as the spectral index values are more reliable here. By incorporating the southern half as well, our vertical $\alpha_{\rm nth,1.5-6GHz}$ profile would have been severely affected by a flattening towards the map edges (see Sect 5.2.1. Still, similar edge artifacts also appear in the northern part of the map, which imposed a limit in z-height up to which reliable spectral index values could be measured. The average value within the box along the mid-plane of $\alpha_{\rm nth,0} = -0.82$ was adopted as the mid-plane (i.e. injection-) spectral index for the above inner boundary condition. Averaging over the same region in the $B_{\rm eq}$ map, we obtained a global value for the mid-plane magnetic field strength of $B_0 = 10.4\,\mu$G. To take account of IC losses, we used the above-determined $U_{\rm rad}/U_{\rm mag}$ ratio of 0.41.

While using $\alpha_{\rm nth,0}$, B_0, and $U_{\rm rad}/U_{\rm mag}$ as fixed input parameters to SPINNAKER, we varied the exponential magnetic field scale height $h_{\rm B}$ and, depending on the considered CR transport mechanism, the convection speed $v_{\rm conv}$ or the diffusion coefficient D (as well as the exponent μ in Eq. 6.16), until we found a model that describes our data reasonably well. Heesen et al. (2015, submitted) found that convection models produce approximately exponential vertical intensity profiles, while diffusion results in nearly Gaussian profiles. Furthermore, diffusion models predict a very flat slope of the spectral index profile at low z. However, the spectral index profile of NGC 891 steepens rapidly in the inner part, and therefore we found it to be incompatible with diffusion-dominated CR transport. Hence we only present our best-fitting

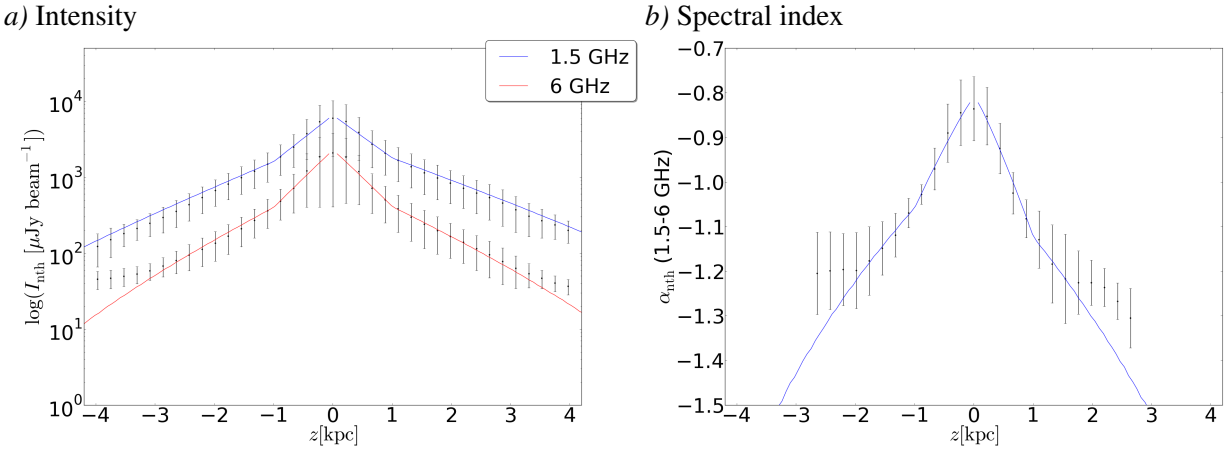

Figure 6.7: Global vertical profiles of the non-thermal intensity in NGC 891 at 1.5 and 6 GHz and the non-thermal spectral index between the two frequencies. Positive z values are on the northwest side and negative ones on the southeast side of the mid-plane. The intensity profiles represent the average profiles between radial distances of ±10.8 kpc, while the spectral index profile was averaged between distances of −10.8 and 0 kpc. The solid lines show the intensity and spectral index profiles corresponding to our best-fitting two-component model obtained by solving the vertical diffusion-loss equation for purely convective CR transport. The modelling was performed separately for the northwest and southeast side of the galaxy. Parameters of our best-fit model are listed in Table 6.6.

convection model, the predicted intensity and spectral index profiles of which are shown along with the data in Fig. 6.7 *a)* and *b)*, respectively. Since the z-distribution of NGC 891 consists of a disk and a halo component, we considered a two- component model with different magnetic field scale heights and $h_{\rm B1}$ and $h_{\rm B2}$ and convection speeds $v_{\rm conv,1}$ and $v_{\rm conv,2}$, below and above a certain transition height $z_{\rm t}$. We generated separate models for the east and west side of the galaxy (in Fig. 6.7 $z < 0$ and $z > 0$, respectively), deciding on the quality of the fits by visual comparison with the data[4]. By intending to simultaneously fit the intensity profiles (at 1.5 and 6 GHz) and the spectral index profile, a significant degeneracy between the free parameters ($h_{\rm B}$ and $v_{\rm conv}$ for each component, as well as $z_{\rm t}$) could be avoided. On both sides of the galaxy we found the most reasonable transition point between the disk and halo regime at $z_{\rm t} = 1.0$ kpc. For $z \gtrapprox 3$ kpc, our measured 6 GHz intensity profile most likely overestimates the true emission at this height, as already explained in Sect 6.1.1. Similarly to the case of fitting the synchrotron scale heights at this frequency, we neither took these data points into consideration during our diffusion-loss equation modelling, as evident from Fig. 6.7 *a)*. From this plot it is clearly evident that (especially in the eastern half) this plateau of extended emission at 6 GHz is what causes the flat spectral index values towards the map edges. Consequently, we also neglected the flat outer parts of the spectral index profile (Fig. 6.7 *b)*), which occur already at $z \gtrapprox 2$ kpc. Furthermore, we allowed our model to slightly overpredict the 1.5 GHz intensities above $z_{\rm t}$ with respect to the data, since here the data may still underestimate the true intensities by a small amount due to missing short-spacings.

[4] A follow-up analysis based on the χ^2-distribution in the $h_{\rm B}$-$v_{\rm conv}$ parameter space is being planned.

Table 6.6: Parameters of the best-fit CR transport model for NGC 891

	Upper side (west)	Lower side (east)
$v_{\mathrm{conv},1}$ [km s^{-1}]	120^{+15}_{-15}	140^{+10}_{-10}
$v_{\mathrm{conv},2}$ [km s^{-1}]	290^{+400}_{-170}	270^{+1260}_{-120}
h_{B1} [kpc]	$1.9^{+2.0}_{-0.9}$	$1.6^{+0.9}_{-0.6}$
h_{B2} [kpc]	$3.5^{+1.0}_{-0.7}$	$2.9^{+0.9}_{-0.6}$
z_{t} [kpc]	1.0	1.0

The convection speeds and magnetic field scale heights of our best-fit model are given in Table 6.6. Upper and lower error limits for each parameter were estimated based on the variation of the model profiles within the error limits of the intensity and spectral index data points. In our best-fit model, the CREs have an initial convection speed of $v_{\mathrm{conv},1} \approx 130\,\mathrm{km\,s^{-1}}$ and are accelerated to $v_{\mathrm{conv},2} \approx 280\,\mathrm{km\,s^{-1}}$ at heights above 1 kpc, which is comparable to the speeds we obtained at 6 GHz assuming a constant magnetic field and equipartition. While $v_{\mathrm{conv},1}$ is constrained very well by the shape of the inner part of the intensity and spectral index profiles, the actual value of $v_{\mathrm{conv},2}$ depends largely on the extent to which the intensities at large z are underestimated at 1.5 GHz and overestimated at 6 GHz. Within the uncertainties, a constant convection speed around the value of $v_{\mathrm{conv},1}$ is possible. Moreover, the synchrotron spectral index in the disk, and thus our result for $v_{\mathrm{conv},1}$, is influenced by our estimate of the thermal fraction.
On average, our model features scale heights of the disk and halo magnetic field components of $h_{\mathrm{B1}} \approx 1.8\,\mathrm{kpc}$ and $h_{\mathrm{B2}} \approx 3.2\,\mathrm{kpc}$. Neglecting the two values at the outer radii in each case, the average synchrotron scale heights we measured in Sect. 6.1 are $h_{\mathrm{syn,disk}} \approx 0.3\,\mathrm{kpc}$ and $h_{\mathrm{syn,halo}} \approx 1.3\,\mathrm{kpc}$. If energy equipartition is assumed, these lead to magnetic field scale heights of $h_{\mathrm{B,eq}} = h_{\mathrm{syn}}(3 - \alpha_{\mathrm{nth}})$ (Beck & Krause 2005). With $\alpha_{\mathrm{nth}} = -0.9$ we obtain $h_{\mathrm{B,eq,disk}} = 1.17\,\mathrm{kpc}$ and $h_{\mathrm{B,eq,halo}} = 5.07\,\mathrm{kpc}$. Running `BoxModels` on the B_{eq} map in a single column (as done above for the intensity and spectral index maps), using a two-component exponential fit, yields $h_{\mathrm{B,eq,disk}} = 0.34\,\mathrm{kpc}$ and $h_{\mathrm{B,eq,halo}} = 5.98\,\mathrm{kpc}$. While there is a remarkable discrepancy between the $h_{\mathrm{B,eq,disk}}$ values obtained with the two different methods, one of them is still compatible with our best-fitting h_{B1} value within the error limits. On the contrary, h_{B2} is $\approx 40\%$ lower than the equipartition value, indicating that equipartition is not a valid assumption in the halo of NGC 891.

Another source of uncertainty we have not mentioned so far is related to the synchrotron spectral index in the disk. Here, one likely observes a mixed spectrum of newly injected CREs and a slightly older population of CREs that have already lost a fraction of their initial energy but are still confined in SN-generated ISM bubbles and hence are not yet part of the vertical outflow. A spectral-age analysis of the non-thermal superbubble in the dwarf irregular galaxy IC 10 (Heesen et al. 2015) suggests such a scenario. Therefore, actual injection spectral indices in NGC 891 may be flatter than our assumed value of −0.82, while the effective values of the vertical spectral index profile around the mid-plane may be steeper. This, in turn, would flatten the slope of the spectral index profile at low z, which implies that for the disk component lower magnetic field

scale heights and/or higher convection speeds than those we determined above are possible.

In case of convection-dominated CR transport, the non-linear behaviour of the synchrotron scale heights as a function of CRE lifetime (Sect. 6.3) indicates that the decrease of the synchrotron intensity in z-direction is primarily due to the vertical decrease of the magnetic field strength rather than due to radiative energy losses. This suggests that the halo of NGC 891 is non-calorimetric, i.e. the CREs do not lose all their energy within the galaxy and are hence able to escape. To check whether this is consistent with the results of our diffusion-loss equation modelling, we determine the critical convection speed at which the CRE lifetime is equal to their escape time. According to Heesen et al. 2015 (submitted) this speed is defined as $v_{\mathrm{crit}} = h_{\mathrm{B}}/(2t_{1/2})$. At the transition height of 1 kpc we measure field strengths of $\approx 8\,\mu$G, implying lower-limit lifetimes of 27 Myr at 1.5 GHz and 14 Myr at 6 GHz. With $h_{\mathrm{B}} = 3.2$ kpc, this leads to required convection speeds of 59 and 114 km s^{-1}, respectively. These values are less than the lower error limits of our determined convection speeds in the halo, which shows that NGC 891 is a clearly non-calorimetric galaxy, where CRE energy losses do not dominate the vertical emission gradients.

The question whether we observe a galactic wind in NGC 891 can in principle be answered by comparing the convection speed to the escape velocity $v_{\mathrm{esc}} = \sqrt{2}v_{\mathrm{rot}}$. With a rotation velocity of 225 km s^{-1} (Swaters et al. 1997), we find $v_{\mathrm{esc}} = 318$ km s^{-1}, which is comparable to the halo convection speed of 280 km s^{-1}. Since this value is not well constrained in terms of an upper error limit, the presence of a galactic wind in NGC 891 is very likely. Also a possible acceleration or deceleration of the outflow within the halo, which is not known at this point, will influence whether it is able to leave the gravitational potential of the galaxy and thus qualify as a wind. CRs can stream along the magnetic field lines at the Alfvén speed $v_{\mathrm{A}} = B_{\mathrm{ord}}/\sqrt{4\pi\rho_{\mathrm{ion}}}$, which needs to be subtracted from the convection speed to obtain the actual wind speed. Since we have not determined the ordered magnetic field component, we use the average equipartition field strength in the halo of $\approx 5\,\mu$G as an upper limit to estimate v_{A}. From X-ray observations of NGC 891, Hodges-Kluck & Bregman (2013) found typical electron number densities in the halo of $n_{\mathrm{e}} \approx 5 \cdot 10^{-3}$ cm^{-3}, which according to Eq. 2.18 yields $v_{\mathrm{A}} \lessapprox 150$ km s^{-1} and hence $v_{\mathrm{wind}} \gtrapprox 130$ km s^{-1}.

As mentioned earlier, to also produce meaningful CR transport models for NGC 4565 would particularly require spectral index data of much better quality. Nonetheless, given the relatively faint halo emission of this galaxy and the fact that its vertical intensity distribution is well-represented not only by exponential profiles but also by Gaussian ones (Sect. 6.1.2), we expect diffusion models to be favoured over convection models for this galaxy.

7 Polarization and magnetic field distribution

In this chapter we present our measurements of the distribution of polarized radio emission in NGC 891 and NGC 4565, and draw inferences from these measurements about properties of the magnetic field distribution and the origin of the polarized emission within the two galaxies. In the first part we address the results of the "regular" MS-MFS imaging of our polarization data, while the second section begins with an introduction to the principles of RM synthesis, a method which provides additional, three-dimensional information on the intrinsic magnetic field geometry. This includes a description of the essential parameters of the method as well as its strengths and weaknesses, and is followed by an overview of the various RM-synthesis related data processing steps we performed. While describing the results of running RM synthesis on our L-band and C-band data, we also point out the disadvantage of missing essential data at frequencies within the gap between these two widely separated bands.
The final section deals with the distribution of the fractional degree of polarization within the galaxies. Here, our main purpose is to compare our data to the results of D97, who in particular measured a decrease of the fractional polarization in the upper halo of both galaxies.

7.1 Polarization information from MS-MFS imaging

The maps of polarized intensity and polarization position angle generated from our full-bandwidth MS-MFS imaging in Stokes Q and U (as described in Sect. 3.4.7) are presented in this section. Figures 7.1 (NGC 891) and 7.2 (NGC 4565) display the polarized intensity as contours overlaid on the corresponding total intensity maps, as well as the observed electric field vectors rotated by 90° to represent the apparent orientation of the magnetic field component perpendicular to the line of sight. Although the polarization angles do not provide any information on the field direction, we will occasionally refer to their graphic representation as magnetic field vectors throughout this chapter. In Figures 7.1 and 7.2, panel *a)* shows the result for the D-array observations at 1.5 GHz. We did not detect any significant polarized emission in the 1.5 GHz B- and C-array data, because, as evident from the D-array images, the disks of both galaxies are largely depolarized at this frequency, while polarization in the halo remains undetected in B- and C-array due to a lack of sensitivity, especially to large-scale polarized structures. Panel *b)* in each case shows the combination of the 6 GHz D-array and Effelsberg data. This was accomplished using the Stokes Q and U channels of the same 4.85 GHz Effelsberg observations that were already used for the merging in Stokes I (see Sect. 3.4.8). To obtain the single-dish Q and U

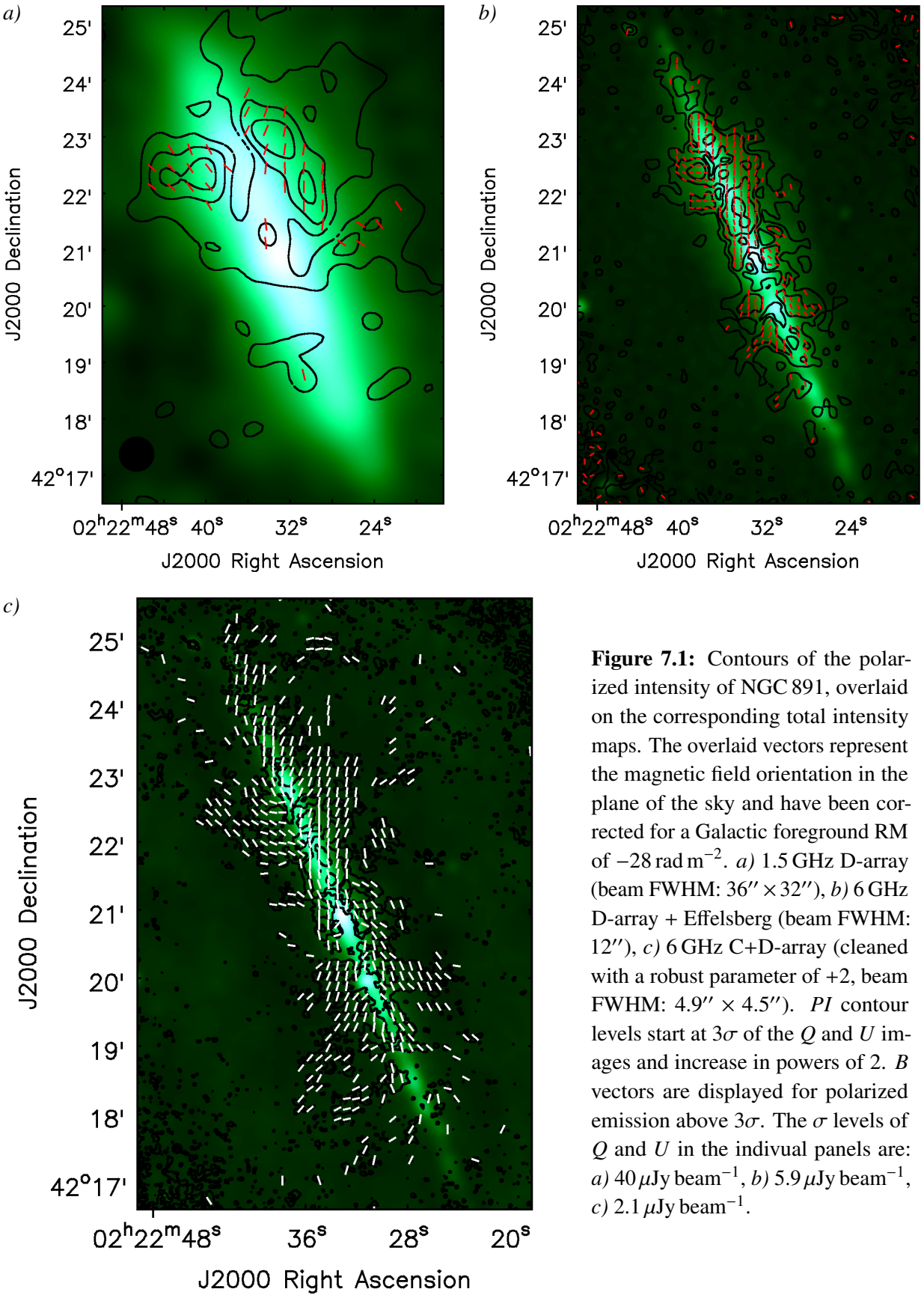

Figure 7.1: Contours of the polarized intensity of NGC 891, overlaid on the corresponding total intensity maps. The overlaid vectors represent the magnetic field orientation in the plane of the sky and have been corrected for a Galactic foreground RM of $-28\,\mathrm{rad\,m^{-2}}$. *a)* 1.5 GHz D-array (beam FWHM: $36'' \times 32''$), *b)* 6 GHz D-array + Effelsberg (beam FWHM: $12''$), *c)* 6 GHz C+D-array (cleaned with a robust parameter of +2, beam FWHM: $4.9'' \times 4.5''$). *PI* contour levels start at 3σ of the Q and U images and increase in powers of 2. B vectors are displayed for polarized emission above 3σ. The σ levels of Q and U in the indivual panels are: *a)* $40\,\mu\mathrm{Jy\,beam^{-1}}$, *b)* $5.9\,\mu\mathrm{Jy\,beam^{-1}}$, *c)* $2.1\,\mu\mathrm{Jy\,beam^{-1}}$.

maps at 6 GHz, we extrapolated the 4.85 GHz maps using the non-thermal spectral index between 4.85 and 8.35 GHz. This does not account for any frequency-dependent depolarization effects, but nevertheless appeared to be the most reasonable approach given the data products on hand. We computed thermal intensity maps at 4.85 and 8.35 GHz by applying the method described in Sect. 4.2, and smoothed them to the resolution of the Effelsberg telescope at 4.85 GHz. By subtraction of the smoothed thermal maps from the Effelsberg total power map at each frequency, we formed the corresponding non-thermal maps. We used the resulting distribution of the non-thermal spectral index between 4.85 and 8.35 GHz to scale the 4.85 GHz Q and U maps to 6 GHz and subsequently merged them with the JVLA D-array images. From the merged Q and U images, the displayed polarized intensity and position angle maps were formed. In panel *c)* we show the polarization maps resulting from combined imaging of the 6 GHz C- and D-array data. Here, a robust-weighting of +2 was used for both galaxies, which considerably improved the signal-to-noise ratio compared to the robust-0 case.

7.1.1 NGC 891

Since the location of NGC 891 on the sky is fairly near to the Galactic plane, the effect of Faraday-rotating plasma in the Galactic foreground on the polarized signal from NGC 891 needs to be taken into account. In the map of the Galactic Faraday sky presented by Oppermann et al. (2012), we find an RM value of $-74\,\mathrm{rad\,m^{-2}}$ for the nearest resolution element. However, our RM synthesis results for this galaxy (which we present in Sect. 7.2.2) rather suggest a foreground RM of $-28\,\mathrm{rad\,m^{-2}}$. Such a discrepancy is understandable considering that at $\approx 30'$ the resolution of the Galactic RM map is much lower than that of our observations. The foreground RM of $-28\,\mathrm{rad\,m^{-2}}$ results in a rotation of the polarization plane of $-58°$ at 1.5 GHz and $-4°$ at 6 GHz. Here, a negative sign corresponds to clockwise rotation, hence we performed the foreground correction by rotating our magnetic field vectors by these values in counterclockwise direction.

In the 1.5 GHz data (Fig. 7.1 *a)*), polarized emission appears mainly in two extended regions in the northeast and northwest quadrant of the halo. Parts of the well-known X-shaped halo component of the magnetic field are visible in the polarized regions. Except for a local maximum slightly north of the centre, the disk is largely depolarized. The intermediate-resolution image at 6 GHz (panel *b)*) basically shows the same polarized morphology as observed at 4.85 GHz by D97. At least on the eastern side, the observed distribution reflects the dumbbell shape of the total radio emission, with indications of the X-shaped field geometry being present in all four (lower) halo quadrants. Also, there is a larger amount of vertically extended emission above the centre on the west side than on the east side. While we observe more polarized emission near the disk than at 1.5 GHz, the southern disk is still mostly depolarized. Hummel et al. (1991a) found that at 1.5 GHz the primary cause for the depolarization in the disk of NGC 891 is most likely Faraday dispersion by the turbulent magnetic field component. At 6 GHz, however, the disk depolarization is primarily due to local disordering of the magnetic field, e.g. by star formation or due to instabilities that bend the field lines and draw them out of the galactic plane (see Sukumar & Allen 1991). Thus, at 6 GHz the disk emission is depolarized already at its origin, rather than by a turbulent field layer. The regular magnetic field component is typically strongest in the regions between the spiral arms, often forming so-called magnetic arms, which can extend

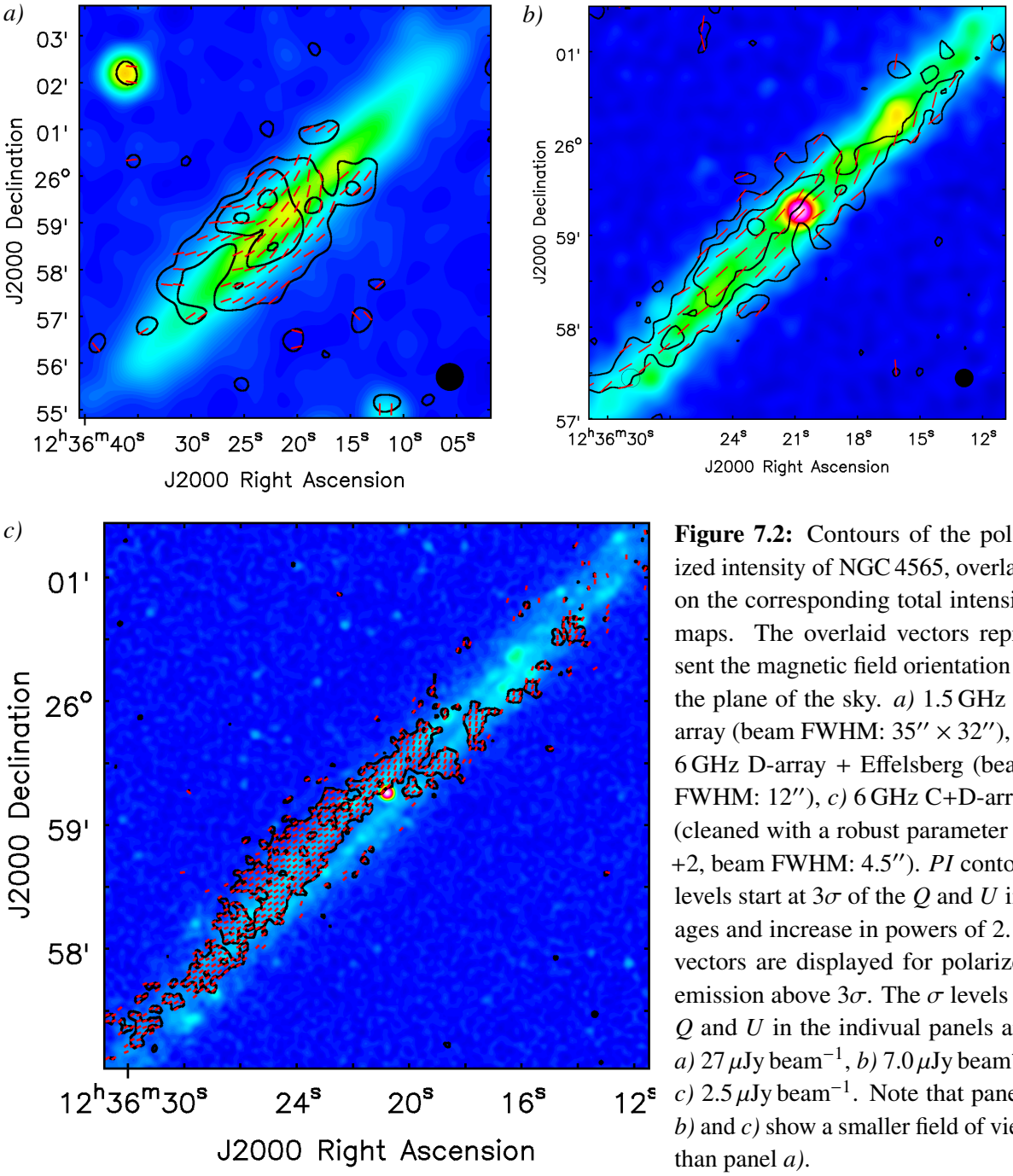

Figure 7.2: Contours of the polarized intensity of NGC 4565, overlaid on the corresponding total intensity maps. The overlaid vectors represent the magnetic field orientation in the plane of the sky. *a)* 1.5 GHz D-array (beam FWHM: $35'' \times 32''$), *b)* 6 GHz D-array + Effelsberg (beam FWHM: $12''$), *c)* 6 GHz C+D-array (cleaned with a robust parameter of +2, beam FWHM: $4.5''$). *PI* contour levels start at 3σ of the Q and U images and increase in powers of 2. B vectors are displayed for polarized emission above 3σ. The σ levels of Q and U in the indivual panels are: *a)* 27 μJy beam^{-1}, *b)* 7.0 μJy beam^{-1}, *c)* 2.5 μJy beam^{-1}. Note that panels *b)* and *c)* show a smaller field of view than panel *a)*.

out to larger radii than the optical spiral arms (see e.g. Beck 2007). Hence, the reason why the depolarization is observed only in the southern half of the galaxy might be that here we have a direct view on the end section of one or more magnetic arms, which would imply that the magnetic field is mainly oriented parallel to the line of sight. Accordingly, in the northern half the (magnetic) spiral arm nearest to the observer is probably mostly oriented in the direction of the major axis. In the 6 GHz C+D-array map (panel *c)*) many of the extraplanar features are further resolved into narrow vertical filaments. One such filament appears near the northern edge

of the disk, where it forms an arc turning over to the west. Another prominent vertical feature is located in the northwest quadrant of the halo, at a larger distance from the plane than the bulk of the polarized emission. This filament creates the impression of joining ends with the northern arc, and thereby forming a nearly closed loop, since the field vectors are aligned very well with both structures. Interestingly enough, this loop-like feature extends above the disk in about the same direction as the major filament seen in the HI map of Oosterloo et al. (2007). On the other hand, it should be noted that these data are not corrected for missing short spacings, and it cannot be ruled out that parts of the filamentary features are merely deconvolution artifacts or noise peaks amplified by the primary-beam correction. Moreover, a loop-like structure could not be confirmed by our RM synthesis results (see below).

7.1.2 NGC 4565

Near the location of NGC 4565, the Galactic RM map of Oppermann et al. (2012) shows a value of $+6\,\mathrm{rad\,m^{-2}}$, while D97 reports a foreground RM of $-3\,\mathrm{rad\,m^{-2}}$. We therefore assume that foreground Faraday rotation is negligible for this galaxy and hence according corrections are not necessary.

Apart from a predominantly plane-parallel magnetic field orientation, our D-array data at 1.5 GHz (Fig. 7.2 *a)*) also show field lines bending away from the plane, especially on the northeast side of the galaxy, where they seem to hint at an X-shaped halo field configuration (provided that the emission originates from a sufficiently thin layer to not be significantly Faraday-rotated). This is also evident from the 1.5 GHz map of Sukumar & Allen (1991) and (at least on the west side) in the 4.85 GHz map of D97. Although this feature is discussed by neither of these authors, it suggests that at least on the northeast side the emission observed at the largest (projected) distances from the mid-plane is generated in the halo rather than being beam-broadened disk emission.

The polarized structure seen in the short-spacing corrected 6 GHz D-array map (panel *b)*) clearly has its origin in the disk, since no polarized halo component can be identified at this frequency. Our high-resolution data at 6 GHz (panel *c)*) shows that the bulk of the polarized emission originates from the front[1] side of the disk on the southeast side. In addition, polarized regions appear on the back side of the disk in the northwestern half of the galaxy. This may be explained by a similar spiral-arm related antisymmetry as for NGC 891, but in this case with the front and back side resolved from each other, due to the lower inclination angle. The antisymmertric polarization distribution suggests that in the southeastern half a magnetic arm is in the foreground on the front side and a non-magnetic arm is in the foreground on the back side, while in the northwestern half the situation is vice-versa.

[1]The front side of the galaxy is the side northeast of the mid-plane, compare Fig 1.2.

7.2 RM synthesis

Measuring polarized synchrotron radiation at a given frequency only provides two-dimensional information on the magnetic field structure, since the polarized intensity (intrinsically) is a measure of the magnitude of the magnetic field vector projected onto the plane of the sky ($B_\perp$), and the polarization angle corresponds to the field orientation in this plane. As mentioned in Sect. 2.5, the effect of Faraday rotation can be utilized to obtain information on the line-of-sight magnetic field component $B_\parallel$. The key quantity in this case is the rotation measure (RM), which is defined by Eq. 2.25.

Traditionally, RMs are determined directly from the different polarization angles observed at different frequencies. However, adding multiples of 180° to the rotation of the polarization vector between two frequencies would result in the same observed angle difference. This requires at least a third observing frequency and a linear least-squares fit to the polarization angles as a function of λ^2. Still, this so-called $n\pi$ ambiguity is not easily resolved with only a small number of observing frequencies, as Fig. 1 of Rand & Lyne (1994) illustrates. Another serious problem is bandwidth depolarization, wich occurs if the polarization vector rotates by 90° or more within a given frequency band. While this effect can be prevented by splitting up the band into narrow frequency intervals for imaging Stokes Q and U, the S/N of faint sources may fall below the detection limit if the chosen frequency intervals are too small. Also, traditional RM measurements cannot account for variations in the Faraday-rotating medium along the line of sight.

A method exists to overcome the above obstacles and moreover to correct for depolarization arising from differential Faraday rotation (for line-of-sight polarization angle differences less than 90°). It was initially introduced by Burn (1966) and further developed by Brentjens & de Bruyn (2005) (all formulas in this section are taken from this publication), who named the technique RM synthesis.
If a source of polarized emission is extended in line-of-sight direction, the observed rotation measure may depend on the place of origin of the emission on the line of sight through the source, which is the case if Faraday rotation happens within the source itself, rather than in a non-emitting foreground layer. This position-dependent RM is known as Faraday depth $\phi(r)$, the formal definition of which remains unchanged:

$$\phi(r) = 0.81 \int_0^{r_0} \left(\frac{n_\mathrm{e}}{\mathrm{cm}^{-3}}\right)\left(\frac{B_\parallel}{\mu G}\right) \mathrm{d}r \ \mathrm{rad\,m}^2 \tag{7.1}$$

The classical RM, on the other hand, can be understood as the difference between two Faraday depth values, and often refers to the net amount of Faraday rotation within a polarized structure that is not resolved in Faraday depth.

The distribution of the polarized emission can be expressed as a function of Faraday depth, $F(\phi)$, which is called the Faraday dispersion function and relates to the complex polarization vector $P(\lambda^2) = Q(\lambda^2) + iU(\lambda^2) = pI(\lambda^2)e^{2i\phi\lambda^2}$ as its Fourier transform:

$$F(\phi) = \int_{-\infty}^{+\infty} P(\lambda^2) e^{-2i\phi\lambda^2} \, \mathrm{d}\lambda^2 \tag{7.2}$$

Since in practice only a finite range in λ^2 space is sampled (and in particular $\lambda^2 < 0$ is unphysical), RM synthesis provides the reconstructed Faraday dispersion function $\tilde{F}(\phi)$, which can be approximated as a sum over the individual frequency channels[2] (see Brentjens & de Bruyn 2005):

$$\tilde{F}(\phi) = F(\phi) * R(\phi) \approx K \sum_{c=1}^{N} w_c P_c e^{-2i\phi(\lambda_c^2 - \lambda_0^2)} \tag{7.3}$$

where $K = \left(\sum_{c=1}^{N} w_c\right)^{-1}$, w_c is the weight[3] of the cth frequency channel, and λ_0 is usually set to the central wavelength within the observing band. The above expression corresponds to the convolution of $F(\phi)$ with the rotation measure spread function (RMSF) $R(\phi)$. The latter is given by

$$R(\phi) \approx K \sum_{c=1}^{N} w_c e^{-2i\phi(\lambda_c^2 - \lambda_0^2)} \tag{7.4}$$

and represents the instrumental response for measuring $F(\phi)$, in analogy to the synthesized beam in aperture synthesis interferometry.

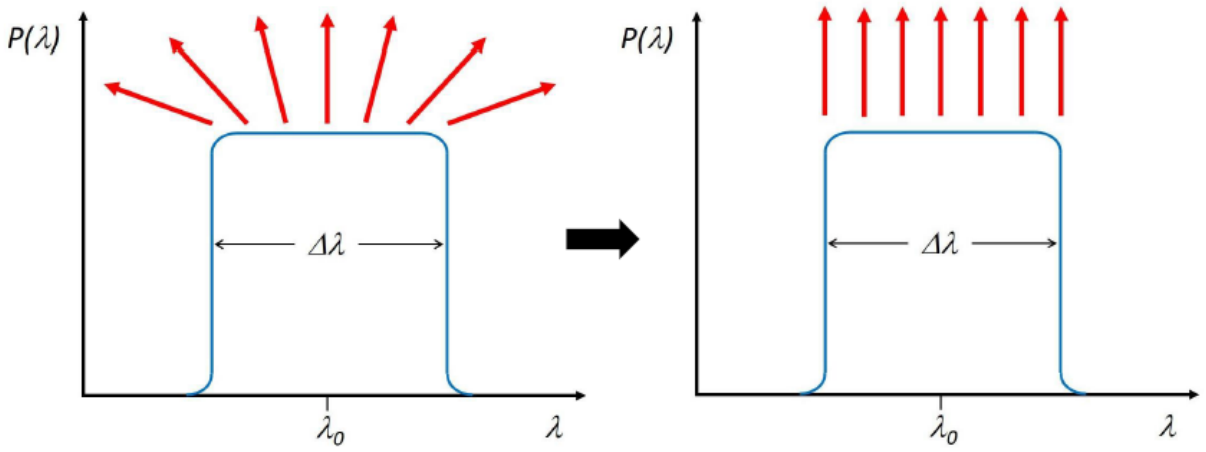

Figure 7.3: Illustration of the basic principle of RM synthesis. The RM for a given line of sight is determined by the de-rotation of the polarization vector across multiple wavelength channels such that the vector addition of all channels maximizes the signal. Image credit: U. Klein

Obtaining $\tilde{F}(\phi)$ (for a particular line of sight) from polarization data in multiple frequency channels can be visualized as finding the value of ϕ for which adding up the accordingly rotated complex polarization vectors of all channels results in the maximum possible polarized intensity. A simple illustration of this process is given in Fig. 7.3. By combining the polarized signal from all channels, the S/N of the full bandwidth is achieved, while at the same time the effects of bandwidth depolarization, differential Faraday rotation, and the $n\pi$ ambiguity are minimized. Furthermore, depending on the distribution of synchrotron-emitting sources and Faraday-rotating

[2] In this chapter, the term frequency channel does not necessarily refer to an individual channel of the original *uv* data, since any number of such channels can be averaged to form a single channel of an image cube.

[3] In our case, a uniform weighting across the frequency band is used, i.e. $w_c = 1$ for each channel.

plasma along a given line of sight, $\tilde{F}(\phi)$ will show emission at multiple values of ϕ, and is hence also called Faraday spectrum.
The shape of the Faraday spectrum is shown for three simplified cases in Fig. 7.4. An idealized point source with an intrinsic RM of $+100\,\mathrm{rad\,m^{-2}}$ will produce the $F(\phi)$ spectrum shown in the top panel, which is simply a delta function at this value, with the amplitude corresponding to the polarized flux density of the source. In the centre panel, the signal of this source is Faraday-rotated within a layer of magnetized plasma having an RM of $-50\,\mathrm{rad\,m^{-2}}$, which shifts the measured RM to $+50\,\mathrm{rad\,m^{-2}}$. If the rotating medium emits synchrotron radiation by itself (bottom panel), it adds a continuous distribution of Faraday depths to the spectrum. For a uniform magnetic field and electron distribution in this source (in which case it is also known as a Burn slab), the observed structure in $F(\phi)$ has the shape of a boxcar function.

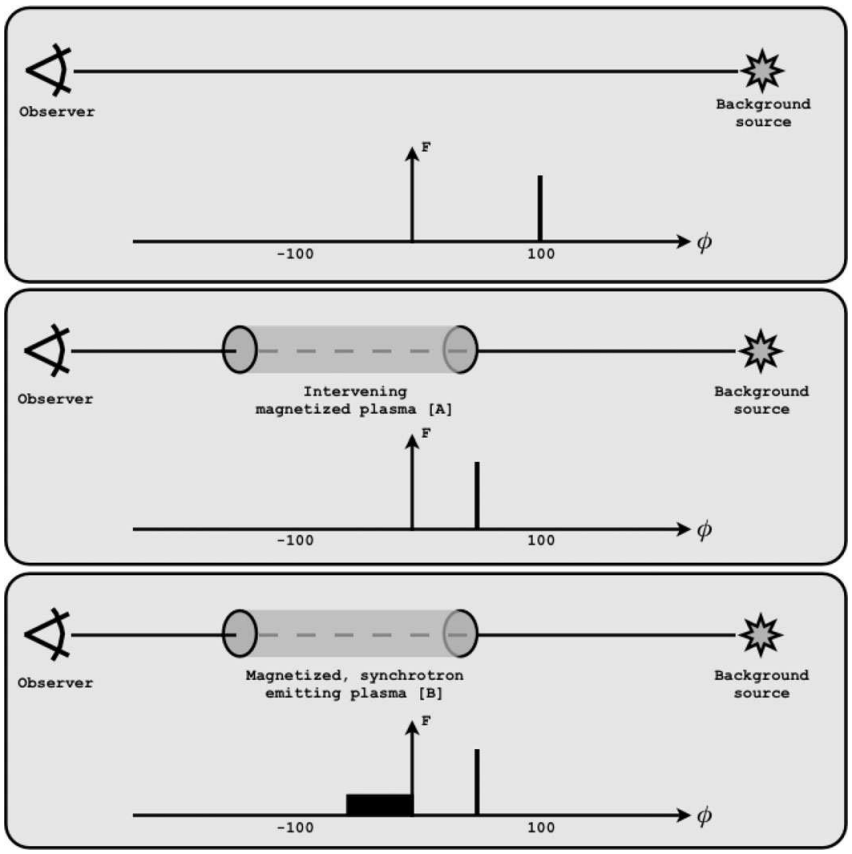

Figure 7.4: The observed Faraday spectrum for three idealized situations. The Faraday depth ϕ is given in $\mathrm{rad\,m^{-2}}$. Image taken from Heald (2009). See text for an explanation of the individual panels.

For real observations, the Faraday spectrum is convolved with the RMSF, as explained above. The resolution in Faraday depth space is given by the FWHM $\delta\phi$ of the RMSF:

$$\delta\phi \approx \frac{2\sqrt{3}}{\Delta\lambda^2} \tag{7.5}$$

where $\Delta\lambda^2$ is the separation in λ^2-space between the lowest and highest frequency channel. The

maximum width in ϕ space that extended structures (e.g. Burn slabs) may have to be fully detectable is determined by the shortest wavelength of the observing band:

$$\text{maxscale} \approx \frac{\pi}{\lambda^2_{\text{min}}} \tag{7.6}$$

This is similar to the problem of missing short spacings in aperture synthesis. Lastly, the maximum absolute Faraday depth value at which emission can be detected depends on the channel width $\delta\lambda^2$:

$$||\phi_{\text{max}}|| \approx \frac{\sqrt{3}}{\delta\lambda^2} \tag{7.7}$$

RM synthesis suffers from a range of further shortcomings, apart from the above-given natural limitations in measuring Faraday depths:

- With a frequency-dependent angular resolution a correct determination of Faraday depths would not be possible. This makes it necessary to enforce a common synthesized beam size for all frequency channels by applying either a common *uv*-taper or common restoring beam. Therefore, the final angular resolution is always limited by the beam size at the lowest frequency.

- The noise level in the individual channel images is higher than for an image formed using the full bandwidth, which implies also higher cleaning thresholds. This can result in stronger residual side lobe patterns than one would obtain with MFS imaging.

- RM synthesis is unable to recover emission that is completely depolarized by differential Faraday rotation. Sources in which this effect occurs can only partially be probed in line-of-sight direction, and are hence called Faraday-thick.

- The intrinsic emission spectra of sources can be an issue, as RM synthesis will treat spectral variations over the sampled frequency range as bandwidth depolarization. This has no significant effect on the observed Faraday depths as the ratio between Q and U remains unchanged. However, for steep spectral indices (as observed in the halos of edge-on galaxies), amplitudes in the Faraday spectrum, and hence the intrinsic polarized intensity of a source, may be severely over- or underpredicted, depending on the sign of the spectral index.

Just like the synthesized beam of an interferometric observation, the RMSF features side lobes (in this case due to incomplete sampling of the λ^2 domain), which can make it difficult to identify structures in the Faraday spectrum even at fairly high amplitudes. To solve this problem, Heald et al. (2009) developed a deconvolution method called `RM-CLEAN`, which applies the `CLEAN` algorithm of Högbom (1974) to the one-dimensional case of deconvolution in the Faraday depth domain.

7.2.1 From data cubes in Stokes Q and U to RM maps and derotated polarization angles

To prepare our polarization data for the application of RM synthesis, we first generated images cubes in Q and U, with one image plane per spectral window (for a description of the *uv* data structure, see Sect. 3.1). The individual images were obtaind by running MS-MFS clean on each spectral window, using one Taylor-term and a robust weighting of +2. For both frequency bands we imaged the combination of all array configurations, i.e. B+C+D-array for L-band and C+D-array for C-band. After cleaning, all images were smoothed to a resolution of 12″ and corrected for the primary beam at the respective frequencies.

Without applying RM synthesis, for a rotation measure of 100 rad m^{-2} (as can occur in disks of edge-on galaxies), bandwidth depolarization within L-band would reduce the observed degree of polarization to ≈10% of the intrinsic polarization degree (complete depolarization happens at $RM = 109$ rad m^{-2}), while for C-band this fraction would still be ≈99%. On the other hand, for an RM of 50 rad m^{-2}, L-band data would still show ≈70% of the intrinsic value.
In our case, the maximum rotation of the polarization vector across a single spectral window occurs for the lowest-frequency spectral window in L-band[4], which ranges from 1.295 to 1.311 GHz, corresponding to a λ^2 range between 523 and 536 cm^2. A rotation of 90° within this range would require an absolute RM value of 1208 rad m^{-2}. Rotation measures of this order have only been observed in AGNs so far, while for normal galaxies, maximum values of a few hundred rad m^{-2} are usual. Moreover, in L-band we observe much lower RMs due to strong depolarization by differential Faraday rotation and/or internal Faraday dispersion (see below). Therefore, one image plane per spectral window is sufficient in our case to avoid significant bandwidth depolarization as well as the $n\pi$ ambiguity problem.

By running the RM synthesis code written by M. Brentjens on the Q and U frequency cubes, we generated Faraday cubes in Q, U, as well as PI. These cubes have the Faraday depth ϕ as the third axis, and thus represent $\tilde{F}(\phi)$. For both galaxies, RM synthesis was performed separately for the L-band and C-band data, and was also run using the Q and U channels of both frequency bands together. In case of the L-band cubes as well as for the combined L+C-band cubes we sampled the ϕ domain between -2000 and +2000 rad m^{-2}, with a channel separation of 8 rad m^{-2}. The C-band Faraday cubes range from -8000 to +8000 rad m^{-2} and have a channel separation of 256 rad m^{-2}.

Using `RM-CLEAN`, we cleaned the Faraday spectra down to the 5σ-noise level in the individual planes of the Faraday Q and U cubes. The cleaned PI cubes were then corrected for the polarization bias. Since the image planes had already been primary-beam corrected, we used a routine written by B. Adebahr, which performs the following procedure: each pixel in the sky plane is averaged along the ϕ axis of the cube, with the exclusion of regions containing polarized emission. In this averaged map, a parabola is fitted to each one-dimensional cross-section of pixels through the pointing centre. The parabolic fits in all directions collectively form a model of the noise floor, which is then subtracted from each channel of the PI cube.

[4]The lowest-frequency data we used for imaging are those in the fourth L-band spectral window, as the first three spectral windows of each L-band data set were flagged entirely due to strong RFI contamination.

After applying these corrections, the following data products were computed from the Faraday cubes:

- A *PI* map, consisting of the maximum value along the ϕ axis of the *PI* cube for each pixel in RA-DEC space.
- A map of the peak RM[5], which for each pixel corresponds to the ϕ value at which the maximum in the *PI* cube occurs.
- The derotated (i.e. "intrinsic") polarization angles, which at each position are calculated from the peak RM value and the values in the corresponding ϕ plane of the Faraday Q and U cubes.

Each of the above maps were computed only in regions where the polarized intensity is higher than 5 times the noise in the Faraday Q and U image planes.

7.2.2 Results

In Table 7.1 the parameters given by Eq. 7.5-7.7 are listed for the L-band, C-band, and L+C-band cubes. The dirty RMSF (before running `RM-CLEAN`) in *PI* for all three cases is shown in Fig. 7.5. We find that while there is a huge difference between the FWHMs of the RMSF in the L-band and C-band cubes, the maximum detectable ϕ scale in both cases is similar to or less than the RMSF FWHM, which determines the Faraday-depth resolution. As a result of combining the data in both bands, apart from an improved S/N, we achieve a twice as high ϕ resolution as for L-band alone, while being able to detect structures in ϕ space on the same large scales as for C-band alone. However, the large gap in the λ^2 coverage between the two bands introduces severe side-lobe levels to the RMSF, in the same way as side lobes of an interferometric synthesized beam are caused by gaps in the *uv* coverage. As evident from Fig. 7.5 *c)*, the average side-lobe amplitudes form a structure that has a width similar to that of the C-band RMSF. As we shall see below, this effect makes it impossible in our case to observe much higher RM values than in L-band alone.

Table 7.1: Characteristic parameters of the Faraday cubes in L-band, C-band, and the combination of both bands. All values are given in rad m^{-2}.

	$\delta\phi$	maxscale	$\|\|\phi_{\max}\|\|$
L-band (λ16-23 cm)	124	126	1211
C-band (λ4-6 cm)	2065	1960	5188
L+C-band (λ4-23 cm)	68	1960	1211

[5]To avoid confusion, we note that this term has been adopted, even though it is technically a specific value of Faraday depth.

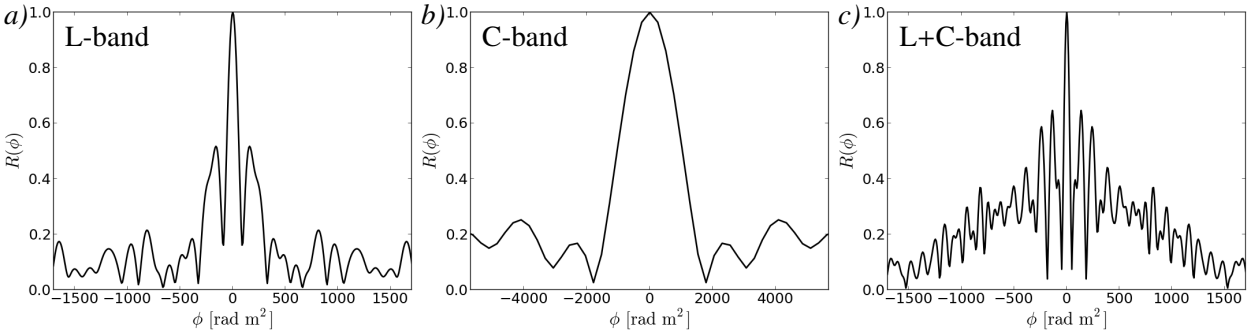

Figure 7.5: Polarized intensity of the RMSF resulting from the application of RM synthesis to our different sets of polarization data. *a)* L-band (λ16-23 cm), *b)* C-band (λ4-6 cm), *c)* L- and C-band combined. Note the different scale on the ϕ axis in panel *b)*.

7.2.2.1 NGC 891

By applying RM synthesis to the L-band data of NGC 891, the overall extent of the polarized intensity distribution (Fig. 7.6 *a)*) has increased considerably compared to the map obtained by regular MS-MFS imaging. In particular, polarized emission now also appears in the southeast and southwest quadrants of the halo, which means that the reason for the absence of this emission in Fig. 7.1 *a)* is most likely bandwidth depolarization or differential Faraday rotation. Inspecting the histogram of the peak RM values in the Faraday *PI* cube for L-band revealed the highest pixel count at $-28\,\mathrm{rad\,m^{-2}}$ and a symmetric distribution of RMs around this value, which we hence adopted as the Galactic foreground RM for NGC 891. In all three peak RM maps of this galaxy (Fig. 7.6 *c)* and *d)* , Fig. 7.8 *a)*), this foreground value has been subtracted. Accordingly, the derotated magnetic field vectors overlaid on these maps have been corrected for the foreground RM as well.
In L-band our maximum detectable scale in ϕ space is $126\,\mathrm{rad\,m^{-2}}$, which means that structures that extend over a range in ϕ space larger than this value (and are not already depolarized by other effects) are completely depolarized by differential Faraday rotation. This explains why in Fig. 7.6 *c)* we only find RM values within $\approx \pm 50\,\mathrm{rad\,m^{-2}}$. Thus, at least in the disk, the L-band data are only probing a thin emitting layer of the galaxy that is near to the observer, while emission from behind this layer is depolarized by differential Faraday rotation. On the other hand, parts of the halo may in fact be Faraday-thin, as here the intrinsic RMs are expected to be significantly lower than in the disk.

The polarized intensity pattern we obtain in C-band (Fig. 7.6 *b)*) is similar to that in Fig. 7.1 *b)*, but with a higher amount of detected extraplanar emission. However, some of the visible extraplanar structures, such as the rather diffuse high-z emission on the west side or the elongated feature above the centre on the east side are possibly just residual cleaning artifacts. We find the majority of absolute values in the C-band RM map (Fig. 7.6 *d)*) to be less than $100\,\mathrm{rad\,m^{-2}}$. This implies that at 6 GHz relatively little Faraday rotation ($\lessapprox 15°$) occurs throughout most parts of the galaxy, so that at this frequency one roughly observes the intrinsic magnetic field orientation already without applying RM synthesis. The major shortcoming of performing RM synthesis in C-band is that due to the broad RMSF it does not enable us to resolve any line-of-sight variations

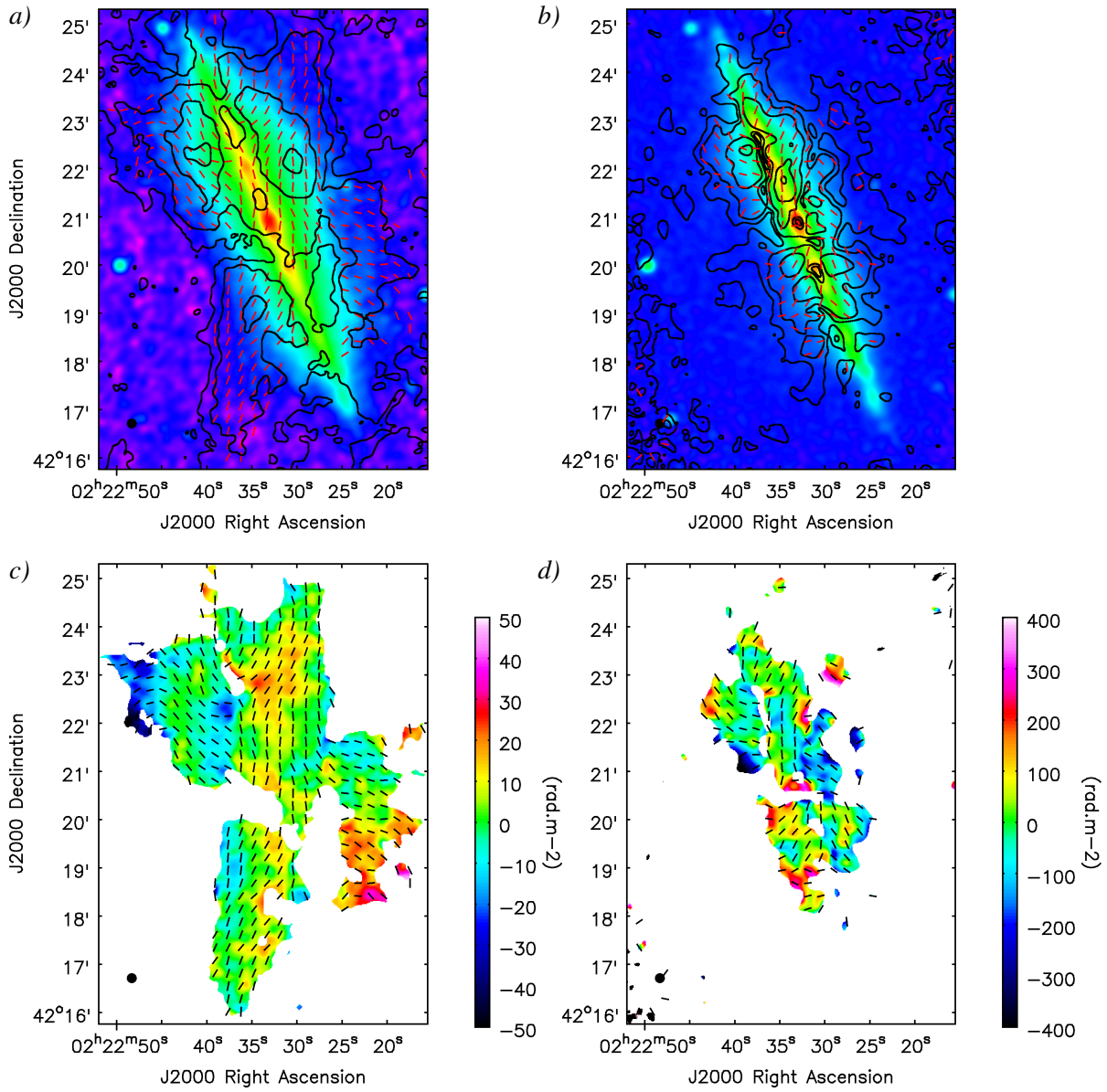

Figure 7.6: RM synthesis results for NGC 891. *a)* Contours of the polarized intensity obtained from running RM synthesis on the L-band B+C+D-array data, overlaid on the 1.5 GHz B+C+D-array total intensity map. *b)* Contours of the polarized intensity obtained from running RM synthesis on the C-band C+D-array data, overlaid on the 6 GHz D-array+Effelsberg total intensity map. *c)* Peak RM map obtained from running RM synthesis as specified for panel *a)* . *d)* Peak RM map obtained from running RM synthesis as specified for panel *b)* . The *B* vectors shown in all panels have been derotated according to the respective peak RM values and are shown for emission above 5σ in the respective Faraday Q and U cubes. The σ level in the Faraday Q and U cube channels is $20\,\mu$Jy beam^{-1} in panels *a)* and *c)*, and $8\,\mu$Jy beam^{-1} in panels *b)* and *d)*. The beam FWHM in all panels is $12''$.

in the magnetized medium, such as field reversals.
As discussed further above, the emission producing the *PI* maximum in C-band originates from the front edge of the northern part of the disk. In this region, we observe similar polarization angles ($\approx 20°$ clockwise from the mid-plane) in the RM synthesis maps of both frequency bands (Fig. 7.6 *c)* and *d)*). Considering the fairly low rotation measures in this region, this is an indication that our choice of $-28\,\mathrm{rad\,m^{-2}}$ for the foreground correction of the angles in Fig. 7.1 is appropriate.
In both the L-band and C-band RM synthesis data, in the northern part of the disk an entirely depolarized region is visible, which is elongated along the mid-plane. Here, the magnetic field direction seems to change from parallel to the plane to almost perpendicular to the plane on an unresolved spatial scale, which leads to beam depolarization.

In the RM map resulting from the combination of the L- and C-band data (Fig. 7.8 *a)*) we observe only slightly higher absolute RMs than in the pure L-band RM map, for the above-specified reasons. We do not probe much deeper into the galaxy by combining the two bands, since for the L-band data part of the polarization information is lost due to differential Faraday rotation and cannot be recovered. The extreme side-lobe patterns furthermore make it impossible to recover structures at larger Faraday depths with `RM-CLEAN`. Since the two frequency bands probe very different structures in ϕ space, replacing the L-band data by S-band observations (i.e. 2-4 GHz) is expected to considerably improve upon our present situation.

The L-band and L+C-band RM maps show mostly positive values in the northwest and southeast quadrants, while mainly negative values are found in the northeast quadrant. This pattern seems suggestive of a quadrupolar halo field configuration (which would, however, not explain the positive region near the disk in the southwest quadrant). However, the data do not provide any information on possible field reversals along the line of sight, and hence do not allow any conclusive statements on the three-dimensional field geometry.

7.2.2.2 NGC 4565

For both frequency bands, the RM-synthesis based polarized intensity maps of NGC 4565 (Fig. 7.7 *a)* and *b)*) show a similar distribution to that observed in the MS-MFS-based maps. In the C-band image we additionally observe two extraplanar features elongated parallel to the disk, which are clearly residual side-lobe artifacts arising from a low cleaning threshold in the Q and U channel maps.

The very low L-band RMs between $\approx \pm 15\,\mathrm{rad\,m^{-2}}$ (see Fig. 7.7 *c)*) indicate that only emission from an outer layer of the galaxy is observed, for the same reasons as already mentioned for the case of NGC 891. The derotated magnetic field vectors show deviations from a plane-parallel orientation, however not as coherently as in Fig. 7.2 *a)* , which may be attributed to the large difference in angular resolution.
Like for NGC 891, the polarization angles of NGC 4565 in C-band do not differ much from those obtained without RM synthesis. While the C-band RM distribution (Fig. 7.7 *d)*) mainly shows values between $\approx \pm 150\,\mathrm{rad\,m^{-2}}$, we observe two regions with RMs of up to $300\,\mathrm{rad\,m^{-2}}$ on the northwest side of the galaxy. These are possibly associated with inter-arm regions viewed

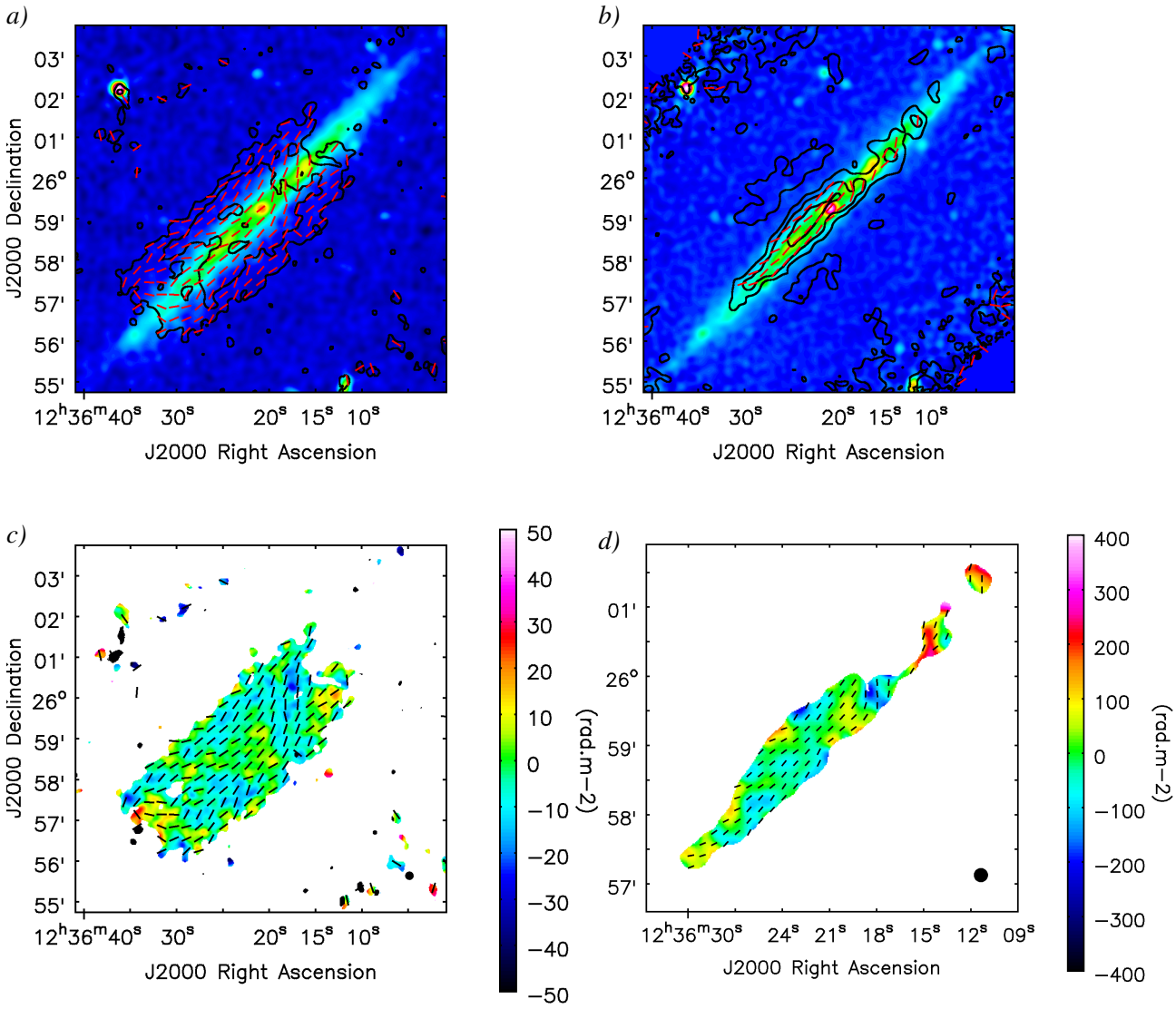

Figure 7.7: RM synthesis results for NGC 4565. *a)* Contours of the polarized intensity obtained from running RM synthesis on the L-band B+C+D-array data, overlaid on the 1.5 GHz B+C+D-array total intensity map. *b)* Contours of the polarized intensity obtained from running RM synthesis on the C-band C+D-array data, overlaid on the 6 GHz D-array+Effelsberg total intensity map. *c)* Peak RM map obtained from running RM synthesis as specified for panel *a)* . *d)* Peak RM map obtained from running RM synthesis as specified for panel *b)* . The *B* vectors shown in all panels have been derotated according to the respective peak RM values and are shown for emission above 3σ in the respective Faraday Q and U cubes in panels *a)* and *c)*, and above 5σ in panels *b)* and *d)*. The σ level in the Faraday Q and U cube channels is $18\,\mu$Jy beam^{-1} in panels *a)* and *c)*, and $6\,\mu$Jy beam^{-1} in panels *b)* and *d)*. The beam FWHM in all panels is $12''$. Note that panel *d)* shows a smaller field of view than the other panels.

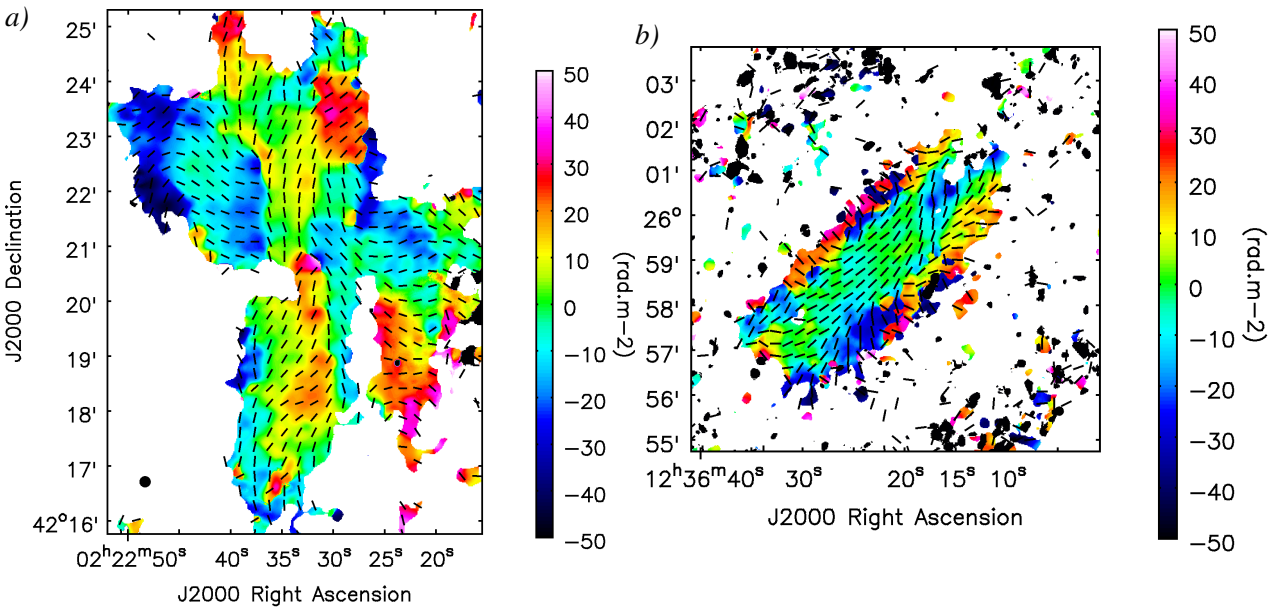

Figure 7.8: Peak RM maps obtained from running RM synthesis on the combination of the L-band B+C+D-array and C-band C+D-array data of NGC 891 (panel *a)*) and NGC 4565 (panel *b)*). The overlaid B vectors in both panels have been derotated according to the respective peak RM values and are shown for emission above 5σ in the respective Faraday Q and U cubes in panel *a)* and above 3σ in panel *b)*. The σ level in the Faraday Q and U cubes is $10\,\mu$Jy beam^{-1} in panel *a)* and $12\,\mu$Jy beam^{-1} in panel *b)*. The beam FWHM in all panels is $12''$.

end-on, i.e. at the turn-over point from the front to the rear side, where the magnetic field has its maximum line-of-sight component. This picture is supported by the fact that both regions coincide with minima in the total intensity map (see Fig. 7.7 *b)*).

For the combination of L- and C-band, we face the same problem as in the case of NGC 891, i.e. emission at Faraday depths of order $\pm 100\,\mathrm{rad\,m^{-2}}$, like those appearing in the disk as found from the pure C-band data, cannot be identified due to the high side lobes of the RMSF. However, as the halo (or rather the detected parts of it) becomes somewhat more Faraday-thin compared to the L-band data alone by including the C-band data, more distinct vertical magnetic field components are revealed (Fig. 7.8 *b)*). On the northeastern side, field vectors seem to take on an orientation perpendicular to the plane at some height above the disk, while the southwestern side shows indications of an X-shaped halo field.
At the largest probed vertical heights, RM values up to $\approx \pm 30\,\mathrm{rad\,m^{-2}}$ are observed. Positive RMs dominate in the western half of the southwestern edge and in the eastern half of the northeastern edge, and vice versa for negative RMs. This antisymmetry suggests the presence of a quadrupolar field in the halo of this galaxy as well. On the other hand, it cannot be ruled out that the distinctness of this structure is an edge artifact, possibly arising from the fact that we did not correct our Q and U data cubes for missing short spacings.

7.3 Fractional polarization in the halo

We present maps of the fractional polarization $p = \sqrt{(Q^2 + U^2)/I^2}$ for NGC 891 in Fig. 7.9 and for NGC 4565 in Fig. 7.10. Panels *a)* and *b)* in both figures show the p distributions obtained from the 1.5 GHz D-array maps and from the merged 6 GHz D-array and Effelsberg maps, respectively, using the Q and U maps resulting from full-bandwidth MS-MFS imaging. In all cases, an overall increase of p with vertical distance from the plane is evident, which is primarily a consequence of the high depolarization of the disk emission. Especially at 6 GHz the fractional polarization in both galaxies shows a clear anticorrelation with the Hα emission in the disk plane. Particularly in the halo, higher fractional polarizations are reached at 6 GHz than at 1.5 GHz, since Faraday depolarization effects are stronger at the lower frequency.

If the fractional polarization is calculated from the polarized intensity distribution obtained using RM synthesis (panels *c)* and *d)* of Fig. 7.9-7.10), values of $p > 75\%$ (and even $p > 100\%$) are reached at large vertical heights. These unphysical values show that the polarized intensities inferred from the Faraday cubes are highly overestimated, as a consequence of the spectral behaviour within the frequency bands being erroneously treated as bandwidth depolarization. This effect is particularly severe in the halo, where the steepest spectral indices occur. The extraplanar spectra are furthermore affected by missing short spacings, which our Q and U cubes were not corrected for. In this case, short-spacing corrections would have to be done for each cube channel separately.

By averaging the p maps obtained without RM synthesis in boxes of 21.6 and 34.6 kpc width in major-axis direction for NGC 891 and NGG 4565, respectively, we created vertical fractional polarization profiles. At 6 GHz, the JVLA I, Q, and U maps were first smoothed to a resolution of 25″ for NGC 891 and 20″ for NGC 4565 (before primary-beam correction, merging with Effelsberg maps, and forming the p maps), to be comparable to the results of D97 at 4.85 GHz. The resulting vertical profiles at both frequencies are shown in Fig. 7.11.
Since our vertical p profiles at 1.5 GHz are at least slightly influenced by the effect of bandwidth depolarization, and since we observed at 6 GHz instead of 4.85 GHz, comparing our p profiles to those of D97 in terms of their absolute values seems hardly reasonable. Nevertheless, we note that up to $z \approx 3$ kpc in case of NGC 891 and at least up to $z \approx 2$ kpc for NGC 4565 we obtain very similar p values at 6 GHz to those found by D97 at 4.85 GHz. However, we observe a notably different behaviour of these profiles for larger z heights. While for D97 $p_{4.85\mathrm{GHz}}$ of NGC 891 drops to $\approx 3\%$ at 4 kpc, our $p_{6\mathrm{GHz}}$ profile remains constant near the maximum value of $\approx 9\%$ out to at least 5 kpc. Similarly, for NGC 4565 $p_{4.85\mathrm{GHz}}$ of D97 decreases from $\approx 28\%$ at ≈ 2 kpc to less than 20% at 4 kpc, whereas our data suggest that $p_{6\mathrm{GHz}}$ stays constant at $\approx 38\%$ at least out to 3 kpc. A possible reason for the drop at high z in the $p_{4.85\mathrm{GHz}}$ profiles of D97 may be that the use of the `AIPS` task `IMERG` by this author to combine the VLA and Effelsberg images distributed the Effelsberg flux in a way that resulted in too high total intensities in the upper halo. In case of NGC 891, D97 explained the decrease of $p_{4.85\mathrm{GHz}}$ by the transport of small-scale turbulent fields from the disk into the halo through enhanced star-forming activity. That such a process may take place is consistent with the fact that NGC 4565 (which has a very low SFR) shows a higher overall fractional polarization and a steeper increase of $p_{4.85\mathrm{GHz}}$ and $p_{6\mathrm{GHz}}$ with z than NGC 891 – a trend that was already observed for a larger sample of galaxies at 10.55 GHz

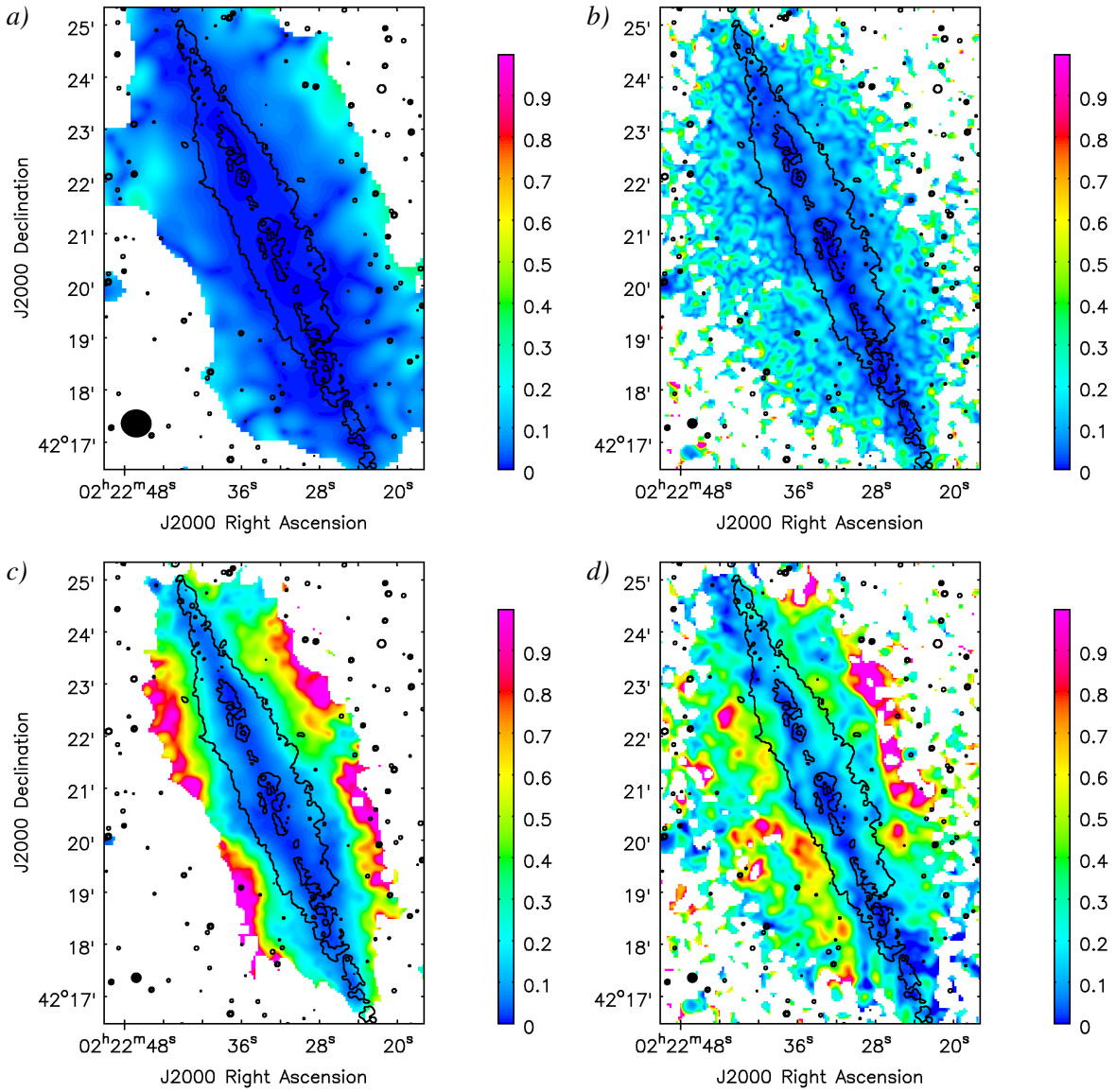

Figure 7.9: Fractional polarization maps of NGC 891. *a)* 1.5 GHz D-array polarized intensity map obtained by full-bandwidth MS-MFS imaging (Fig. 7.1 *a)*), divided by the corresponding total intensity map. *b)* 6 GHz D-array+Effelsberg polarized intensity map obtained by full-bandwidth MS-MFS imaging (Fig. 7.1 *b)*), divided by the corresponding total intensity map. *c)* RM-synthesis based L-band polarized intensity map (Fig. 7.6 *a)*), divided by the 1.5 GHz B+C+D-array total intensity map. *d)* RM-synthesis based C-band polarized intensity map (Fig. 7.6 *b)*), divided by the 6 GHz D-array+Effelsberg total intensity map. The beam FWHM is $36'' \times 32''$ in panel *a)* and $12''$ in panels *b)-d)* . All fractional polarization maps have been cut off at the 5σ level in the used total intensity maps. Overlaid in each panel are contours of the KPNO Hα image provided by M. Patterson (priv. comm.), smoothed to a resolution of $3.5''$. These contour levels are at 5, 30, and 100 μJy beam^{-1}.

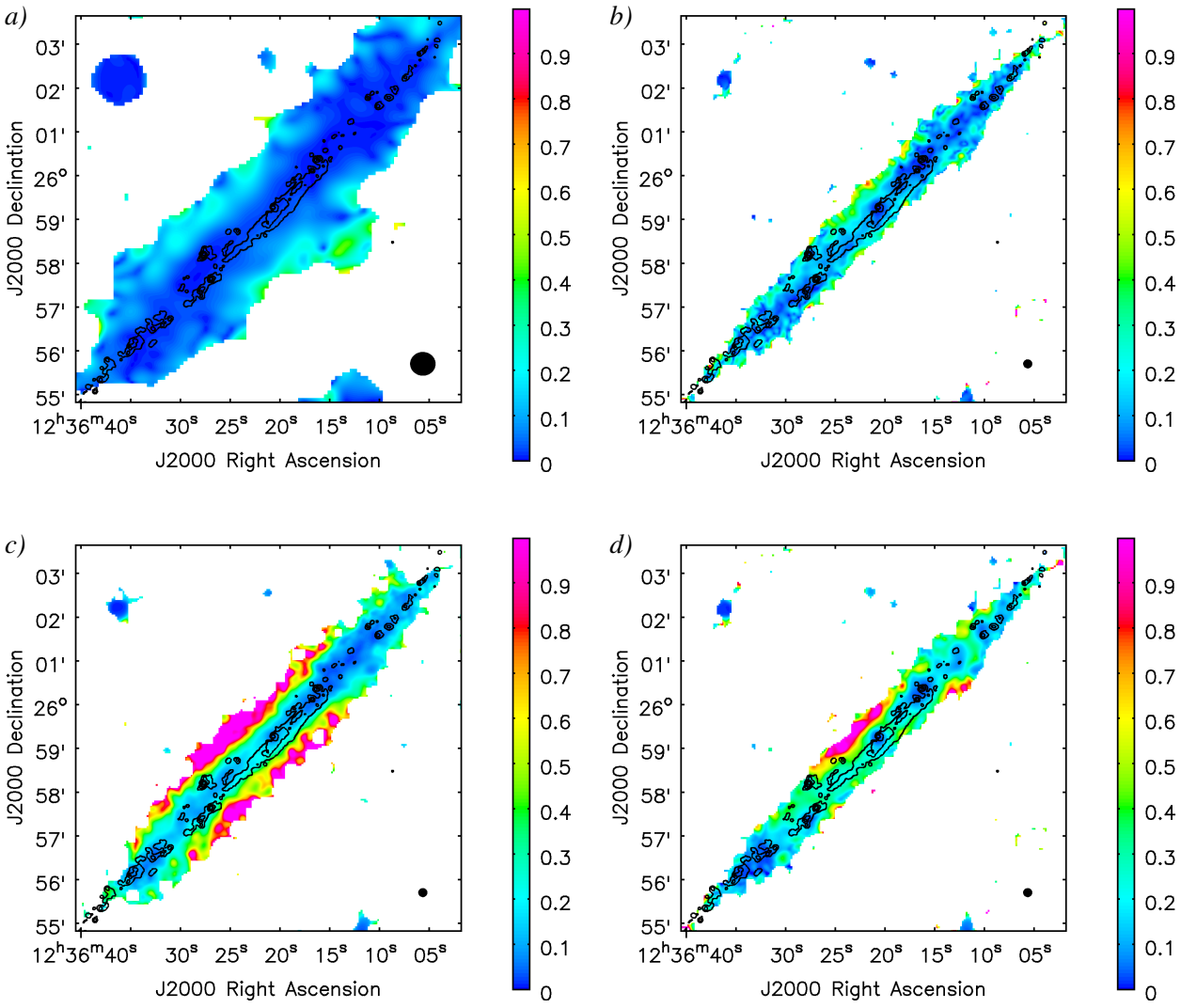

Figure 7.10: Fractional polarization maps of NGC 4565. *a)* 1.5 GHz D-array polarized intensity map obtained by full-bandwidth MS-MFS imaging (Fig. 7.2 *a)*), divided by the corresponding total intensity map. *b)* 6 GHz D-array+Effelsberg polarized intensity map obtained by full-bandwidth MS-MFS imaging (Fig. 7.2 *b)*), divided by the corresponding total intensity map. *c)* RM-synthesis based L-band polarized intensity map (Fig. 7.7 *a)*), divided by the 1.5 GHz B+C+D-array total intensity map. *d)* RM-synthesis based C-band polarized intensity map (Fig. 7.7 *b)*), divided by the 6 GHz D-array+Effelsberg total intensity map. The beam FWHM is $35'' \times 32''$ in panel *a)* and $12''$ in panels *b)-d)* . All fractional polarization maps have been cut off at the 5σ level in the used total intensity maps. Overlaid in each panel are contours of the KPNO Hα image provided by M. Patterson (priv. comm.), smoothed to a resolution of $3.5''$. These contour levels are at 10, 25, 50, and 100 μJy beam^{-1}.

by Dumke et al. (1995). Still, as indicated by our results, this mechanism apparently does not lead to a decrease of p in the outermost parts of the halo.

Lastly, we observe for both galaxies that, contrary to $p_{6\mathrm{GHz}}$, $p_{1.5\mathrm{GHz}}$ increases continuously up to the largest z heights. We cannot rule out that this is a consequence of missing short spacings, which seem to have a greater effect on Stokes I than on Stokes Q and U.

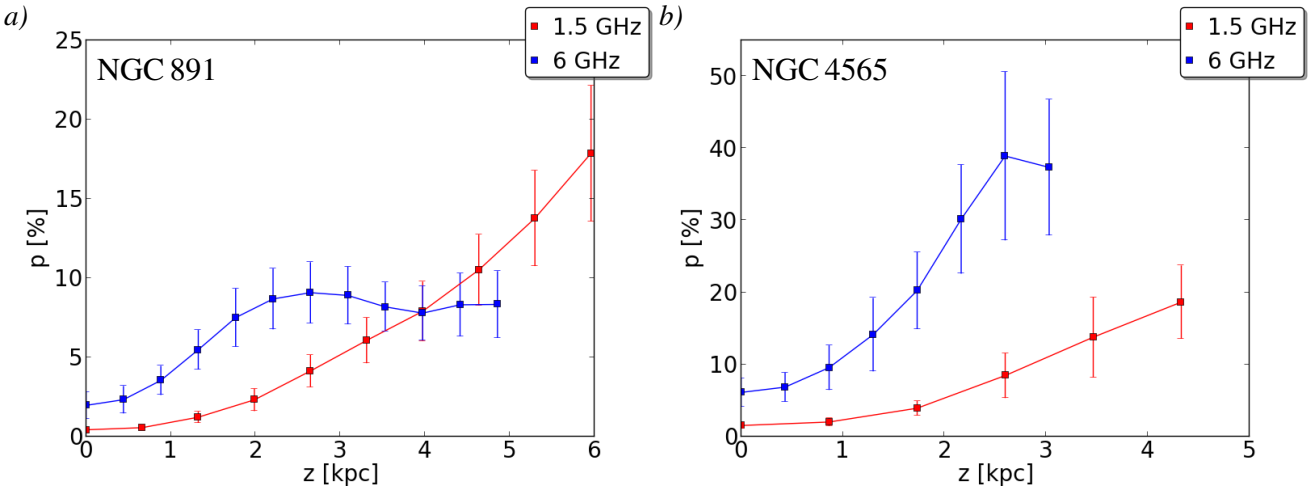

Figure 7.11: Fractional polarization at 1.5 GHz (red) and 6 GHz (blue) as a function of height perpendicular to the major axis, averaged across the radial extent of each galaxy. *a)* NGC 891, *b)* NGC 4565.

8 Summary, conclusions, and outlook

Over the course of this thesis, the full data reduction of broad-band JVLA observations of the edge-on spiral galaxies NGC 891 and NGC 4565 in the framework of the CHANG-ES project (using three array configurations and two frequency bands centred at 1.5 and 6 GHz) was performed, followed by an analysis of various physical properties of these two objects. While a range of properties indicated by previous observations could be verified at a higher confidence level by the newly obtained JVLA data, also a number of new scientific insights about both objects have been gained. In particular, the spatial distribution of the total and polarized radio radio emission (and hence also of the magnetic field structure) in both galaxies has been probed at a higher angular resolution and sensitivity than previously possible. For both galaxies, the following activities have been performed for the first time:

- Computing two-dimensional spectral index maps (in particular, also for the spectral index *within* a given frequency band)
- Studying the spectral index distribution in vertical direction without being significantly affected by the lack of short-spacing data
- Determining the spatial distribution of the total magnetic field strength (assuming energy equipartition)
- Estimating the spatially resolved distribution of thermal radio emission
- Determining vertical radio continuum scale heights from thermal-subtracted emission maps
- Investigating scale heights as a function of position along the galactic disk
- Obtaining first information on the frequency dependence of scale heights
- Analyzing the spectral index distribution and vertical emission profiles with regard to CR propagation

Moreover, the magnetic field structure of NGC 4565 was studied for the first time using the RM synthesis technique (while in case of NGC 891 we were able to improve upon a previous analysis of Adebahr (2013), who used broad-band WSRT data at 1.4 GHz). Also, for NGC 4565 we obtained a rather spectacular radio image at our highest resolution, which reveals a ring-shaped geometry of the inner spiral arms, and hence shows that the radio emission from the disk of the galaxy closely follows the distribution seen at FIR wavelengths. This is the first time the spiral arm pattern of a galaxy of such high inclination (86°) could be resolved into its front and rear side at radio frequencies.
In addition, a major section of this thesis is concerned with the challenges of broad-band spectral

index imaging. By performing various tests on our in-band spectral index data, we investigated in detail the multiple sources of error inherent to such broad-band measurements and inferred a range of important corrections that need to be applied.

In the following, our main findings for the two galaxies will be discussed in a comparative manner. Even though both are known to be normal spiral galaxies that show only minor signs of interaction with companion (dwarf) galaxies, various physical parameters determined in this and previous works show substantial differences in comparison of the two objects. While both galaxies lie in a similar range of mass and radial extent, many of their properties happen to be consistent with NGC 891 being like an upscaled version of NGC 4565, with most of the differences between them apparently being related to their very different SFRs.

Located at a similar distance, and being somewhat smaller in its physical disk diameter, NGC 891 is ≈6 times brighter in radio continuum than NGC 4565. In particular, the radio continuum emission in NGC 891 is considerably more extended in vertical direction than in NGC 4565 (which is the case at basically all other wavelengths as well). In fact, these two galaxies possess one of the brightest and one of the weakest known radio halos, respectively.

The two galaxies differ largely in their synchrotron spectral index distribution, with spectral indices being consistently steeper in NGC 4565 than in NGC 891, in the halo as well as in the disk. This is evident from the in-band spectral index maps at both 1.5 and 6 GHz, and consequently also from the two-point spectral index maps between the two frequencies. By comparing the local differences between the two spectral indices at 1.5 and 6 GHz to predictions by standard spectral aging models, we found in case of NGC 891 that our data are consistent with mainly continuous injection of CRs into the ISM, while in NGC 4565 the spectral steepening between the two frequencies can mostly be explained better by single-shot injection models. While these standard models are probably too simple to describe the spectral evolution due to synchrotron losses in a realistic manner, our findings indicate that the current CR injection rates in NGC 4565 must be significantly lower than in NGC 891. These can be readily associated with lower supernova rates and hence with the much lower SFR of NGC 4565. A possible scenario that may explain the strong spectral steepening we observe in NGC 4565 is that the galaxy is currently in a quiescent phase following a former period of high star-forming activity. Currently, rather than forming new stars, the ISM of the galaxy may be primarily consumed for feeding the central black hole, as indicated by the likely presence a strong central bar flow. To investigate whether supernova rates are indeed low enough to cause significant spectral aging, they need to be compared to the CRE energy loss rates. Determining how local supernova rates influence the observed CRE spectra in an edge-on galaxy is not straightforward, however, owing to the long lines of sight through the disk.

The vertical emission distribution in both galaxies is fitted well by two-component exponential profiles. For NGC 891, the scale height of the halo component shows a radial increase and hence reflects the dumbbell-shaped apperance of its overall extraplanar radio continuum emission. Already the fact that we measure basically identical scale heights at both 1.5 and 6 GHz suggests that the vertical CR transport in this galaxy is dominated by convection rather than diffusion. In case of NGC 4565, the scale heights we obtained are relatively constant with radius at 1.5 GHz, which seems plausible as no dumbbell shape is evident from the radio intensity maps. Still, at

6 GHz we do observe a strong increase of the halo scale height at the outermost radii. While the reason for this discrepancy is unclear, we find that if these outer data points are neglected, the scale heights at 6 GHz are somewhat lower than those at 1.5 GHz. Compared to the case of NGC 891, this frequency dependence of the scale heights is significant, and therefore indicates that diffusion of CRs from the disk into the halo likely plays a vital role in NGC 4565. Yet, we find the globally averaged scale heights to be similar for both galaxies (as known from past measurements), especially if the values at the outermost radii are not considered.

By solving the one-dimensional diffusion-loss equation, we applied a model of the vertical CR transport in NGC 891, whereas the insufficient reliability of extraplanar spectral index measurements in NGC 4565 did not allow such an analysis for this galaxy. We successfully reproduced the vertical distributions of synchrotron intensity and synchrotron spectral index in NGC 891 by assuming a 2-component pure convection model. A purely diffusive model, on the other hand, was not able to represent our data to a satisfactory extent. While generally a combination of convective and diffusive vertical CR transport is expected, our modelling clearly shows that convection is the dominating mechanism in this galaxy. The resulting outflow velocity is not well constrained, but is likely to be higher than $300\,\mathrm{km\,s^{-1}}$, which would be sufficient to escape the gravitational potential of the galaxy as a galactic wind. In this picture, the vertical decrease of the synchrotron intensity is primarily due to the vertical decrease of the total magnetic field strength, rather than due to radiative energy losses. This appears to be consistent with the frequency-independence of the measured synchrotron scale heights. In particular, the scale height of the halo magnetic field in our best-fit convection model is $\approx 40\%$ lower than the value expected in case of energy equipartition, which indicates that the equipartition condition breaks down in the halo of NGC 891. As our CR transport modelling in this work is based only on the global vertical profiles of the galaxy, we cannot yet provide a conclusive statement on the radial dependence of the vertical magnetic field gradient. However, the dumbbell-shaped behaviour of the halo scale heights already suggests that the field gradient decreases with radius. This, on the other hand, may point to a close connection between vertical magnetic field gradients and the field pattern in the halo of this galaxy, which is characterized by plane-parallel field lines above the centre and a radially increasing component in vertical direction.

Total equipartition magnetic field strengths in the disk of NGC 891 are consistently higher than in NGC 4565, with average values of $\approx 10\,\mu$G and $\approx 5\,\mu$G, respectively. According to the equipartition model of the radio-FIR correlation (Niklas & Beck 1997), the field strength relates to the SFR as $B_{\mathrm{eq}} \propto \mathrm{SFR}^{0.34}$, and moreover the non-thermal flux density behaves as $I_{\mathrm{nth}} \propto \mathrm{SFR}^{1.3}$. Assuming that the SFRs of both galaxies follow these relations, it is now possible to constrain these SFRs more tightly within the large scatter between different literature values. Considering the SFR values given in Table 1.1, we find that the ratio between the above field strengths of the two galaxies as well as the ratio between their integrated non-thermal flux densities (at both 1.5 and 6 GHz; see Table 4.2) agree best with $(\mathrm{SFR_{N891}}/\mathrm{SFR_{N4565}})^{0.34}$ and $(\mathrm{SFR_{N891}}/\mathrm{SFR_{N4565}})^{1.3}$, respectively, if $\mathrm{SFR_{N891}} = 3.3\,\mathrm{M_\odot\,yr^{-1}}$ and $\mathrm{SFR_{N4565}} = 0.74\,\mathrm{M_\odot\,yr^{-1}}$ are assumed.

While the X-shaped geometry of the magnetic field in the halo of NGC 891 has been known for some time, and is likely the result of convective disk-halo outflows, we have now detected clear sings that such a field configuration exists in the halo of NGC 4565 as well. Our polarization

data (especially after applying RM synthesis) show that extraplanar magnetic field lines systematically deviate from a plane-parallel orientation, which was only marginally hinted at in past observations.
The extraplanar RM patterns in both galaxies suggest a quadrupolar halo field configuration, as predicted by models of galactic dynamos that are coupled to convective outflows. This can only be regarded as a tentative interpretation, however, as our data do not provide any information on field reversals along the line of sight. Lastly, NGC 891 shows a lower fractional degree of polarization than NGC 4565, particularly in the halo, which may be attributed to its higher SFR, resulting in a more efficient transport of turbulent fields from the disk into the halo. On the other hand, also enhanced depolarization within the prominent extraplanar ionized gas layer of NGC 891 appears to be a reasonable explanation.

It is obvious that star formation plays an important role in regulating convective disk-halo outflows and therefore has a major impact on the vertical extent of radio halos, although the connection between the two processes is still only vaguely understood. Given the above equipartition relation between SFR and magnetic field strength, the small scatter in the synchrotron scale heights of different galaxies in spite of their different SFRs seems plausible if the field strength does not show a significant vertical decrease. However, the vertical field gradient is generally not negligible, as a study by Heesen et al. (2015, submitted) and our work on NGC 891 have shown. These gradients, in turn, certainly depend on how efficiently the field is transported from the disk into the halo. Moreover, it is well-known by now that scale heights can vary with radius, and we are currently beginning to reliably probe the relation between scale height and frequency within individual galaxies. As demonstrated by our analysis in Chapter 6, the data quality currently provided by the JVLA (and certainly by other modern radio interferometers as well) is sufficient for studying the spatial and spectral behaviour of galactic synchrotron scale heights. Therefore, observing edge-on galaxies at multiple additional frequencies appears to be highly promising for obtaining a well-established scaleheight-frequency relation, which in turn would be extremely useful to put further constraints on the nature of disk-halo outflows. By properly sampling the spatially resolved CRE spectral energy distribution (eventually also extending the range to lower radio frequencies, using e.g. LOFAR, WSRT, or low-frequency JVLA bands), also more realistic spectral evolution models than those considered in this work could be tested.
But already without performing these follow-up observations, analyzing the 1.5 and 6 GHz data of the remaining galaxies in the CHANG-ES sample in a similar fashion as presented in this thesis is expected to provide substantial new insights to the interrelations of various key quantities. These parameters include radio luminosities, vertical scale heights, outflow velocities, magnetic field strengths, gravitational potential, and quantities related to star-forming activity. Comprehensive studies of this kind making use of the entire CHANG-ES sample have recently been started by the consortium (Li et al. 2016; Krause et al. 2016, in prep, Vargas et al. 2016, in prep.).
However, apart from the currently available CHANG-ES data sets, additional observations in S-band (2-4 GHz) will be essential for further polarization studies. S-band data should then replace the L-band data in RM synthesis, to avoid complete depolarization by differential Faraday rotation beyond a certain Faraday depth, while still achieving a reasonable Faraday depth resolution to probe the magnetic field structure in line-of-sight direction. In addition, it needs to be ensured that single-dish data of reasonable quality are available for each galaxy above a certain

angular size, at all observing frequencies, to correct for missing short-spacings. It is desirable to carry out these single-dish observations at the same frequencies (and ideally also the same bandwidths) as the interferometric measurements. An according extrapolation of single-dish maps may introduce artifacts to the short-spacing corrected images, as our own results indicate. Observations of all CHANG-ES galaxies with the Green Bank Telescope (GBT) fulfilling the above requirements have recently been performed, however due to delays in the installation of broad-band receivers and present commissioning requirements, it was not possible to acquire the relevant data products in time for the studies presented here. Hence, we made use of 4.85 GHz images taken with the Effelsberg telescope to apply short-spacing corrections to our 6 GHz JVLA data. In fact, the Effelsberg telescope is largely superior to the GBT in terms of data processing capabilities, as advanced and and well-tested software for the reduction of Effelsberg data exists. We therefore hope for a soon installation of broad-band spectropolarimeters in Effelsberg.
In the long run, the sensitivity in observing galactic radio halos will be considerably improved by the Square Kilometre Array (SKA), which is soon to be constructed. Yet, in the meantime, upcoming studies using the currently available technology can already be expected to rapidly push forward our knowledge in this field.
Lastly, the disk-halo connection is playing an ever increasing role in numerical simulations of galaxy formation and evolution. Providing well-constrained observational parameters such as outflow velocities to numerical models (including MHD simulations) will largely improve our understanding of why we observe such a diverse range of galaxy properties in the local universe.

Acknowledgements

The research presented here would not have been possible without the direct and indirect input and support of many people who kept regular company with me from the beginning of my doctoral studies to the completion of this thesis, and who I've met along the way.
First of all, I owe my deepest gratitude to Marita Krause, for being probably the most pleasant thesis advisor one could wish for. I thank her for her perpetual helpfulness and patience, and for sharing her deep knowledge about magnetic fields and galaxies in general. I will gladly remember the multitude of inspiring scientific and non-scientific discussions we had, and especially her encouraging words during the final phase of my thesis work.
Sincere thanks go to Michael Kramer for letting me be part of his fundamental radio-astrophysics group and for keeping up an inspiring and positive working climate. Despite his ever busy schedule, he has always been a helpful contact person in organizational matters. I thank him especially for supporting my three-month trip to NRAO in New Mexico right at the beginning of my doctoral studies.
I am also highly indebted to Uli Klein, whom I know since I took my first radio astronomy lectures given by him, and whom I afterwards chose as the supervisor of my diploma thesis. Already during this part of my career, he constantly managed to further increase my interest in radio astronomy, which continued throughout the years of producing this PhD thesis. Also, the annual conferences organized by Uli were something I would regret to have missed.
A great many thanks must go to Aritra Basu for his invaluable advice and motivation, especially during the past year. He was willing to help me out with many crucial issues, from the separation of thermal and non-thermal radio emission, to reasonably calculating magnetic field strenghts, to understanding the observed spectral properties of edge-on galaxies in comparison to face-on galaxies.
I am equally thankful to Rainer Beck for his extremely useful ideas and willingness to answer the various scientific questions I had, of course in particular regarding all kinds of magnetic field issues.
Many thanks go to Peter Müller for providing invaluable support in terms of software for data processing and analysis. It is incredible how quickly and reliably he responded to any kind of requests for new functions in NOD3.
Also Theresa Wiegert deserves my deep gratitude, who not only was my most important contact person regarding JVLA data reduction during my NRAO visit, but also great company during spare time within these three months. I thank her particularly for taking me on the fantastic trip through Arizona, including the Grand Canyon. And also afterwards, it has always been a pleasure to work with her and to meet her again at the yearly CHANG-ES workshops.
Likewise, I have to thank Kristina Nyland and Jeff Lapierre for being excellent hosts and "tour guides" during both of my New Mexico visits.

A great amount of thanks also go to Judith Irwin, who did (and still does) a fantastic job at leading the CHANG-ES project and making it easy to connect with and a pleasure to collaborate with the various members of this fantastic research group.
I have to thank Jana Köhler for being the perfect office mate – quiet when important work needs to be done, while always being there for nice conversations during the mutual breaks. And most of all, I thank her for the constant supply of tea as well as “nerve food“ such as Hallorenkugeln.
Of course I equally thank all my other current and former colleagues of the galaxy and magnetism working group here in Bonn, who have all been very helpful to me in more than one occasion: Björn Adebahr, Ancor Damas, Andreas Horneffer, Henrik Junklewitz, Maja Kierdorf, Ann Mao, Carolina Mora, David Mulcahy, and Dominic Schnitzeler.
Thanks a lot also to Kira Kühn and Le Tran for their great helpfulness in administrative matters.
I am deeply grateful to my ex-colleague and good friend Nadya Ben Bekhti, for being just an allround great person to have around, whether it be during tea breaks at the AIfA, at conferences, or while enjoying the highlight of Bonn’s otherwise rather sparse nightlife offering that is the Depeche Mode parties at the Sofa. I likewise thank Benjamin Winkel for staying in good contact since my diploma thesis times.
Moreover, I thank Gyula ”Josh“ Józsa for his great help in finishing the journal publication of my diploma thesis results and more, which still formed an integral part of my work during my first year at the MPIfR.
I thank Ralf-Jürgen Dettmar, Jayanne English, George Heald, Arpad Miskolczi, Rich Rand, Yelena Stein, Carlos Vargas, Rene Walterbos, and all other members of the CHANG-ES team for the great opportunities to collaborate.
I also thank Volker Heesen for making the extremely useful `SPINNAKER` code available.
Furthermore, thanks a lot to Pavel Kroupa for his willingness to step in as the second referee of this thesis.
Big thanks go to my long-term friends Michael Brockamp and Philipp Hagen, who accompanied me during my studies of physics nearly from the beginning.
Last but definitely not least, I owe sincere gratitude to my family, for believing in my success, for their perpetual support, and especially for their patience during the final phase of this work.

Bibliography

Adebahr, B. 2013. *Cosmic ray propagation and magnetic fields in nearby star-forming galaxies, with emphasis on the prototypical case of M82*. PhD thesis, Ruhr-Universität Bochum.

Allen, R. J., R. Sancisi, & J. E. Baldwin 1978. Radio continuum observations of the edge-on disc galaxy NGC 891. *A&A*, 62:397–409.

Aniano, G., B. T. Draine, K. D. Gordon, & K. Sandstrom 2011. Common-Resolution Convolution Kernels for Space- and Ground-Based Telescopes. *PASP*, 123:1218–1236.

Arshakian, T. G. & R. Beck 2011. Optimum frequency band for radio polarization observations. *MNRAS*, 418:2336–2342.

Baldwin, J. E. 1954. Radio Emission from the Andromeda Nebula. *Nat.*, 174:320–321.

Basu, A., R. Beck, P. Schmidt, & S. Roy 2015. Synchrotron spectral index and interstellar medium densities of star-forming galaxies. *MNRAS*, 449:3879–3888.

Basu, A., D. Mitra, Y. Wadadekar, & C. H. Ishwara-Chandra 2012. GMRT 333-MHz observations of six nearby normal galaxies. *MNRAS*, 419:1136–1152.

Beck, R. 2007. Magnetism in the spiral galaxy NGC 6946: magnetic arms, depolarization rings, dynamo modes, and helical fields. *A&A*, 470:539–556.

Beck, R. 2015. Magnetic fields in the nearby spiral galaxy IC 342: A multi-frequency radio polarization study. *A&A*, 578:A93.

Beck, R., P. Biermann, D. T. Emerson, & R. Wielebinski 1979. Radio continuum observations of NGC 891 and NGC 253 at 8.7 GHz. *A&A*, 77:25–30.

Beck, R., A. Brandenburg, D. Moss, A. Shukurov, & D. Sokoloff 1996. Galactic Magnetism: Recent Developments and Perspectives. *ARA&A*, 34:155–206.

Beck, R. & M. Krause 2005. Revised equipartition and minimum energy formula for magnetic field strength estimates from radio synchrotron observations. *Astronomische Nachrichten*, 326:414–427.

Berkhuijsen, E. M., C. Horellou, M. Krause, N. Neininger, A. D. Poezd, A. Shukurov, & D. D. Sokoloff 1997. Magnetic fields in the disk and halo of M 51. *A&A*, 318:700–720.

Bhatnagar, S., T. J. Cornwell, K. Golap, & J. M. Uson 2008. Correcting direction-dependent gains in the deconvolution of radio interferometric images. *A&A*, 487:419–429.

Bhatnagar, S., U. Rau, & K. Golap 2013. Wide-field wide-band Interferometric Imaging: The WB A-Projection and Hybrid Algorithms. *ApJ*, 770:91.

Bietenholz, M. F., N. Bartel, & M. P. Rupen 2010. Supernova 1986J Very Long Baseline Interferometry. II. The Evolution of the Shell and the Central Source. *ApJ*, 712:1057–1069.

Blandford, R. & D. Eichler 1987. Particle acceleration at astrophysical shocks: A theory of cosmic ray origin. *Phys. Rep.*, 154:1–75.

Brandenburg, A., K. J. Donner, D. Moss, A. Shukurov, D. D. Sokoloff, & I. Tuominen 1993. Vertical Magnetic Fields above the Discs of Spiral Galaxies. *A&A*, 271:36.

Braun, R., G. Heald, & R. Beck 2010. The Westerbork SINGS survey. III. Global magnetic field topology. *A&A*, 514:A42.

Bregman, J. N. & J. C. Houck 1997. The Hot Gas Surrounding the Edge-on Galaxy NGC 891. *ApJ*, 485:159–166.

Bregman, J. N. & R. A. Pildis 1994. X-ray-emitting gas surrounding the spiral galaxy NGC 891. *ApJ*, 420:570–575.

Breitschwerdt, D., J. F. McKenzie, & H. J. Voelk 1991. Galactic winds. I - Cosmic ray and wave-driven winds from the Galaxy. *A&A*, 245:79–98.

Breitschwerdt, D., J. F. McKenzie, & H. J. Voelk 1993. Galactic winds. II - Role of the disk-halo interface in cosmic ray driven galactic winds. *A&A*, 269:54–66.

Brentjens, M. A. & A. G. de Bruyn 2005. Faraday rotation measure synthesis. *A&A*, 441:1217–1228.

Briggs, D. S. 1995. High Fidelity Interferometric Imaging: Robust Weighting and NNLS Deconvolution. In *American Astronomical Society Meeting Abstracts*, volume 27 of *Bulletin of the American Astronomical Society*, P. 112.02.

Brinks, E. & W. B. Burton 1984. A high resolution hydrogen line survey of Messier 31. II - The warped flaring hydrogen layer. *A&A*, 141:195–214.

Broeils, A. H. & R. Sancisi 1985. The 'thick' radio disk of NGC 4565. *A&A*, 153:281–283.

Buffie, K., V. Heesen, & A. Shalchi 2013. Theoretical Explanation of the Cosmic-Ray Perpendicular Diffusion Coefficient in the Nearby Starburst Galaxy NGC 253. *ApJ*, 764:37.

Burn, B. J. 1966. On the depolarization of discrete radio sources by Faraday dispersion. *MNRAS*, 133:67.

Buta, R. 1990. Weakly barred, early-type ringed galaxies. I - The Seyfert galaxy NGC 3081. *ApJ*, 351:62–74.

Calzetti, D., R. C. Kennicutt, C. W. Engelbracht, C. Leitherer, B. T. Draine, L. Kewley, J. Moustakas, M. Sosey, D. A. Dale, K. D. Gordon, G. X. Helou, D. J. Hollenbach, L. Armus, G. Bendo, C. Bot, B. Buckalew, T. Jarrett, A. Li, M. Meyer, E. J. Murphy, M. Prescott, M. W. Regan, G. H. Rieke, H. Roussel, K. Sheth, J. D. T. Smith, M. D. Thornley, & F. Walter 2007. The Calibration of Mid-Infrared Star Formation Rate Indicators. *ApJ*, 666:870–895.

Cesarsky, C. J. 1980. Cosmic-ray confinement in the galaxy. *ARA&A*, 18:289–319.

Chiaberge, M., R. Gilli, F. D. Macchetto, & W. B. Sparks 2006. Low Radiative Efficiency Accretion at Work in Active Galactic Nuclei: The Nuclear Spectral Energy Distribution of NGC 4565. *ApJ*, 651:728–734.

Ciardullo, R., G. H. Jacoby, & W. E. Harris 1991. Planetary nebulae as standard candles. VII - A test versus Hubble type in the NGC 1023 group. *ApJ*, 383:487–497.

Condon, J. 2015. An Analysis of the VLASS Proposal. *ArXiv e-prints*.

Condon, J. J. 1987. A 1.49 GHz atlas of spiral galaxies with B(T) = +12 or less and delta = -45 deg or greater. *ApJ*, 65:485–541.

Condon, J. J. 1992. Radio emission from normal galaxies. *ARA&A*, 30:575–611.

Condon, J. J. 2002. Continuum 1: General Aspects. In *Single-Dish Radio Astronomy: Techniques and Applications*, S. Stanimirovic, D. Altschuler, P. Goldsmith, and C. Salter, eds., volume 278 of *Astronomical Society of the Pacific Conference Series*, Pp. 155–171.

Conway, J. E., T. J. Cornwell, & P. N. Wilkinson 1990. Multi-Frequency Synthesis - a New Technique in Radio Interferometric Imaging. *MNRAS*, 246:490.

Cornwell, T. J. 2008. Multiscale CLEAN Deconvolution of Radio Synthesis Images. *IEEE Journal of Selected Topics in Signal Processing*, 2:793–801.

Cornwell, T. J., K. Golap, & S. Bhatnagar 2008. The Noncoplanar Baselines Effect in Radio Interferometry: The W-Projection Algorithm. *IEEE Journal of Selected Topics in Signal Processing*, 2:647–657.

Dahlem, M., R.-J. Dettmar, & E. Hummel 1994. Spatially correlated diffuse Hα and radio continuum emission from the halo of NGC 891. *A&A*, 290:384–392.

Dahlem, M., U. Lisenfeld, & G. Golla 1995. Star formation activity in spiral galaxy disks and the properties of radio halos: Observational evidence for a direct dependence. *ApJ*, 444:119–128.

Dahlem, M., M. G. Petr, M. D. Lehnert, T. M. Heckman, & M. Ehle 1997. Evidence for a New "Superwind" Galaxy - NGC 4666. *A&A*, 320:731–745.

Dalla Vecchia, C. & J. Schaye 2008. Simulating galactic outflows with kinetic supernova feedback. *MNRAS*, 387:1431–1444.

de Vaucouleurs, G., A. de Vaucouleurs, H. G. Corwin, Jr., R. J. Buta, G. Paturel, & P. Fouqué 1991. *Third Reference Catalogue of Bright Galaxies. Volume I: Explanations and references. Volume II: Data for galaxies between 0^h and 12^h. Volume III: Data for galaxies between 12^h and 24^h.*

Dettmar, R.-J. 1990. The distribution of the diffuse ionized interstellar medium perpendicular to the disk of the edge-on galaxy NGC 891. *A&A*, 232:L15–L18.

Dettmar, R. J. 1992. Extraplanar Diffuse Ionized Gas and the Disk-Halo Connection in Spiral Galaxies. *FCPH*, 15:143–208.

Dettmar, R. J. & H. Schulz 1992. The Ionization of the Diffuse Gas in NGC891 and the Decaying Dark Matter Theory. *A&A*, 254:L25.

Dorfi, E. A. & D. Breitschwerdt 2012. Time-dependent galactic winds. I. Structure and evolution of galactic outflows accompanied by cosmic ray acceleration. *A&A*, 540:A77.

Draine, B. T. 2011. *Physics of the Interstellar and Intergalactic Medium*.

Dumke, M. 1997. *Das interstellare Medium nicht wechselwirkender Edge-on-Galaxien*. PhD thesis, Universität Bonn.

Dumke, M. & M. Krause 1998. Radio and Polarization Properties in the Disk and Halo of Edge-On Spirals. In *IAU Colloq. 166: The Local Bubble and Beyond*, D. Breitschwerdt, M. J. Freyberg, and J. Truemper, eds., volume 506 of *Lecture Notes in Physics, Berlin Springer Verlag*, Pp. 555–558.

Dumke, M., M. Krause, R. Wielebinski, & U. Klein 1995. Polarized radio emission at 2.8cm from a selected sample of edge-on galaxies. *A&A*, 302:691.

Duric, N., E. Bourneuf, & P. C. Gregory 1988. The separation of synchrotron and bremsstrahlung radio emission in spiral galaxies. *AJ*, 96:81–91.

Duric, N. & D. Dixon 1991. Separation of Synchotron and Thermal Emission in Spiral Galaxies. *International Cosmic Ray Conference*, 2:724.

Ehle, M., R. Beck, R. F. Haynes, A. Vogler, W. Pietsch, M. Elmouttie, & S. Ryder 1996. Magnetic fields and hot gas in the spiral galaxy NGC 1566 as derived from ATCA radio polarization and ROSAT X-ray observations. *A&A*, 306:73.

Eilek, J. A., D. B. Melrose, & M. A. Walker 1997. Synchrotron Aging in Filamented Magnetic Fields. *ApJ*, 483:282–295.

Ekers, R. D. & R. Sancisi 1977. The radio continuum halo in NGC 4631. *A&A*, 54:973.

Fletcher, A., R. Beck, A. Shukurov, E. M. Berkhuijsen, & C. Horellou 2011. Magnetic fields and spiral arms in the galaxy M51. *MNRAS*, 412:2396–2416.

Fraternali, F., T. Oosterloo, & R. Sancisi 2004. Kinematics of the ionised gas in the spiral galaxy NGC 2403. *A&A*, 424:485–495.

Frick, P., R. Stepanov, R. Beck, D. Sokoloff, A. Shukurov, M. Ehle, & A. Lundgren 2016. Magnetic and gaseous spiral arms in M83. *A&A*, 585:A21.

Garcia-Burillo, S. & M. Guelin 1995. The distorted kinematics of molecular gas in the center of NGC 891. *A&A*, 299:657.

Garcia-Burillo, S., M. Guelin, J. Cernicharo, & M. Dahlem 1992. Molecular gas distribution and dynamics of the edge-on spiral galaxy NGC 891 - Discovery of a molecular halo. *A&A*, 266:21–36.

Gioia, I. M. & G. Fabbiano 1987. Radio continuum observations of early- and late-type spiral galaxies. *ApJ*, 63:771–802.

Hanasz, M., D. Wóltański, & K. Kowalik 2009. Global Galactic Dynamo Driven by Cosmic Rays and Exploding Magnetized Stars. *ApJ*, 706:L155–L159.

Harnett, J., M. Ehle, A. Fletcher, R. Beck, R. Haynes, S. Ryder, M. Thierbach, & R. Wielebinski 2004. Magnetic fields in barred galaxies. III. The southern peculiar galaxy NGC 2442. *A&A*, 421:571–581.

Heald, G. 2009. The Faraday rotation measure synthesis technique. In *IAU Symposium*, K. G. Strassmeier, A. G. Kosovichev, and J. E. Beckman, eds., volume 259 of *IAU Symposium*, Pp. 591–602.

Heald, G., R. Braun, & R. Edmonds 2009. The Westerbork SINGS survey. II Polarization, Faraday rotation, and magnetic fields. *A&A*, 503:409–435.

Heald, G., G. Józsa, P. Serra, L. Zschaechner, R. Rand, F. Fraternali, T. Oosterloo, R. Walterbos, E. Jütte, & G. Gentile 2011. The Westerbork Hydrogen Accretion in LOcal GAlaxieS (HALOGAS) survey. I. Survey description and pilot observations. *A&A*, 526:A118.

Heald, G. H., R. J. Rand, R. A. Benjamin, & M. A. Bershady 2007. Integral Field Unit Observations of NGC 4302: Kinematics of the Diffuse Ionized Gas Halo. *ApJ*, 663:933–947.

Heald, G. H., R. J. Rand, R. A. Benjamin, J. A. Collins, & J. Bland-Hawthorn 2006. Imaging Fabry-Perot Spectroscopy of NGC 5775: Kinematics of the Diffuse Ionized Gas Halo. *ApJ*, 636:181–199.

Heesen, V., R. Beck, M. Krause, & R.-J. Dettmar 2009a. Cosmic rays and the magnetic field in the nearby starburst galaxy NGC 253. I. The distribution and transport of cosmic rays. *A&A*, 494:563–577.

Heesen, V., E. Brinks, M. G. H. Krause, J. J. Harwood, U. Rau, M. P. Rupen, D. A. Hunter, K. T. Chyży, & G. Kitchener 2015. The non-thermal superbubble in IC 10: the generation of cosmic ray electrons caught in the act. *MNRAS*, 447:L1–L5.

Heesen, V., E. Brinks, A. K. Leroy, G. Heald, R. Braun, F. Bigiel, & R. Beck 2014. The Radio Continuum-Star Formation Rate Relation in WSRT SINGS Galaxies. *AJ*, 147:103.

Heesen, V., M. Krause, R. Beck, & R.-J. Dettmar 2009b. Cosmic rays and the magnetic field in the nearby starburst galaxy NGC 253. II. The magnetic field structure. *A&A*, 506:1123–1135.

Ho, L. C., A. V. Filippenko, W. L. W. Sargent, & C. Y. Peng 1997. A Search for "Dwarf" Seyfert Nuclei. IV. Nuclei with Broad Hα Emission. *ApJ*, 112:391–414.

Hodges-Kluck, E. J. & J. N. Bregman 2013. A Deep X-Ray View of the Hot Halo in the Edge-on Spiral Galaxy NGC 891. *ApJ*, 762:12.

Högbom, J. A. 1974. Aperture Synthesis with a Non-Regular Distribution of Interferometer Baselines. *A&A*, 15:417.

Howk, J. C. & B. D. Savage 1997. Extraplanar Dust in the Edge-On Spiral NGC 891. *AJ*, 114:2463.

Howk, J. C. & B. D. Savage 1999. A Search for Extraplanar Dust in Nearby Edge-on Spirals. *AJ*, 117:2077–2101.

Howk, J. C. & B. D. Savage 2000. The Multiphase Halo of NGC 891: WIYN Hα and BVI Imaging. *AJ*, 119:644–667.

Hughes, T. M., M. Baes, J. Fritz, M. W. L. Smith, T. J. Parkin, G. Gentile, G. J. Bendo, C. D. Wilson, F. Allaert, S. Bianchi, I. De Looze, J. Verstappen, S. Viaene, M. Boquien, A. Boselli, D. L. Clements, J. I. Davies, M. Galametz, S. C. Madden, A. Rémy-Ruyer, & L. Spinoglio 2014. A resolved analysis of cold dust and gas in the nearby edge-on spiral NGC 891. *A&A*, 565:A4.

Hummel, E., R. Beck, & M. Dahlem 1991a. The magnetic field structure in the radio halos of NGC 891 and NGC 4631. *A&A*, 248:23–29.

Hummel, E., M. Dahlem, J. M. van der Hulst, & S. Sukumar 1991b. The large-scale radio continuum structure of the edge-on spiral galaxy NGC 891. *A&A*, 246:10–20.

Hummel, E., R. Sancisi, & R. D. Ekers 1984. Radio continuum observations of the edge-on spiral galaxies NGC 4244, 4565, and 5907. *A&A*, 133:1–10.

Ipavich, F. M. 1975. Galactic winds driven by cosmic rays. *ApJ*, 196:107–120.

Irwin, J., R. Beck, R. A. Benjamin, R.-J. Dettmar, J. English, G. Heald, R. N. Henriksen, M. Johnson, M. Krause, J.-T. Li, A. Miskolczi, S. C. Mora, E. J. Murphy, T. Oosterloo, T. A. Porter, R. J. Rand, D. J. Saikia, P. Schmidt, A. W. Strong, R. Walterbos, Q. D. Wang, & T. Wiegert 2012a. Continuum Halos in Nearby Galaxies: An EVLA Survey (CHANG-ES). I. Introduction to the Survey. *AJ*, 144:43.

Irwin, J., R. Beck, R. A. Benjamin, R.-J. Dettmar, J. English, G. Heald, R. N. Henriksen, M. Johnson, M. Krause, J.-T. Li, A. Miskolczi, S. C. Mora, E. J. Murphy, T. Oosterloo, T. A. Porter, R. J. Rand, D. J. Saikia, P. Schmidt, A. W. Strong, R. Walterbos, Q. D. Wang, & T. Wiegert 2012b. Continuum Halos in Nearby Galaxies: An EVLA Survey (CHANG-ES). II. First Results on NGC 4631. *AJ*, 144:44.

Jaffe, W. J. & G. C. Perola 1973. Dynamical Models of Tailed Radio Sources in Clusters of Galaxies. *A&A*, 26:423.

Kalberla, P. M. W. & J. Kerp 2009. The Hi Distribution of the Milky Way. *ARA&A*, 47:27–61.

Kamphuis, P., B. W. Holwerda, R. J. Allen, R. F. Peletier, & P. C. van der Kruit 2007. A dust component ˜2 kpc above the plane in NGC 891. *A&A*, 471:L1–L4.

Kardashev, N. S. 1962. Nonstationarity of Spectra of Young Sources of Nonthermal Radio Emission. *SvA*, 6:317.

Kennicutt, Jr., R. C., C.-N. Hao, D. Calzetti, J. Moustakas, D. A. Dale, G. Bendo, C. W. Engelbracht, B. D. Johnson, & J. C. Lee 2009. Dust-corrected Star Formation Rates of Galaxies. I. Combinations of Hα and Infrared Tracers. *ApJ*, 703:1672–1695.

Keppel, J. W., R.-J. Dettmar, J. S. Gallagher, III, & M. S. Roberts 1991. Extraplanar ionized gas and kinematics in the edge-on galaxy NGC 891. *ApJ*, 374:507–515.

Klein, U. & A. Fletcher 2015. *Galactic and Intergalactic Magnetic Fields*.

Klein, U., R. Wielebinski, & R. Beck 1984a. A survey of the distribution of 2.8 cm-wavelength radio continuum in nearby galaxies. V - A small sample of edge-on galaxies. *A&A*, 133:19–26.

Klein, U., R. Wielebinski, & R. Beck 1984b. High frequency radio continuum investigation of M51. *A&A*, 135:213–224.

Kormendy, J. & J. C. Barentine 2010. Detection of a Pseudobulge Hidden Inside the "Box-shaped Bulge" of NGC 4565. *ApJ*, 715:L176–L179.

Krause, M. 1993. High Resolution Observations of the Magnetic Field in IC 342. In *The Cosmic Dynamo*, F. Krause, K. H. Radler, and G. Rudiger, eds., volume 157 of *IAU Symposium*, P. 305.

Krause, M. 2009. Magnetic Fields and Star Formation in Spiral Galaxies. In *Revista Mexicana de Astronomia y Astrofisica Conference Series*, volume 36 of *Revista Mexicana de Astronomia y Astrofisica Conference Series*, Pp. 25–29.

Krause, M. 2011. Magnetic fields and star formation as seen in edge-on galaxies. *ArXiv e-prints*.

Krause, M., R. Wielebinski, & M. Dumke 2006. Radio polarization and sub-millimeter observations of the Sombrero galaxy (NGC 4594). Large-scale magnetic field configuration and dust emission. *A&A*, 448:133–142.

Kregel, M. & P. C. van der Kruit 2005. Structure and kinematics of edge-on galaxy discs - IV. The kinematics of the stellar discs. *MNRAS*, 358:481–502.

Kronberg, P. P., H. Lesch, & U. Hopp 1999. Magnetization of the Intergalactic Medium by Primeval Galaxies. *ApJ*, 511:56–64.

Kulsrud, R. & W. P. Pearce 1969. The Effect of Wave-Particle Interactions on the Propagation of Cosmic Rays. *ApJ*, 156:445.

Laine, S., P. N. Appleton, S. T. Gottesman, M. L. N. Ashby, & C. A. Garland 2010. Warm Molecular Hydrogen Emission in Normal Edge-on Galaxies NGC 4565 and NGC 5907. *AJ*, 140:753–769.

Lerche, I. & R. Schlickeiser 1980. The effect of convection on the propagation of relativistic galactic electrons. *ApJ*, 239:1089–1106.

Lerche, I. & R. Schlickeiser 1981. On the transport and propagation of relativistic electrons in galaxies. *ApJ*, 47:33–85.

Lerche, I. & R. Schlickeiser 1982. On the transport and propagation of relativistic electrons in galaxies The effect of adiabatic deceleration in a galactic wind for the steady state case. *A&A*, 107:148–160.

Lesch, H. & M. Chiba 1997. On the Origin and Evolution of Galactic Magnetic Fields. *FCPH*, 18:273–368.

Li, J.-T., R. Beck, R.-J. Dettmar, G. Heald, J. Irwin, M. Johnson, A. A. Kepley, M. Krause, E. J. Murphy, E. Orlando, R. J. Rand, A. W. Strong, C. J. Vargas, R. Walterbos, Q. D. Wang, & T. Wiegert 2016. CHANG-ES - VI. Probing Supernova energy deposition in spiral galaxies through multiwavelength relationships. *MNRAS*, 456:1723–1738.

Longair, M. S. 2011. *High Energy Astrophysics*.

Mac Low, M.-M. & A. Ferrara 1999. Starburst-driven Mass Loss from Dwarf Galaxies: Efficiency and Metal Ejection. *ApJ*, 513:142–155.

Mapelli, M., B. Moore, & J. Bland-Hawthorn 2008. Lopsided galaxies: the case of NGC 891. *MNRAS*, 388:697–708.

Mora, S. C. & M. Krause 2013. Magnetic field structure and halo in NGC 4631. *A&A*, 560:A42.

Moss, D., D. Sokoloff, R. Beck, & M. Krause 2010. Galactic winds and the symmetry properties of galactic magnetic fields. *A&A*, 512:A61.

Mouhcine, M., R. Ibata, & M. Rejkuba 2010. A Panoramic View of the Milky Way Analog NGC 891. *ApJ*, 714:L12–L15.

Mulcahy, D. D. 2014. *Nearby Spiral Galaxies at Low Frequencies*. PhD thesis, Universität Bonn.

Mulcahy, D. D., A. Horneffer, R. Beck, G. Heald, A. Fletcher, A. Scaife, B. Adebahr, J. M. Anderson, A. Bonafede, M. Brüggen, G. Brunetti, K. T. Chyży, J. Conway, R.-J. Dettmar, T. Enßlin, M. Haverkorn, C. Horellou, M. Iacobelli, F. P. Israel, H. Junklewitz, W. Jurusik, J. Köhler, M. Kuniyoshi, E. Orrú, R. Paladino, R. Pizzo, W. Reich, & H. J. A. Röttgering 2014. The nature of the low-frequency emission of M 51. First observations of a nearby galaxy with LOFAR. *A&A*, 568:A74.

Murgia, M. 1996. Laurea thesis, univ. of bologna.

Murphy, E. J. 2009. The Far-Infrared-Radio Correlation at High Redshifts: Physical Considerations and Prospects for the Square Kilometer Array. *ApJ*, 706:482–496.

Näslund, M. & S. Jörsäter 1997. Surface photometry of the edge-on spiral NGC 4565. I. V-band data and the extended optical warp. *A&A*, 325:915–922.

Neininger, N. & M. Dumke 1999. Intergalactic Cold Dust in the NGC 4631 Group. *Proceedings of the National Academy of Science*, 96:5360–5365.

Neininger, N., M. Guelin, S. Garcia-Burillo, R. Zylka, & R. Wielebinski 1996. Cold dust and molecular line emission in NGC4565. *A&A*, 310:725–736.

Niklas, S. & R. Beck 1997. A new approach to the radio-far infrared correlation for non-calorimeter galaxies. *A&A*, 320:54–64.

Niklas, S., U. Klein, & R. Wielebinski 1997. A radio continuum survey of Shapley-Ames galaxies at λ 2.8cm. II. Separation of thermal and non-thermal radio emission. *A&A*, 322:19–28.

Norman, C. A. & S. Ikeuchi 1989. The disk-halo interaction - Superbubbles and the structure of the interstellar medium. *ApJ*, 345:372–383.

Oosterloo, T., F. Fraternali, & R. Sancisi 2007. The Cold Gaseous Halo of NGC 891. *AJ*, 134:1019.

Oppermann, N., H. Junklewitz, G. Robbers, M. R. Bell, T. A. Enßlin, A. Bonafede, R. Braun, J. C. Brown, T. E. Clarke, I. J. Feain, B. M. Gaensler, A. Hammond, L. Harvey-Smith, G. Heald, M. Johnston-Hollitt, U. Klein, P. P. Kronberg, S. A. Mao, N. M. McClure-Griffiths, S. P. O'Sullivan, L. Pratley, T. Robishaw, S. Roy, D. H. F. M. Schnitzeler, C. Sotomayor-Beltran, J. Stevens, J. M. Stil, C. Sunstrum, A. Tanna, A. R. Taylor, & C. L. Van Eck 2012. An improved map of the Galactic Faraday sky. *A&A*, 542:A93.

Pacholczyk, A. G. 1970. *Radio astrophysics. Nonthermal processes in galactic and extragalactic sources*.

Parker, E. N. 1979. *Cosmical magnetic fields: Their origin and their activity*.

Pizzo, R. F. & A. G. de Bruyn 2009. Radio spectral study of the cluster of galaxies Abell 2255. *A&A*, 507:639–659.

Pohl, M. & R. Schlickeiser 1990. Implications of the unification of cosmic ray transport and Galactic wind models. *A&A*, 239:424–436.

Pohl, M., R. Schlickeiser, & E. Hummel 1991. A statistical analysis of cosmic ray propagation effects on the low frequency radio spectrum of spiral galaxies. *A&A*, 250:302–311.

Popescu, C. C., R. J. Tuffs, N. D. Kylafis, & B. F. Madore 2004. Far Infrared mapping of NGC 891. *A&A*, 414:45–52.

Ptuskin, V. S., H. J. Voelk, V. N. Zirakashvili, & D. Breitschwerdt 1997. Transport of relativistic nucleons in a galactic wind driven by cosmic rays. *A&A*, 321:434–443.

Radburn-Smith, D. J., R. S. de Jong, A. C. Seth, J. Bailin, E. F. Bell, T. M. Brown, J. S. Bullock, S. Courteau, J. J. Dalcanton, H. C. Ferguson, P. Goudfrooij, S. Holfeltz, B. W. Holwerda, C. Purcell, J. Sick, D. Streich, M. Vlajic, & D. B. Zucker 2011. The GHOSTS Survey. I. Hubble Space Telescope Advanced Camera for Surveys Data. *ApJ*, 195:18.

Radburn-Smith, D. J., R. S. de Jong, D. Streich, E. F. Bell, J. J. Dalcanton, A. E. Dolphin, A. M. Stilp, A. Monachesi, B. W. Holwerda, & J. Bailin 2014. Constraining the Age of the NGC 4565 H I Disk Warp: Determining the Origin of Gas Warps. *ApJ*, 780:105.

Rand, R. J. 1997. A Very Deep Spectrum of the Diffuse Ionized Gas in NGC 891. *ApJ*, 474:129–139.

Rand, R. J. 1998. Further Spectroscopy of the Diffuse Ionized Gas in NGC 891 and Evidence for a Secondary Source of Ionization. *ApJ*, 501:137–152.

Rand, R. J., S. R. Kulkarni, & J. J. Hester 1990. The distribution of warm ionized gas in NGC 891. *ApJ*, 352:L1–L4.

Rand, R. J., S. R. Kulkarni, & J. J. Hester 1992. Warm ionized gas in the edge-on galaxies NGC 4565 and NGC 4631. *ApJ*, 396:97–103.

Rand, R. J. & A. G. Lyne 1994. New Rotation Measures of Distant Pulsars in the Inner Galaxy and Magnetic Field Reversals. *MNRAS*, 268:497.

Rand, R. J., K. Wood, R. A. Benjamin, & S. E. Meidt 2011. Infrared Spectroscopy of the Diffuse Ionized Halos of Edge-on Galaxies. *ApJ*, 728:163.

Rau, U. & T. J. Cornwell 2011. A multi-scale multi-frequency deconvolution algorithm for synthesis imaging in radio interferometry. *A&A*, 532:A71.

Relaño, M., U. Lisenfeld, P. G. Pérez-González, J. M. Vílchez, & E. Battaner 2007. On the Metallicity Dependence of the 24 μm Luminosity as a Star Formation Tracer. *ApJ*, 667:L141–L144.

Rieke, G. H., A. Alonso-Herrero, B. J. Weiner, P. G. Pérez-González, M. Blaylock, J. L. Donley, & D. Marcillac 2009. Determining Star Formation Rates for Infrared Galaxies. *ApJ*, 692:556–573.

Rossa, J., M. Dahlem, R.-J. Dettmar, & R. P. van der Marel 2008. HST/ACS Observations of Star Formation Driven Outflows in Nearby Edge-on Spiral Galaxies: Dependence of Halo Morphology on Star Formation Activity. *ArXiv e-prints*.

Rossa, J. & R.-J. Dettmar 2003a. An Hα survey aiming at the detection of extraplanar diffuse ionized gas in halos of edge-on spiral galaxies. I. How common are gaseous halos among non-starburst galaxies? *A&A*, 406:493–503.

Rossa, J. & R.-J. Dettmar 2003b. An Hα survey aiming at the detection of extraplanar diffuse ionized gas in halos of edge-on spiral galaxies. II. The Hα survey atlas and catalog. *A&A*, 406:505–525.

Rossa, J., R.-J. Dettmar, R. A. M. Walterbos, & C. A. Norman 2004. A Hubble Space Telescope WFPC2 Investigation of the Disk-Halo Interface in NGC 891. *AJ*, 128:674–686.

Roy, S. & A. Pramesh Rao 2004. Sgr A* at low radio frequencies: Giant Metrewave Radio Telescope observations. *MNRAS*, 349:L25–L29.

Rupen, M. P. 1991. Neutral hydrogen observations of NGC 4565 and NGC 891. *AJ*, 102:48–106.

Ruzmaikin, A. A., D. D. Sokolov, & A. M. Shukurov, eds. 1988. *Magnetic fields of galaxies*, volume 133 of *Astrophysics and Space Science Library*.

Sanders, D. B., J. M. Mazzarella, D.-C. Kim, J. A. Surace, & B. T. Soifer 2003. The IRAS Revised Bright Galaxy Sample. *AJ*, 126:1607–1664.

Sault, R. J. & M. H. Wieringa 1994. Multi-frequency synthesis techniques in radio interferometric imaging. *A&A*, 108:585–594.

Schechtman-Rook, A. & M. A. Bershady 2013. Near-infrared Detection of a Super-thin Disk in NGC 891. *ApJ*, 773:45.

Schechtman-Rook, A. & M. A. Bershady 2014. Near-infrared Structure of Fast and Slow-rotating Disk Galaxies. *ApJ*, 795:136.

Schmidt, P., G. I. G. Józsa, G. Gentile, S.-H. Oh, Y. Schuberth, N. Ben Bekhti, B. Winkel, & U. Klein 2014. Structure and kinematics of the nearby dwarf galaxy UGCA 105. *A&A*, 561:A28.

Schulz, E. 2014. Dwarf Galaxies in the Halo of NGC 891. *ApJ*, 790:76.

Schwab, F. R. 1984. Relaxing the isoplanatism assumption in self-calibration; applications to low-frequency radio interferometry. *AJ*, 89:1076–1081.

Scoville, N. Z., D. Thakkar, J. E. Carlstrom, & A. I. Sargent 1993. The scale height and radial distribution of molecular gas in NGC 891. *ApJ*, 404:L59–L62.

Shapiro, P. R. & G. B. Field 1976. Consequences of a New Hot Component of the Interstellar Medium. *ApJ*, 205:762–765.

Shklovsky, I. S. 1952. *Ast. Zh.*, 29:418.

Simmons, J. F. L. & B. G. Stewart 1985. Point and interval estimation of the true unbiased degree of linear polarization in the presence of low signal-to-noise ratios. *A&A*, 142:100–106.

Sofue, Y. & N. Nakai 1994. CO observations of edge-on galaxies. 4. NGC 4565: Radial variation of the H2-to-H I ratio. *PASJ*, 46:147–154.

Soida, M., M. Krause, R.-J. Dettmar, & M. Urbanik 2011. The large scale magnetic field structure of the spiral galaxy NGC 5775. *A&A*, 531:A127.

Sokoloff, D. D., A. A. Bykov, A. Shukurov, E. M. Berkhuijsen, R. Beck, & A. D. Poezd 1998. Depolarization and Faraday effects in galaxies. *MNRAS*, 299:189–206.

Strickland, D. K., T. M. Heckman, E. J. M. Colbert, C. G. Hoopes, & K. A. Weaver 2004. A High Spatial Resolution X-Ray and Hα Study of Hot Gas in the Halos of Star-forming Disk Galaxies. I. Spatial and Spectral Properties of the Diffuse X-Ray Emission. *ApJ*, 151:193–236.

Strong, A. W. 1978. The radio halo of NGC 891. *A&A*, 66:205–209.

Strong, A. W., I. V. Moskalenko, & V. S. Ptuskin 2007. Cosmic-Ray Propagation and Interactions in the Galaxy. *Annual Review of Nuclear and Particle Science*, 57:285–327.

Sukumar, S. & R. J. Allen 1991. Polarized radio emission from the edge-on spiral galaxies NGC 891 and NGC 4565. *ApJ*, 382:100–107.

Swaters, R. A., R. Sancisi, & J. M. van der Hulst 1997. The H I Halo of NGC 891. *ApJ*, 491:140–145.

Tabatabaei, F. S., R. Beck, E. Krügel, M. Krause, E. M. Berkhuijsen, K. D. Gordon, & K. M. Menten 2007. High-resolution radio continuum survey of M 33. II. Thermal and nonthermal emission. *A&A*, 475:133–143.

Tabatabaei, F. S., M. Krause, A. Fletcher, & R. Beck 2008. High-resolution radio continuum survey of M 33. III. Magnetic fields. *A&A*, 490:1005–1017.

Tribble, P. C. 1993. Radio spectral ageing in a random magnetic field. *MNRAS*, 261:57–62.

Tüllmann, R., D. Breitschwerdt, J. Rossa, W. Pietsch, & R.-J. Dettmar 2006. The multi-phase gaseous halos of star-forming late-type galaxies. II. Statistical analysis of key parameters. *A&A*, 457:779–785.

Tüllmann, R., R.-J. Dettmar, M. Soida, M. Urbanik, & J. Rossa 2000. The thermal and non-thermal gaseous halo of NGC 5775. *A&A*, 364:L36–L41.

Tully, R. B. 1988. *Nearby galaxies catalog*.

van der Hulst, J. M. & R. Sancisi 2005. Gas Accretion in Galactic Disks. In *Extra-Planar Gas*, R. Braun, ed., volume 331 of *Astronomical Society of the Pacific Conference Series*, P. 139.

van der Kruit, P. C. & L. Searle 1981. Surface Photometry of Edge-On Spiral Galaxies. II - the Distribution of Light and Colour in the Disk and Spheroid of NGC891. *A&A*, 95:116.

Vogler, A., W. Pietsch, & P. Kahabka 1996. ROSAT observations of three edge-on spiral galaxies. *A&A*, 305:74.

Vollmer, B., F. Nehlig, & R. Ibata 2015. The flaring HI disk of the nearby spiral galaxy NGC 2683. *ArXiv e-prints*.

Wardle, J. F. C. & P. P. Kronberg 1974. The linear polarization of quasi-stellar radio sources at 3.71 and 11.1 centimeters. *ApJ*, 194:249–255.

Wentzel, D. G. 1974. Cosmic-ray propagation in the Galaxy - Collective effects. *ARA&A*, 12:71–96.

White, R. L. & R. H. Becker 1992. A new catalog of 30,239 1.4 GHz sources. *ApJ*, 79:331–467.

Wiegert, T., J. Irwin, A. Miskolczi, P. Schmidt, S. C. Mora, A. Damas-Segovia, Y. Stein, J. English, R. J. Rand, I. Santistevan, R. Walterbos, M. Krause, R. Beck, R.-J. Dettmar, A. Kepley, M. Wezgowiec, Q. D. Wang, G. Heald, J. Li, S. MacGregor, M. Johnson, A. W. Strong, A. DeSouza, & T. A. Porter 2015. CHANG-ES. IV. Radio Continuum Emission of 35 Edge-on Galaxies Observed with the Karl G. Jansky Very Large Array in D Configuration – Data Release 1. *AJ*, 150:81.

Wielebinski, R. & A. von Kap-Herr 1977. The radiocontinuum of NGC 4631 at high frequencies. *A&A*, 59:L17.

Yim, K., T. Wong, R. Xue, R. J. Rand, E. Rosolowsky, J. M. van der Hulst, R. Benjamin, & E. J. Murphy 2014. The Interstellar Medium and Star Formation in Edge-On Galaxies. II. NGC 4157, 4565, and 5907. *AJ*, 148:127.

Zimmer, F., H. Lesch, & G. T. Birk 1997. Dissipation of magnetic fields in the Galactic halo. *A&A*, 320:746–756.

Zirakashvili, V. N., D. Breitschwerdt, V. S. Ptuskin, & H. J. Voelk 1996. Magnetohydrodynamic wind driven by cosmic rays in a rotating galaxy. *A&A*, 311:113–126.

Zschaechner, L. K., R. J. Rand, G. H. Heald, G. Gentile, & G. Józsa 2012. HALOGAS: H I Observations and Modeling of the Nearby Edge-on Spiral Galaxy NGC 4565. *ApJ*, 760:37.